

Mechanical behaviour of fluid lubricated faults during earthquake nucleation and propagation

Présentée le 18 août 2020

à la Faculté de l'environnement naturel, architectural et construit
Laboratoire expérimental de mécanique des roches
Programme doctoral en mécanique

pour l'obtention du grade de Docteur ès Sciences

par

Chiara CORNELIO

Acceptée sur proposition du jury

Prof. J.-F. Molinari, président du jury
Prof. M. E. S. Violay, directrice de thèse
Dr E. Bayart, rapporteuse
Prof. D. Faulkner, rapporteur
Prof. B. Lecampion, rapporteur



Acknowledgements

The present thesis summarizes my research carried out during the previous four years in the Laboratory of Experimental Rock Mechanics (LEMR) at École Polytechnique Fédérale de Lausanne (EPFL). This research is funded by EPFL and by SFOE (Swiss Federal Office of Energy) through the EDGAR project (Dimensionnement du réseau de fractures dans les réservoirs géothermaux).

I would like to offer my special thanks to Prof. Marie Violay, for accepting me as PhD student, for creating a stimulating environment favoring interaction, mutual support and scientific (or not) discussions, for guiding me into geophysics science. I would like to thank her for being patient with my slow approach to the experimental world, for the complete understanding of my work and personal needs. It was an honor to learn from you and I hope that this thesis is just the first chapter of our collaboration.

I would like to acknowledge all the members of the committee, Prof. Elsa Bayart, Prof. Daniel Faulkner, and Prof. Brice Lecampion, and the President of the jury Prof. Jean Francois Molinari for having the time and consideration to evaluate my research. Thank you all for the constructive discussion, criticism, and comments.

My grateful thanks are also extended to Dr. Elena Spagnuolo, Dr. Francois Passelegue, Prof. Stefan Nielsen and Prof. Giulio Di Toro. Thank you for the discussion and for the support during the revision processes of our research.

I would like to thank Rosana and her assistants for taking care of all the administrative work. I would like to thank Laurent, Benjamin, and Aurelien for the technical support, for the suggestions and ideas in solving laboratory issues. Thanks to Federica for the warm welcome, for helping me to understand how to manage the students and for the kind words. I would extend my thanks to Michel and Laurent for realizing all the mechanical parts I required despite my bad French.

During these years, I had the pleasure to share the challenges of research with many wonderful people, and some of those become very good friends. I wish to thank all the LEMR crew: Felipe, Mateo, Corentin, Federica, Carolina, Barnaby, Lucas, Henri, Francois, Mathias. The last

Acknowledgements

four years would not be the same without your friendship and kindness. I am very grateful to Eleonora, Alberto, Gianluca, Jacopo (and Chiara!), Angelica, Elena and all the former and current LMS people with whom I had good time together.

Thanks to the friends of a lifetime Luca, Giusy, Claudio, Fabio, Federico, Valentina, Fabrizia, Silvia, Raffaella. Even if with time we have become quite scattered in space, you will always be the best.

Thanks to my family, my parents Renzo and Tiziana, my sisters Federica and Anastasia and their husbands Stefano and Riccardo, for the unconditional love and for always being the most reliable and supportive people I could ever hope to have on my side.

Last, but not least, thanks to Stefano for... too many things. There is no distance (or global pandemic!) which will be able to divide us.

Lausanne, 18th August 2020

Chiara



Abstract

One of the most alarming recent findings in geo-sciences is the worldwide increase in the number of human-induced seismicity. The latter is due to engineering operations in deep reservoirs for hydrocarbon production, wastewater and CO₂ storage and exploitation of geothermal resources which result in the reactivation of nearby faults. While the reactivation of faults due to fluid pressure has been extensively studied, the influence of fluid properties including its viscosity has been overlooked, even if the viscosity of injected fluids can vary of several orders of magnitude. In this thesis, we aim at understanding the influence of fluids viscosity on the phases of the seismic cycle, in particular during seismic slip nucleation, reactivation and propagation.

The first section of this study deals with the effect of pressurized viscous fluid on the fault plane during earthquake nucleation. The nucleation phase is analyzed in the light of the rate and state friction law and our results show a transition from stable to potentially unstable behaviour with the increase of fluid viscosity.

The second section of this thesis focuses on the reactivation of fault in presence of pressurized viscous fluid on the fault plane. The increase of the loading surrounding the fault is simulated by the gradual increase of the shear stress acting on the fault. The results show that fluid viscosity does not influence the onset of the reactivation which appears to follow the Byerlee rule. However, the fluid viscosity influences the dominant fault weakening mechanisms after reactivation.

To better understand this point, the third section focuses on the decay of the dynamic friction coefficient of a lubricated fault during earthquake propagation and fault weakening. The experimental results show that elasto-hydrodynamic theory, original developed for metal contact, is a very efficient lubricating mechanism also for rock contact surfaces. Moreover, the study of the energy balance shows that a low fluid viscosity can inhibit earthquake propagation, while high fluid viscosity can enhance the earthquake propagation.

Finally, in the last section, the experimental results obtained in this thesis are compared with eight well documented cases of induced seismicity. We show that elasto-hydrodynamic might explain the reduction of fault strength during these earthquakes which is proportional to the viscosity of the injected fluid.

The results of this Ph.D. thesis find direct implications for the concept of human-induced

Abstract

seismicity and, more, in general, fluids induced seismicity. The viscosity of the involved fluids has an effect on the lubrication of the fault that should not be ignored. Hence, this study might be the starting point for the development of long-term risk mitigation strategies.

Keywords: Fluid viscosity, Elasto-hydrodynamic lubrication, friction, fault stability, earthquake propagation, fluid induced seismicity.



Résumé

Une des problématiques les plus récentes dans le domaine des géosciences est l'augmentation au niveau planétaire du nombre de tremblements de terre induits par l'Homme. Ce phénomène est dû aux opérations d'ingénierie dans les réservoirs profonds, comme la production d'hydrocarbures, la réinjection des eaux usées, le stockage de CO₂, ou l'exploitation de ressources géothermiques, qui peuvent entraîner la réactivation des failles situées à proximité et dans le réservoir. Alors que la réactivation des failles due à l'extraction ou à l'injection de fluides a été largement étudiée, l'influence des propriétés des fluides, notamment la viscosité, a été sous-évaluée, même si elle peut varier de plusieurs ordres de grandeur. Cette thèse, a pour objectif d'étudier l'influence des fluides visqueux sur le cycle sismique, avec un focus sur le glissement sismique pendant les phases de nucléation, réactivation et propagation.

Dans la première partie de cette thèse, le comportement frictionnel d'une faille saturée par un fluide visqueux sous pression est analysé durant la phase de nucléation d'un tremblement de terre. Cette phase est modélisée à l'aide d'une loi de "rate and state". On y démontre comment l'augmentation de la viscosité du fluide sur une faille en granite entraîne la transition d'un état stable à un autre potentiellement instable. La deuxième partie de cette thèse discute l'effet de la viscosité d'un fluide sur la réactivation des failles. L'augmentation des forces tectoniques autour de la faille a été simulée en laboratoire par une augmentation graduelle de la force de cisaillement sur la faille expérimentale. Les résultats montrent que la viscosité des fluides n'a pas d'effet sur la force de cisaillement nécessaire pour réactiver la faille, qui suit la règle de « Byerlee ». Cependant, elle influence le comportement de la faille après sa réactivation. La troisième partie de cette thèse se concentre sur la relation entre le coefficient de friction dynamique (un paramètre important pour comprendre la propagation d'un séisme) et la viscosité du fluide présent au cœur de la faille. Les résultats expérimentaux sur matériaux rocheux confirment la théorie de la lubrification hydrodynamique, initialement développée pour décrire les contacts entre matériaux métalliques. De plus, le bilan énergétique pendant glissement montre qu'un fluide à basse viscosité peut ralentir la propagation d'un séisme, alors qu'un fluide à haute viscosité peut en aider sa propagation. Enfin, la dernière partie de cette thèse compare les résultats expérimentaux obtenus en CH₃ et CH₄ avec huit cas de séismes induits par l'Homme et bien documentés. Nous établissons que le saut de contrainte pendant ces tremblements de terre est proportionnel à la viscosité du fluide injecté, comme

Résumé

prévu par la théorie de la lubrification hydrodynamique. Les résultats de cette thèse doctorale s'appliquent aux séismes induits par l'Homme et, plus généralement, à tous les séismes qui impliquent la présence de fluides. La viscosité des fluides présents au cœur des failles a un effet lubrifiant qui ne devrait pas être ignoré. Cette étude est un point de départ pour l'élaboration de stratégies d'injection dans les réservoirs et la gestion des risques sismiques associés.

Mots-clés : viscosité des fluides, lubrification hydrodynamique, friction, stabilité des failles, propagation d'un séisme, séismes induits



Riassunto

Uno dei problemi più importanti nel campo della geoscienza è l'incremento dei terremoti indotti dall'Uomo in tutto il mondo. Questo è dovuto alle operazioni ingegneristiche nei reservoir profondi per la produzione di idrocarburi, esplorazione delle risorse geotermiche, stoccaggio di CO₂ e acque di reflue industriali, che provocano la riattivazione di faglie presenti nel reservoir o in prossimità di esso. Mentre la riattivazione di faglie dovuta all'aumento della pressione dei fluidi è stata ampiamente studiata, l'influenza delle proprietà dei fluidi, compresa la viscosità, è stata sottovalutata. In questa tesi, noi studiamo l'influenza dei fluidi viscosi sulle fasi del ciclo sismico, in particolare la sua influenza sullo scivolamento sismico nelle fasi di nucleazione, riattivazione e propagazione.

Nella prima parte di questa tesi, mostriamo l'effetto di un fluido viscoso sulla fase di nucleazione di un terremoto. La fase di nucleazione è stata studiata mediante la nota legge di "rate and state". In questo primo capitolo si mostra come l'aumento della viscosità del fluido su una faglia in granito promuove la transizione da un suo stato stabile a uno potenzialmente instabile.

La seconda parte della tesi, mostra gli effetti della viscosità dei fluidi nella riattivazione di una faglia. L'aumento degli sforzi tettonici nel suo intorno sono stati simulati con un graduale aumento dello sforzo di taglio sulla faglia sperimentale. Viene mostrato come la viscosità del fluido non abbia un effetto sullo sforzo di taglio per riattivare la faglia, che continua a seguire la regola di Byerlee. Tuttavia, la viscosità dei fluidi ha un'influenza sul comportamento della faglia dopo la sua riattivazione.

Con lo scopo di approfondire questo comportamento della faglia, la terza parte di questa tesi spiega la caduta di attrito di una faglia lubrificata durante un terremoto. I risultati sperimentali dimostrano che la teoria della lubrificazione idrodinamica, teoria originalmente sviluppata per il contatto tra parti meccaniche, resta valida anche in meccanica delle rocce. Inoltre, lo studio del bilancio energetico, per gli esperimenti di attrito condotti in questa parte, mostrano che una bassa viscosità del fluido può avere un effetto di inibizione della propagazione di un terremoto, mentre un fluido ad alta viscosità può promuoverne la propagazione.

Infine, nell'ultima parte della tesi, i dati sperimentali raccolti nel terzo e quarto capitolo, vengono confrontati con otto casi ben documentati di terremoti indotti dall'uomo. La caduta di sforzo stimata dai dati sismologici per i terremoti indotti è proporzionale alla viscosità del

Riassunto

fluido precedentemente iniettato nella faglia, come previsto dalla teoria della lubrificazione idrodinamica.

I risultati di questa tesi di dottorato, trovano applicazione nel campo dei terremoti indotti dall'uomo e, più in generale, per tutti i terremoti che coinvolgono la presenza di fluidi. La viscosità dei fluidi coinvolti nel ciclo sismico hanno un effetto di lubrificazione del piano di faglia che non dovrebbe essere ignorato. Questo studio, quindi, potrebbe essere un punto di partenza per strategia a lungo termini dei rischi di eventi sismici indotti.

Parole chiave: Viscosità dei fluidi, lubrificazione idrodinamica, attrito, stabilità della faglia, propagazione del terremoto, sismicità indotta



Contents

Acknowledgements	i
Abstract (English/French/Italian)	iii
List of Figures	xiii
List of Tables	xxi
1 Introduction	1
1.1 Motivations	1
1.2 Human-induced seismicity	2
1.3 Fault structure and fluid flow in fault zones	7
1.4 Friction	9
1.4.1 Friction of fault rocks	9
1.4.2 Effect of fluid pressure	10
1.5 The lubrication theory and the Stribeck curve	11
1.6 The earthquake cycle	16
1.7 Earthquake nucleation	17
1.7.1 Slip-weakening law	18
1.7.2 Rate and state friction law	20
1.8 Earthquake propagation	23
1.8.1 Thermal weakening processes	24
1.8.2 Weakening processes dependent on fluid behaviour	26
1.8.3 Weakening mechanisms related to wear products	27
1.9 Energy budget	30
1.10 Objective of the thesis	33
1.11 Organization of the thesis	34
2 Effect of fluid viscosity on earthquake nucleation.	39
2.1 Abstract	41
2.2 Introduction	41
2.3 Methods	42

Contents

2.4	Results	51
2.5	Discussion	53
2.6	Conclusions and Implications for Induced Seismicity	58
3	Effect of fluid viscosity on fault reactivation and co-seismic weakening	59
3.1	Abstract	61
3.2	Introduction	61
3.3	Materials and Methods	62
3.4	Results	67
3.4.1	Stage I. Single slip pulses under shear stress-step loading.	68
3.4.2	Stage II: Series of spontaneous slip bursts under shear stress-step loading.	68
3.4.3	Stage III. Unstable slip behavior (achievement of a critical unstable frictional behavior).	68
3.5	Discussion	69
3.5.1	Fault weakening mechanisms	70
3.5.2	Estimation of the breakdown work	79
3.6	Conclusions	82
4	Mechanical behaviour of fluid-lubricated faults	83
4.1	Abstract	85
4.2	Introduction	85
4.3	Method	86
4.3.1	Bulk temperature model and viscosity correction	88
4.3.2	LuGre dynamic friction model	91
4.3.3	Pseudotachylite-bearing faults (Gole Larghe fault zone in Adamello (Italy) and Bear Creek fault zone in Mount Abbot Quadrangle (USA))	92
4.4	Results	93
4.4.1	Apparent friction coefficient	93
4.4.2	Dynamic friction evolution with the Sommerfeld number	95
4.4.3	Microstructural investigation of slipping zones	96
4.5	Discussion	102
4.5.1	Rupture propagation criteria	102
4.5.2	Extrapolation to crustal earthquakes	104
4.6	Conclusions	106
5	Parametric analysis of the elastohydrodynamic lubrication efficiency on induced seismicity	109
5.1	Abstract	111
5.2	Introduction	111
5.3	S parameters for induced seismicity	113

5.4	Case studies of induced seismicity	114
5.5	Case studies	116
5.6	Comparison with theoretical and experimental frameworks	123
5.7	Conclusions	125
6	Conclusions and Perspectives	127
6.1	Summary	127
6.1.1	Nucleation phase in presence of viscous fluids	127
6.1.2	Reactivation phase in presence of viscous fluids	128
6.1.3	Propagation phase in presence of viscous fluid	128
6.1.4	Energy budget for earthquakes in presence of viscous fluids	129
6.1.5	Up-scaling to induced seismic events	129
6.2	Ongoing work	129
6.2.1	Methods	130
6.2.2	Preliminary results	131
6.3	Future work	134
Appendix A HighSTEPS: A High Strain TEMperature Pressure and Speed Apparatus to study Earthquake mechanics		135
A.1	Abstract	137
A.2	Introduction	137
A.3	Design of the apparatus	139
A.4	First Tests on the machine	147
A.5	Future machine development	152
Appendix B Effect of water and rock composition on re-strengthening of cohesive faults during the deceleration phase of seismic slip pulses		153
B.1	Abstract	155
B.2	Introduction	155
B.3	Methods	157
B.4	Results	159
B.5	Discussion	164
B.5.1	Effect of water on friction re-strengthening rate	164
B.5.2	Implications for natural earthquakes	170
B.6	Conclusions	171
Appendix C Table of rotary shear experiments performed by other authors		173
Bibliography		175

Contents

Curriculum Vitae

207



List of Figures

1.1	Schematic view of seismicity induced by fluid injection at depth by a) increase of the pore pressure on fault, with a consequent reduction of the effective state of stress b) change of the stress loading condition on the fault. c) by thermo-elastic deformation of the rock formation around the injection well	3
1.2	World Map of some induced seismicity cases involving fluid extraction or injection	5
1.3	Summary of the injected fluids viscosity in human activities which can induce seismicity. The viscosity varies by 6 orders of magnitude	7
1.4	Fluid flow and fault structure (Modified after Caine et al. (1996))	8
1.5	Mohr circles on a σ_n - τ plane.	11
1.6	Schematic of the lubrication theory.	14
1.7	Schematic of the three lubrication regimes.	16
1.8	Spring-slider system to explain the nucleation of dynamic instability.	18
1.9	Linear slip-weakening law and nucleation model proposed by Ohnaka (2003) .	19
1.10	Schematic illustration of the frictional response to velocity-stepping following the rate and state frictional law.	21
1.11	Stability diagram for velocity weakening material from (Gu et al., 1984).	22
1.12	Dynamic friction coefficient (i.e., steady state friction coefficient in the figure) versus slip-rate from (Di Toro et al., 2011).	24
1.13	Schematic of the energy budget for a) earthquake rupture seismological model and b) laboratory earthquakes.	31
2.1	Sketch of the triaxial cell FIRST, built by the company TOP industry.	43

List of Figures

- 2.2 a) Picture of the sample assembly on the triaxial apparatus FIRST. b) Sketch of the experimental configuration, fluid pressure lines and fluid pressure pump. The fluid pressure P_f is the average of the two measured pressures, P_1 and P_2 . A fluid separator is used for the experiments performed in presence of viscous fluids. c) Experimental curves of the evolution of the apparent friction $\mu = \tau / \sigma'_n$ versus the slip of the fault for experiment ds042 (blue curve) performed under water saturated conditions at 50 MPa effective normal stress. The apparent friction μ is offset considering the seal friction. Green rectangles correspond to zoom-in panel d and e. d) Model inversion of the experimental data with the Persson law resulting in rate-and-state values of a and b for a velocity step from $V_0 = 1 \mu\text{m/s}$ to $V_1 = 0.3 \mu\text{m/s}$. e) Model inversion of the experimental data with the Persson law resulting in rate-and-state values of a and b for a velocity step from $V_0 = 3 \mu\text{m/s}$ to $V_1 = 10 \mu\text{m/s}$ 47
- 2.3 Photographs of the starting samples a) top view b) later view and initial roughness. On both half cylindrical samples, we made a borehole with inclination of 45° respect to the both the slip surfaces and the base of the semi-cylinder in order to allow the fluid to reach easily the fault surfaces. c) Initial surface and roughness of the Lapeyre samples. The RMS surface roughness, obtained using the optical profilometer ContourGT-I 3D Optical Microscope Bruker Nano surfaces Division, was $3 \mu\text{m}$ 48
- 2.4 Experimental curves. a) Experimental curves of the evolution of the apparent friction $\mu = \tau / \sigma'_n$ versus the slip of the fault for experiment ds042 (blue curve) performed under water saturated condition at 50 MPa effective normal stress and ds050 (magenta curve) performed under glycerol 99 saturated conditions at 50 MPa effective normal stress. Zoom of the initial stick-slip in the red box. b) Evolution of the change in fluid volume in millimeters cubed during shearing for experiment ds042 (blue curve) performed under water saturated conditions at 50 MPa effective normal stress and ds050 (magenta curve) performed under glycerol 99 saturated conditions at 50 MPa effective normal stress. Compaction corresponds to a negative fluid volume change; dilation correspond to a positive fluid volume change. 50
- 2.5 Apparent friction coefficient vs slip for all the experiments presented in this work under a) 30 MPa effective normal stress, b) 50 MPa effective normal stress. . . . 52

2.6	Static and steady state friction coefficients. a) Static friction coefficient μ_{static} versus viscosity of the fluid on the slipping surface. For the experiments performed under room humidity conditions, the viscosity of the air ($\eta = 1.88 \cdot 10^{-5}$ Pa.s) trapped in the slip zone was used. b) The steady state friction coefficient for each velocity step versus the computed Sommerfeld number. The Sommerfeld number allows us to distinguish the velocity steps in the boundary lubrication regime and the velocity steps in the mixed regime. Full markers for experiments performed at effective normal stress of 30 MPa, empty markers for experiments performed at 50 MPa effective normal stress.	53
2.7	Rate and state constitutive parameters ($a - b$) obtained with Ruina slip evolution law (x axis) and with Persson state law (y axis) for experiments performed in presence of water with effective normal stress of 30 MPa (filled markers) and at 50 MPa (empty markers). The difference in ($a - b$) values obtained with the two laws is represented by the distance from the black line (slope 1:1).	54
2.8	Rate and state constitutive parameters a) the direct effect (a), b) the evolutive effect (b) and c) the critical distance (d_c) versus fluid viscosity. a) the (a) parameter is almost constant. b) the (b) parameter increases increasing fluid viscosity. c) the (d_c) parameter does not show clear tendency with the fluid viscosity. . .	56
2.9	Average values of ($a - b$) rate and state parameters versus viscosity of the fluid for experiments performed under fault fluid saturated conditions and under boundary lubrication regime. The parameters were obtained using the Persson state law coupled with the friction empirical law. Full markers for experiments performed at 30 MPa effective normal stress and empty markers for experiments performed at 50 MPa effective normal stress.	56
2.10	($a - b$) frictional parameters versus effective normal stress ($\sigma'_n = \sigma_n - P_f$) for experiments a) under room-humidity condition, b) in presence of water ($\eta=1.002$ mPa.s) c) mixture of 60% glycerol 40% water ($\eta=10.8$ mPa.s), d) 85% glycerol 15% water ($\eta=107.5$ mPa.s). In colorbars the slip-rate V_0 in $\mu\text{m/s}$ before each velocity steps.	57
3.1	Initial surface and roughness of the Westerly granite samples.	63
3.2	Experimental assembly	65
3.3	Recorded shear stress τ (measured at the S-beam load cell), fluid pressure P_f and slip-rate V evolution versus time in the experiments (see main text for description). All the experiments were conducted at an effective normal stress of ca. 10 MPa.	66
3.4	Experiment s1409 performed under room-humidity conditions.	67
3.5	Peak friction coefficient vs viscosity of the fluid on the slipping surface.	69

List of Figures

3.6	Apparent friction coefficient μ vs slip-rate V normalized by the maximum imposed slip-rate V_{max} ($V_{max}=0.1$ m/s for all experiments with the exception of s1781 where $V_{max}=0.2$ m/s)	71
3.7	Comparison between measured minimum shear stress during stage III and the estimated minimum shear stress according to flash heating and weakening mechanism (Eq. 3.2) under a) room humidity conditions and in the presence of 100% distilled water b), 60%glyc/40%water c), 85%glyc,15%water d) and, 99% glycerol e)	73
3.8	Thermal pressurization (TP) model geometry and results.	74
3.9	Comparison between experimental minimum shear stress and the predicted minimum shear stress by TP models in presence of a) water, b) 60%glyc/40%water, c) 85%glyc,15%water, d) 99% glycerol.	76
3.10	Comparison between minimum shear stress measured in the experiments and estimated in Finite Element Analysis 2D EHD models in the presence of a) 100% distilled water, b) 60%glyc/40%water, c) 85%glyc,15%water, d) 99% glycerol. . .	77
3.11	Misfit or percent error (3.3) between the measured minimum shear stress and the estimated one for a) Flash-Heating (FH), b) Thermal-Pressurization (TP) and c) Elastohydrodynamics (EHD).	78
3.12	Breakdown work versus the $\Delta U = U_{min} - U_{in}$ for short-lived and long-lived events under a) room humidity conditions (black and grey stars), b) in the presence of water (blue dots), c) in presence of 60%glycerol/40%water mixtures (orange diamonds), 85%glycerol/15%water mixtures (green triangles), and 99% glycerol (purple squares).	80
3.13	Energy budget and breakdown work in experimental and natural earthquakes.	81
4.1	FEA 2D time dependent heat diffusion model.	89
4.2	Evolution of fluids viscosity (water and glycerol/water mixtures) with temperature according to the empirical law of Cheng (2008).	91
4.3	Apparent friction coefficient versus slip, friction coefficients versus viscosity, η , and Sommerfeld number $S = 6 V \eta L / (\sigma_{eff} H_0^2)$	94
4.4	a) Static friction coefficient versus viscosity η . In the semi-logarithmic diagram, the static friction coefficient slightly decreases linearly with increasing η (all values are reported in Table 4.1). b) Peak friction coefficients versus Sommerfeld number. Experiments were performed under the following environmental and hydraulic conditions: 100% water (H2O, blue in colour dots), 60% glycerol/40% water (orange diamonds), 85% glycerol/15% water (yellow triangles) and pure glycerol (99% glycerol, purple squares)	95
4.5	The a) μ_{peak} and b) μ_{dyn} vs slip-rate (V) for experiments performed in the presence of fluids and under room humidity conditions (dry, black stars). . . .	96

4.6	Dynamic friction coefficient versus Sommerfeld number S	98
4.7	Roughness of the sliding surfaces and RMS values in Westerly Granite.	99
4.8	Microphotos of the sliding surfaces and RMS values in Westerly Granite.	100
4.9	Roughness of the sliding surfaces and RMS values in Carrara Marble.	101
4.10	Breakdown work and D_c versus Sommerfeld number.	103
4.11	Sommerfeld number Vs depth for earthquakes magnitude ranging between 1 and 8.	105
4.12	Range of values of η, V, L, H for which a) $S=0.001$, limit between boundary lubrication regime and mixed lubricated regime; b) $S=1$, limit between mixed lubrication regime and fully lubricated regime; c) $S=10$, fully lubricated regime.	106
5.1	Schematic representation of the asperity contacts in the three different regimes.	112
5.2	Mohr-Coulomb circles representing the average in situ stress, fault orientation and Byerlee failure criteria for the a) Basel earthquake, b) Paradox Valley earthquake, c) Youngstown earthquake, d) Prague earthquake, e) Timpson earthquake, f) Pawnee earthquake, g) Fox Creek earthquake, and h) Bowland Shale.	122
5.3	Estimated dynamic friction coefficient vs the Sommerfeld number for induced seismicity cases.	124
5.4	The multiaxis plot of the Sommerfeld number for the human-induced seismicity range of values and real events for a. $S=0.001$ (end of the boundary lubrication regime), b. $S=0.01$ (in the mixed lubrication regime), and c. $S=1$ (beginning of the mixed lubrication regime).	125
6.1	Sketch of the experimental configuration and experimental procedure	131
6.2	Fault reactivation due to fluid injection	132
6.3	Differential fluid pressure evolution along the fault plane and slip evolution during fluid injection	133
A.1	Schematics of the HighSTEPS apparatus.	140
A.2	a) Picture of the HighSTEPS machine. b) Details of the pressure vessel with high pressure ports for pore fluid and confining oil, and uniaxial and coaxial feedthroughs for electronics. c) Jacketed sample with pore pressure lines connected to the pore pressure ports.	141
A.3	a) detailed of the intensifiers, B) details of the motor tower.	142

List of Figures

- A.4 Experimental double direct shear configuration: a) pictures of the central block showing the fluid inlet and the distribution channels, pictures of the side block showing fluid inlet, hole for piezoelectric transducer and distribution channels. b) Schematics of the experimental double-direct-shear configuration. The sample holders are equipped with internal pore fluid channels for application of pore fluid pressure, injection of fluids and measurement of permeability/dilatancy of the fault rocks. c) Sketch of the working principle of the double-direct shear configuration. 146
- A.5 a) Horizontal and b) vertical machine stiffness measure with steel blocks. The horizontal stiffness is 1786 kN/mm for vertical force (F_h) higher than 60 kN. The vertical stiffness is 1379 kN/mm for horizontal force (F_v) higher than 15 kN. . . 148
- A.6 Calcite (Carrara marble) gouge and bare surfaces frictional experiments: a) shear stress versus slip during frictional sliding at $v = 6.6$ cm/s and normal stresses from 10 MPa to 50 MPa. Experiments were performed under double-direct shear configuration on gouge material. d) Steady state shear strength versus normal stress for both gouge material and bare surfaces. Data plot along a single line with a slope of 0.6, in agreement with Byerlee's rule (Byerlee, 1978). 149
- A.7 Example of velocity control and shear stress control experiments performed: a) slide-hold-slide test performed on calcite gouge at 10 MPa normal stress under room temperature and wet conditions; b) velocity step test on quartz gouge at 10 MPa normal stress under room temperature and room humidity conditions; c) high slip velocity friction test on calcite bare surface at 10 MPa normal stress under room temperature and room humidity conditions; d) shear stress control test on calcite gouge at 20 MPa normal stress under room temperature and room humidity conditions. 150
- A.8 a) Horizontal load versus time showing the load control in ramp (kN/s) and constant value (100 kN). b) Confining pressure versus time showing the control in pressure up to 80 MPa. c) Pore fluid pressure versus time showing the control in pore fluid pressure. d) Temperature versus time showing the control in temperature up to 60 °C. 152

- B.1 Evolution of the friction coefficient with time and slip rate for Carrara marble and micro-gabbro slid at seismic slip rates. a) and b) Evolution of the friction coefficient with time in Carrara marble and micro-gabbro. c) and d) Evolution of the friction coefficient measured during deceleration versus log of the sliding velocity. The experiments were conducted at target velocity $V_t=3 \text{ ms}^{-1}$, acceleration and deceleration $=7.8 \text{ ms}^{-2}$, and $\sigma_{eff,n}=20 \text{ MPa}$ (effective normal stress $=\sigma_n-P_f$). Blue curves (S615 and S567): fluid pressure experiments $\sigma_n=25 \text{ MPa}$, $P_f=5 \text{ MPa}$; green curves (S307 and S555): room humidity experiments; red curves (S614 and S585): vacuum experiments were run at $P_{vacuum}=10^{-4} \text{ mbar}$. Two examples of sliding velocity function are drawn in grey. (For interpretation of the colors in the figure(s), the reader is referred to the web version of this article.) 160
- B.2 Influence of $\sigma_{eff,n}$ on the re-strengthening for a) Carrara marble and b) micro-gabbro. Blue dots: fluid pressure experiments; green dots: room humidity experiments; red dots: vacuum experiments $P_{vacuum}=10^{-4} \text{ mbar}$ 161
- B.3 Evolution of the friction coefficient during slip deceleration versus log of the sliding velocity for a) Carrara marble (S409, S341, S296, S264) and b) micro-gabbro (S566, S567, S572 and S573). Experiments were conducted at different power density ($\sigma_{eff,n} V_t$). Target velocity (V_t) ranging from 1 and 6.5 ms^{-1} , acceleration and deceleration $=7.8 \text{ ms}^{-2}$, and $\sigma_{eff,n}$ from 10 to 30 MPa (effective normal stress $=\sigma_n-P_f$). The experiments were all performed under fluid pressure conditions ($P_f=5 \text{ MPa}$). 162
- B.4 Influence of power density (a, b) ($\sigma_{eff,n} V_t$) and slip (c, d) on the friction re-strengthening rate. Blue dots: fluid pressure experiments; green dots: room humidity experiments; red dots: vacuum experiments $P_{vacuum}=10^{-4} \text{ mbar}$. . . 163
- B.5 Microstructural observations of experimental slip surfaces and slipping zones after shearing. (a) Slipping zone after an experiment performed on micro-gabbro (s585, $V=3 \text{ ms}^{-1}$, $\sigma_n=20 \text{ MPa}$, Vacuum conditions see also Violay (2014); Violay et al. (2014a)). The slipping zone is made by quenched melt (i.e., glass matrix, see composition in Table B.3) which wraps grains of plagioclase and pyroxene that survived from frictional melting (Scanning Electron Microscope, back scatter electron image). (b) Slip surface after an experiment performed on calcitic Carrara marble (s614, $V=3 \text{ ms}^{-1}$, $\sigma_n=20 \text{ MPa}$, Vacuum conditions, see Violay (2014); Violay et al. (2014a)). The slip surface is made by micro-to nano-grains of calcite and lime. Small decarbonation vacuoles decorate the recrystallized calcite grains (Scanning Electron Microscope, secondary electron image). 165

List of Figures

- B.6 FEM 2D time dependent heat diffusion model. a) and b) Model geometry with description of the boundary conditions and mesh geometry. c) The snapshot of the temperature distribution at the end of the experiment s585 conducted on gabbro. d) Temperature evolution of the slip zone during slip deceleration ($\tau_r - \tau_{ss}$). e) Melt viscosity evolution during slip deceleration. 166
- B.7 Results of the 1D time dependent heat diffusion model fully coupled with diffusion creep flow law for both room humidity (blue and red curves) and pore fluid (green and yellow curves) conditions. 169

List of Tables

1.1	Injected fluid viscosity ranges from literature data	6
1.2	Experimental studies of stability behaviour on granite material in different conditions of normal stress σ_N , fluid pressure P_f and temperature T . For each experimental study, we report the analyzed material, the experimental condition (gouge, bare surface "bare surf." and fractured surface "fract."), the main analyzed parameter ("Par.") are reported: σ_N for normal stress, T for temperature, RMS for roughness, V for slip-rate, k for permeability. "RH" for room-humidity condition, "Wet" for partially saturated condition and "RT" for room temperature condition.	23
1.3	Experimental studies on the weakening of granite material in different conditions of normal stress σ_N , fluid pressure P_f and temperature T . The experimental condition of V for slip-rate, σ_N for normal stress, P_c confining pressure and T for temperature are reported. For "stick-slip" experiments no slip-rate is reported. "RH" for room-humidity condition and "RT" for room temperature condition. "Mech." reports the suggested weakening mechanisms activated during the laboratory experiments: "FH" for flash heating, "FM" for flash melting, "EHD" for elasto-hydrodynamic, "Powder" for powder lubrication and "TP" for thermal-pressurization.	29
2.1	Rate and state frictional parameters (a), (b), and (d_c) for experiments performed at 30 MPa and 50 MPa effective normal stress. Two different state law variables were used: Slip state variable law ("Slip") or the Persson state variable law ("Persson") depending of the environmental conditions (dry vs wet experiments). For each velocity step the initial slip-rate (V_0), the final slip-rate (V_1) and the dynamic friction coefficient before the change in slip-rate are reported.	44
2.2	Rate and state frictional parameters (a), (b), and (d_c) for experiments performed at 30 MPa and 50 MPa effective normal stress in presence of water, obtained with the slip state variable law ("Slip") and with the Persson state variable law ("Persson"). For each velocity step the initial slip-rate (V_0), the final slip-rate (V_1) and the friction coefficient before the change in slip-rate are reported.	55

List of Tables

3.1	Summary of the experimental conditions. Shear stress at fault reactivation: τ_{imp} . Condition, normal stress σ_n , fluid pressure P_f , effective normal stress σ_{eff} , and peak friction coefficient μ_{peak}	64
3.2	Slip pulse and slip bursts analysis. N.steps are the shear stress step before the Stage III. For each experiment, the number of recorded slip-pulse during the Stage I, the maximum recorded slip-rate, the number of slip bursts during the Stage II and the related maximum slip-rate are reported.	70
3.3	Thermal and hydraulic properties used in the thermal pressurization model and in the heat diffusion model. κ =thermal conductivity, λ =thermal expansion coefficient, β =compressibility coefficient, η_0 =initial viscosity, ρ = density, C = specific heat, WG=Westerly granite. a) Thermal properties of water from Goranson (1942), b) Thermal properties of water/glycerol mixtures from Bates (1936),c) Thermal properties of Westerly granite from Eppelbaum et al. (2014)	75
4.1	Summary of the experimental conditions and results. WG = Westerly Granite, CM = Carrara Marble, V =slip-rate, σ_{eff} =effective normal stress, η_0 =initial kinematic viscosity of the fluid, μ_{static} =static friction coefficient, μ_{peak} = peak friction coefficient, μ_{dyn} = dynamic friction coefficient, W_b = breakdown work for m ² fault, S = Sommerfeld number at μ_{dyn}	87
4.2	Thermal properties of the fluid, Westerly granite and Carrara Marble. κ =thermal conductivity, ρ = density, C = specific heat, WG =Westerly granite. CM =Carrara marble a) Thermal properties of water from Goranson (1942), b) Thermal properties of water/glycerol mixtures from Bates (1936) c) Thermal properties of Westerly granite from Eppelbaum et al. (2014)	90
4.3	Parameters used for computing S and μ_{dyn} for natural exhumed faults with pseudotachylite.	93
5.1	Summary of the case study reporting the magnitude, viscosity of the injected fluid, average values of depth, effective stress P_{eff} , moment of magnitude M_0 , stress drop $\Delta\tau$, slip of the event $\delta=L$, asperity size of the fault H and the Sommerfeld numeber for $V=1$ m/s.	121
B.1	Summary of experimental conditions and results. PF: Pore fluid, RH: Room Humidity, VAC: Vacuum. μ_p peak friction coefficient, μ_{dyn} steady state or dynamic friction coefficient, $\dot{\mu}_r$ friction re-strengthening rate	158
B.2	Thermal properties of the fluid (air and water) and micro-gabbro used in the FEM numerical model, as well as the thermal properties of Carrara marble used for the coupled diffusion model and plasticity flow law. K = thermal conductivity, ρ = density, C = specific heat. Φ the liquid fraction.	165

B.3	Chemical composition of the micro-gabbro (XRD) and of the glass for experiment s585 performed under vacuum conditions (Electron Microprobe Analysis). The analysis does not close to about 100% because only Fe ²⁺ was determined.	168
C.1	Published experimental data reported in 4.6.b. σ_n =normal stress, V slip-rate, μ_{peak} = peak friction coefficient, μ_{dyn} = dynamic friction coefficient, T = estimated temperature at μ_{dyn} , η = melt estimated viscosity, S = Sommerfeld number, Ref.= paper references.	173

List of Symbols

α_1	Viscous coefficient for Lugre model
α_2	Damping coefficient for Lugre model
α_{hy}	Hydraulic diffusivity [$\text{m}^2 \text{s}^{-1}$]
α_{th}	Thermal diffusivity [$\text{m}^2 \text{s}^{-1}$]
β_f, β_r	Compressibility of pore fluid and pores [Pa^{-1}]
γ	Shear Strain rate [s^{-1}]
$\delta, \Delta U$	Displacement (or slip) [m]
ζ	Hurst exponent
ζ_w	Weighting factor for water/glycerol mixtures viscosity
η	Dynamic fluid viscosity [Pas]
θ	State variable
κ	Thermal conductivity [W/(mK)]
λ_f, λ_p	Thermal expansivity of pore fluid and pores [$^{\circ}\text{C}^{-1}$]
μ	Apparent friction
μ_{dyn}	Dynamic (or steady state) friction coefficient
μ_p	Peak friction coefficient
μ_{static}	Static friction coefficient
ρ	Density [kg m^{-3}]
$\Delta\sigma$	Static stress drop [Pa]
σ_m	Mean stress [Pa]
σ_n	Normal stress [Pa]
$\sigma'_n, \sigma_{eff}, P_{eff}$	Effective normal stress normal stress [Pa]
ζ	Empirical coefficient for Stribeck curve
τ	Shear stress (or strength) [Pa]
τ_c	Contact shear strength [Pa]
τ_{dyn}	Dynamic shear stress (or strength) [Pa]
τ_{imp}	Imposed shear stress [Pa]
τ_{min}	Minimum shear stress [Pa]
τ_{peak}	Peak shear stress [Pa]
ϕ	Porosity

List of Symbols

φ	Friction angle [°]
ξ	Exponential empirical coefficient for Stribeck curve
a	Direct effect of rate and state law
A	Nominal area [m ²]
A_r	Real contact area [m ²]
b	Evolution effect of rate and state law
B	Roughness amplitude factor
C_m	Glycerol concentration
C_p	Heat capacity at constant pressure [J kg ⁻¹ K ⁻¹]
d_c	Critical slip distance [m]
D_c	Slip weakening distance [m]
E_r	Radiated energy [J m ⁻²]
F_c	Coulomb friction force for Luge model [N]
F_s	Stiction force for Luge model [N]
G	Shear modulus [Pa]
k	Permeability [m ²]
K	Stiffness [Pa m ⁻¹]
K_c	Critical stiffness [Pa m ⁻¹]
K_f	Stress orientation coefficient
L	Characteristic length for elasto-hydrodynamic [m]
L_c	Critical length [m]
M	Rigidity [N m ⁻¹]
M_0	Seismic moment [N m]
P_c	Confining Pressure [Pa]
P_f	Fluid pressure [Pa]
P_L	Lubricant pressure [Pa]
Re	Reinolds number
S	Sommerfield number
$S_{H,max}$	Maximum horizontal stress [Pa]
$S_{h,min}$	Minimum horizontal stress [Pa]
S_v	Vertical stress [Pa]
t	Time [s]
T	Temperature [°C, K]
T_w	Weakening temperature [°C, K]
ΔV	Fluid volume change [m ³]
V	Slip-rate (or velocity) [m s ⁻¹]
V_w	Critical weakening slip-rate [m s ⁻¹]
ΔW	Potential energy drop [J m ⁻²]

W_b, G_c	Breakdown work [J m^{-2}]
W_h	Frictional work or frictional heating [J m^{-2}]
W_r	Restrengthening work [J m^{-2}]
$2w, H$	Thickness [m]

1 Introduction

1.1 Motivations

The increase in energy demand worldwide makes it necessary to increase the productivity of traditional energy sources (conventional oil and gas extraction) and to develop new energy technologies (i.e., geothermal energy and unconventional oil and gas extraction). Moreover, as climate warming effects become more and more extreme, the world's energy matrix needs to be transferred towards renewable electricity production (Edenhofer et al., 2015). Further, with increasing environmental awareness, more attention is being devoted to the disposal of waste obtained during energy production (i.e., wastewater, CO₂ and nuclear waste) to reduce air and water pollution.

With these perspectives, the 2017 Swiss Federal Energy Act is designed to reduce energy consumption, increase energy efficiency and encourage the use of renewable energy. In this regard, geothermal energy is a very promising direction. However, up to now, no electricity is being produced from geothermal sources in Switzerland. One of the main obstacles is the increase in seismicity and the potential for earthquake hazard associated with water injection during geothermal production. For the safe and efficient development of green geo-energy technology, a better understanding of fluid-induced seismicity and the evaluation of its associated risks is necessary.

Energy production and waste disposal involve the exchange of fluids (i.e., oil, gas, hot water, wastewater, CO₂) between the Earth's surface and underground reservoirs using wellbores. The underground reservoirs consist of porous rocks in which fluids can be stored, collected from or sent to.

Many natural reservoirs which are relevant for EGS and unconventional oil and gas production have transport properties which are not ideal for the energy production industry. Transport

properties include the storage capacity (i.e. porosity) and the permeability of rocks discontinuities. Rocks discontinuities have low porosity constituted of micro-cracks and therefore a low storage capacity. Moreover, fluid migration may be hindered by low permeability rock discontinuities (Wibberley and Shimamoto, 2005).

To increase their productivity, reservoirs need to be stimulated to improve their transport properties and storage capacity. Reservoir stimulation consists of the injection of pressurized fracturing fluid into rock masses to create new micro-cracks or to open pre-existing micro-cracks.

However, rock masses are crosscut by faults, i.e. planar fractures which, subjected to tectonic stress, accommodate the relative displacement of the rocks. Faults are often in a state of stress close to failure (Section 1.3). In these conditions, a small stress perturbation can induce the beginning of the fault displacement, i.e. fault reactivation. After reactivation, the fault displacement can occur as a gradual and slow creep or as an earthquake, i.e. a sudden and fast rupture/failure. Earthquakes consist of the fast release of the elastic energy stored in the rock masses around the fault. If the stress perturbation in the surrounding rocks or the modification of fault rock strength occurs as a consequence of human activities, the resulting earthquake activity is defined human-induced seismicity (Ellsworth, 2013). Much human-induced seismicity is characterized by a magnitude (i.e. the measured amount of released energy) between -2 and 2 (Foulger et al., 2018). However, the 60% of detected human-induced seismicity reported in the HiQuake catalogue (Wilson et al., 2017; Foulger et al., 2018) has a magnitude higher than 2.5 and is felt by the population. Larger magnitude events can lead to social concern, economic damage and casualties (Grigoli et al., 2017; Foulger et al., 2018). Moreover, many countries worldwide define thresholds in magnitude that, if they are overcome, lead to the interruption or reduction of energy production activities.

1.2 Human-induced seismicity

In the last 25 years, in some areas of the world (e.g. the mid-continent region of the US (Ellsworth, 2013)) the number of earthquakes increased compared to the seismicity recorded before the start of the energy production activities.

The physical processes through which human activities related to the production of energy can lead to human-induced seismicity are:

- a. Increase of fluid pressure: fluid injection in rock masses can increase the fluid pressure in the rock pores or a pre-existing fault near the injection point and can, consequently, decrease the effective mean stress leading to fault reactivation. (Figure 1.1a), (Section

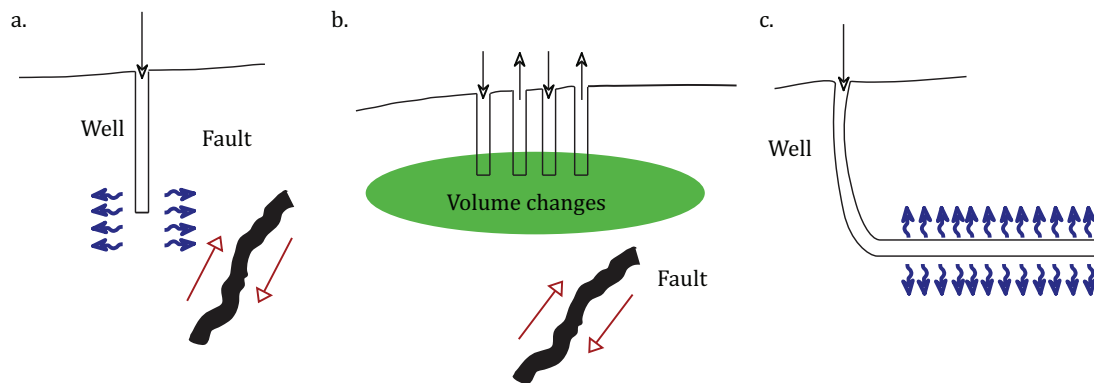


Figure 1.1: Schematic view of seismicity induced by fluid injection at depth by a) increase of the pore pressure on fault, with a consequent reduction of the effective state of stress b) change of the stress loading condition on the fault. c) by thermo-elastic deformation of the rock formation around the injection well

1.4.2).

- b. Volume change and related stress change: fluid injection or removal in rock bodies can change the stress acting on a fault which can lead to fault reactivation (Figure 1.1b)
- c. Thermo-elastic deformation: injection of cold fluid into hot rock bodies can alter the state of stress near the injection point by a thermal-contraction of the rock bodies. This effect is more important the larger the temperature gradient between the fluid and the host rock (Figure 1.1c).
- d. Chemical alteration: injection of fluids containing chemical agents which are commonly used in energy production activities to increase the permeability of the host rock can lead to chemical alteration. Chemical reactions of dissolution and deposition of minerals can change the transport properties of the rock bodies and the fault strength.

Below, we analyze in detail the relation between the physical processes defined above with the human activities of energy production leading to human-induced seismicity.

Deep geothermal energy production. Three different types of geothermal energy sources exist: i) vapour dominant, where steam is contained in the fractures of the hot rock, ii) liquid dominant, where hot water is contained in the rock, iii) enhanced geothermal system (EGS), where the hot dry rock required reservoir stimulation to allow fluid flow in a network of fractures. Seismicity has been recorded for all the three types of geothermal system. In "The Geysers" vapour dominant geothermal plant (California, US), the large temperature difference between the injected fluid and the geothermal reservoir caused reservoir rocks to contract, leading to human-induced seismicity events, with magnitude up to 4.4 (Figure 1.2) (Guilhem

et al., 2014; Ross et al., 1999; Eberhart-Phillips and Oppenheimer, 1984). Conversely, for EGSs most of the human-induced seismicity is registered in the early stages of the stimulation when the network of fractures has to be created by fluid injection. This was the case for the Soultz event in France (Calò et al., 2014; Baisch et al., 2010; Charléty et al., 2007; Cornet et al., 2007), Basel event in Switzerland (Mukuhira et al., 2010; Deichmann and Giardini, 2009; Deichmann and Ernst, 2009; Häring et al., 2008) and Cooper Basin event in Australia (Baisch et al., 2006, 2009; Asanuma et al., 2005).

Conventional oil and gas production. Many conventional oil and gas projects are designed to maintain the pore pressure within the reservoir at the natural pore pressure value of the system (i.e., pre-production level). To maintain equilibrium, the volume of fluids removed and then injected in the reservoir have to be equivalent. For example, the extraction of gas in Groeningen (The Netherlands) was associated to an increase in seismicity up to a magnitude 3.6 event (van Thienen-Visser and Breunese, 2015; van Elk et al., 2017; Dost et al., 2018). This earthquake, which occurred in 2012, raised the public concern and catalyzed a renewed effort to understand the induced seismicity in the area to limit the occurrence of future larger events (Dempsey and Suckale, 2017). In 2016, a new study of equilibrium between injected volume and extracted volume was proposed to counteract the compaction of the reservoir (Hofmann, R., 2016).

Unconventional oil and gas production (shale oil and shale gas). Hydrocarbon can remain trapped in the rock pores over geologic time due to the extremely low permeability of the shale rocks. To access the oil/gas reservoir in shale formations, a horizontal wellbore is usually drilled. Moreover, new fractures have to be created in this low permeability rock to extract the hydrocarbon. Fracturing activities can be associated with induced seismicity. For example, between 2015 and 2016, in Fox Creek site (Alberta, Canada) a series of three earthquakes with magnitudes 3.6, 3.9 and 4.1 led to the partial stop of the fracturing operations (Wang et al., 2016; Schultz et al., 2017; Zhang et al., 2019). In this particular case, such high magnitude events were explained by the reactivation of an un-mapped major fault close to the injection point (Schultz et al., 2017). However, induced seismicity can also occur during the production phase in a similar fashion to conventional the conventional oil and gas extraction.

Wastewater disposal in deep aquifers. The wastewater is the fluid waste product of the extraction activities of gas and oil. In addition to fluid injection related to reservoir stimulation, wastewater is injected close to the oil and gas production sites for disposal, especially in the United States. Most wastewater disposal wells typically involve injection at relatively low pressures into large porous aquifers that have high natural permeability and are specifically targeted to accommodate large volumes of fluid without inducing seismic events. However, the large increase of seismicity in Oklahoma (US) since 2008 is attributed to the large volume of injected wastewater (Keranen et al., 2013, 2014). Also in China, the re-injection of wastewater

1.2. Human-induced seismicity

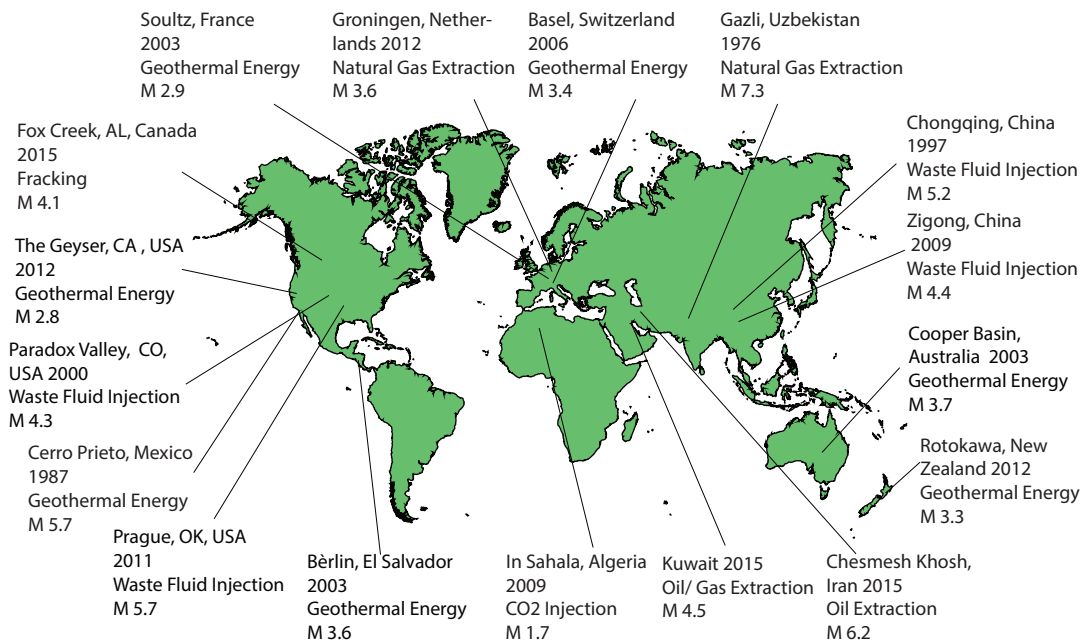


Figure 1.2: World Map of some induced seismicity cases involving fluid extraction or injection.

coming from the gas production led to two large events; one in the Rongchang gas field (Chongqing) in 1997 (Lei et al., 2008) and one in the southwestern Sichuan Basin in 2009 (Lei et al., 2013).

CO₂ capture and storage. One of the ways to reduce the amount of carbon in the atmosphere is by capturing the CO₂ and storing it underground (i.e. CO₂ sequestration activities). Currently, only a few projects are currently developing this technology and the risk of induced seismicity linked with this activity is still difficult to quantify. The magnitude 1.7 event in In Salah CO₂ project (Algeria) is one of the few examples of human-induced seismicity due to the CO₂ sequestration (Verdon et al., 2015; Rutqvist et al., 2010; Bissell et al., 2011; Morris et al., 2011a,b).

The injected fluids used for the energy production activities mentioned above (i.e., water, wastewater, brine, fracturing fluid, CO₂) differ significantly from each other. They have different thermal (thermal conductivity κ , heat capacity C_p) and physical properties (density ρ , viscosity η , compressibility β).

In particular, the viscosity of the fluids involved in human-induced seismicity can change up to 6 orders of magnitude (Figure 1.3).

The viscosity of a fluid is defined as the resistance of a fluid to deform. It is a function of temperature, pressure and strain rate (i.e., the ratio between the slip-rate and the thickness of deforming fluid film). If a fluid has a viscosity which is constant with slip-rate, it is defined as

Table 1.1: Injected fluid viscosity ranges from literature data

Fluid	η [mPa.s]	Ref.
Fracturing Fluids		
	200-2500	Esmailirad et al. (2016a,b)
	100	Shimizu et al. (2011)
	20-600	Fallahzadeh et al. (2015)
	270	Bennour et al. (2015)
	80	Ishida et al. (2004)
	5	Chen (2012)
	100-5100	Zhang et al. (2010)
	50-500	Economides and Boney (2000)
Wastewater		
	10	Szafranski and Duan (2018)
	35	Lu and Wei (2011)
	500	Cheryan and Rajagopalan (1998)
	48-57	Fu (2017)
Brine		
	8.9	Barbour et al. (2019)
	4	Hornbach et al. (2016)
	1-8	Yuan et al. (2015)
CO2		
	0.5-1	Bando et al. (2004)
	0.018-4.82	Wildenschild et al. (2011)
	0.006	Nobakht et al. (2007)

Newtonian (e.g., water and glycerol).

So far, most of the modeling studies aimed at understanding human-induced seismicity considered the viscosity of water at ambient temperature as an input parameter ($\eta = 1$ mPa s) (Garagash and Germanovich, 2012; Segall and Lu, 2015; Chang and Segall, 2016). However, the real viscosity of the injected fluids ranges from 60 μ Pa s (at $T = 20$ °C and atmospheric pressure) for CO2 (Nobakht et al., 2007) to 5000 mPa s for fracturing fluids (Table 1.1). During reservoir stimulation, high viscosity fluids are used to reduce the leak-off (i.e., the fluid loss into the porous matrix) (Williams, 1970), but also to control the fracture shape geometry (Zoback et al., 1977; Chen, 2012).

The fluid viscosity also controls the fluid diffusion in rocks, faults and fractures. The diffusivity is defined as $\alpha_{hy} = \frac{k}{\eta\phi\beta}$, where k is the permeability of the fracture. Keeping the other parameters constant, if the fluid viscosity is low, the diffusivity is high. Under these conditions, the fluid flow is enhanced and the increase of fluid pressure is negligible. On the other hand, if the viscosity is high, the diffusivity is low. Under these conditions, the fluid flow is reduced and the fluid pressure can increase, possibly leading to fault reactivation. Moreover, fluid viscosity

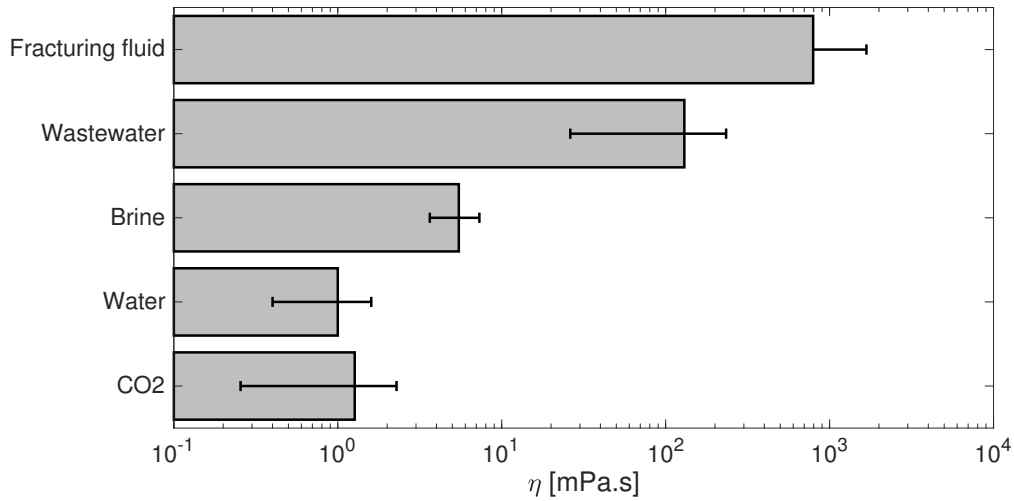


Figure 1.3: Summary of the injected fluids viscosity in human activities which can induce seismicity. The viscosity varies by 6 orders of magnitude

can also affect fault strength during earthquake propagation, controlling fault lubrication (Brodsky and Kanamori, 2001) as shown by elasto-hydrodynamic theory (Section 1.5).

In this thesis, we investigate the role of fluid viscosity in the framework of induced seismicity and more in general in natural earthquakes involving viscous fluids within granitic fault surfaces. Granite was chosen as an analogous for the target lithology for geo-reservoirs.

1.3 Fault structure and fluid flow in fault zones

In order for fluids to flow through them, geo-reservoirs must contain discontinuities, fractures, or faults. These features are the result of an elastic-brittle response to the stress perturbation of rocks. The upper part of the Earth's crust is characterized by low-grade conditions, i.e., low temperature (<300°C) and low pressures (<300 MPa). Under these conditions, rocks accommodate deformation in a nearly linear manner according to their elastic parameter until brittle failure occurs (Cox and Scholz, 1988; Lockner and Beeler, 2002).

Brittle failure of rocks can be described as the completion of a process of the progressive development of cracks during loading, which may occur at all scales (Paterson and Wong, 2005b; Scholz, 2019a; Ohnaka, 2013). When confining pressures are applied to rocks, brittle failure takes place when multiple cracks merge. These cracks are mostly oriented sub-parallel to the direction of maximum compressive stress (Jaeger et al., 2007). The coalescence of these cracks can lead to the formation of a fault, which corresponds to a plane where the relative displacement of the two rock opposing surfaces occurs (Jaeger et al., 2007).

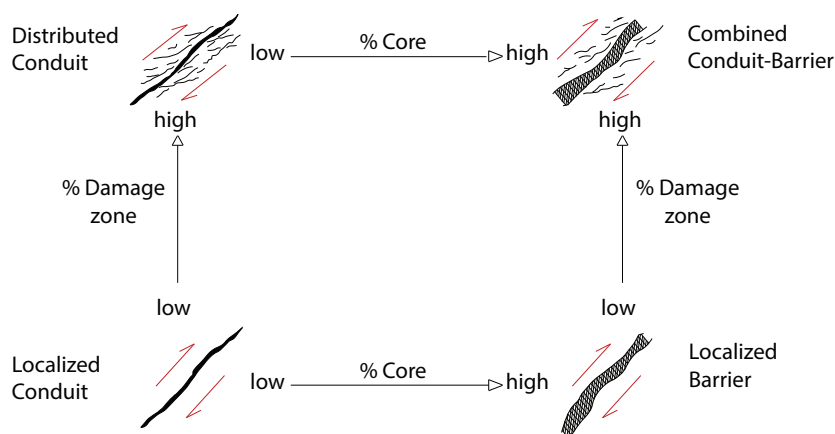


Figure 1.4: Fluid flow and fault structure (Modified after Caine et al. (1996))

Geologic faults are generally complex systems composed by a distribution of fault-rocks with various mineralogies, transport properties and frictional behaviours (De Barros et al., 2016; Faulkner et al., 2010; Evans et al., 1997; Caine et al., 1996).

The primary components of a fault zone are the fault core, damage zone, and the intact protolith (Chester and Logan, 1986; Caine et al., 1996; Faulkner et al., 2010). The fault core is the portion of the fault zone where most of the displacement is accommodated. It can include individual slip surfaces, unconsolidated gouge volumes, geochemically altered volumes or cataclasite volumes. The damage zone is the network of supplementary and secondary structures close to the fault core which can enhance the fault zone permeability. It includes veins, fractures, cleavage, and folds. This zone is usually characterized by heterogeneity and anisotropy in the permeability structure and elastic properties of the fault zone (Rempe et al., 2013). The intact zones instead have the same elastic and permeability properties of the rocks surrounding the fault. No scale relationship is implied between the components, nor must all of the components be present in any given fault zone. The structure of a fault strongly depends on its slip history: immature faults have accommodated lower slip compared to mature faults. The fault's structure changes over geologic time. Mitchell and Faulkner (2009) showed that the width of the damage zone can be related to the slip history of the fault core: the higher the slip (but lower than 100 m), the larger the fault width.

In function of its structure, the fault can act as a barrier or a conduit for the fluid flow (Caine et al., 1996; Faulkner et al., 2010). Generally, immature faults are more hydraulically conductive than mature faults (Figure 1.4).

1.4 Friction

The motion of a fault or a pre-existing fracture is controlled by friction, which is a contact property of the slip surfaces.

Friction is the resistance to relative motion that occurs when two bodies that are in contact are sliding tangentially to their contact plane. The first systematic understanding of friction was obtained by Leonardo Da Vinci. He discovered two main laws: i) the tangential force (or shear force) is proportional to the normal force acting on the slip plane and ii) the frictional force is independent of the contact surface area. These results were then developed by Amontons (1699) and the proportionality of the friction force to the normal force is known as "Amontons' Law". Coulomb (1821) confirmed Amontons' results and undertook a quantitative examination of dry friction between solid bodies with various materials, surfaces compositions, slip-rates, contact times, and temperatures. He also defined the difference between static and kinematic friction coefficients. The static friction coefficient is the ratio between the tangential force and the normal force necessary to start the body movement. The kinematic friction coefficient is proportional to the tangential force necessary to keep the body moving. Moreover, in addition to Amontons' law, Coulomb recognized the contribution of the adhesion on the evolution of the shear force. He highlighted the increase of the static friction with the stationary time of a body.

Later on, Bowden and Tabor (1950) introduced the dependency of dry friction on surface roughness. In particular, they recognized that surfaces have a topography characterized by the presence of asperities. The sum of the individual areas of the asperity contacts constitutes the real contact area (A_r), which is much smaller than the apparent contact area (A , i.e. the geometrical area of contact). Moreover, further studies reported that the real contact area is also proportional to the normal stress acting on the plane, the time of contact and the initial surface roughness (Bowden et al., 1939; Dieterich and Kilgore, 1994; Persson, 2000a).

1.4.1 Friction of fault rocks

One of the key parameters in the understanding of earthquakes mechanics is the friction of fault rocks. Rabinowicz (1958), Biegel et al. (1992), Wang and Scholz (1995) performed experimental measurements of the apparent friction, defined as the ratio of shear strength (i.e., shear force over the deforming surface) and normal stress (i.e., normal force over the deforming surface) of the deforming surface (i.e., $(\mu = \tau / \sigma_n)$) using experimental devices. They observed that the apparent friction evolves from the static friction at the initiation of slip to a steady-state friction value over a distance D_{ss} . When sliding starts, the interlocking of asperities results in an increase of the shear force. This stage is followed by an increase in the apparent friction defined slip hardening behaviour. This behaviour is motivated by the production of wear particles (i.e. gouge material) on the surface which increases the contact

area during slip. The slip hardening behaviour proceeds up to the achievement of the steady-state value of friction. More studies focused on the understanding and measurement of the steady-state friction both using bare surfaces and gouge material, an artificial layer of wear particles with controlled thickness.

Shear strength at the reactivation stage for a wide variety of rocks is independent of the rock lithology and was summarized by the Byerlee's rule (Byerlee, 1978):

$$\begin{cases} \tau = 0.85 \sigma_n & \text{for } \sigma_n < 200 \text{ MPa} \\ \tau = 50 + 0.6 \sigma_n & \text{for } \sigma_n > 200 \text{ MPa} \end{cases} \quad (1.1)$$

At low normal stress, the variation of the roughness of the sliding surfaces or the granulometry of gouge particles produce large variations in steady state friction.

Exceptions to Byerlee's rule are the minerals with a plate-like structure (i.e. graphite, talc and other phyllosilicates) which have a steady-state friction coefficient lower than the other bulk structure minerals (see Moore and Lockner (2004) for a complete description of phyllosilicates frictional behaviour).

1.4.2 Effect of fluid pressure

The presence of fluids on the slip surface has the mechanical effect of reducing the effective normal stress acting on the fault:

$$\sigma' = \sigma_n - P_f \quad (1.2)$$

where σ_n is the total normal stress and P_f is the fluid pressure. From equation 1.2 is possible to write the shear stress τ at the failure as:

$$\tau = \mu_s (\sigma_n - P_f) \quad (1.3)$$

where μ_s is the static friction.

In a shear stress-normal stress plane, the state of the stress of a fault can be represented by the Mohr circle. The change in stress configuration of a fault due to an increase of the pore pressure (P_f) and a consequent decrease of the effective normal stress σ' can be represented by shifting the Mohr circle to the left side of the diagram (Figure 1.5).

Using this representation, fault reactivation occurs when the Mohr circle becomes tangent to the linear Mohr-Coulomb failure criterion (i.e. the shear stress acting on the fault matches the shear strength of the fault)(Coulomb, 1821) (Figure 1.5).

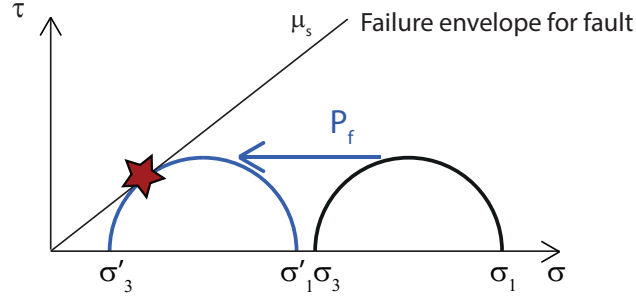


Figure 1.5: Mohr circles on a σ_n - τ plane. The increase of the fluid pressure shifted the Mohr circle on the left, closer to the failure envelope of the fault. The reactivation of the fault occurs when the Mohr circle is tangent to the failure envelope (red star)

1.5 The lubrication theory and the Stribeck curve

The considerations above were made for dry contact, i.e. direct contact between surface asperities, or considering only the direct effect of fluid on the effective pressure. In Section 1.3, we showed that faults can host fluids and in Section 1.2 we analyzed the properties of these fluids. In particular, the viscosity of fluids can vary by many orders of magnitude. We will now explain the fluids lubrication theory, in which the viscosity of fluid plays a key role.

The first formulation of lubrication theory was made in the XIX century, when the increase of industrial demand drove the attention of experimental and theoretical research to the understanding of lubrication processes between mechanical contacts. Petrov (1883) formulated the hydrodynamic lubrication law after experimental studies of journal bearings. In 1886, Reynolds published the theory of hydrodynamic lubrication. In hydrodynamic lubrication theory, the coefficient of friction of a spherical contact between two surfaces covered by a lubricant is proportional to the thickness of the fluid film H and the length of the contact (i.e the distance between two asperities) L ($\mu = H/L$). This relation is true only if the lubricating film thickness h is larger than the roughness of the two surfaces h (i.e., the height of the contact).

To understand the principles of hydrodynamic lubrication, we can use the Navier-Stokes equation of incompressible fluid dynamics between two sub-parallel planes (1.4).

$$\rho \frac{d\vec{u}}{dt} = -\nabla p + \eta \nabla^2 \vec{u} + \rho \vec{f} \quad (1.4)$$

Where ρ is the fluid density, \vec{u} is the slip-rate vector in the x direction (Figure 1.6), p is the fluid pressure and η is the fluid viscosity. Navier-stokes equation (1.4) can be simplify considering that 1) the body force term \vec{f} is negligible (i.e. weight of the fluid film is much smaller than the viscous and pressure effects) and 2) under the assumption of thin fluid thickness: considering the two characteristic dimensions L on X direction (characteristic dimension of pressure

Chapter 1. Introduction

change) and H on the plane Z (mean height of the fluid film), a thin fluid film is defined as $L \gg H$ (Figure 1.6). The assumption of thin fluid thickness allows for:

- the consideration that the fluid flow is laminar (i.e. the Reynolds number $Re = UH \frac{\rho}{\eta}$ is much smaller than the geometric factor L/H).
- the neglect of the change of fluid pressure across the fluid film in (1.4), i.e. the inertial term of 1.4 is negligible ($\frac{dp}{dz} \sim 0$)

Under the above assumptions, (1.4) reduces to

$$\begin{cases} \frac{dp}{dx} = \eta \frac{d^2 u}{dz^2} \\ \frac{dp}{dz} = 0 \end{cases} \quad (1.5)$$

From (1.5), it emerges that the dynamics are dominated by the balance between the viscous stress $\left(\eta \frac{d^2 u}{dz^2}\right)$ and the dynamic pressure $\left(\frac{dp}{dx}\right)$.

Double integration of 1.5 along the z axis gives:

$$u = \frac{1}{2\eta} \frac{\partial p}{\partial x} z^2 + Az + B \quad (1.6)$$

The boundary conditions for impermeable surfaces and slip between the solid surface and the fluid film (i.e., at $z = h$), can be written as

$$\begin{cases} \text{At } z = 0 & u = 0, w = 0 \\ \text{At } z = h & u = V, w = 0 \end{cases} \quad (1.7)$$

Where w is the slip-rate in the z direction.

The slipping zone height includes both the initial distance between the plane surfaces and any elastic displacement caused by fluid pressurization. Applying (1.7) to (1.6) gives

$$u = \frac{1}{2\eta} \frac{\partial p}{\partial x} (z^2 - zh) + \frac{z}{h} V \quad (1.8)$$

The continuity equation for an incompressible fluid is:

$$\frac{du}{dx} + \frac{dw}{dz} = 0 \quad (1.9)$$

Integrating 1.9 across the fluid film results in

$$v = - \int_0^{h(x,t)} \frac{\partial u}{\partial x} dz \quad (1.10)$$

1.5. The lubrication theory and the Stribeck curve

Interchanging integration and differentiation in 1.10 and substituting u from 1.8, we obtain:

$$v = -\frac{\partial}{\partial x} \left[\frac{1}{2\eta} \int_0^h (z^2 - zh) dz \right] - \frac{\partial}{\partial x} \int_0^h \left[\frac{z}{h} V \right] dz + V \frac{\partial h}{\partial x} \quad (1.11)$$

Evaluating the integrals and taking into account that

$$v = -U = \frac{dh}{dt} \quad (1.12)$$

we obtain the Reynolds equation:

$$\frac{\partial}{\partial x} \left(\frac{h^3}{\eta} \frac{\partial p}{\partial x} \right) = -6V \frac{\partial h}{\partial x} + 6h \frac{\partial V}{\partial x} + 12U \quad (1.13)$$

If we assume that:

- surfaces are rigid (i.e. constant V , $\partial V / \partial x = 0$)
- the change of thickness during time is negligible ($dh/dt = -U \approx 0$),

Reynolds equation 1.13 can be simplified:

$$\frac{d}{dx} \left(h^3 \frac{dp}{dx} \right) = -6\eta V \frac{dh}{dx} \quad (1.14)$$

The typical behaviour of a lubricated system can be illustrated by considering a tapered slider with body force F_N moving over a plane covered by a lubricant. We impose the following boundary conditions to 1.14: the far field lubricant pressure P_0 is imposed at $x = 0$ and $x = L$. The lubricant pressure rises in the region $0 \leq x \leq L$ and therefore exerts a force that is in the same direction but opposite compared to the block body force. The variation of the lubricant pressure is defined as

$$P_L = 6\eta V L \frac{\Delta H}{H^3} \quad (1.15)$$

Where H is the mean height of the lubricant and ΔH is the mean height variation of the lubricant caused by the asperities on the surfaces. If ΔH is of the same order of magnitude of H (as is the case for laboratory samples) (1.15) can be simplified to

$$P_L = 6\eta V \frac{L}{H^2} \quad (1.16)$$

Moreover, H is given by the sum of the initial asperity height H_0 and the elastic deformation D_E . Following the Hooke law, we can define D_E as

$$D_E = \frac{LP_L}{E} \quad (1.17)$$

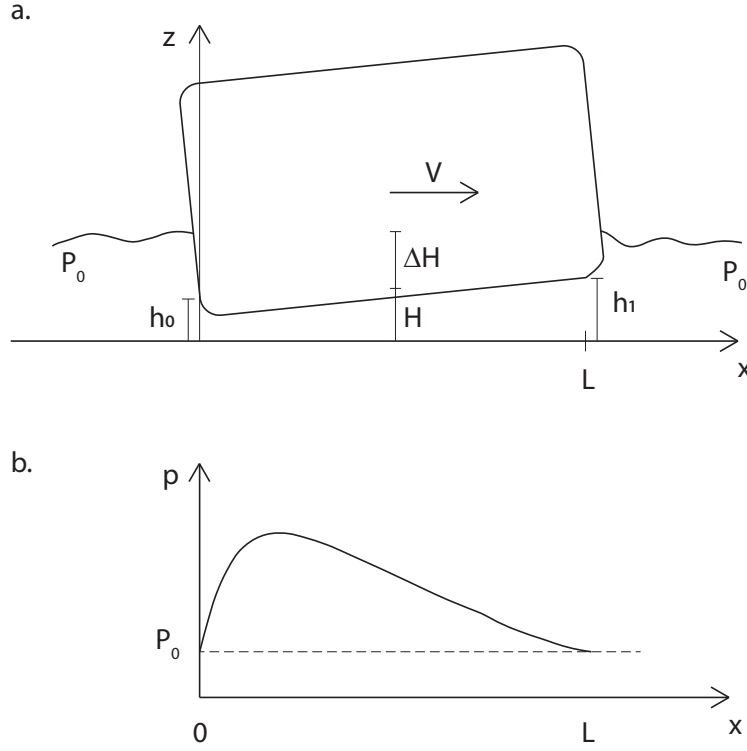


Figure 1.6: Schematic of the lubrication theory. a) Motion of a body on a layer of fluid with average height $H = (h_0 + h_1)/2$ and a variation ΔH . The characteristic length L is the length over which it is possible to observe a decrease in fluid pressure. V is the relative slip-rate between the two solid surfaces. b) Increase of the fluid pressure with respect to the initial P_0 , due to the motion of the body on a layer of fluid. Modified from (Brodsky and Kanamori, 2001).

Combining 1.16 and 1.17, we can define a critical lubrication length $L_{c,lub}$ for our experimental samples for which $D_E = H_0$:

$$L_{c,lub} = \left(\frac{H_0^3 E}{6\eta V} \right)^{0.5} \quad (1.18)$$

The L in the experimental conditions presented in Chapter 2 is lower than the $L_{c,lub} \sim 0.15m$ and therefore the elastic deformation of the asperity is negligible. In Chapter 3 and Chapter 4, where measurements of the displacement δ perpendicular to the fault plane were available and the cumulative displacements on the fault plane were significant, the average height is $H \propto H_0 + \delta$. However, in all the chapters we neglected the inelastic deformation and the compressibility of the fluid, and therefore its effect on the storage capacity of the fault.

If ΔH is not on the same order of H , as it is the case for natural fault, but we can consider that

the plane is self similar, $\Delta H = KL$, where K is the $\sim 10^{-3}$ (Brodsky et al., 2016),

$$P_L = 6\eta V \frac{KL^2}{H^3} \quad (1.19)$$

In 1902, Stribeck determined the dependence of the tangential force (i.e., the force necessary to move the tapered body tangentially to the lubricated surface) on the slip-rate, drawing the well known Stribeck curve. To draw the Stribeck curve, the dimensionless Sommerfeld number is used (Sommerfeld, 1964). The Sommerfeld number is defined as the ratio between the pressure due to lubrication P_L and the pressure from the static loading σ_n (i.e., body force F_N divided by the contact area). Considering two parallel surfaces, the Sommerfeld number is defined as:

$$S = 6 \frac{\eta V}{\sigma_n} \frac{L}{H^2} \quad (1.20)$$

The Sommerfeld number represents the importance of lubrication in determining the frictional properties of a system. For small Sommerfeld numbers, the lubrication process is almost negligible and the lubrication pressure supports only an insignificant fraction of the normal stress. In this case, the two sliding surfaces are in contact at the asperities and the friction coefficient is determined by the solid surface properties and by the adhesive force (Persson, 2000d). In the case of rock sliding surfaces the friction coefficient is the one defined by the Coulomb criterion. This behaviour is known as boundary lubrication regime, and $\mu = \mu_{solid}$ (Figure 1.7).

For large Sommerfeld numbers the lubrication pressure completely supports the normal stress and, theoretically, no normal stress is supported by the asperities. Only the viscous resistance of the fluid contributes to the friction coefficient. This behaviour is known as hydrodynamic lubrication regime. The magnitude of the shear strength of the fluid is $\eta \partial u / \partial z$. From equation 1.5, $\partial u / \partial z$ scales with $P_L H / (L\eta)$. As a consequence, for large Sommerfeld numbers, the apparent friction coefficient is defined as:

$$\mu = S \frac{H}{L} \quad (1.21)$$

Between the boundary and the hydrodynamic lubrication regimes is the mixed lubrication regime. In this regime, the apparent friction coefficient is determined the sum of the friction coefficient of the lubricant and the friction of the solid asperity contacts. If $P_0 = 0$, then the global friction coefficient can be written as:

$$\mu = \mu_{solid}(1 - S) + S \frac{H}{L} \quad (1.22)$$

The frictional properties of fault rocks and their evolution with displacement, slip-rate, depend-

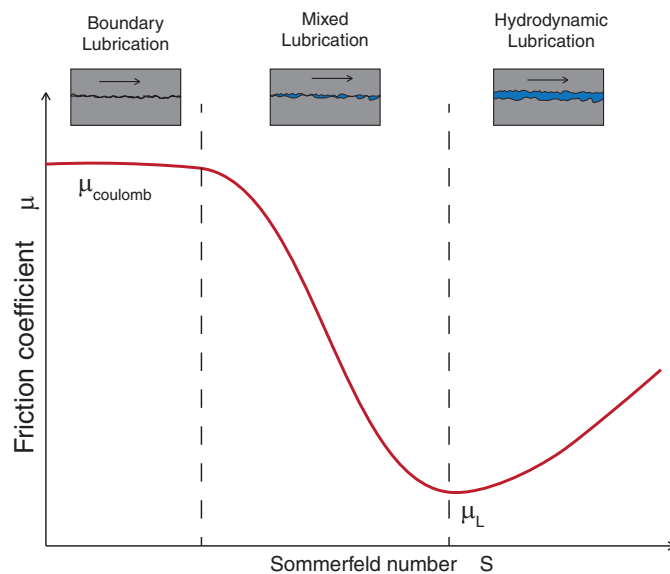


Figure 1.7: Schematic of the three lubrication regimes.

ing on the availability of pore fluid and the properties of the fluid (i.e., viscosity), contribute to defining the slip behaviour of faults.

1.6 The earthquake cycle

Frictional behaviour of faults influence the occurrence of earthquakes, which are sudden slippages along a pre-existing fault or plate interface (Scholz, 1998). Unstable slip events and rupture propagation are repeated during the geological time. Between one earthquake and the following, faults usually undergo different styles of slip events, which are included in the definition of "seismic cycle".

Considering the deformation process of a region including a fault, it is possible to divide the entire earthquake cycle into five phases, starting right after the occurrence of an earthquake (Ohnaka, 2003).

- **Phase I:** After the arrest of an earthquake, the fault begins to heal (i.e. recovery of strength). It was experimentally demonstrated that the re-strengthening is due to an increase of the real contact area due to asperity interlocking and asperity ploughing (Dieterich, 1972; Scholz and Engelder, 1976; Iwasa and Yoshioka, 1998; Violay et al., 2019).
- **Phase II:** Under the effect of tectonic loading, the fault surface starts to deform and the region surrounding the fault accumulates elastic strain. For stresses lower than a certain threshold, no seismic activity is produced by the fault (spatial and temporary

gap, Kanamori (1981)). With time, the tectonic stresses gradually approach the critical level at which an earthquake can occur. Precursory seismic activities characterize the end of this phase. In the presence of fluids, a reduction of fault permeability due to the self-sealing can lead to an increase of the fluid pressure from its hydrostatic value up to the lithostatic one (Sibson et al., 1988).

- **Phase III:** Crustal deformation starts to concentrate locally along the fault and rupture nucleation begins to occur when the tectonic stresses reach a critical level and enough elastic strain energy is accumulated in the surrounding of the fault.
- **Phase IV:** The nucleation process leads to a rupture developing in the fault, accompanied by a fast stress drop and dissipation of the elastic strain energy, resulting in the radiation of seismic waves (i.e., mainshock of an earthquake sequence). The rupture propagation increases the permeability on the fault and the fluid pressure drops to the hydrostatic value.
- **Phase V:** The arrest of the mainshock results in the redistribution of local stresses on the fault and around the fault. In the presence of fluids, self-sealing of the fault can occur when minerals precipitate in fault porosity and reduce fault permeability. Minerals can precipitate due to a decrease in their solubility in fluid with the decrease of fluid pressure occurring during seismic slip (Sibson et al., 1988). In this phase, aftershock activity occurs. After this phase, the seismic cycle starts again.

The earthquake cycle described above is appropriate to define the recurrence of large earthquakes. However, not every fault expresses the release of elastic strain energy through large earthquakes. The release of elastic strain can also occur through slow slip events, characterized by the release of the moment magnitude over long periods (from hours to days or weeks), without the generation of high-frequency body waves (Beroza and Jordan, 1990; Kanamori and Hauksson, 1992; Linde et al., 1996). In other cases, faults can undergo deformation without releasing strain energy from the surrounding rocks (i.e., under constant stress) giving rise to creep events or stable slip events.

We will now analyze in more detail the mechanical behaviour of a fault during the nucleation and the propagation phases of an earthquake and the physical laws and laboratory studies conducted to understand these two phases.

1.7 Earthquake nucleation

Stick-slip is a short sudden movement commonly observed in frictional sliding of various materials. Brace and Byerlee (1966) introduced the analogy between stick-slip and earthquake mechanics.

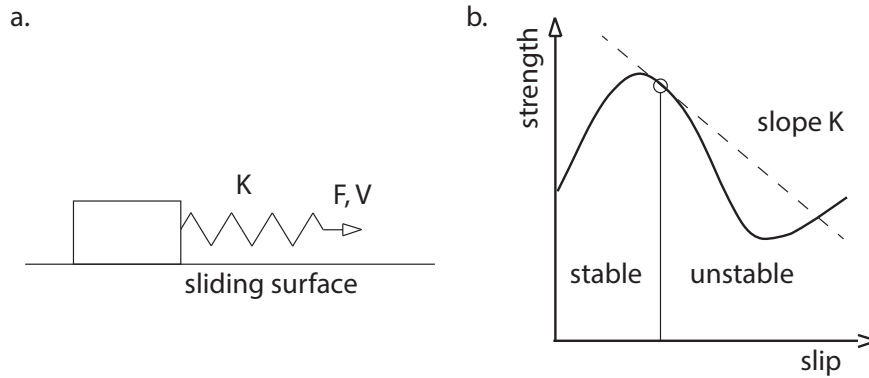


Figure 1.8: Spring-slider system to explain the nucleation of dynamic instability. a) Schematic of the system. b) Instability occurs when the strength along the interface is released faster than the imposed strength by the loading system K .

The mechanics of stick-slip episodes can be explained by a spring slider model. In this model, a block mass (e.g. rock mass) is free to slide on a surface (e.g. a fault), pulled by a spring of stiffness K (e.g. elasticity of the surrounding fault medium) exerting a tangential force F which allows the movement of the block at a constant slip-rate V . The tangential force F initially increases to ensure the slip of the body at the desired slip-rate V (Figure 1.8a). Once the system is close to the peak strength three different behaviours can occur (Figure 1.8b):

- Slip-strengthening with stable sliding: the block starts to slip but the strength of the interface increases and dynamic rupture can not occur.
- Slip-weakening with stable sliding: the strength of the fault decreases with the displacement, but the release rate of the strength is smaller than the stiffness of the surrounding medium;
- Slip-weakening with unstable sliding: The strength of the interface decreases with the displacement faster than the stiffness of the medium. The release of strength is fast enough to radiate elastic waves, the block mass accelerates and a stick-slip event occurs.

Two main friction laws are used in earthquake mechanics to explain this last scenario, i.e. the nucleation of instabilities: slip-weakening law and rate and state friction law (RSF law).

1.7.1 Slip-weakening law

In the slip-weakening model, the friction coefficient between two interfaces is a function of slip only (Ida, 1972; Campillo and Ionescu, 1997; Uenishi and Rice, 2003). For slip equal to 0, the friction coefficient is equal to the static value μ_s (Byerlee, 1978). When the body starts to slip along the interface, the apparent friction $\mu = \tau / \sigma_n$ decreases to reach the dynamic friction

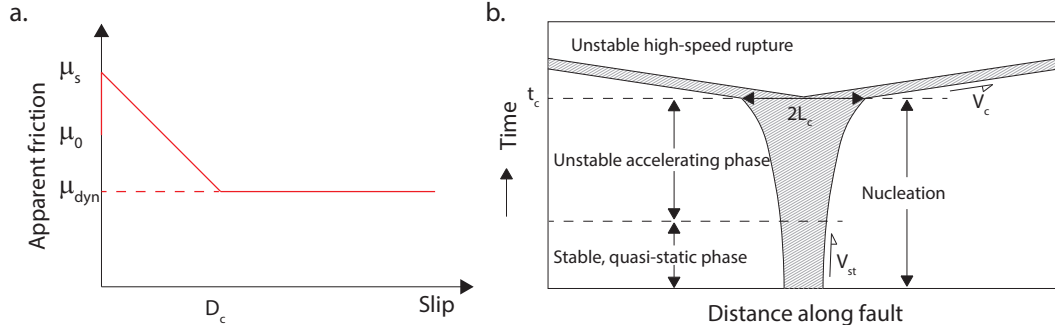


Figure 1.9: Linear slip-weakening law and nucleation model proposed by Ohnaka (2003). a) Once $D = D_c$, $\mu = \mu_{dyn}$ and μ remains constant until the stop of the slip. b) Hatched zone corresponds to the zone in which the slip weakening progresses with time. The length L_{sc} is the critical length allowing the transition from stable sliding to the acceleration of the sliding velocity. The length L_c corresponds to the critical nucleation length from which the rupture becomes dynamic and can propagate at rupture speeds close to elastic wave velocities.

coefficient $\mu_{dyn} < \mu_s$ over a critical slip distance called D_c . The simplest expression of the slip-weakening law assumes a linear decrease of μ with the slip $D < D_c$. The slip-weakening law has been adopted by several authors to describe the earthquake generation process (Abercrombie and Rice, 2005; Wibberley and Shimamoto, 2005; Sone and Shimamoto, 2009; Huang et al., 2014; Ikari et al., 2013; Brantut and Viesca, 2015). Ohnaka (2003) proposed a model for shear rupture nucleation based on the slip-weakening law and previous theoretical studies (Ida, 1972; Palmer and Rice, 1973; Andrews, 1976; Campillo and Ionescu, 1997; Uenishi and Rice, 2003). The rupture nucleation initiates during a stable or a quasi-stable sliding at a steady-state rupture velocity V_{st} . The rupture length L slowly increases up to a first critical distance L_{sc} . Once the rupture length L overcome L_{sc} , the nucleation extends spontaneously up to the critical length L_c with a rupture velocity slightly higher than V_{st} . Finally, for $L > L_c$ the rupture propagates at a constant high rupture velocity V_c (Figure 1.9). Following theoretical results (Ida, 1972; Campillo and Ionescu, 1997; Uenishi and Rice, 2003), the critical nucleation length is a function of the dynamic stress drop $\Delta\tau$ and of the critical slip distance D_c :

$$L_c = \beta_L \frac{M}{(\mu_s - \mu_{dyn})\sigma_n} D_c \quad (1.23)$$

where M is the rigidity of the system and β_L is a dimensionless coefficient (Cammenga et al., 1977).

One asperity with size L can slip seismically only if $L > L_c$, otherwise it will slip aseismically (i.e., stable slip). Moreover, the critical distance D_c is function of the roughness of the interface (Ohnaka, 2003). Therefore, the higher the roughness is, the larger D_c and L_c will be.

1.7.2 Rate and state friction law

The rate and state friction (RSF) law describes the second-order changes of the friction coefficient leading to the earthquake nucleation. The RSF law is described by two equations in which the friction coefficient is expressed as a function of the slip-rate V and a state variable θ having units of time.

$$\mu = \mu_0 + a \ln\left(\frac{V}{V_0}\right) + b \ln\left(\frac{V_0 \theta}{d_c}\right) \quad (1.24)$$

Where μ_0 is a constant that represents friction coefficient at steady-state for a reference slip-rate V_0 , μ is the friction at the new steady-state slip-rate V , and a and b are empirical parameters, also named the direct and evolution effect respectively (Lockner and Beeler, 2002). The state variable θ can be interpreted as the average lifetime of contacts: the average of elapsed time between the formation of contacts and their replacement by new contacts (Scholz, 2002). The critical slip distance d_c , after a change in slip-rate from V_0 to V , is interpreted as the distance over which friction evolves from a local peak to a steady-state. The physical interpretation is that the population of contacts in equilibrium with V_0 is totally renewed by a new one in equilibrium with the new slip-rate V (Marone, 1998).

The establishment of this frictional law is based on rock friction experiments performed at low sliding slip-rates (ranging from 10^{-9} and 10^{-6} m/s) (Dieterich, 1979; Ruina, 1983; Marone, 1998).

The differential term $d\theta/dt$ defines the evolution law. The most used forms of the evolution law are the "aging law" (Dieterich, 1979) and the "slip law" (Ruina, 1983). The "aging law" is defined as:

$$\frac{d\theta}{dt} = 1 - \frac{V\theta}{d_c} \quad (1.25)$$

In Dieterich's model, friction primarily depends on the time-dependent microstructural evolution.

The "slip law":

$$\frac{d\theta}{dt} = -\frac{V\theta}{d_c} \ln\left(\frac{V_0 \theta}{d_c}\right) \quad (1.26)$$

In Ruina's law any change in friction coefficient, including strengthening during quasi-stationary contact, requires slip (Marone, 1998). Independent of the initial microphysical assumptions, both laws successfully fit the frictional behaviour of rock and fault gouge during experiments giving similar results and differences are difficult to distinguish in the experiments (Marone, 1998).

In addition to the "aging law" and to the "slip law", Persson (2000d), proposed another state variable law to take into account the effect of fluids on the frictional behaviour of a rock surface. Persson's state evolution law comes from the idea that the transition between stable and unstable behaviour of a system depends on the nucleation of "solid structures" in a lubricated

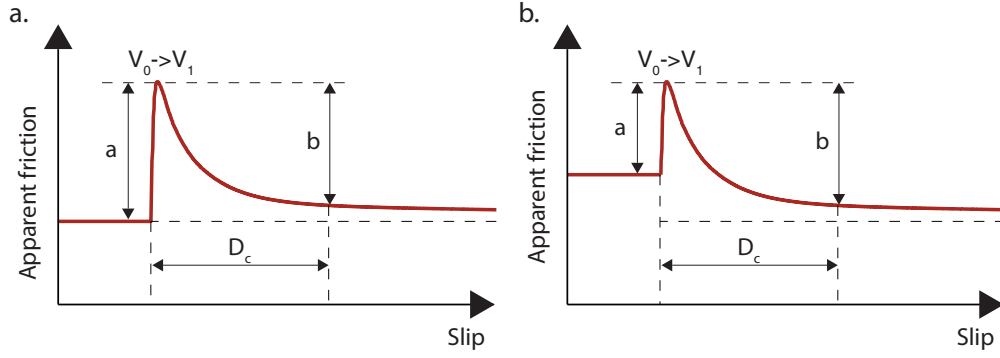


Figure 1.10: Schematic illustration of the frictional response to velocity-stepping following the rate and state frictional law. a) Velocity-strengthening behaviour ($a - b > 0$). b) Velocity weakening behaviour ($a - b < 0$).

film (Persson, 2000b,c).

$$\frac{d\theta}{dt} = (1 - \theta)(-\ln(1 - \theta))^{\frac{2}{3}} - \frac{V\theta}{d_c} \quad (1.27)$$

where d_c is a characteristic length over which the "solid structures" in the lubrication film start to behave as a fluid. The Persson's state evolution law can only be used when sliding the presence of a viscous fluid in the boundary lubrication regime defined by the hydrodynamic theory (i.e. low Sommerfeld number, Section 1.5).

Combining (1.24) with (1.25) or (1.26) or (1.27), two different regimes are observed as a function of the frictional parameters ($a - b$) defined in (1.28)

$$(a - b) = \frac{\Delta\mu_{ss}}{\ln\left(\frac{V}{V_0}\right)} \quad (1.28)$$

If $(a - b) > 0$, the effect on the friction is defined velocity-strengthening (i.e. $\mu(V) > \mu(V_0)$) (Figure 1.10a). If $(a - b) < 0$, the effect of friction is defined velocity-weakening (i.e. $\mu(V) < \mu(V_0)$).

In this second case, the transition from stable slip to unstable rupture can occur (Figure 1.11). In fact, stick-slip instabilities in the RSF law framework are predicted to occur when (Gu et al., 1984; Scholz, 1998; Scuderi et al., 2017):

$$\sigma'_n = \overline{\sigma}_c = \frac{K d_c}{(a - b)} \quad (1.29)$$

where σ'_n is the effective normal stress

The stability diagram for velocity weakening material was reported by Gu et al. 1984 (Figure 1.11). The diagram shows that velocity step $\Delta V = V - V_0$ necessary to de-stabilize a system is a function of the critical value of effective normal stress, $\overline{\sigma}_c$.

For granitic rocks, early studies mapped the region in the $\sigma_c - V_1 / V_0$ space where unstable

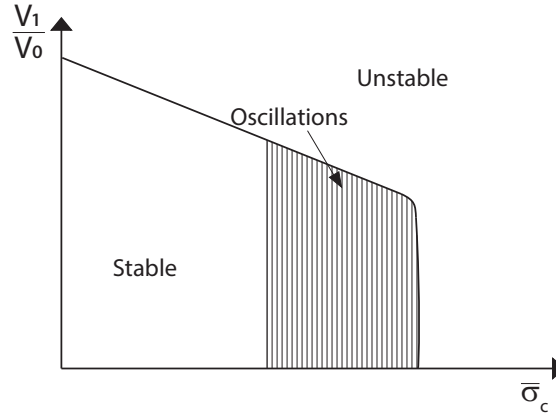


Figure 1.11: Stability diagram for velocity weakening material from (Gu et al., 1984).

behaviour (stick-slip) or stable behaviour are observed (Brace, 1972; Stesky et al., 1974; Byerlee and Brace, 1968). They found that stability is favoured by high temperature and low normal stress. Dry and wet fault gouges of granitoid composition were widely studied as well (Lockner and Byerlee, 1986; Blanpied et al., 1995; Lockner et al., 1987; Solberg and Byerlee, 1984) to investigate the effect of temperature, fluid pressure, normal stress and slip-rate on the rate and state frictional parameters and on the critical distance D_c . The transition from stable to unstable regimes was observed for temperatures higher than 90 °C, but lower than 350 °C. At higher temperatures ($T > 350$ °C), the difference $(a - b)$ becomes strongly positive. With normal stress at room temperatures, $(a - b)$ becomes negative with increasing normal stress for $\sigma_n < 15$ MPa (Leeman et al., 2018), but $(a - b)$ becomes strongly positive at higher normal stress (Lockner et al., 1987).

Table 1.2: Experimental studies of stability behaviour on granite material in different conditions of normal stress σ_N , fluid pressure P_f and temperature T . For each experimental study, we report the analyzed material, the experimental condition (gouge, bare surface "bare surf." and fractured surface "fract."), the main analyzed parameter ("Par.") are reported: σ_N for normal stress, T for temperature, RMS for roughness, V for slip-rate, k for permeability. "RH" for room-humidity condition, "Wet" for partially saturated condition and "RT" for room temperature condition.

Reference	Material	Exp	Par.	σ_n [MPa]	P_f [MPa]	T °C
Stesky et al. (1974)	Granite	fract.	T	440	RH	300-700
Okubo and Dieterich (1984)	Sierra G.	bare surf.	RMS	3.45	RH	RT
Solberg and Byerlee (1984)	Granite	gouge	σ_N	2.5-500	RH	RT
Tullis and Weeks (1986)	Granite	bare surf.	σ_N	27-84	RH	RT
Lockner et al. (1987)	Granite	gouge	T	390-460	RH	22-845
Linker and Dieterich (1992)	Westerly G.	bare surf.	σ_N	5 - 7	RH	RT
Kilgore et al. (1993)	Westerly G.	bare surf.	σ_N	5-150	RH	RT
Blanpied et al. (1998)	Westerly G.	gouge	T	400	100	23-600
Brown (1998)	Westerly G.	bare surf.	Stability	3.3-23	RH	RT
Ohnaka and Shen (1999)	Tsukuba G.	bare surf.	RMS	6.2	RH	RT
Biran et al. (2009)	Timna G.	bare surf.	RMS	2.5-15	RH	RT
Moore and Lockner (2013)	Westerly G.	gouge	T	100	RH	250
Mitchell et al. (2016)	Westerly G.	bare surf.	T	5-40	wet	20-600
Harbord et al. (2017)	Westerly G.	bare surf.	RMS	30-200	RH	RT
Leeman et al. (2018)	Quartz	gouge	V	4-14	RH	RT
Ishibashi et al. (2018)	Westerly G.	bare surf.	k	9-12	0.04-0.8	RT

1.8 Earthquake propagation

Earthquake ruptures propagate at \sim km/s and co-seismic slip-rates of 1 to 10 m/s are achieved on the fault surface (Rowe and Griffith, 2015; Heaton, 1990). Under these conditions, fault rocks experience an abrupt temperature increase due to frictional heating and a significant reduction of frictional strength. The reduction of strength is associated with dynamic weakening and lubrication mechanisms: thermal (flash heating, flash melting, thermal pressurization, water-vaporization) and/or mechanical (wear formation, powder lubrication, silica gel formation) and/or thermo-chemical (decarbonation, dehydroxylation) decomposition of fault rocks and minerals. The most prominent weakening mechanism, involving the melting of silicate minerals in rocks, was observed both in natural fault rocks (i.e., pseudotachylyte, (Sibson, 1975; Di Toro et al., 2006)) and in laboratory experiments (Di Toro et al., 2006, 2011). The pseudotachylytes are glassy fault rocks generated by frictional melting and are the only reliable markers of seismic slip.

In Figure 1.12 reported by Di Toro et al. (2011), it is possible to observe how the dynamic friction coefficient decreases as a function of the slip-rate for a wide variety of geological materials. In the following part, we present the physics of the weakening mechanisms which were defined

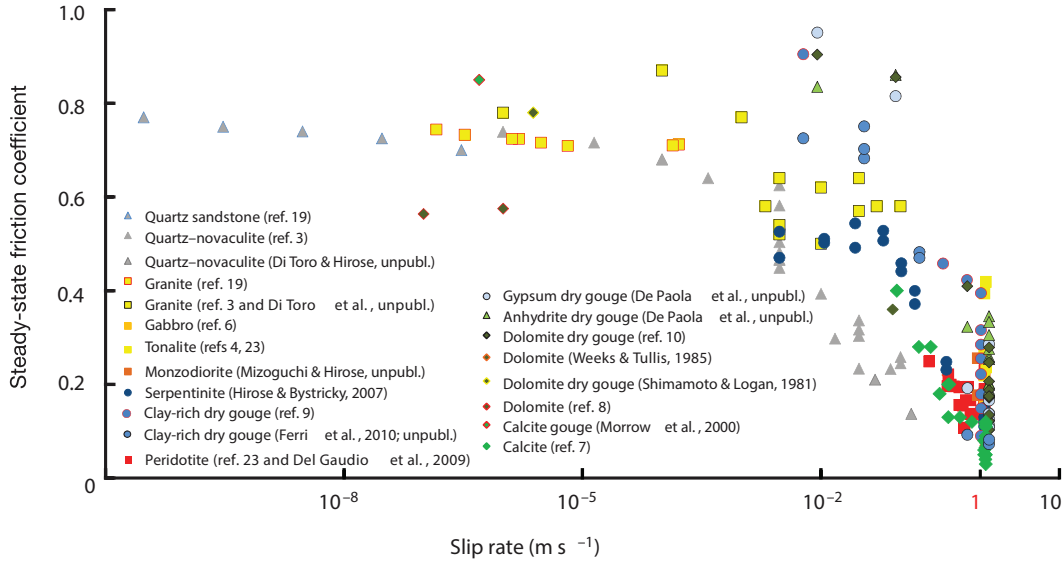


Figure 1.12: Dynamic friction coefficient (i.e., steady state friction coefficient in the figure) versus slip-rate from (Di Toro et al., 2011).

mainly in theoretical models and then applied to laboratory experiments performed at co-seismic slip-rates. Authors agree on the partial overlap of mechanisms and on the difficulty to distinguish them during the experiments. Other authors suggest that the mechanisms at the scale of the asperities (but controlling the bulk fault strength) occur first and are followed by mechanisms occurring on the whole surface (Rice, 2006; Violay et al., 2015).

A compilation of the existing data about high-velocity friction experiments and stick-slip experiments on granite rock bare surfaces and the processes proposed to control the dynamic weakening during earthquake propagation are presented in 1.3.

1.8.1 Thermal weakening processes

Flash heating theory is based on the observation that fault asperity contacts constitute the real area of contact (Bowden and Tabor, 1950). Asperities sustain a high normal stress and during an earthquake they have an intense, highly localized heating (Rice, 2006). The produced heat is proportional to the contact lifetime, slip-rate and shear stress. The contact frictional strength decreases by thermal degradation of the asperities. The degradation of a large amount of asperities determines the reduction of the whole fault surface strength. The first model of flash heating applied to earthquake mechanics was proposed by Rice (2006). In this model, contacts of uniform size D (i.e., with lifetime D/V), have a constant shear strength τ_c when they are at low temperatures. After they achieve a weakening temperature T_w , shear strength decreases to zero. The weakening temperature is specific to the rock composition. The temperature rises up to T_w and is estimated from a simple one-dimensional heat conduction analysis in

which the heat rate per unit area at the sliding asperity contact is calculated as $\tau_c V$. A critical slip-rate V_w defines the moment at which T_w is achieved and τ_c decreases to 0. When the slip-rate $V < V_w$, no weakening will occur, but if $V > V_w$, the fault undergoes weakening. In this model, the evolution of the apparent friction coefficient μ , has the value μ_s at $V < V_w$ and decreases to μ_w at $V > V_w$ according to:

$$\begin{cases} \mu = \mu_s & \text{if } V < V_w \\ \mu = \mu_s \frac{V_w}{V} & \text{if } V > V_w \end{cases} \quad (1.30)$$

In which V_w is defined as:

$$V_w = \frac{\pi \alpha_{th}}{D} \left[\frac{\rho C (T_w - T_f)}{\tau_c} \right]^2 \quad (1.31)$$

where α_{th} is the thermal diffusivity, ρC is the heat capacity per unit volume, T_f is the average temperature of the fault surface.

From an experimental perspective, Goldsby and Tullis (2011) and Rice (2006), estimated V_w for many rocks types to be in the range between 0.1 and 0.5 m/s. Additional laboratory experiments imposing high slip-rates on rock surfaces all agree on the role of flash heating controlling the decrease of friction coefficient at $V > V_w$ (Tsutsumi and Shimamoto, 1997; Hirose and Shimamoto, 2005; Goldsby and Tullis, 2002; Tullis and Goldsby, 2004; Passelègue et al., 2014).

Melt lubrication (Tsutsumi and Shimamoto, 1997; Hirose and Shimamoto, 2005) process is specific to rocks containing silicates. At the same time, it is the only fault weakening process with direct natural evidence in the form of pseudotachylite rocks (Sibson, 1975; Spray, 1993; Di Toro and Pennacchioni, 2004). In these rocks, the frictional strength after the initial decrease by flash heating increases again during the transition from isolated patches of molten asperities to a continuous layer of melt on the sliding surface. The pseudotachylite formation has been observed for relatively small normal stress σ_n and for specific lithology (e.g granite, gabbro and more in general silicate bearing rocks). This behaviour is due to the rapid solidification of the first patches of melted asperities due to low average temperature on the sliding surface (Tsutsumi and Shimamoto, 1997). In this way, the two sliding surfaces are locally welded together. However, with the continuing sliding and the increase of the frictional strength the average temperature of the sliding surface increases again and a continuous layer of fluid melt covers the sliding surface.

In the presence of fluids, flash heating and flash melting are still active mechanisms in microgabbro (Violay et al., 2014b), in basalt (Violay et al., 2015) and in granite (Passelègue et al., 2016b; Acosta et al., 2018). However, the water has a cooling effect on the asperities and leads to a delay in the formation of melt patches (Violay et al., 2014b).

1.8.2 Weakening processes dependent on fluid behaviour

Thermal pressurization (Sibson, 1973) mechanism defines the reduction of fault strength occurring by a decrease in effective normal stress σ'_n due to a pore fluid increase. The pore fluid pressure increases because temperature rises due to frictional heating, leading to a larger thermal expansion of the pore fluid compared to the pore space. This mechanism is favored when slip is localized, the shear-induced dilatancy is low and the host rock is impermeable. These conditions all limit the diffusion of pore fluid in the surrounding medium. Thermal pressurization is described by the following equations (Rice, 2006):

$$\frac{\partial T}{\partial t} = \frac{1}{(\rho C)_{eff}} \mu_0 (\sigma_n - P_f) \frac{v}{2w} + \alpha_{th} \frac{\partial^2 T}{\partial y^2} \quad (1.32)$$

$$\frac{\partial P_f}{\partial t} = \frac{(\lambda_f - \lambda_r)}{(\beta_f + \beta_r)} \frac{\partial T}{\partial t} + \alpha_{hy} \frac{\partial^2 P_f}{\partial y^2} \quad (1.33)$$

Where y is the axis perpendicular to the fault plane, ρ is the rock density, C rock specific heat, μ_0 the peak friction coefficient, V the slip-rate, α_{th} the thermal diffusivity of the fluid, λ the isobaric thermal expansion coefficient and β the compressibility (subscripts f and r stand for fluid and rock, respectively). The hydraulic diffusivity of the fault is expressed as a function of the fault's permeability (k) and the fluid viscosity (η) as $\alpha_{hy} = k/(\eta(T) \beta_f)$.

Thermal pressurization was largely investigated with numerical models (Viesca and Garagash, 2015; Wibberley and Shimamoto, 2005; Garagash and Germanovich, 2012; Rempel and Rice, 2006). Viesca and Garagash (2015) suggested that thermal-pressurization may become important for large slip earthquakes. Similarly, Rempel and Weaver (2008) showed that with long displacement allowing dissipation of the pore pressure increase by thermal pressurization, the temperature can rise again and lead to the melting of the surface.

Violay et al. (2015), Acosta et al. (2018) and Badt et al. (2020) employed experiments and numerical models to show the effect of thermal pressurization on fault slip behaviour on bare surfaces. Violay et al. (2015) showed that thermal pressurization can occurs if a small volume of fluids is trapped in a low permeability fault. Under these conditions, the diffusion of fluids outside the fault is negligible and fluids can effectively pressurize. Acosta et al. (2018) showed the role of water's phase transition in limiting thermal pressurization at the asperity scale during stick-slip experiments. (Badt et al., 2020) performed dedicated experiments on Frederick diabase at sub-seismic slip-rates and high confining pressure. They observed a strengthening behaviour of the rock under room-humidity condition and a weakening behaviour under fluid saturated conditions. They invoked thermal-pressurization as the only possible weakening mechanisms for their experiments.

Thermal pressurization was addressed as an efficient weakening mechanism for experiments performed under partially saturated conditions on clay-rich gouge material (Mizoguchi et al., 2009; Ferri et al., 2010; Ujiie et al., 2011; Faulkner et al., 2011; Ujiie et al., 2013; Chen et al., 2013; Boulton et al., 2017; Aretusini et al., 2019) or in coal gouge (O'Hara et al., 2006).

Elasto-hydrodynamic lubrication (EHD) (Brodsky and Kanamori, 2001) mechanism applies the lubrication theory (Section 1.5) to the friction of rock surfaces. According to EHD theory, a layer of viscous fluid can decrease the strength of the fault surface. The presence of a highly viscous fluid in natural faults can be due to injection activities (Section 1.2) or to the rock melt produced by frictional heating during seismic slip. The behaviour of a lubricated fault can be distinguish three different lubrication regimes: boundary lubrication regime, mixed lubrication regime, elasto-hydrodynamic (or hydrodynamic) regime. The fault shear strength dependence with the Sommerfeld number S can be expressed as (Bizzarri, 2012; Brodsky and Kanamori, 2001):

$$\tau(S) = \begin{cases} \mu_{static} \sigma_{eff} + \frac{w}{u} P_{lub}, & \text{if } S < 1 \\ \frac{w}{u} P_{lub}, & \text{if } S \geq 1 \end{cases} \quad (1.34)$$

where $S = P_{lub}/\sigma_n$ is the Sommerfeld number, $P_{lub} = 6\eta r \delta^2 V / (2w)^3$ the lubricant pressure, η the viscosity of the fluid, $r=0.001$ (Brodsky and Kanamori, 2001) the dimensionless roughness, δ the slip distance, and w the average thickness of the slurry film, V the measured slip-rate. The Sommerfeld number (Section 1.5 describes the transition between three lubrication regimes (boundary, mixed or fully lubricated regimes) which are associated with the evolution of the strength of the fault. So far, only numerical models analyze the possibility of EHD mechanism in controlling fault strength during seismic slip (Brodsky and Kanamori, 2001; Bizzarri, 2012).

The melt fluid layer produced by flash melting has a lubricating effect on the fault. Under this condition and in agreement with the hydrodynamic theory (Section 1.5), the fault strength is of the order of $\tau = \eta V / h$ where η is the melt viscosity at a given temperature and for a given rock composition (Giordano et al., 2008), V the slip-rate and h the thickness of the melt layer. The viscosity of the fluid layer in the case of melt formation is of the order of 100 Pa.s (Giordano et al., 2008), 3 orders of magnitude higher than the fluid analyzed for the induced seismicity activities (Section 1.2). Faults containing pseudotachylyte rocks are an example of natural lubricated faults.

1.8.3 Weakening mechanisms related to wear products

Upon sliding, asperity contacts mechanically degrade and produce fine wear products, often consisting of nanoparticles (~ 10 -100 nm diameter size). With displacement, isolated patches of wear products can form a third body layer, defined as fault gouge, whose properties control

the overall fault core properties. This is the case in mature faults.

Powder lubrication (Reches and Lockner, 2010) is a weakening mechanism given by the lubrication effect of nanosize gouges particles present on the fault surface. The nanoparticles act as a solid lubricant on the fault surface (Bowden and Tabor, 1950). The nanoparticles and, more generally, gouges are the product of fault slip in many lithologies (Wilson et al., 2005). Chen et al. (2017) showed that powder lubrication operates at the intermediate slip-rates in a range of 0.01–0.1 m/s for granitic rocks in the form of powder rolls.

The following weakening mechanisms are specific for certain rock compositions: carbonatic rocks or silica-bearing rocks.

Decarbonation (Han et al., 2007) is the thermal decomposition of carbonate minerals (calcite and dolomite), which is associated with weakening of rock surfaces. During seismic slip, frictional heating causes the decomposition of calcite into lime (CaO) and CO₂ at temperatures between 700°C and 900°C (Han et al., 2007). Similarly, dolomite decomposes to Mg-calcite and CO₂ ($T=550^\circ\text{C}$) and then Mg-calcite decomposes to periclase (MgO) and CO₂ ($T=900^\circ\text{C}$) (De Paola et al., 2011). All these reactions are endothermic (i.e they limit the temperature increase by frictional heating) and result in the production of wear particles which under seismic deformation conditions can contribute to fault weakening through a variety of proposed processes or mechanisms:

- powder lubrication (Han et al., 2010): spherical wear particles rolling between two rock surfaces reduce the bulk strength;
- localization processes (Brantut and Platt, 2017; Platt et al., 2015; Smith et al., 2015; Platt et al., 2014): at high strain-rate the wear particles localize in a weaker thin shear band. Moreover, in the presence of fluids, the localization of particles can lead to thermal-pressurization of trapped fluid (Rice et al., 2014; Platt et al., 2015; Brantut and Platt, 2017).
- viscous flow processes in the deforming wear product at high strain rate and temperature (diffusion creep and dislocation creep) (Verberne et al., 2014a; Green et al., 2015). De Paola et al. (2015) and Pozzi et al. (2019) suggested that diffusion creep and dislocation creep can occur also without thermally-activated phase transitions, but they can be enhanced by the grain-size evolution during sliding.

Other works focused on the early stages of seismic deformation of rock surfaces and discussed the dynamic weakening motivated by flash amorphization and decomposition of calcite asperity contacts directly into lime and amorphous carbon by dislocation avalanches (Spagnuolo et al., 2015).

1.8. Earthquake propagation

Table 1.3: Experimental studies on the weakening of granite material in different conditions of normal stress σ_N , fluid pressure P_f and temperature T . The experimental condition of V for slip-rate, σ_N for normal stress, P_c confining pressure and T for temperature are reported. For "stick-slip" experiments no slip-rate is reported. "RH" for room-humidity condition and "RT" for room temperature condition. "Mech." reports the suggested weakening mechanisms activated during the laboratory experiments: "FH" for flash heating, "FM" for flash melting, "EHD" for elasto-hydrodynamic, "Powder" for powder lubrication and "TP" for thermal-pressurization.

Reference	Mat.	V [m/s]	σ_N [MPa]	P_c [MPa]	P_f [MPa]	T [°C]	Mech.
Di Toro et al. (2004)	Granite	0.003-0.1	5	-	RH	RT	FH/FM
Tullis and Goldsby (2004)	Westerly G	0.001-2	5	-	RH	RT	FH/FM
Spray (2005)	Westerly G.	2-4	0.25-0.5	-	RH	RT	FM/EHD
Reches and Lockner (2010)	Sierra W. G.	0.01-1	0.7-7.1	-	RH	RT	Powder
Goldsby and Tullis (2011)	Westerly G	0.4	5	-	RH	RT	FH
Hirose et al. (2012)	Inada G.	0.004-0.27	0.21-6.3	-	RH	RT	Powder
Passelègue et al. (2014)	Westerly G	0.36	5	-	RH	RT-330	FH
Passelègue et al. (2016b)	Westerly G	0.03-3	5-20	-	RH -5	RT	FH/FM
Lockner et al. (2017)	Westerly G	Stick-slip	-	40-400	RH	RT	FH
Chen et al. (2017)	Granite	0.001-1	1.1-14.4	-	RH	RT	Powder
Acosta et al. (2018)	Westerly G.	stick-slip	-	50-95	RH-25	RT	FM/TP
Aubry et al. (2018)	Westerly G	stick-slip	-	45-180	RH	RT	FM

Experiments performed in presence of pressurized fluid on Carrara Marble samples showed that the first stage of the weakening is associated with subcritical crack growth. Temperature increase at a later stage of slip triggered decarbonation Violay et al. (2013, 2015).

Silica gel formation mechanism is responsible for fault weakening by the formation of a specific wear product (silica gel) and requires silica bearing rocks. (Goldsby and Tullis, 2002; Di Toro and Pennacchioni, 2004; Nakamura et al., 2012; Rowe et al., 2019). This process can occur for large slip (> 0.5 - 1.0 m) and moderate slip-rate (> 1 mm/s), in the presence of air humidity. The concept is that granulation within the shear zone (wear of asperities) produces fine silica particles which adsorb water to their surfaces and form a gel. The gel is weak during sliding and then becomes stronger when sliding stops (it becomes an amorphous solid). In presence of fluids, Mizoguchi et al. (2009) suggested silica gel formation as a possible weakening mechanism activated for the Nojima gouge during experiments performed under partially saturated condition.

To complete the understanding of earthquakes mechanics, the evolution of the strength of the fault (and consequentially the evolution of the apparent friction coefficient) has to be related with the energy dissipation and, more generally, to the energy balance during earthquake rupture.

1.9 Energy budget

An earthquake produces an average slip $\Delta\delta$ over a rupture area A on a fault surface. The energy balance associated to rupture propagation in a pre-stressed medium can be written as follows:

$$\Delta W = W_b + W_h + E_r + W_r \quad (1.35)$$

where ΔW is the potential energy drop $\Delta W = \sigma_m + \Delta\delta A$, W_b is the breakdown work (or fracture energy, the energy spent to extend the rupture area during the earthquake), E_r is the radiated energy (i.e., the energy transported by the seismic waves), W_h is the energy dissipated as heat in the fault plane, and W_r is the restrengthening work (i.e. the energy spent during the rupture arrest) (1.13.a).

A part of the earthquake energy is used for near and off-fault damage associated with the rupture (Rice et al., 2005; Andrews, 2005; Nielsen et al., 2016) and it can be included into the breakdown work W_b (Kanamori and Rivera, 2013) From a seismological point of view, the breakdown work can be estimated from the measurements of radiated energy and earthquake source parameters. During an earthquake, in the volume of rocks surrounding the rupture area, a sudden decrease of stress occurs called static stress drop $\Delta\sigma = \sigma_1 - \sigma_2$, where σ_1 is the stress before the earthquake and σ_2 is the stress after the earthquake (Figure 1.13). The mean stress is defined as $\sigma_m = (\sigma_1 + \sigma_2)/2$. To quantify the size of an earthquake, the seismic moment M_0 is used (Maruyama, 1963). The seismic moment M_0 is determined from the integral of the far-field displacement from geodetic data or from seismic radiation as:

$$M_0 = G\Delta\delta A \quad (1.36)$$

where G is the shear modulus of the surrounding medium.

The static stress drop is estimated following:

$$\Delta\sigma = C G \frac{\Delta\delta}{L} \quad (1.37)$$

where C is a geometric constant of order unity and L is the characteristic length scale of the rupture $L \sim A^{0.5}$. The geometric constant C depends on the character of the rupture: for a circular crack, $C \sim 7/16\pi$ and for an infinite length crack of half-width W , with $L \gg W$, $C \sim 2\pi$. Combining (1.36) and (1.37), the static stress drop can be estimated following

$$\Delta\sigma = C M_0 A^{-3/2} \quad (1.38)$$

In seismology, E_r is measured from the radiated seismic waves and used to estimate W_b from source parameters like the seismic moment M_0 and static stress drop $\Delta\sigma$, as (Abercrombie

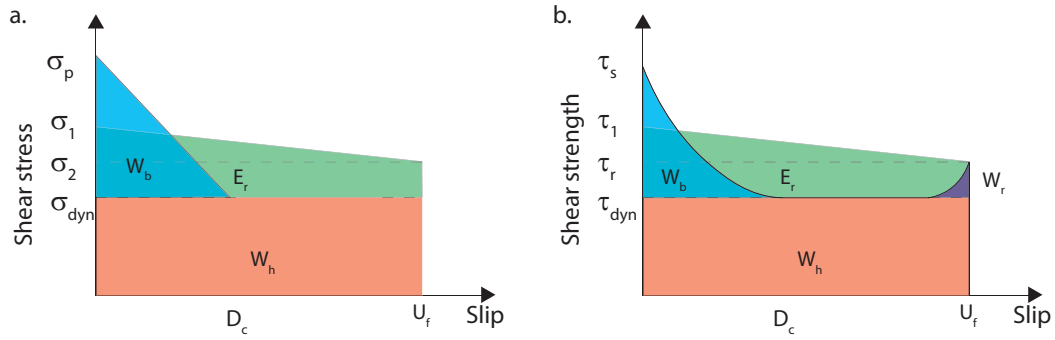


Figure 1.13: Schematic of the energy budget for a) earthquake rupture seismological model and b) laboratory earthquakes. W_b (blue area) is the breakdown work dissipated during the instability. For the seismological model, shear stress evolves linearly with slip accordingly with the slip-weakening model (Ida, 1972). E_r (green area) corresponds to the radiated energy and W_h (red area) is the frictional energy. W_r is restrengthening work. D_c is the critical slip necessary to reach σ_{dyn} or τ_{dyn} and U_f corresponds to the final value of the displacement.

and Rice, 2005; Viesca and Garagash, 2015):

$$W_b = \left(\frac{\Delta\sigma}{2} - \frac{GE_r}{M_0} \right) \delta \quad (1.39)$$

However, the estimate of W_b performed in seismology is sensitive to the uncertainties in the measurement of E_r from the seismic waves. Moreover, this method is sensitive to the assumption done regarding the static stress drop: the final stress σ_2 might be either higher (undershoot), equal, or lower (overshoot) compared to the dynamic fault stress σ_{dyn} (Abercrombie and Rice, 2005; Viesca and Garagash, 2015). In Figure 1.13a, for example, a case of overshooting is reported. In seismological studies, no information about the actual fault strength (and therefore the dynamic fault stress σ_{dyn}) is accessible through the source parameters.

The evolution of fault strength is represented by the slip-weakening model (Section 1.7.1). This model assumes that the fault strength during the propagation of a rupture is represented as a linear decrease with slip from a peak strength τ_p to a residual strength τ_{dyn} (Ida, 1972). The strength decreases until slip reaches a critical value D_c . In this framework, the sum of the breakdown and frictional energy per unit area can be represented by the integral of the strength as a function of slip (Figure 1.13a).

The schematic partitioning of the total energy into radiated, breakdown, restrengthening and frictional energy is also valid to estimate energy during laboratory earthquakes, where, unlike in seismological studies, either the evolution of the experimental fault strength or the initial state of stress are measured directly (Figure 1.13b). However, in laboratory experiments, the

energy budget is in reference to an area which is much smaller compared to the entire area of an earthquake rupture.

The breakdown work or fracture energy W_b is defined as (Palmer and Rice, 1973):

$$W_b = \int_0^{D_c} (\tau(U) - \tau_{dyn}) dU \quad (1.40)$$

where D_c is the slip distance at which the measured shear strength becomes constant τ_{dyn} . The frictional heating W_h is the energy dissipated through heat

$$W_h = \tau_{dyn} U_f \quad (1.41)$$

The restrengthening work W_r is the the energy during the deceleration phase of the natural (Tinti et al., 2005b) and experimental (Violay et al., 2019) earthquakes and can be computed as:

$$W_r = \int_{D_c}^{U_f} (\tau(U) - \tau_{dyn}) dU \quad (1.42)$$

Where U_f is the total slip the event.

The estimation of the individual terms of the energy budget was performed with the following types of experiments: those which measured the evolution of stress during sample failure (e.g., (Wong, 1982; Ohnaka, 2003)), or during stick-slip instabilities (e.g., (Aubry et al., 2018; Passelègue et al., 2016a)), while other experiments measured the evolution of shear strength during high slip-rate deformation (e.g., (Nielsen et al., 2016)).

For sample failure and stick slip-experiments the energy partitioning can be analyzed in the frame of shear crack propagation. The breakdown work in this condition can be obtained using the slip-weakening model and the recorded stress drop (Rice, 1968; Wong, 1982; Ohnaka, 2003). The values of σ_1 and σ_2 are known when performing experiments equipped with dynamic strain gauges. In some cases, E_r was estimated similarly as in seismology, from the measurement of the acoustic emissions, which are the laboratory analogue of the seismic waves (Passelègue et al., 2016b). In other cases, the dynamic stress state was measured using dynamic strain gauges to resolve the near-fault stress field and dynamic stress drop. Passelègue et al. (2016a) studied the breakdown work in stick-slip triaxial experiments on pre-cut samples of Westerly granite. They showed that breakdown work increases with confining pressure and fault slip, and that breakdown work is smaller in pre-cut experiments than in intact rock experiments on the same material (Wong, 1982; Ohnaka, 2003).

Bayart et al. (2016) studied the influence of fluid lubricant on fracture energy performing stick-slip experiments in PMMA samples within the boundary lubrication regime (Section 1.5). They showed that the fracture energy, computed using the Linear Elastic Fracture Mechanics

(LEFM) theory (Irwin, 1968), is higher for experiments in presence of a lubricant on the sliding surface than for experiments performed under dry condition. They also showed that the increase of the fracture energy is independent of the fluid viscosity but is instead a function of the applied normal stress and fluid rheology. They associated the increase of fracture energy in presence of a lubricant with the larger critical slip distance D_c and stress drop $\Delta\sigma$ compared to the dry condition.

For high slip-rate deformation experiments (i.e. rotary shear experiments), the energy partition is analyzed as the frictional energy dissipation in a simulated fault point belonging to an infinite planar fault. In this framework, the breakdown work, the frictional heating and the restrengthening work are computed directly from the shear strength measurement over slip. Unlike sample failure and stick slip experiments, the rotary shear experiments can apply slip of the same order of magnitude as natural earthquakes (Di Toro et al., 2010). However, rotary shear experiments cannot reproduce the rupture propagation (i.e. stress drop at the tip of the crack) and no measurements of the initial and final stress are possible.

Violay et al. (2014b) showed that for small slip (<0.1 m) both the lithology and the availability of pressurized fluid played a role on the breakdown work. In microgabbro rocks, the presence of fluids increased the breakdown work whereas in Carrara marble the converse occurred. For larger slip (>1 m), the breakdown work was similar independently from rock composition and fluid availability.

1.10 Objective of the thesis

The effect of fluid for the generation and propagation of earthquake has been largely investigated by both experimental techniques and by numerical modelling. The results have been extrapolated for natural earthquakes, but also for induced seismicity. However, the reference fluid has mostly been water. In the reality, the fluid that can be present in a fault is not only water, but can be industrial fluids (brine, wastewater, fracturing fluids) in the case of induced seismicity or melt in case of natural earthquakes. The viscosity of these fluids can range over 6 orders of magnitude. Moreover, fault weakening has been interpreted as a consequence of several processes, such as flash heating and melting, silica gel formation, decomposition reactions, superplastic flow and thermal pressurization; many of these processes are rock-type dependent. However, though the presence of fluids is pervasive in faults, the role of fluids on fault weakening has been mainly conjectured based on theoretical models and the role of fluid viscosity has been overlooked.

In this thesis, we study the frictional properties of a fault system in presence of fluids with variable viscosity. In particular, we reproduced both the nucleation and the propagation phases of an earthquake at the laboratory scale.

In this doctoral research, we have addressed four main aspects:

- Frictional properties concerning fault stability and earthquake generation for a lubricated fault at low slip-rates
- Efficiency of the Elastohydrodynamic lubrication as a weakening mechanism that can be potentially activated during the fault reactivation and earthquake propagation for a lubricated fault
- Analysis of the energy dissipated during the rupture processes as a function of the slip-rate (e.g earthquake phase) and fluid viscosity trapped on the slip surfaces.
- Parametric analysis for the upscaling of the laboratory results for human-induced seismic events considering the viscosity of the injected fluid as a variable of the problem.

1.11 Organization of the thesis

This thesis has been written in a compilation of articles format following the EPFL guidelines, in which the candidate was first author. The articles are published or submitted for publication in peer-reviewed journals. As a result, in the introduction section of each chapter, the literature review may be repeated.

The thesis is structured as follow:

- **Chapter 2:** The content of this chapter has published in *Geophysical Research Letters* in May 2020. The chapter investigates how a lubricated fault responds to velocity perturbations due to earthquake nucleation. To achieve this goal bare surfaces samples were tested under two effective normal stresses and in the presence of pressurized fluids with varying viscosity (from 1 *mPa s* to 1226 *mPa s*), to keep the ratio between fluid pressure and normal stress on the fault equal to 0.2. Experiments were performed in a direct shear configuration in the triaxial apparatus FIRST (EPFL). The result was modelled with a rate and state law modified for lubricated fault surfaces. The chapter discusses the fault stability parameters for sub-seismic slip-rates in presence of pressurized fluid with varying viscosity.

Reference:

Cornelio, C. and Violay, M., (2020a). Effect of fluid viscosity on earthquake nucleation., *Geophysical Research Letters*. <https://doi.org/10.1029/2020GL087854>

- **Chapter 3:** The content of this chapter has been published in *Journal of Geophysical Research: Solid Earth* in January 2020. The chapter investigates the mechanical behaviour of the experimental faults in presence of viscous fluid at the onset of the reactivation.

The experiments have been performed in a rotary shear configuration using SHIVA (INGV, Rome) by exploiting a novel experimental technique for rotary shear apparatus (which should reproduce better geo-engineering operational conditions) which consists of increasing the imposed shear stress at a given fluid pore pressure up to the onset of fault reactivation. The research reports experimental evidence, validated by numerical models, that once the fluid-pressurized fault is frictionally unstable and slip-rate accelerates, the associated fault weakening mechanism (flash heating, thermal pressurization or elastohydrodynamic lubrication) depends on fluid viscosity. Moreover, the measured breakdown work is independent of the particular weakening mechanism and is similar in magnitude with the one of induced and natural earthquakes for a given seismic slip distance. This similarity would also allow us to scale the experimental observations to natural conditions.

Reference:

Cornelio, C., Passelègue, F. X., Spagnuolo, E., Di Toro, G., Violay, M. (2020). Effect of fluid viscosity on fault reactivation and coseismic weakening. *Journal of Geophysical Research: Solid Earth*, 125, e2019JB018883. <https://doi.org/10.1029/2019JB018883>

- **Chapter 4:** The content of this chapter has been published in *Nature Communications* in March 2019. The chapter investigates the mechanical behaviour of the experimental fault lubricated by the presence of pressurized viscous fluid during the propagation phase of an earthquake. Around 40 experiments have been performed using the rotary shear configuration of SHIVA (INGV, Rome) varying the effective normal stress (up to 20 MPa), the imposed trapezoidal slip-rate function with a plateau ranging between 10 $\mu\text{m/s}$ and 3 m/s and the experimental condition (i.e. room-humidity experiments and fault saturated with pressurized fluid condition). The experimental results showed that elasto-hydrodynamic lubrication may be an efficient fault weakening mechanism, independent of rock lithology. Moreover, the presence of highly viscous fluids significantly reduces the fault resistance. Finally, considerations about the energy dissipated in these varying conditions are made.

Reference:

Cornelio, C., Spagnuolo, E., Di Toro, G., Nielsen S., Violay, M., (2019). Mechanical behaviour of fluid-lubricated faults. *Nat Commun* 10, 1274. <https://doi.org/10.1038/s41467-019-09293-9>.

- **Chapter 5:** The content of this chapter has been published in *Geophysical Journal International* in April 2020. This chapter includes a parametric analysis of realistic geo-engineering effective stresses and environmental conditions which were compared with a series (8 cases) of well-documented cases of induced seismicity in the presence of fluids with different viscosities. First, the range of values for the parameters necessary

to describe the influence of viscous fluid on earthquakes reactivation are determined. Second, the effect of injected fluid viscosity on the weakening mechanism activated during earthquake propagation and the dynamic strength of the fault is defined by the dimensionless Sommerfeld number S . Finally, a comparison between the analyzed eight induced seismicity cases and the decay of the dynamic friction coefficient due to elasto-hydrodynamic is reported.

Reference:

Cornelio, C. and Violay, M., (2020b). Parametric analysis of the elastohydrodynamic lubrication efficiency on induced seismicity, *Geophysical Journal International*, Volume 222, Issue 1, July 2020, Pages 517–525,. <https://doi.org/10.1093/gji/ggaa180>

- **Chapter 6:** Conclusions and perspectives: in this chapter, the major outcomes of this research and present possibilities for further works and developments linked to the work presented in this thesis.

Moreover, in the appendix, there are included two more articles published in peer reviewed in which the candidate was not the first author of the paper, but for which she actively participated in the discussion and writing of the manuscript. In particular:

- **Appendix A:** The content of this Appendix is under review in *International journal of rock mechanics and mining sciences*. The Appendix A presents a new state of art apparatus HighSTEPS installed at EPFL (Switzerland) in April 2018. Mechanical details of the apparatus are presented in this chapter, as well as the possible experimental procedure that can be followed. Measurements of the machine stiffness have been performed. Measurements on friction, velocity dependence of friction, healing and creep properties of carbonate material replicate the values presented in the literature.
- **Appendix B:** The content of this Appendix has been published in *Earth and Planetary Science Letters* in September 2019. The Appendix B presents the first results of friction experiments that, by reproducing seismic slip conditions, aim at understanding the effect of rock composition and water content on the slip deceleration and fault re-strengthening during earthquakes.

To achieve this goal, rotary shear experiments were performed in SHIVA (INGV, Rome). The experimental results showed that at constant deceleration rate, and under room humidity conditions and low power density (i.e. product of normal stress per slip-rate), re-strengthening rate during the deceleration stage is much faster in carbonate bearing rocks than in silicate-bearing rocks. Moreover, in silicate-bearing rocks, the re-strengthening rate increased with the power density. The presence of liquid water further enhanced this trend. On the other hand, in carbonate bearing rocks the re-

strengthening rate decreased drastically with power density and in the presence of liquid water.

Reference:

M. Violay, F. Passelegue, E. Spagnuolo, G. Di Toro, C. Cornelio, (2019). Effect of water and rock composition on re-strengthening of cohesive faults during the deceleration phase of seismic slip pulses, *Earth and Planetary Science Letters*, 55-64, 522. <https://doi.org/10.1016/j.epsl.2019.06.027>.

2 Effect of fluid viscosity on earthquake nucleation.

Authors: Chiara Cornelio¹, Marie Violay¹.

¹ Laboratory of Experimental Rock Mechanics (LEMR), ENAC, EPFL, Switzerland;

Reference: Cornelio, C. and Violay, M., (2020b). Effect of fluid viscosity on earthquake nucleation., Geophysical Research Letters. <https://doi.org/10.1029/2020GL087854>

Contributions: Original idea was from C. Cornelio and M.Violay. C.Cornelio performed the experiments and the analysis of the results. C. Cornelio and M.Violay co-wrote the manuscript.

Highlights:

- the viscosity of the pressurized fluid on the experimental fault did not influence the static friction coefficient;
- the fluid viscosity influenced the dynamic friction coefficient in agreement with the elasto-hydrodynamic theory;
- the $(a - b)$ rate and state friction parameter evolves with fluid viscosity, and for high viscosity we observed a transition from positive to negative $(a - b)$ values. This suggests that the use of high fluid viscosity in geo-reservoirs might promotes unstable slip behavior and earthquake nucleation.

2.1 Abstract

Injection of fluids in geo-reservoirs can reduce the effective stresses at depth, lubricating the nearby faults, promoting slip and, potentially, earthquakes. High-viscous fluids are often used during hydraulic-fracturing and production phases in geo-reservoirs. Here, we performed dedicated experiments to study the influence of fluid viscosity on earthquake nucleation. We performed frictional sliding experiments at 30 and 50 effective normal stresses and fluids viscosity ranging from 1 mPa.s to 1226 mPa.s, and modelled them with a rate and state friction law. In the presence of fluid, the state variable is defined as the ability of the fluid to flow. Our results showed that static friction slightly decreases with increasing viscosity, the dynamic friction is governed by the dimensionless Sommerfeld number ($S = 6\eta VL/(\sigma'_n H^2)$). Moreover, we observed that the $(a - b)$ parameters of the rate-and-state friction law decrease with increasing viscosity down to $(a - b) < 0$, possibly promoting unstable slip and earthquake nucleation.

2.2 Introduction

In the last 30 years, the increase in human-induced earthquakes associated with wastewater disposal, gas storage or geothermal exploitation (Ellsworth, 2013; Zoback, 2007a) has become an important scientific and social issue. As a consequence, the seismic activity rates increased in stable continental regions far from active tectonic margins (Calais et al., 2016). The principal explanation has been that long-term fluid injections nearby pre-existing faults can i) modify the stress field conditions of the fault by changing the reservoir volume and stresses or can ii) decrease the effective normal stress acting on a fault causing its reactivation (Ellsworth, 2013; Keranen et al., 2013; King Hubbert and Rubey, 1959; McGarr et al., 2014; Weingarten et al., 2015). Under this condition, fluid overpressure is not the only parameter governing fault reactivation and the associated seismicity. The injection procedures (Noël et al., 2019) and the fluid thermal and physical properties (Acosta et al., 2018) are also key parameters to understand fault reactivation. Moreover, in geoengineering practice, the viscosity of the injected fluids varies over four orders in magnitude, from 0.001 Pa s for liquid water to ~ 0.1 for wastewater disposal (Fu, 2017; Lu and Wei, 2011; Szafranski and Duan, 2018), up to ~ 10 Pa s for fracturing fluids (Cornelio and Violay, 2020b; Economides and Boney, 2000; Esmaeilirad et al., 2016b,a; Zhang et al., 2010).

The fluid injection procedure can involve long-term low-pressure injections to minimize the associated seismicity. In this situation the viscous fluid might have time to diffuse and flow throughout the whole rupture area of the fault surface.

Furthermore, recent experimental studies have shown that fluid viscosity controls seismic source parameters, including stress drops, the weakening distance, weakening rate and the

earthquake energy budget (Cornelio et al., 2019, 2020).

To model the mechanical behavior of these earthquakes, the failure conditions to initiate rupture are often treated using the isotropic Mohr-Coulomb theory, where the critical shear stress (τ_{crit}) is given by $\tau = \mu(\sigma_n - P_f)$, where τ and σ_n are the shear stress and the normal stress that act on the fault plane, respectively; μ is the coefficient of friction; and P_f is the pore pressure. On the other hand, the slip behavior during fault reactivation, i.e., the earthquake potential of a fault is often modelled with rate-and-state friction (RSF) laws, which provide a comprehensive analysis of the slip behavior. In this framework, the frictional response of a fault varies with the previous loading history and depends on both the instantaneous slip-rate (V) and a state variable (θ) that considers the gradual evolution of the sliding interfaces (Dieterich, 1978; Ruina, 1983). The RSF theory suggests that stable sliding is favored by increasing pore fluid pressure, and a low injection rate (Heslot et al., 1994; Ikari et al., 2009; Niemeijer and Collettini, 2014; Noël et al., 2019; Scholz, 1998; Scuderi et al., 2016; Segall and Rice, 1995). However, how the viscosity affects the evolution of the rate-and-state friction parameters and therefore the fault stability itself are currently not clear.

In this work, we conducted frictional sliding experiments in a vertically saw-cut triaxial configuration at different effective normal stresses. We have run tests under dry (room-humidity) and low to high viscous fluid fault saturated conditions. Further, we examine the stability behavior of the fault under these end-member conditions in the light of the rate-and-state frictional parameters. Here, we attempt to quantify the frictional strength and stability of granitic faults saturated with viscous fluids.

2.3 Methods

We performed frictional tests using a recently installed triaxial deformation apparatus, oil-confining medium called FIRST, located at EPFL, Switzerland (Figure 2.1, Figure 2.2a). FIRST is a unique high-pressure triaxial deformation apparatus built by Top Industrie and equipped with six syringe pumps. The concept is based on the triaxial apparatus developed by Borgomano et al. (2020). The hydraulic triaxial cell can reach a maximum confining pressure of 200 MPa (using silicon-oil as confining medium), a maximum axial stress of 1.5 GPa and a maximum fluid pressure of 200 MPa.

Two syringe pumps are used for the confining pressure, two syringe pumps for the axial pressure and two syringe pumps for pore fluid pressure. For confining pressure and axial stress, the pumps work alternatively to allow an infinite reservoir volume.

A servo-controlled heating collar is wrapped around the vessel and allows heating up to 200 °C. The temperature is measured and controlled by three K-type thermocouples located inside the vessel. The cylindrical rock sample of 38 mm diameter and 76 mm length is jacketed in a PVC sleeve to separate the confining oil from the sample and from the fluid pressure. It is

sandwiched between two anvils. Two o-rings are placed on the anvils for perfect sealing of the sample.

Two high pressure anti-corrosion fluids separator of 500 ml are located between the fluids pump and the sample to perform experiments with highly viscous or highly corrosive fluids. The fluid pressure is measured and controlled by pressure transducers placed between the sample and the fluid separators.

The axial deformation of the sample is measured by both external displacement LVDT in contact with the moving piston and with two internal LVDTs with a resolution of μm . In our experiments the average of the internal LVDTs displacement measurement was used to control the axial piston movement. The top piston and the bottom part of the piston can equipped with P- and S- homemade ultrasonic transducer.

Up to 12 stain gauges connected in in quarter bridge can be glued on the sample and

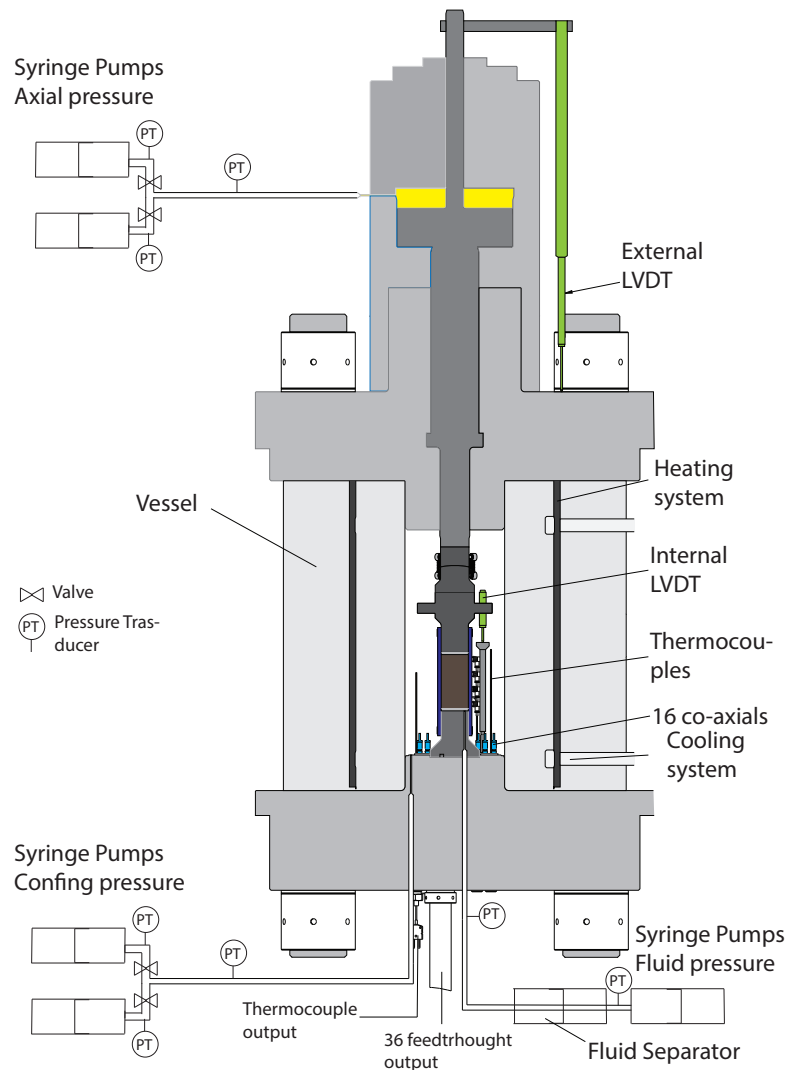


Figure 2.1: Sketch of the triaxial cell FIRST, built by the company TOP industry.

Chapter 2. Effect of fluid viscosity on earthquake nucleation.

connected through a connecting tube between the triaxial cell and the bottom 36 axial feedthroughs to the data acquisition system (DAQ) or to a digital oscilloscope to be recorded in continuously at high recording frequency (2 MHz) (not used in this series of experiments). The base of the vessel is internally equipped with 16 co-axial connectors for acoustic emission monitoring, 1 fiber optic port and 4 thermocouples ports.

Experimental data are corrected by the axial stiffness of the machine (540 KN/mm, using the internal LVDTs) both at 30 MPa and 50 MPa confining pressure. The tests were conducted on bare surfaces in an axially pre-cut configuration on Lapeyrate granite cylinders (Figure 2.3), following the method described in (Harbord et al., 2017). The experimental assembly consists of two semi-cylinders of 37 mm diameter cut along a vertical axis plane (Figure 2.2). Before beginning the experiments, the two half cylinders are offset using ~10 mm-high silicon spacers, creating an initial contact area of ~1950 mm², allowing up to 5 mm displacement. Sliding surfaces were roughened using 120 SiC abrasive paper to produce an initial roughness of ~3 μm (Figure 2.3c). The normal stress on the fault equals the confining pressure, $\sigma_n = P_c$, and shear stress, τ , is proportional to the pressure of the vertical piston σ_a :

$$\tau = \sigma_a \frac{A_0}{A_{sliding}} \quad (2.1)$$

where A_0 is the two semi-cylinder base area, and $A_{sliding}$ is the sliding surface contact area $A_{sliding} = A_i + 2r\delta(t)$ where A_i is the initial contact area, $2r$ is the sample diameter and δ is the slip of the fault. To facilitate fluid saturation of the fault plane, two 5-mm diameter boreholes having inclinations of ~45 degrees with respect to the fault surface were drilled at ~2.5 mm from the edge of the half-cylinder sample through the material on both sides of the fault (Figure 2.3a and Figure 2.3b).

We run experiments under room humidity conditions (i.e., dry in the following figures) with a confining pressure P_c of 30 MPa and 50 MPa. We also perform experiments under drained fault conditions, with 4 different %weight/%weight mixtures of distilled water and glycerol used as fluids: 100% distilled water (water in the following figures), 40%water/60%glycerol (glyc60 in the following figures), 15%water/85%glycerol (glyc85 in the following figures), and 1%water/99%glycerol (the remaining 1% being impurities, glyc99 in the following figures). Viscosity values were measured using a calibrated Ubbelohde capillary viscometer (Cannon Instrument Company) at a temperature of 20 °C (Table 2.1).

Table 2.1: Rate and state frictional parameters (a), (b), and (d_c) for experiments performed at 30 MPa and 50 MPa effective normal stress. Two different state law variables were used: Slip state variable law (“Slip”) or the Persson state variable law (“Persson”) depending of the environmental conditions (dry vs wet experiments). For each velocity step the initial slip-rate (V_0), the final slip-rate (V_1) and the dynamic friction coefficient before the change in slip-rate are reported.

σ_n	Cond	η	P_f	μ_{static}	V_0	V_1	μ_{ss}	$a - b$	d_c	ΔS	State Law
------------	------	--------	-------	----------------	-------	-------	------------	---------	-------	------------	-----------

2.3. Methods

Chapter 2. Effect of fluid viscosity on earthquake nucleation.

						1	3	0.494	0.0039	19.55	21.70	Persson
						10	0.3	0.515	0.0061	31.38	2.20	Persson
						0.3	1	0.507	0.0034	2.93	7.36	Persson
						3	10	0.508	0.0054	13.93	74.34	Persson
						0.3	1	0.442	0.0038	0.76	21.60	Persson
						1	3	0.430	0.0001	5.99	72.33	Persson
ds049	60	glyc60	10.8	10	0.5254	10	0.3	0.370	-0.0013	9.64	219.80	Persson
						0.3	1	0.463	-0.0002	4.46	22.08	Persson
						1	3	0.465	0.0013	3.56	73.91	Persson
						3	10	0.405	0.0003	12.37	222.40	Persson
						1	0.3	0.150	0.0022	0.28	213.30	Persson
						1	3	0.142	-	-	2150.45	-
						3	10	0.120	-	-	7226.19	-
ds047	60	glyc85	100	10	0.4075	10	0.3	0.122	-0.0006	1.17	217.67	Persson
						0.3	1	0.125	-0.0002	2.30	728.53	Persson
						1	3	0.124	-	-	2194.33	-
						3	10	0.127	-	-	7371.91	-
						1	0.3	0.189	-0.0009	29.47	293.90	Persson
						0.3	1	0.159	-0.0012	24.80	984.09	Persson
						1	3	0.151	-	-	2965.61	-
ds050	60	glyc99	1226	10	0.4124	3	10	0.124	-	-	9969.41	-
						0.3	1	0.119	-0.0009	27.22	1005.49	Persson
						1	3	0.113	-	-	3029.45	-
						3	10	0.103	-	-	10154.55	-

The experiments in the presence of fluids were conducted at constant effective confining pressures ($P_{c,eff} = P_c - P_f$) of 30 and 50 MPa, and at constant $P_f/P_c = 0.2$ (i.e with $P_f = 6$ and 10 MPa respectively). At target fluid pressure P_f , we allowed the fluid pressure to equilibrate by waiting 30 min and two hours for experiments performed with water and with water/glycerol mixtures, respectively.

The apparent friction (μ) was calculated as the ratio between the shear stress (τ) and the effective normal stress ($\sigma'_n = \sigma_n - P_f = P_{c,eff}$ in our configuration):

$$\mu = \frac{\tau}{\sigma'_n} = \frac{\tau}{(\sigma_n - P_f)} \quad (2.2)$$

Shear strength (τ) was corrected for the increasing contact area with slip. Static friction (μ_{static}) values were obtained at the end of the elastic loading of the fault (Figure 2.4a). To get insight into fault stability, we studied the slip-rate dependence of friction by imposing different velocity steps (0.3-1-3-10-0.3-1-3-10 $\mu\text{m/s}$) for a total displacement of 2.5 mm (Figure 2.5). The data were recorded at a maximum of 100 Hz.

For each step, we suddenly increased the slip-rate (i.e. velocity step) inducing an immediate

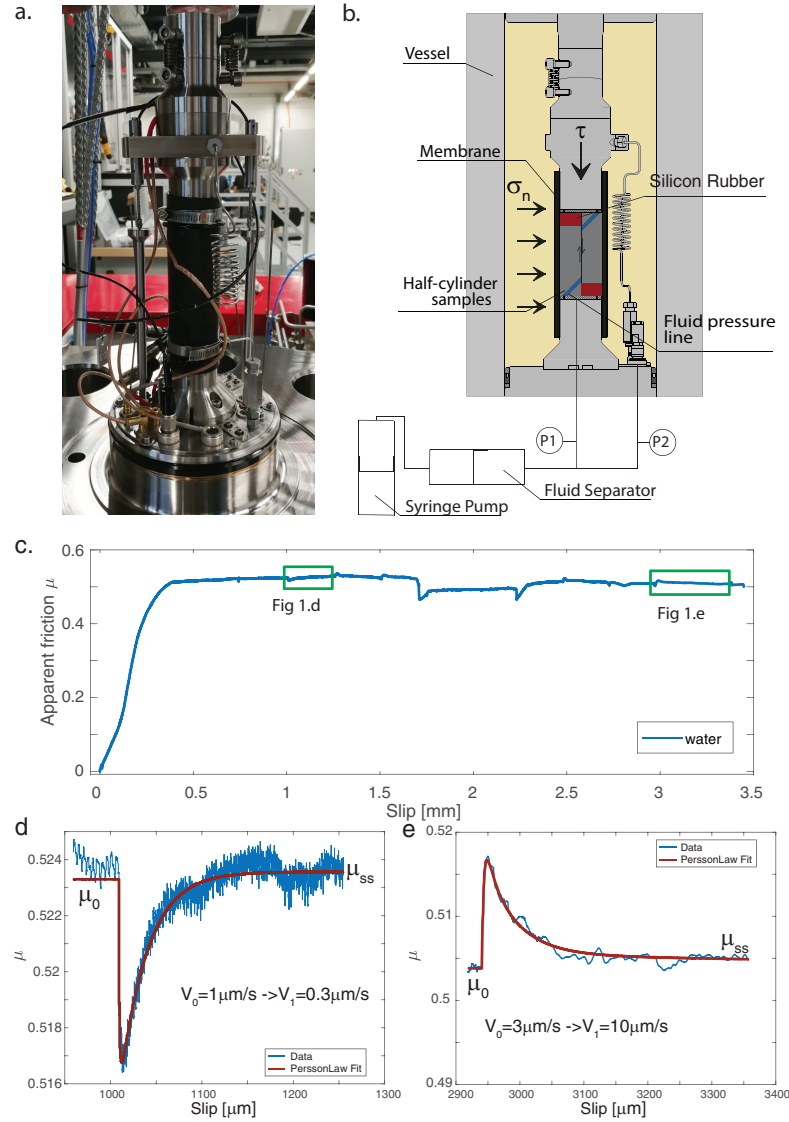


Figure 2.2: a) Picture of the sample assembly on the triaxial apparatus FIRST. b) Sketch of the experimental configuration, fluid pressure lines and fluid pressure pump. The fluid pressure P_f is the average of the two measured pressures, $P1$ and $P2$. A fluid separator is used for the experiments performed in presence of viscous fluids. c) Experimental curves of the evolution of the apparent friction $\mu = \tau / \sigma'_n$ versus the slip of the fault for experiment ds042 (blue curve) performed under water saturated conditions at 50 MPa effective normal stress. The apparent friction μ is offset considering the seal friction. Green rectangles correspond to zoom-in panel d and e. d) Model inversion of the experimental data with the Persson law resulting in rate-and-state values of a and b for a velocity step from $V_0 = 1 \mu\text{m/s}$ to $V_1 = 0.3 \mu\text{m/s}$. e) Model inversion of the experimental data with the Persson law resulting in rate-and-state values of a and b for a velocity step from $V_0 = 3 \mu\text{m/s}$ to $V_1 = 10 \mu\text{m/s}$.

increase in apparent friction followed by an exponential decay over some critical slip distance (d_c), to a new steady state value of the frictional resistance (Scholz, 1998). To retrieve the rate

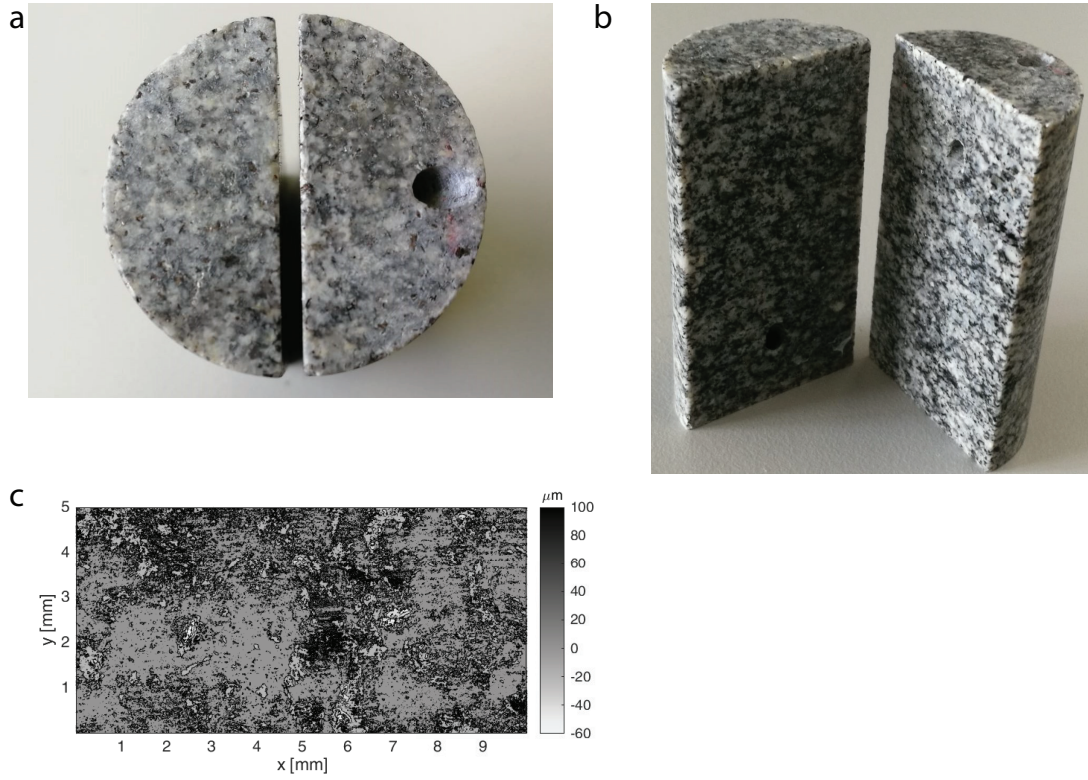


Figure 2.3: Photographs of the starting samples a) top view b) lateral view and initial roughness. On both half cylindrical samples, we made a borehole with inclination of 45° respect to the both the slip surfaces and the base of the semi-cylinder in order to allow the fluid to reach easily the fault surfaces. c) Initial surface and roughness of the Lapeyrate samples. The RMS surface roughness, obtained using the optical profilometer ContourGT-I 3D Optical Microscope Bruker Nano surfaces Division, was $3 \mu\text{m}$

and state frictional constitutive parameters, we modeled each velocity step with the empirical law for apparent friction evolution as a function of time and slip-rate:

$$\mu = \mu_0 + a \ln\left(\frac{V}{V_0}\right) + b \ln\left(\frac{V_0 \theta}{d_c}\right) \quad (2.3)$$

Where μ_0 is the value of the apparent friction coefficient during steady-state slip at slip-rate V_0 , V is the frictional slip-rate, θ is a state variable (Ruina, 1983), and a and b are empirical constants. We used the Ruina slip-dependent evolution law for the experiments performed under room-humidity conditions (and in presence of water for comparison):

$$\theta = -\frac{V\theta}{d_c} \ln\left(\frac{V_0 \theta}{d_c}\right) \quad (2.4)$$

Moreover, we used the Persson state evolution law for the experiments performed in the

presence of all fluids on the fault. The Persson state evolution law comes from the idea that the transition between stable and unstable behavior of a system permeated with fluid depends on the nucleation of solid structures in a lubricated film (Persson, 2000b,c).

$$\theta = (1 - \theta)(-ln(1 - \theta))^{2/3} - \frac{\theta V}{d_c} \quad (2.5)$$

where d_c is a characteristic length over which the solid structures in the lubrication film start to behave as a fluid. The Persson state evolution law can only be used when sliding in the presence of viscous fluid is in the boundary lubrication regime.

In fact, when sliding on a lubricated surface, three regimes of lubrication are possible: boundary lubrication regime (BL), mixed regime (ML), and elastohydrodynamic lubrication (EHD). The transition from one regime to another is governed by the dimensionless Sommerfeld number S , defined as $S = 6 \frac{\eta V L}{\sigma'_n H^2}$, where η is the fluid viscosity at the mean estimated surface temperature under steady state conditions, L is the characteristic slip length, and H is the initial average asperity height. For low values of S ($S < 10^{-3}$, i.e. boundary lubrication regime) the normal stress is supported by the solid–solid contacts. For high values of S ($S > 1$, i.e. fully lubricated regime) the normal stress is supported by the interstitial fluid; and for intermediate values of S ($10^{-3} < S < 1$, i.e. mixed lubricated regime) the normal stress is partially supported both by the solid–solid contacts and by the fluid. For each velocity step between slip-rate V_0 and V , we computed S at steady state with $H=3 \mu\text{m}$ as the initial asperity height (Figure 2.3c) and L as equal to the length of the contact area evolving with slip $L = L_i + \delta$, where L_i is the length of the sample minus the length of the silicon spacer is the effective normal pressure and σ'_n is the effective normal pressure.

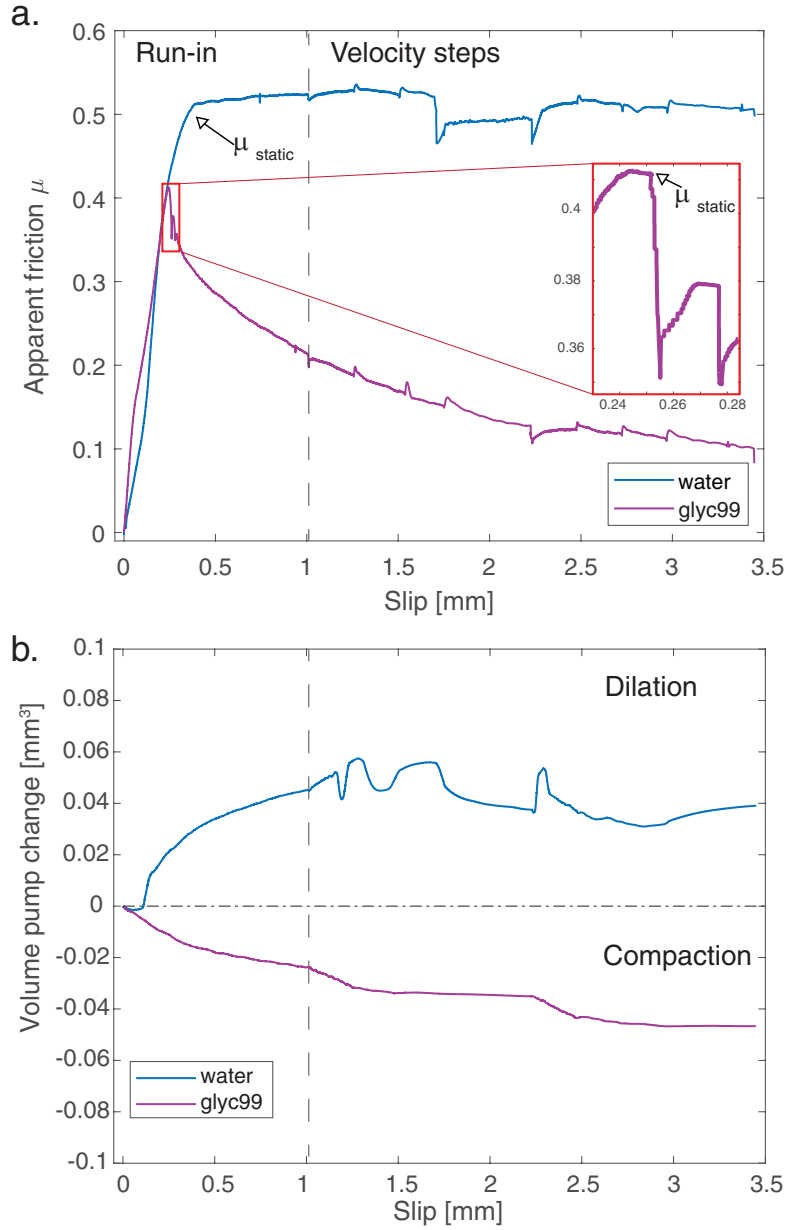


Figure 2.4: Experimental curves. a) Experimental curves of the evolution of the apparent friction $\mu = \tau / \sigma'_n$ versus the slip of the fault for experiment ds042 (blue curve) performed under water saturated condition at 50 MPa effective normal stress and ds050 (magenta curve) performed under glycerol 99 saturated conditions at 50 MPa effective normal stress. Zoom of the initial stick-slip in the red box. b) Evolution of the change in fluid volume in millimeters cubed during shearing for experiment ds042 (blue curve) performed under water saturated conditions at 50 MPa effective normal stress and ds050 (magenta curve) performed under glycerol 99 saturated conditions at 50 MPa effective normal stress. Compaction corresponds to a negative fluid volume change; dilation correspond to a positive fluid volume change.

2.4 Results

At the beginning of the experiments, during the sample loading phase at $1 \mu\text{m/s}$ slip-rate, the shear stress acting on the fault increased until the static friction coefficient was overcome and slip initiated. Immediately following this, the faults showed different behavior as a function of the fluid trapped on the fault surface (Figure 2.2c and Figure 2.4a). During experiments performed under room-humidity conditions and in the presence of water, both at 30 MPa and 50 MPa effective normal stress, slip hardening behavior was observed. Indeed, at 30 MPa effective confining pressure, the apparent friction increased from the static value 0.481 (μ_{static}) to 0.531 under room humidity condition. In presence of water the static friction coefficient increased from 0.451 (μ_{static}) to 0.540. The experiments at 50 MPa effective confining pressure performed under room humidity conditions and in the presence of water showed a slip neutral behavior with constant apparent friction coefficients where were equal to the static values ($\mu_{static}=0.499$ for room humidity and $\mu_{static}=0.513$ for water) (Figure 2.5). On the contrary, the experiments performed in presence of more viscous fluids ($\eta > 10.8 \text{ mPa.s}$, i.e. glyc60, glyc85 and glyc99), showed a slip softening behavior. For example, for glyc85, the apparent friction decays from the static value 0.409 (μ_{static}) to 0.371 at 30 MPa, and from 0.408 (μ_{static}) to 0.155, at 50 MPa. For glyc99, the apparent friction decays from the static value 0.385 (μ_{static}) to 0.108 at 30 MPa, and from 0.412 (μ_{static}) to 0.213 at 50 MPa.

Regarding the fault stability, independent of the macroscopic behavior of the fault (i.e. slip neutral or slip softening), each velocity step reached a detrended steady state friction coefficient (Figure 2.6b). We observed a decay of the μ_{ss} with an increase of the Sommerfeld number from values ranging between 0.4 and 0.6 in boundary lubrication regime and between 0.1- 0.3 in mixed lubrication regime. Importantly, the experiments performed at 50 MPa and with fluids characterized by $\eta \geq 10.8 \text{ mPa.s}$ showed stick-slip behavior during the initial phase of loading (Figure 2.4a and Figure 2.5). Furthermore, to better understand the effect of viscosity on the stability of the fault and earthquake nucleation, we model the sample's frictional response to velocity steps for the experiments performed in boundary regimes with a rate-and-state law (Carlson and Batista, 1996). The limit between the boundary regime and the mixed lubrication regime was set at $S < 10^{-3}$ following (Cornelio et al., 2019) (Figure 2.4).

For experiments performed at 30 MPa effective normal stress, $(a - b)$ values are comprised between 0.001 and 0.009, i.e. velocity-strengthening behavior, for experiments performed under room-humidity condition, between 0.003 and 0.009 for experiments performed under water fault saturated condition, between 0.001 and 0.004 for experiments performed under glyc60 fault saturated condition, between 0.003 and 0.0049 for experiments performed under glyc85 fault saturated condition (Table 2.1). For, experiments performed at 50 MPa effective normal stress, $(a - b)$ values are comprised between -0.003 and -0.004, i.e. velocity weakening behavior, under room-humidity condition, 0 and 0.006 for experiments performed under water fault saturated condition, -0.001 and 0.004 for experiments performed under glyc60

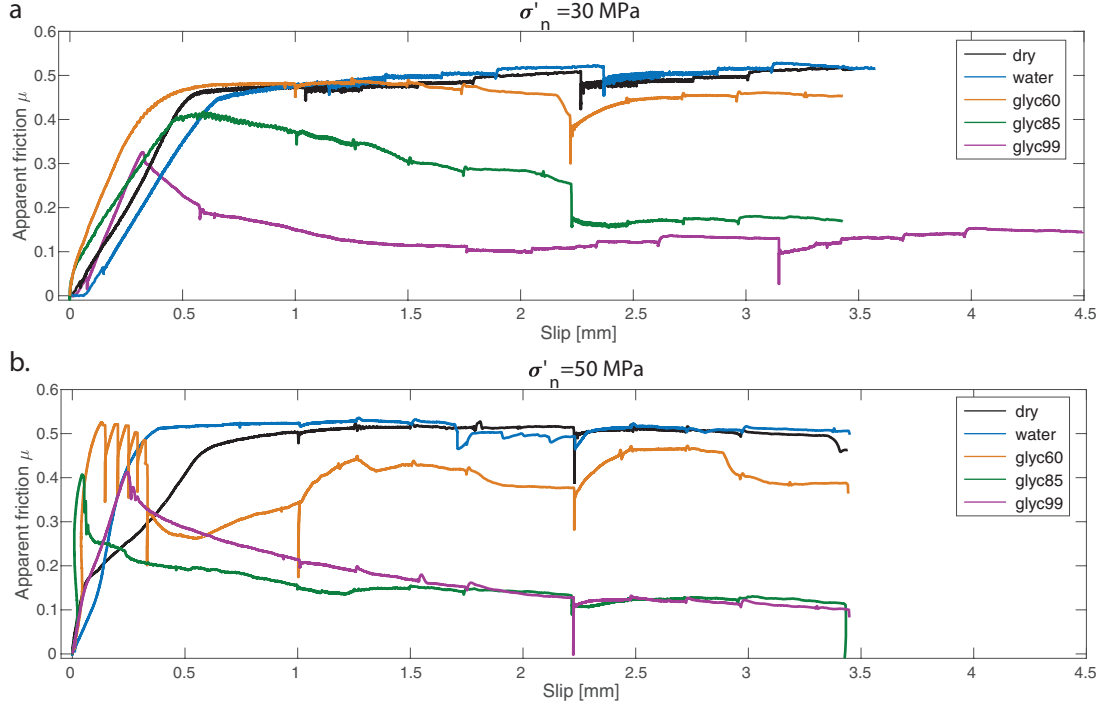


Figure 2.5: Apparent friction coefficient vs slip for all the experiments presented in this work under a) 30 MPa effective normal stress, b) 50 MPa effective normal stress.

fault saturated condition, -0.001 and 0.002 for experiments performed under glyco85 saturated condition, and ~ -0.001 for experiments performed under glyco99 fault saturated condition (Table 2.1).

The fluid volume evolution during shearing showed two opposite behaviors as a function of the fluid composition. The experiments performed with water suggested general dilatant trends while the experiments performed with mixtures of water and glycerol or pure glycerol showed generally compaction. We estimated the change of the fluid layer thickness (ΔH) using the evolution of the fluid volume change (ΔV) during experiments, under the hypothesis that fluid volume variation happens only on the fault plane (maximum possible value of ΔH):

$$\Delta H = \frac{\Delta V}{2r L_{tot}} \quad (2.6)$$

where $L_{tot} = L + L_{rubber}(\delta)$ and $L_{rubber}(\delta) = L_{rubber,0} - \delta$ is the length of the silicon spacer deforming elastically with slip and defined as the difference between the initial length $L_{rubber,0}$ and the slip (δ). The experiments showed a negligible change of ΔH and, as a consequence, of the initial H . Importantly, no layer of gouge material was recovered on the sample surfaces after experiments performed in presence of fluids, suggesting that ΔH is not affected by wear processes.

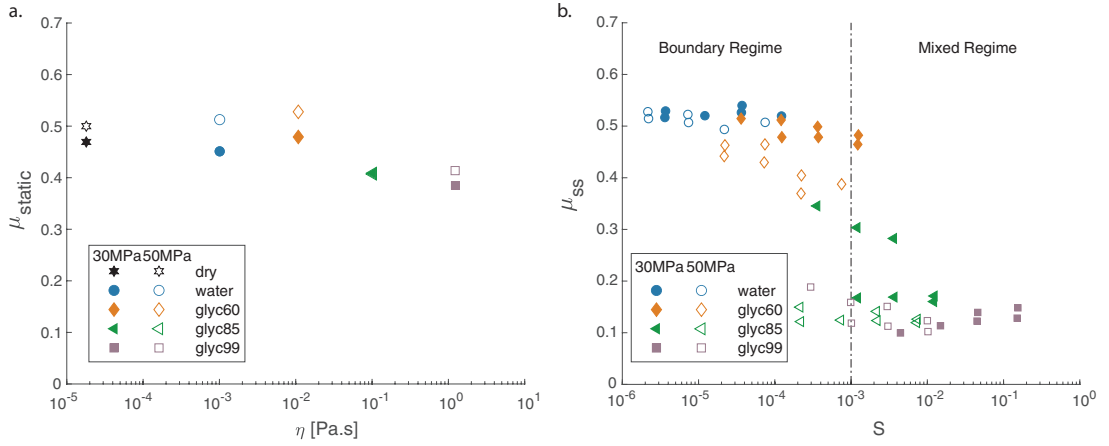


Figure 2.6: Static and steady state friction coefficients. a) Static friction coefficient μ_{static} versus viscosity of the fluid on the slipping surface. For the experiments performed under room humidity conditions, the viscosity of the air ($\eta = 1.88 \cdot 10^{-5}$ Pa.s) trapped in the slip zone was used. b) The steady state friction coefficient for each velocity step versus the computed Sommerfeld number. The Sommerfeld number allows us to distinguish the velocity steps in the boundary lubrication regime and the velocity steps in the mixed regime. Full markers for experiments performed at effective normal stress of 30 MPa, empty markers for experiments performed at 50 MPa effective normal stress.

2.5 Discussion

In agreement with previous studies conducted under room humidity condition, in the presence of water (Passelègue et al., 2016b) and in the presence of more viscous fluids (Cornelio et al., 2019), μ_{static} was independent of the effective normal stress and decreased slightly with increasing fluid viscosity (from ~ 0.50 under room-humidity conditions and at $\eta = 1.001 - 10.8$ mPa.s to ~ 0.39 at $\eta = 1226$ mPa.s) (Figure 2.6a), indicating that the highly viscous fluids only had a marginal effect on the frictional strength of the fault rocks.

On the contrary, the apparent friction coefficient showed a systematic decay with slip (Figure 2.4 and Figure 2.5), depending of the fluid viscosity. In particular the friction coefficient at the steady state of each velocity step, μ_{ss} , decreased with an increasing Sommerfeld number S (Figure 2.6b). This behavior can be described by an elasto-hydrodynamic theory as detailed in Cornelio et al. (2019). However, note that here the data are highly scattered, because μ_{ss} is controlled by both the effect of the lubrication of the fault by the presence of fluid and by the performed velocity steps. Under the boundary lubrication regime, the direct effect parameter (a) of the rate and state law was independent of the fluid viscosity (Figure 2.8a), the evolutive effect parameter (b) increased with viscosity (Figure 2.8b), and the critical distance d_c showed no clear tendency with viscosity (Figure 2.8c). Therefore, the ($a - b$) values of the rate and state law decreased for larger values of viscosity (Figure 2.9). In particular, for the highest viscosity ($\eta = 1226$ mPa.s), we observed a transition to negative values of ($a - b$) (Figure 2.9). Negative

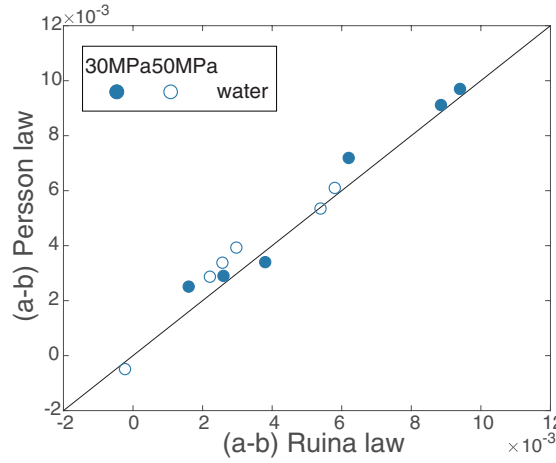


Figure 2.7: Rate and state constitutive parameters ($a - b$) obtained with Ruina slip evolution law (x axis) and with Persson state law (y axis) for experiments performed in presence of water with effective normal stress of 30 MPa (filled markers) and at 50 MPa (empty markers). The difference in ($a - b$) values obtained with the two laws is represented by the distance from the black line (slope 1:1).

values suggest unstable slip behavior and potential earthquake nucleation. We point out that the fluid water experiments were modelled with both the slip evolution dependent law (Ruina, 1983) and the Persson state evolution law (Persson, 2000b), and showed only small differences ($\sim 10^{-4}$) (Table 2.2 and Figure 2.7).

Furthermore, the increase of the fluid viscosity can reduce the hydraulic diffusivity of the fault following ($\alpha_{hy} = k/(\beta\eta)$), where k is the permeability of the material, β is the storage capacity. For example, Faulkner et al. (2018) observed a decrease of the ($a - b$) parameter with a decrease of the hydraulic diffusivity of a layer of gouge, changing the permeability (k) of the gouge layer sandwiched on the fault planes. The average values of $a - b$ (Figure 2.9) can be a result of a fluid pressure increase/compaction of the fluid film associated with the change in hydraulic diffusivity at vary fluid viscosity (Faulkner et al., 2018). Moreover, a local increase of the fluid pressure on the fault plane can justify the global decrease of the friction coefficient with the slip ($\propto 1/\sqrt{\delta}$)

Moreover, in agreement with theoretical models (Dieterich, 1992; He et al., 1998; Chambon and Rudnicki, 2001) and previous experimental studies on both bare surfaces (Harbord et al., 2017; Linker and Dieterich, 1992) and gouge materials (Leeman et al., 2018; Marone et al., 1990; Rathbun et al., 2008; Scuderi et al., 2016), and independent of the fluid condition, the increase of the effective normal stress acting on the experimental fault, promoted a decrease of ($a - b$) values down to negative ($a - b$) values at 50 MPa (Figure 2.10). For both gouge materials and sliding on bare surfaces this behavior has been attributed to an increase of the critical stiffness (K_c) of the fault plane. Indeed, combined with the elastic dislocation theory, the rate

Table 2.2: Rate and state frictional parameters (a), (b), and (d_c) for experiments performed at 30 MPa and 50 MPa effective normal stress in presence of water, obtained with the slip state variable law (“Slip”) and with the Persson state variable law (“Persson”). For each velocity step the initial slip-rate (V_0), the final slip-rate (V_1) and the friction coefficient before the change in slip-rate are reported.

	Slip					Persson	
	V_0	V_1	μ_0	$(a - b)$	d_c	$(a - b)$	d_c
ds038	1	0.3	0.505	0.0038	2.08	0.0034	2.41
	0.3	1	0.5171	0.0026	1.80	0.0029	1.79
	1	3	0.5206	0.0062	0.08	0.0072	0.00
	3	10	0.5268	0.0089	5.00	0.0091	30.67
	10	0.3	0.52	0.0016	3.91	0.0025	10.80
	1	3	0.5297	0.0094	0.49	0.0097	0.57
ds042	V_0	V_1	μ_0	$(a - b)$	d_c	$(a - b)$	d_c
	1	0.3	0.523	0.00	30.35	0.00	35.60
	0.3	1	0.5283	0.0022	7.24	0.0029	8.80
	1	3	0.523	0.0030	7.22	0.0039	19.55
	10	0.3	0.494	0.0058	22.82	0.0061	31.38
	0.3	1	0.515	0.0026	10.82	0.0034	2.93
	3	10	0.5074	0.0054	6.64	0.0054	13.93

and state formulation states that if the stiffness of the elastic medium (K) is smaller than the critical fault stiffness (K_c), frictional instability can occur. The parameter K_c is defined by the effective normal stress and the rate and state constitutive parameters (a , b , d_c) of the fault: $Kc = ((b - a)(\sigma_n - Pf))/d_c$, where d_c is the critical slip distance and $(b - a)$ is the friction rate parameter.

Finally, the evolution of fluid volumes during shearing suggested a predominant shear-enhanced dilatancy for experiments performed with water. This result is in agreement with Beeler and Tullis (1997) and can be explained as the vertical movement of the fault plane necessary to overcome the asperities. However, when a mixture of water and glycerol or pure glycerol was trapped on the slip surface, the experiment showed only a general compaction behavior. Shear enhanced compaction is due to fluid layer thinning during sliding, which is very efficient at high viscosity.

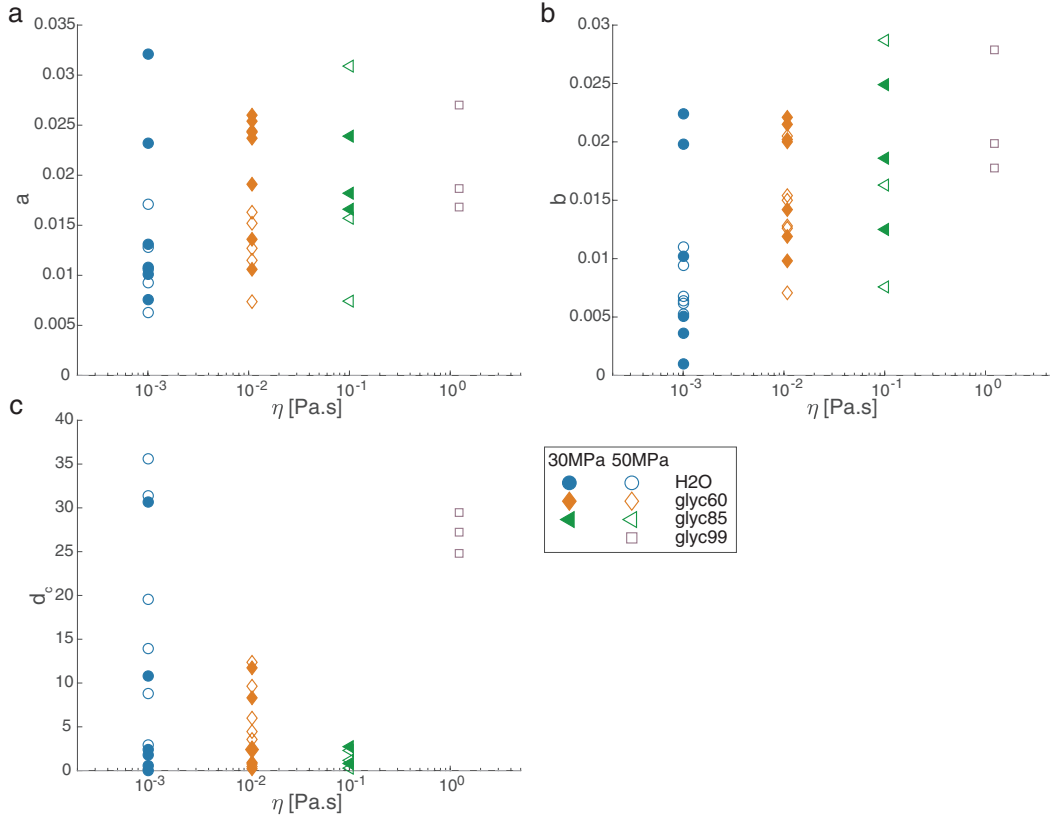


Figure 2.8: Rate and state constitutive parameters a) the direct effect (a), b) the evolutive effect (b) and c) the critical distance (d_c) versus fluid viscosity. a) the (a) parameter is almost constant. b) the (b) parameter increases increasing fluid viscosity. c) the (d_c) parameter does not show clear tendency with the fluid viscosity.

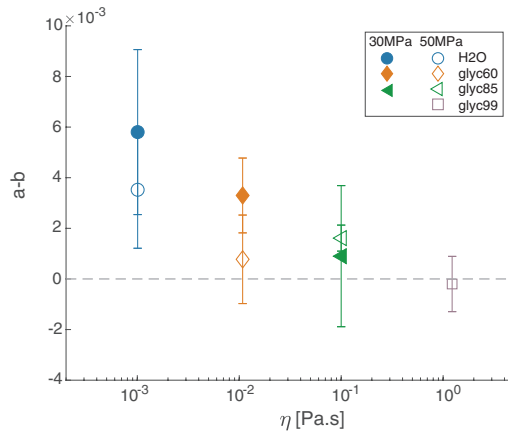


Figure 2.9: Average values of $(a - b)$ rate and state parameters versus viscosity of the fluid for experiments performed under fault fluid saturated conditions and under boundary lubrication regime. The parameters were obtained using the Persson state law coupled with the friction empirical law. Full markers for experiments performed at 30 MPa effective normal stress and empty markers for experiments performed at 50 MPa effective normal stress.

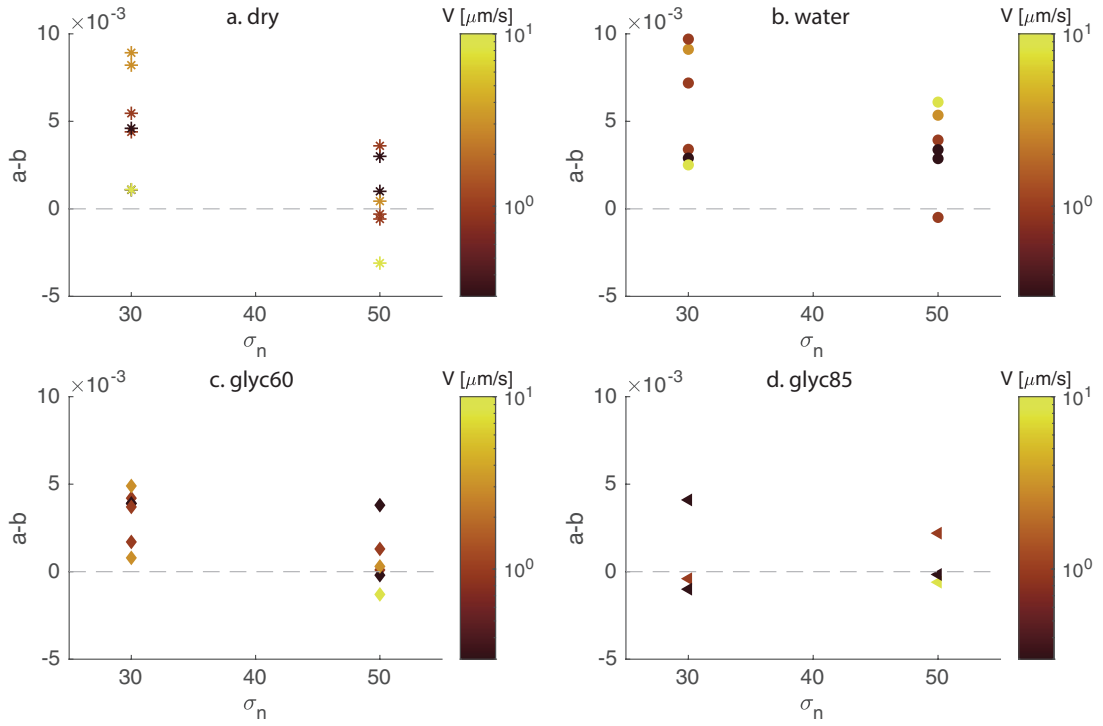


Figure 2.10: (*a – b*) frictional parameters versus effective normal stress ($\sigma'_n = \sigma_n - P_f$) for experiments a) under room-humidity condition, b) in presence of water ($\eta=1.002$ mPa.s) c) mixture of 60% glycerol 40% water ($\eta=10.8$ mPa.s), d) 85% glycerol 15% water ($\eta=107.5$ mPa.s). In colorbars the slip-rate V_0 in $\mu\text{m/s}$ before each velocity steps.

2.6 Conclusions and Implications for Induced Seismicity

We conducted ten vertically saw cut triaxial experiments on Lapeyrate semi-cylindrical samples with four various fluid viscosities and two effective normal stress. We subjected the fault to variations of the slip-rate in order to estimate the rate and state parameters of the studied system and understand if slip behavior is governed by fluid viscosity. We analyzed our results on the light of the Persson state variable law. The results showed that:

1. The fluid viscosity did not influence the static friction coefficient of the faults;
2. Steady state friction coefficient decreases with increasing the Sommerfeld number in agreement with elasto-hydrodynamic theory;
3. During velocity steps and under the boundary lubrication regime:
 - a. The increase of normal stress tends to destabilize the fault
 - b. The increase of the viscosity of the pressurized fluid on the slip surface tends to destabilize the fault
4. High fluid viscosity promotes shear-enhanced compaction.

It is important to recall that high fluid viscosity strongly limits fracture leak off (enhancing the efficiency of the hydro-fracturing mechanism) and reduces diffusion rate in the fault zone, reducing the area over-pressurized by fluids. The area over-pressurized by fluid has an important influence on the probability of earthquake occurrence as observed by Shapiro and Dinske (2009). Our experimental results demonstrated that fluid viscosity has a role in the determination of the empirical $(a - b)$ parameter of an experimental fault. We suggest that a similar behavior can be expected in the case of induced seismicity in geo-reservoirs. Under specific conditions of fault geometry and surrounding stress of the fault, high fluid viscosity might favor unstable slip and earthquake nucleation if the system and the reservoir are saturated with viscous fluid.

3 Effect of fluid viscosity on fault reactivation and co-seismic weakening

Authors: Chiara Cornelio¹, Francois Passelègue¹, Elena Spagnuolo², Giulio Di Toro^{2,3}, Marie Violay¹.

¹ Laboratory of Experimental Rock Mechanics (LEMR), ENAC, EPFL, Switzerland;

² Istituto Nazionale di Geofisica e Vulcanologia, INGV, Rome, Italy;

³ Dipartimento di Geoscienze, Università degli studi di Padova, Padua, Italy.

Reference: Cornelio, C., Passelègue, F. X., Spagnuolo, E., Di Toro, G., & Violay, M. (2020). Effect of fluid viscosity on fault reactivation and coseismic weakening. *Journal of Geophysical Research: Solid Earth*, 125, e2019JB018883. <https://doi.org/10.1029/2019JB018883>

Contributions: C. Cornelio has prepared and characterized samples used in this study. E. Spagnuolo and C. Cornelio have run the experiments. All authors have contributed to the testing strategy and methodology. C. Cornelio modelled results with input of F. Passelègue and M. Violay. C. Cornelio has written the manuscript. All the co-authors have edited and guided discussion of the manuscript.

Highlights:

- The viscosity of the injected fluid does not influence the initial strength of experimental faults;
- Fault weakening mechanisms during simulated seismic slip depend on fluid viscosity;
- The magnitude of the breakdown energy is independent of the fault weakening mechanism.

3.1 Abstract

High-viscosity fluids are often used during hydraulic fracking operations in geo-reservoirs. Here, we performed dedicated experiments to study the influence of fluid viscosity on fault reactivation and associated induced earthquakes. Experiments were conducted in the rotary-shear machine SHIVA on experimental fault of Westerly Granite saturated by fluids with increasing viscosity (at room temperature) from 0.1 mPa s (water) to 1.2 Pa s (99% glycerol). Fault reactivation was triggered at constant effective normal-stress by step-wise increasing the shear stress acting on the fault. Our results showed that independent of the viscosity, fault reactivation followed a Coulomb-failure criterion. Instead, fluid viscosity affected the fault weakening mechanism: flash-heating was the dominant weakening mechanism in room-humidity and water-saturated conditions, whereas the presence of more viscous fluids favored the activation of elasto-hydrodynamic lubrication. Independent of the weakening mechanism, the breakdown work W_b dissipated during seismic faulting increased with slip U following a power law ($W_b \propto U^{1.25}$) in agreement with seismological estimates of natural and induced earthquakes.

3.2 Introduction

Earthquakes rupture nucleating and propagating along faults result from the frictional response of fault materials to local or far-field ambient stress variations. In nature, stress can increase slowly due to tectonic loading up to the critical strength of faults, or change suddenly due to (1) earthquake ruptures propagating in the vicinity of the fault or (2) fluid migration (Gomberg et al., 1997; Harris, 1998; Kilb et al., 2000; Miller et al., 2004; Sibson, 1992). In geo-reservoirs, induced earthquakes triggered by pore pressure variations (i.e., effective stress variations) during engineering operations are a major issue for the future development of hydrocarbon production, geothermal resources, CO₂ and nuclear waste storage (Cornet et al., 1997; Ellsworth, 2013; Guglielmi et al., 2015; Majer et al., 2007). Faults respond to stress variations by either (1) remaining in a locked state or (2) slipping stably at low slip-rates ($\ll 1$ mm/s) or (3) accelerating towards seismic slip-rates ($\gg 1$ mm/s, unstable regime), depending on the initial stress conditions and wall rock stiffness (Scholz, 2019b). The frictionally stable and unstable regimes (Gu et al., 1984) can be described in the framework of the rate and state friction law (Dieterich, 1979; Rice and Ruina, 1983) where the frictional response of a fault varies with the previous loading history, and depends on both the instantaneous slip-rate V and a state variable accounting for the evolution with time of the sliding interface. To understand the effect of the fluid pressure on the rate-and-state friction law variables, velocity controlled experiments under pore fluid conditions have been conducted (Scuderi et al., 2016; Ikari et al., 2009; Niemeijer and Collettini, 2014). However, controlling the shear stress and the

pore pressure (the pressure of the fluid in saturated and drained condition) up to the onset of slip events rather than controlling the slip-rate and measuring the shear strength evolution is more representative to reservoir engineering and natural conditions, where stress variations and frictional properties of the fault materials control the mechanical response of the fault zone (Cornet, 2016; Goertz-Allmann et al., 2011; Wu et al., 2018; Zoback and Harjes, 1997). A first step in this direction was recently achieved by studying the effect of pore fluid variations on experimental fault reactivation (Giacomel et al., 2018; Passelègue et al., 2018; Scuderi et al., 2017; Ye and Ghassemi, 2018). However, the composition of the fluid used in these studies was limited to pure water or water and carbon dioxide mixtures and the role of fluid viscosity was neglected. In geo-engineering practice, the viscosity of the injected fluids varies over four orders in magnitude, from 1 mPas for liquid water to 10 Pas for fracturing fluids (Economides and Boney, 2000) and recent experimental studies showed that fluid viscosity controls seismic source parameters, including stress drops, the weakening distance and the earthquake energy budget (Cornelio et al., 2019). Here, we discuss the role of fluid viscosity on both the onset of fault reactivation and the associated slip events by exploiting a novel experimental technique. This consists of loading an experimental fault under realistic geo-engineering effective stress and environmental conditions (Giacomel et al., 2018), which span from room humidity to high viscosity fluid pressurized conditions.

3.3 Materials and Methods

We conducted seven shear-stress controlled experiments on the rotary shear apparatus named SHIVA (Slow to High Velocity Apparatus, see Di Toro et al. (2010) and Niemeijer et al. (2011) for details on the machine and the acquisition system). Experiments were performed on 50 mm diameter full cylinders of Westerly granite, selected as an analogous of the target lithology for geothermal reservoirs. Westerly granite is a homogeneous, isotropic, fine grain size (<1 mm), low porosity (<2% measured using the triple-weighing method) and low permeability ($\sim 10^{-19}$ m²) rock (Nasseri et al., 2009). The low porosity and permeability result in negligible fluid diffusion in the rock matrix during the experiments discussed here. The samples were prepared following the procedure described by Nielsen et al. (2012) to ensure sample alignment and parallelism of the opposite sliding surfaces once the cylinders were installed in the sample holders of SHIVA. Sliding surfaces were roughened by using 80 SiC abrasive paper to produce small irregularities called asperities. The 3-Dimensional surface roughness was measured as the quadratic mean (Root mean square RMS). The RMS was determined on 10 x 16 mm rectangular area of the surface of the Westerly granite sample before the experiments (Figure 3.1) using an optical profilometer Contour GT-I 3D Optical Microscope, Bruker Nano surfaces Division. The scan of the surfaces was performed by stitching images of 20 x 20 μ m with an overlap of 20% between two adjacent areas. The RMS of the fault surface of Westerly granite

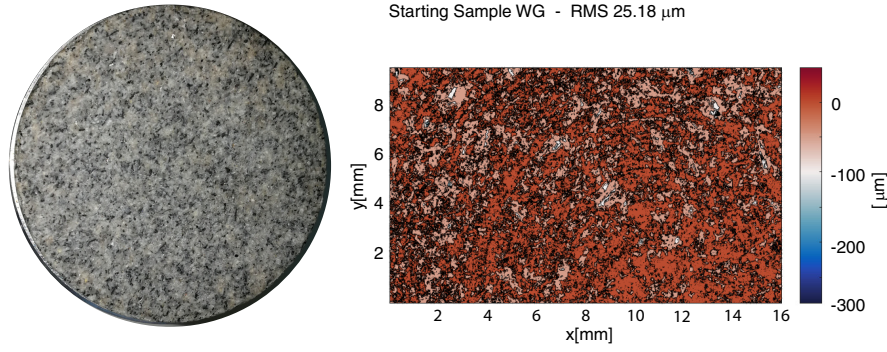


Figure 3.1: Initial surface and roughness of the Westerly granite samples. a) Photo of the initial 50 mm in diameter sample of Westerly granite. b) The RMS surface roughness obtained using the optical profilometer.

before sliding was around $RMS=25.18 \mu m$ so we assumed an initial average asperity height of $w_0=25 \mu m$ (Figure 3.1). Experiments were conducted at the same effective stress conditions $\sigma'_n = \sigma_n - P_f \simeq 10$, where a normal stress σ_n of ~ 13 MPa and a fluid pressure P_f of ~ 2.7 MPa (pressure of the fluid in the slipping surface) were applied and maintained constant during the experiments (Table 3.1). To perform experiments in the presence of fluids, SHIVA was equipped with a pressurizing system which consisted of a fluid pressure vessel, a membrane pump (with a 30 cm^3 fluid capacity), a pressure multiplier that imposed up to 15 MPa of fluid pressure, a pressure regulator and valves and pipes (Violay et al., 2013, 2014b, 2015). The tests were performed under drained conditions, i.e. the vessel was connected to the fluid reservoir to keep the fluid pressure macroscopically constant during the entire experiment (Figure 3.2b). The procedure for experiments performed in presence of fluids consisted in 1) applying an initial axial stress $\sigma_n=0.8$ MPa, 2) increasing the fluid pressure by injecting fluids radially in the vessel up to 0.5 MPa, 3) increasing the axial stress σ_n up to the target value, 4) increasing the fluid pressure up to the target value. Once the target effective normal stress of ~ 10 MPa was achieved, the shear stress τ was gradually increased by controlling the torque with step-wise increments corresponding to ~ 0.5 MPa (resolution of 0.1 MPa) and a hold time of $\Delta t=200$ s for $\tau < 3$ MPa and $\Delta t=1000$ s for $\tau \geq 3$ MPa (Figure 3.3). The torque was controlled by the engine via feedback control on the motor current with an update frequency of 16 kHz. The control system is an open loop control on the shear stress which is measured downstream of the slip surface via an independent measure on the S-beam load cell (Figure 3.2a). This independent measure ensures the achievement of spontaneous evolution of both shear strength and slip (and slip-rate) of the experimental fault. Two encoders recorded the spontaneous evolution of the slip (and slip-rate) in response to the applied torque. The torque step-wise increase was applied up to the onset of a main frictional instability (see result section for full description)

Chapter 3. Effect of fluid viscosity on fault reactivation and co-seismic weakening

Table 3.1: Summary of the experimental conditions. Shear stress at fault reactivation: τ_{imp} . Condition, normal stress σ_n , fluid pressure P_f , effective normal stress σ_{eff} , and peak friction coefficient μ_{peak} .

Exp	Cond	η [mPas]	σ_n [MPa]	P_f [MPa]	σ_{eff} [MPa]	τ_{imp} [MPa]	μ_{peak}
s1409	RH		9.847		9.847	6.364	0.646
s1487	RH		9.741		9.741	6.069	0.623
s1407	Water	1.002	12.109	2.702	9.407	6.822	0.725
s1488	60%glyc	10.8	11.861	2.641	9.22	7.321	0.794
s1781	85%glyc	108.4	12.463	2.473	9.99	6.977	0.698
s1596	99%glyc	1226	11.902	2.738	9.164	6.968	0.76
s1406	99%glyc	1226	12.08	2.729	9.352	6.538	0.699

defined as the spontaneous acceleration of the fault slip-rate up to a target velocity of $V_{max}=0.1$ m/s (or $V_{max}=0.2$ m/s for the experiment s1781). At this slip-rate, the control system automatically switched from constant shear stress to constant slip-rate control maintaining $V_{max}=0.1$ m/s (or $V_{max}=0.2$ m/s for experiment s1781) until either the spontaneous recovery of the imposed shear stress or the manual arrest of the experiment. Normal stress σ_n , pore fluid pressure P_f , slip, slip-rate V and shear stress τ were acquired at 125 Hz and determined using the procedure suggested in Niemeijer et al. (2011) and Tsutsumi and Shimamoto (1997). The elastic and inelastic slip and the slip-rate were corrected for the stiffness of the apparatus ($K=0.07$ MPa/ μm , (3.1):

$$V_{samp} = V_{meas} - K^{(-1)} d\tau/dt \quad (3.1)$$

The experimental conditions and the evolution of the shear stress and slip-rate for all the explored conditions are reported in Table 3.1 and Figure 3.3, respectively. Four different %weight/%weight mixtures of distilled water and glycerol were used as pressurized fluids: 100% distilled water, 40%water/60%glycerol, 15%water/85%glycerol, 99%glycerol (the remaining 1% being impurities). Viscosity values of 1.002 mPas (distilled water), 10.9 mPas (40%water/60%glycerol), 108.4 mPas (15%water/85%glycerol), and 1226.0 mPas (99%glycerol), were measured using calibrated Ubbelohde capillary viscometers (Cannon Instrument Company) at a temperature of 20 °C.

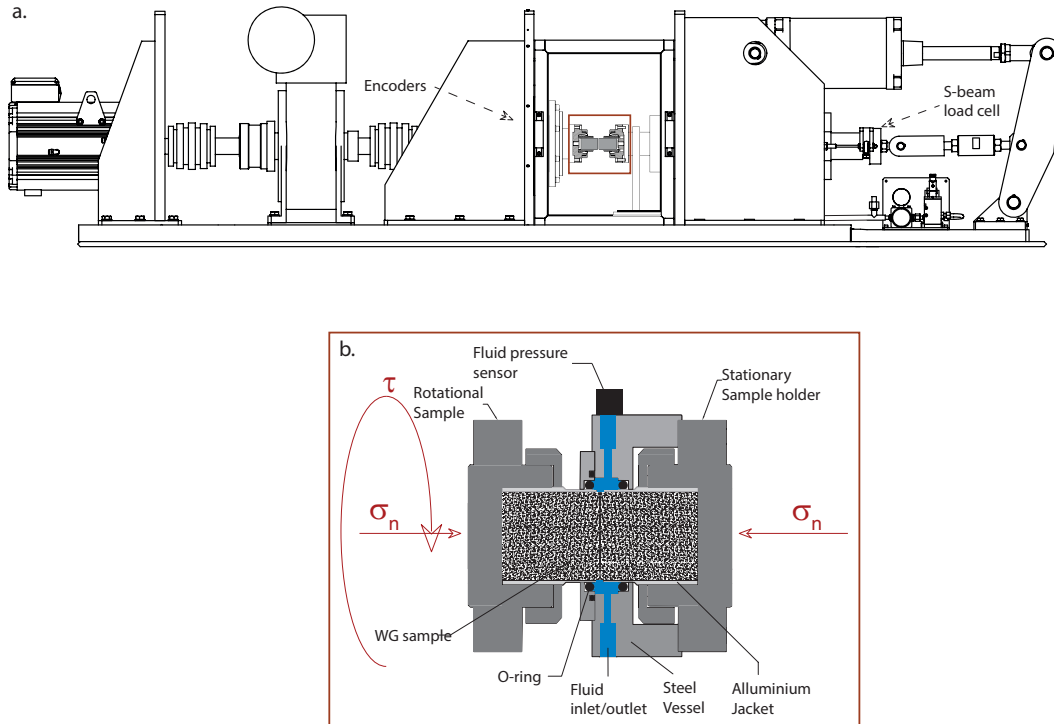


Figure 3.2: Experimental assembly. a) Sketch of the apparatus SHIVA (modified from Pas-selègue et al. (2016b)). The approximate position of the encoders and the S-beam cell are reported; and b) zoom on the sample assembly and fluid pressure vessel. The fluid pressure is kept constant during the experiments thanks to the membrane pump that is directly connected to the pressure vessel.

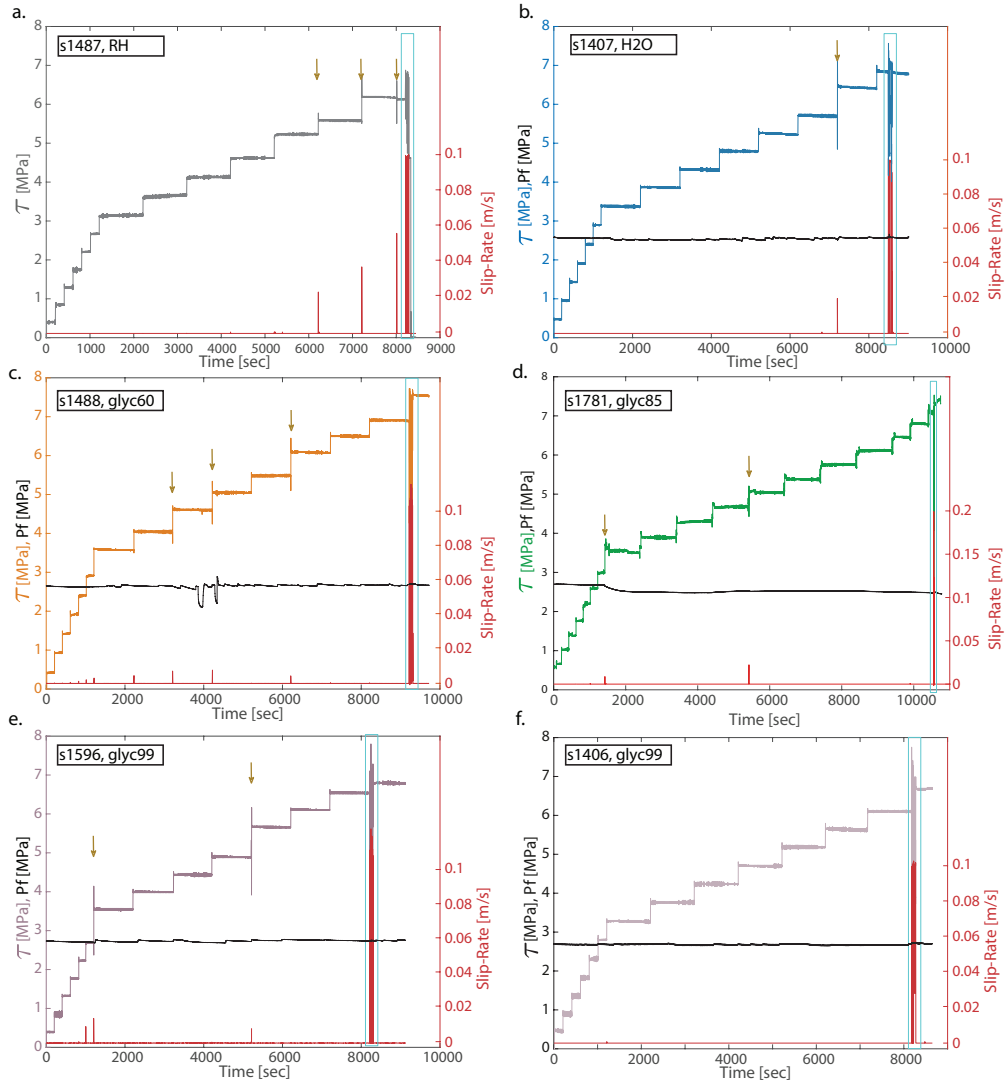


Figure 3.3: Recorded shear stress τ (measured at the S-beam load cell), fluid pressure Pf and slip-rate V evolution versus time in the experiments (see main text for description). All the experiments were conducted at an effective normal stress of ca. 10 MPa. a) Experiment s1487, room-humidity (RH) conditions. b) Experiment s1407, distilled water (1 mPas). c) Experiment s1488, mixture of 40% water/60% glycerol ($\eta=10.8$ mPas). d) Experiment s1781= mixture of 15% water/85% glycerol ($\eta=109$ mPas). e) Experiment s1596, pure glycerol or 99%glycerol ($\eta=1226$ mPas). f) Experiment s1406, pure glycerol or 99%glycerol ($\eta=1226$ mPas). The ocher-in-color arrows mark the slip bursts (see description of stage II in the main text) and the cyan rectangle the achievement of a critical unstable frictional behavior (see description of stage III in the main text).

3.4 Results

The evolution of shear stress and slip rate during the experiments can be described by three stages (I, II and III) (Figure 3.4).

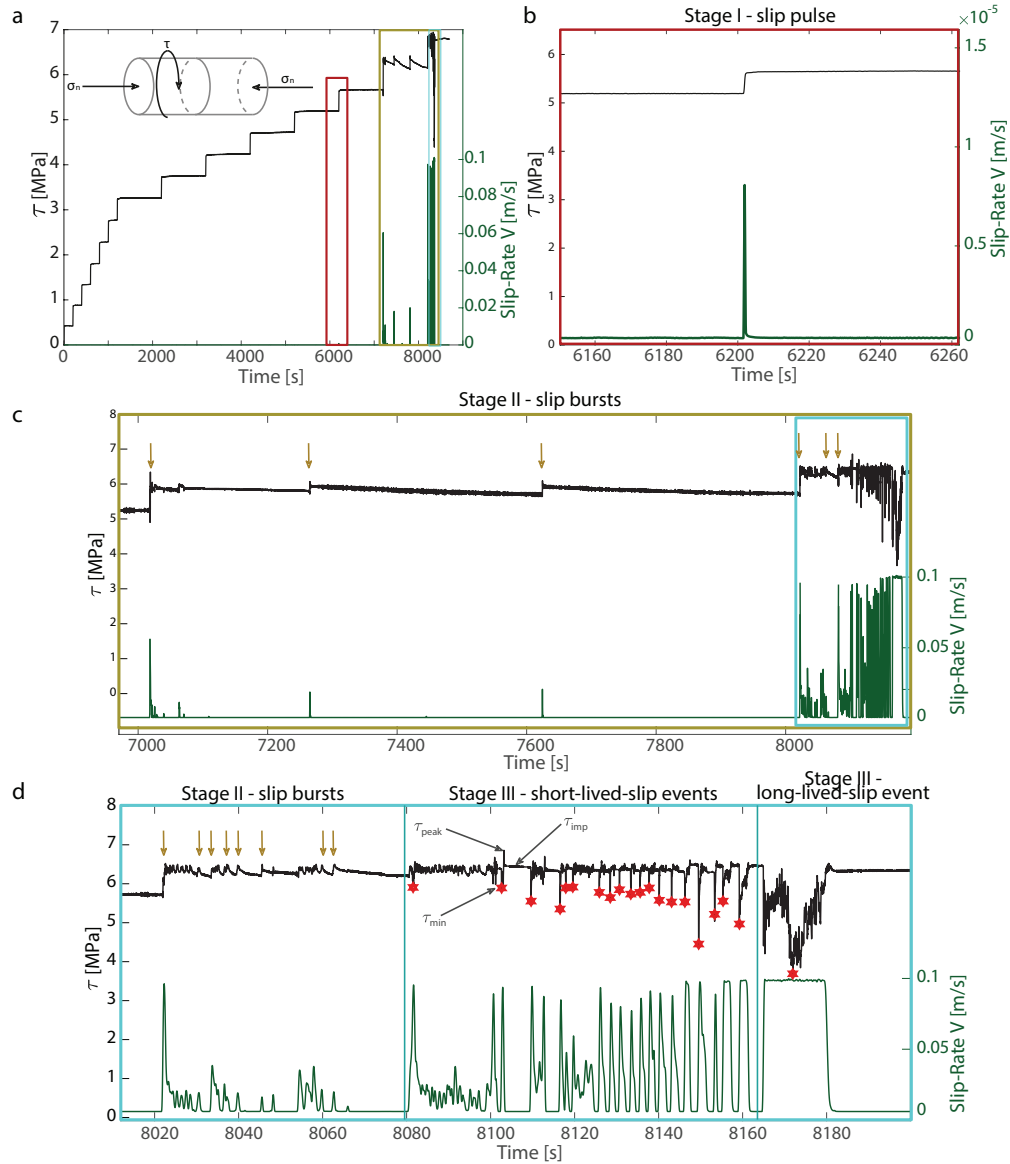


Figure 3.4: Experiment s1409 performed under room-humidity conditions. a) Shear stress τ and slip-rate V versus time. b) Zoom of the slip pulse associated to a shear stress perturbation during stage I. c) Zoom on the slip bursts (other arrows) during stage II. d) Zoom of the series of short-lived slip events and single long-lived slip event corresponding to the stage III. The red stars indicated the minimum shear stress reached at each event τ_{min} .

3.4.1 Stage I. Single slip pulses under shear stress-step loading.

In all the experiments and independent of the presence and viscosity of fluids, from the beginning of the experiment (i.e., $\tau=0$ MPa) to $\tau=2.5$ MPa, the experimental fault remained locked (elastic loading) and no slip was measured. From $2.5<\tau<6$ MPa, each increment of shear stress resulted in a single slip pulse with a total slip distance $\Delta U_{tot}<0.3$ mm and maximum slip-rate $V \sim 10^{-5}$ m/s (Figure 3.4b). These short-lived slip pulses did not induce any measurable drop in shear stress, suggesting that the experimental fault recovered quickly from the stress perturbation.

3.4.2 Stage II: Series of spontaneous slip bursts under shear stress-step loading.

With increasing shear stress and independent of the presence and viscosity of the fluid, we observed spontaneous but isolated slip events with total slip distances between $0.3\text{mm} < \Delta U_{tot} < 0.25\text{m}$ occurring at $V < 0.1$ m/s (this was the maximum allowed spontaneous slip rate – see methods section). Differently to the slip pulses of Stage I, these slip bursts were associated to shear stress drops of less than 10% of the imposed shear stress τ_{imp} (Figure 3.3 and Figure 3.4c).

3.4.3 Stage III. Unstable slip behavior (achievement of a critical unstable frictional behavior).

For $\tau > 6$ MPa, and in particular for an apparent friction coefficient $\mu = \tau/\sigma'_n = 0.71 \pm 0.07$ (Figure 3.5), the frictional macroscopic behavior of the fault became unstable, independent of the presence and viscosity of the fluids. The unstable frictional behavior initiated with the occurrence of tens of short-lived-slip events with $\Delta U_{tot} < 0.25$ m at $V \simeq 0.1$ m/s ending with a long lived-slip event with $\Delta U_{tot} > 0.25$ m at the maximum allowed $V = 0.1$ m/s (Figure 3.4d). The threshold slip rate of 0.1 m/s was selected because big enough to allow for the frictional weakening of the fault and, approaching the slip-rate, multiple slip events were induced in our experimental configuration as the fault is running in a marginally stable behavior (Spagnuolo et al., 2016). Each short-lived slip event consisted in a shear stress drop $\Delta\tau$ (difference between the imposed shear stress τ_{imp} and the minimum value of the shear stress τ_{min}) and in the spontaneous recovery to a peak shear stress (τ_{peak}) slightly higher than the imposed shear stress (see in Figure 3.4d and Figure 3.12a for a zoom on the first short-lived-slip event of s1488). In the long-lived-slip event at the maximum allowed $V = 0.1$ m/s, U increased with increased fluid viscosity from 0.36 m for 100% distilled water) to 0.72 m for 99% glycerol. The experiment was then manually stopped once the shear stress recovered (spontaneously) the τ_{imp} (Figure 3.4d).

To understand the influence of fluid viscosity on the fault weakening mechanism active during

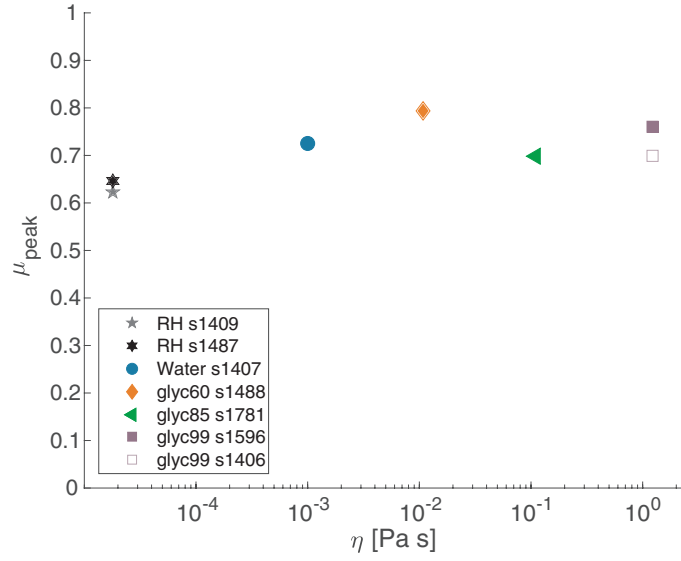


Figure 3.5: Peak friction coefficient vs viscosity of the fluid on the slipping surface. For the experiments performed under room humidity conditions, the viscosity of the air ($\eta = 1.88 \cdot 10^{-5}$ Pa s) trapped in the slip zone was used. The unstable behavior of the experimental fault occurred at an effective friction coefficient of 0.71 ± 0.04 , independently of the viscosity of the fluid.

stage III (especially during the last long-lived slip event), we analyzed the evolution of the apparent friction coefficient μ with the evolution of the slip-rate V (Figure 3.6) performing comparative analyses of the system (fault + apparatus) behavior at the onset of unstable frictional (slip) events. For the experiments performed under room-humidity conditions and in presence of 100% distilled water (Figure 3.6a), we observed an exponential decay of μ with V once a critical slip-rate V_w of 0.040 m/s for room humidity conditions and 0.042 m/s for pressurized water was overcome (Figure 3.6a). Instead, in the experiments performed with fluids with higher viscosities, the slip-rate for weakening scattered from 0.04 m/s to the maximum target V of 0.1-0.12 m/s and the decay of μ had a poor dependence with V (Figure 3.6b). These differences in the critical (weakening) slip-rate and μ decay imply that the fluid viscosity affects the type of fault weakening mechanism during the experimental seismic sequence.

3.5 Discussion

According to mechanical data and regardless of the viscosity of the fluid, fault reactivation occurred at $\mu \approx 0.71$ (Figure 3.5) compatible with the Byerlee friction law (Byerlee, 1978). To understand the influence of fluid viscosity on the first two stages, we compared the mechanical results in terms of recorded slip-rate V and slip U . For the stage I, the number of the slip pulses

Chapter 3. Effect of fluid viscosity on fault reactivation and co-seismic weakening

is directly linked to the number of shear stress steps performed during the experiment. Indeed, every shear step triggered a single slip pulse (Table 3.2). The maximum slip-rate reached during the pulse is independent of the fluid viscosity. During stage II the number of the slip bursts is independent of the number of shear steps required to reach the fault reactivation. Indeed, several slip bursts happened during a shear step. However, both the number of slips burst and the maximum slip velocity reached during these events at stage II are independent of the fluid viscosity (Table 3.2).

Table 3.2: Slip pulse and slip bursts analysis. N.steps are the shear stress step before the Stage III. For each experiment, the number of recorded slip-pulse during the Stage I, the maximum recorded slip-rate, the number of slip bursts during the Stage II and the related maximum slip-rate are reported.

exp	cond.	N.steps	Stage I		Stage II	
			n. Slip-pulses	max V [10^{-5} m/s]	n. slip-bursts	max V [m/s]
s1409	RH	14	11	8.24	13	0.048
s1487	RH	13	11	5.07	3	0.058
s1407	H2O	14	12	5.45	1	0.021
s1488	glyc60	15	12	6.01	4	0.012
s1781	glyc85	15	13	4.74	2	0.014
s1596	glyc99	14	10	3.24	2	0.173
s1406	glyc99	14	12	1.21	0	-

3.5.1 Fault weakening mechanisms

Given the presence of fluids, the low imposed effective stresses, the room temperature experiments, the possible fault weakening mechanisms that can be activated in these experiments are: flash heating (FH) and thermal pressurization (TP), and Elastohydrodynamic (EHD) lubrication (see also Cornelio et al. (2019) for discussion). In the discussion below we also included the dependence of viscosity with temperature for the cases where viscosity is explicitly involved, TP and EHD. The FH mechanism is a weakening process acting on a fault surface due to the local increase of the temperature of the asperities populating the sliding surface with consequent reduction of the frictional strength (Beeler et al., 2008; Goldsby and Tullis, 2011; Passelègue et al., 2014; Rice, 2006). The macroscopic evolution of the shear stress τ can be written as a function of the slip velocity following:

$$\tau = [(\mu_{peak} - \mu_w) \frac{V_w}{V} + \mu_w] \sigma_n \quad (3.2)$$

where $\mu_{peak}=0.71$ is the friction coefficient (Figure 3.5), μ_w is the friction coefficient at the weakened state and V_w the critical weakening velocity allowing thermal degradation of as-

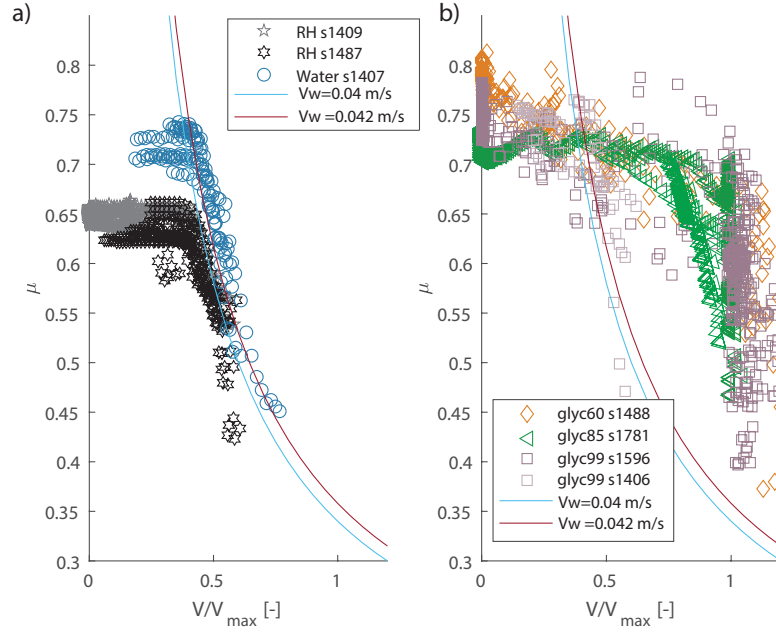


Figure 3.6: Apparent friction coefficient μ vs slip-rate V normalized by the maximum imposed slip-rate V_{max} ($V_{max}=0.1$ m/s for all experiments with the exception of s1781 where $V_{max}=0.2$ m/s). a) For the experiments performed in room-humidity conditions (black and grey in color stars) and in presence of distilled water (blue dots), we observed an exponential decay of μ with V/V_{max} . b) For the experiments performed with fluids with higher viscosities than water (orange diamonds for experiment performed in presence of mixture 60%glycerol/40%water; green triangles for experiment with 85%glycerol/15%water; pale and dark purple squares for the two experiments with 99% glycerol), we did not recognize a systematic relationship between μ and V/V_{max} .

perities during their contact lifetimes, σ_n is the normal stress. If the predicted minimum shear stress (or friction coefficient) from (3.2) is similar to the measured one, the weakening mechanism is likely FH. For Westerly Granite, $\mu_w=0.1-0.2$ (Cornelio et al., 2019; Goldsby and Tullis, 2011; Passelègue et al., 2014) and, based on our experimental evidence, V_w slightly increased from $V_w=0.040$ m/s under room humidity conditions to $V_w=0.042$ m/s in the presence of pressurized fluids (Figure 3.6a). This result is in agreement with the experiments conducted on silicate rocks in the presence of water that demonstrated a cooling effect of water on the asperities which delayed or even buffered the activation of flash heating and weakening mechanisms (Acosta et al., 2018; Passelègue et al., 2016b; Violay et al., 2014b, 2015). Based on the flash heating model (Rice, 2006) we can estimate the asperity diameter $D = \pi \alpha_{th} / V_w [\rho C (T_w - T_0) / \tau_c]^2 \sim 13 \mu\text{m}$, where $\alpha=1.25 \cdot 10^{-6} \text{ m}^2\text{s}^{-1}$ is the thermal diffusivity, $\rho=2650 \text{ kg m}^{-3}$ rock density, $C=900 \text{ Jkg}^{-1}\text{K}^{-1}$ is the heat capacity, $T_w=900 \text{ }^\circ\text{C}$ is the weakening temperature, $T_0=25 \text{ }^\circ\text{C}$ is the initial temperature, $\tau_c=5.6 \cdot 10^9 \text{ Pa}$ is the contact stress (data for Westerly granite, Passelègue et al. (2014)). According to (3.2), the fast decrease in shear stress measured during experiments conducted under room-humidity and water saturated condi-

tions can be well explained by flash heating and weakening theory (Figure 3.7a-b). However, the poor fit of the estimated minimum shear stress due to the activation of FH with respect to the measured one in the experiments conducted with fluids with higher viscosities than distilled water (Figure 3.6b, Figure 3.7c-e) suggests the activation of other fault lubricating mechanisms as discussed below. To quantify the mismatch (Figure 3.7) during stage III between the minimum shear stress measured in the experiments and the estimated shear stress due to FH (3.2), we computed the percent error between the two shear stresses. The percent error is computed as the average of the absolute difference between the estimated values of shear stress $\tau_{min,pred}$ and the experimental values $\tau_{min,meas}$ divided by the experimental values $\tau_{min,meas}$ for each short-lived slip-event “i”:

$$Percent_{error} = \frac{\sum_{(i=0)}^n (|\tau_{(min,pred)} - \tau_{(min,meas)}|)}{\tau_{(min,meas)}_i} \frac{1}{n}, \quad (3.3)$$

where n is the number of short-lived slip events for each experimental condition. In the case of FH, the mismatch between the minimum shear stress estimated with (3.2) and the measured shear stress increases from ca. 4% for the experiments conducted with water to ca. 52% for the experiments conducted with 99% glycerol (see summary Figure 3.11 below).

The TP mechanism assumes that fluids present in the fault have an expansion coefficient higher than that of rocks (Rice, 2006; Sibson, 1973). Because of the temperature increase due to frictional heating, the fluid pressure increases and induces a reduction of the effective normal stress acting on the fault. If this mechanism was triggered in our experiments, it would localize on the slipping zone (= between the two sliding surfaces of Westerly granite), since we performed our experiments under drained conditions and no fluid overpressure was recorded at the pump during testing (Figure 3.3). Thermal pressurization can be described by the following equations (Rice, 2006):

$$\frac{\partial T}{\partial t} = \frac{1}{(\rho C)_{eff}} \mu_0 (\sigma_n - P_f) \frac{v}{2w} + \alpha_{th} \frac{\partial^2 T}{\partial y^2} \quad (3.4)$$

$$\frac{\partial P_f}{\partial t} = \frac{(\lambda_f - \lambda_r)}{(\beta_f + \beta_r)} \frac{\partial T}{\partial t} + \alpha_{hy} \frac{\partial^2 P_f}{\partial y^2} \quad (3.5)$$

Where y is axis perpendicular to the fault plane, ρ is the rock density, C rock specific heat, μ_0 the peak friction coefficient ($\tau_{imp}/(\sigma_n - P_{f,imp})$), V the slip-rate and α_{th} the thermal diffusivity of the fluid, λ the isobaric thermal expansion coefficient, β the compressibility (subscripts f and r stand for fluid and rock, respectively). The hydraulic diffusivity of the fault is expressed as a function of the fault's permeability (k) and the fluid viscosity (η) with $\alpha_{hy} = k/(\eta(T) \beta_f)$.

We compared the measured minimum shear stress of each slip-event triggered in the presence

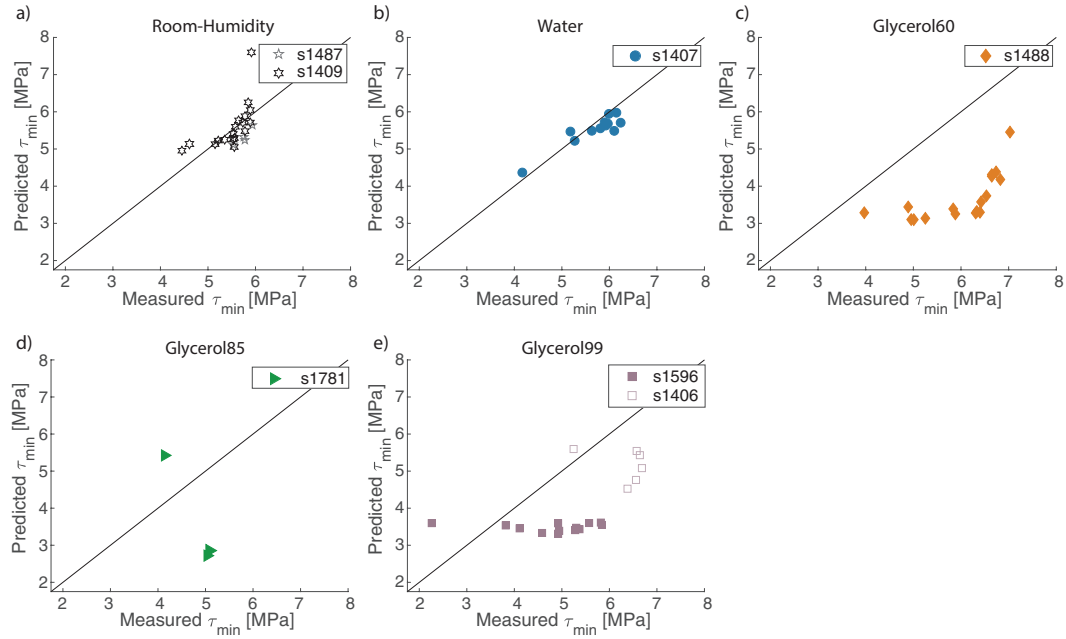


Figure 3.7: Comparison between measured minimum shear stress during stage III and the estimated minimum shear stress according to flash heating and weakening mechanism (3.2) under a) room humidity conditions and in the presence of 100% distilled water b), 60%glyc/ 40%water c), 85%glyc,15%water d) and, 99% glycerol e). The fit between measured and estimated shear stress is very good in Figure 3.7a-b, suggesting the activation of FH in the case of experiments performed under room humidity and 100% water conditions. Instead, the poor fit in the case of experiments performed with the more viscous fluids (Figure 3.7c-d-e) suggests the activation of other fault lubricating mechanism than FH (see discussion and Figure 3.8, 3.9 and Figure 3.11).

of viscous fluids in our experiments with the theoretical estimated minimum shear stress associated to the TP mechanism via (3.4) and (3.5). The minimum shear stress due to TP was estimated using a coupled Finite Element Analysis (FEA) 2D time-dependent model in @Matlab. In this model, we computed both the heat source and its dissipation in time and space. We considered a 2D sample (50 x 55 mm, or the diameter vs. height of each cylinder of Westerly granite), an initial effective normal stress of 10 MPa (the one imposed the experiments) and a friction coefficient equal to the μ_{peak} (Figure 3.5) and included the presence in the slipping zone of a viscous fluid. Fluid viscosity coincides with the experimental one (see Table 3.3). Two different materials were used to simulate the slipping zone and the bulk material (Westerly Granite). The thermal and hydraulic properties of the slipping zone were defined as a linear combination of the thermal properties of the fluid and of the rock. Except for temperature dependency on fluids viscosity, the fluids and rock properties were considered constant during the modeled experiments and are reported in Table 3.3. We applied the empirical formulation proposed by Cheng (2008) to correct the lubricant viscosity

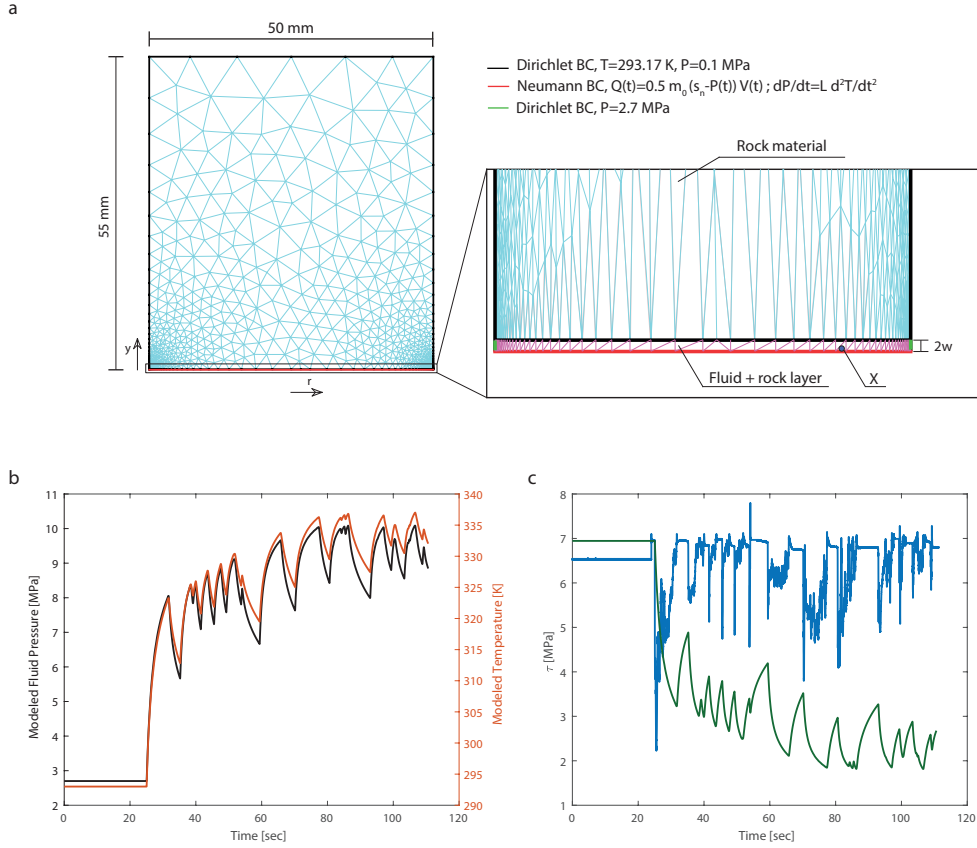


Figure 3.8: Thermal pressurization (TP) model geometry and results. a) Mesh and Boundary Conditions of the model with zoom on the slipping zone. b) Temperature and fluid pressure distribution for the experiment s1596 (glyc 99%) during the stage III on the point X (r,y)=(16.7, 0 mm). c) Measured shear stress (blue curve) and modeled shear stress (green curve) using the TP model.

with the temperature estimated in the model (note that glycerol acts as a Newtonian fluid at the investigated slip-rates). The permeability evolution of the slip zone cannot be measured in the experiment and it was considered constant and equal to $k=10^{-13}$ m² (Ye and Ghassemi, 2018). This assumption is considered valid since negligible shortening (and consequently dilation) variation was measured during the experiments and no off fault damage was observed on post mortem samples. The permeability of the bulk material $k=10^{-19}$ m² (Acosta et al., 2018; Nasser et al., 2009). The bulk material was regarded as very low porous media (3% porosity, measured with the helium pycnometer), whereas the initial porosity on the fault plane is defined as $\phi = 1 - A_r / A = 0.95$ where A_r is the real contact area and A is the nominal area of the slip surface. In the model, the experimental fault is sheared at the recorded slip-rate $V(t, r)$ over a thin slip zone of thickness $2w=50$ μ m equal to the initial height of the asperities (see Figure 3.1). We assumed that all the mechanical energy is dissipated as heat and no heat is lost by radiation, so the heat flux $Q(r, t) = 0.5 \tau(t) V(r, t)$ is function of time t and the the radial

distance r from the centre of the sample. A Neumann boundary condition was applied to the bottom external edge of the model (i.e. slip zone Figure 3.8a) to consider the flux of heat due to shearing and the coupled increase of fluid pressure. On the other three external boundaries, a constant temperature $T = 293.15 \text{ K}$ as the initial temperature of the two materials and a constant pressure $P = 0.1 \text{ MPa}$ for the bulk material and an initial fluid pressure $P = 2.7 \text{ MPa}$ for the slipping zone were imposed. At the inner boundary between the slip zone and the wall-rock, the continuity of the solution was granted.

Table 3.3: Thermal and hydraulic properties used in the thermal pressurization model and in the heat diffusion model. κ =thermal conductivity, λ =thermal expansion coefficient, β =compressibility coefficient, η_0 =initial viscosity, ρ = density, C = specific heat, WG=Westerly granite. a) Thermal properties of water from Goranson (1942), b) Thermal properties of water/glycerol mixtures from Bates (1936),c) Thermal properties of Westerly granite from Eppelbaum et al. (2014)

	water ^a	glyc60 ^b	glyc85 ^b	glyc99 ^b	WG ^c
κ [W/(mK)]	0.6	0.38	0.31	0.25	3.07
λ [10^{-3}]	1.21	1.93	2.23	2.41	0.02
β [10^{-10} Pa^{-1}]	5.1	3.37	2.65	2.1	14.9
η_0 [Pa s]	0.001	0.01	0.109	1.226	-
ρ [kg m^{-3}]	1000	1151	1219	1255	2650
C [J (kg K) ⁻¹]	4180	3121	2678	2430	900

According to our simulations, the estimated minimum shear stress associated to TP mechanism at 2/3 of the sample radius (maximum effect) is not consistent with the minimum shear stress measured in the experiments (Figure 3.8c). Indeed, TP mechanism would result in (1) larger shear stress drops and (2) smaller minimum shear stress compared to the measured ones (Figure 3.9). Importantly, the minimum shear stress estimated with the thermal pressurization model is at least 35% higher than the measured minimum shear stress, independent of the viscosity of the fluid (see Figure 3.11b). According to the FEA 2D model, the activation of TP is not consistent with the experimental evidence. Instead, the minimum shear stress measured in the experiments conducted with fluids with higher viscosities than water could result from the activation of EHD. EHD is a weakening mechanism induced by overpressure generated by the shearing of a thin viscous fluid between two sub-parallel and rough surfaces (e.g., the experimental faults). Here we test this hypothesis using the model proposed by Brodsky and Kanamori (2001) and refined by Bizzarri (2012). The model is parameterized using the Sommerfeld number, which is a measure of the lubrication pressure normalized by the normal stress. The fault shear strength dependence with the Sommerfeld numbers S_0 can

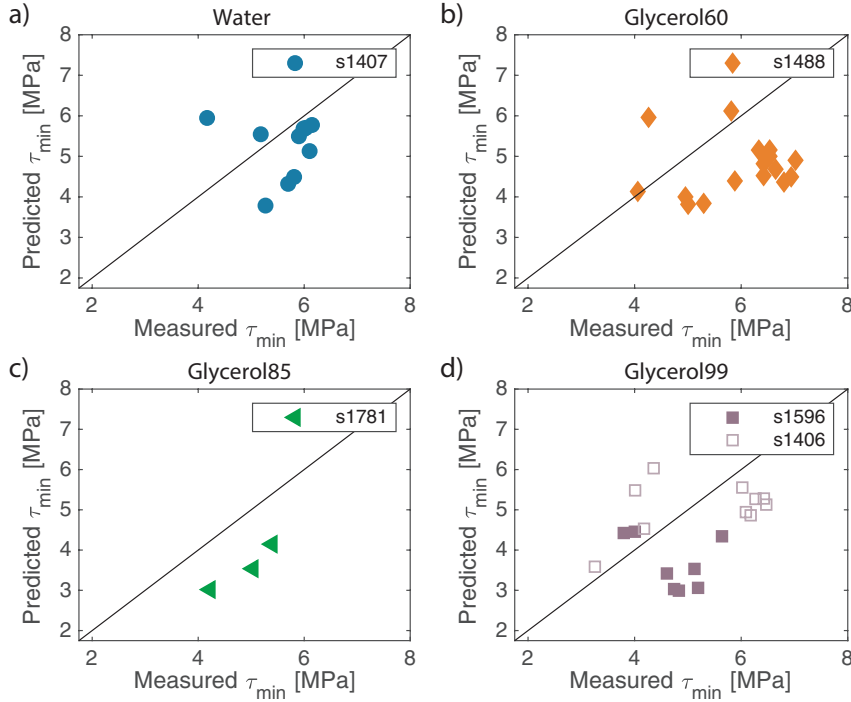


Figure 3.9: Comparison between experimental minimum shear stress and the predicted minimum shear stress by TP models in presence of a) water, b) 60%glyc/40%water, c) 85%glyc,15%water, d) 99% glycerol. The poor fit of the experimental data with the estimates of minimum shear stress according to the Finite Element Analysis 2D model suggest that TP mechanism was never activated in the experiments discussed here.

be expressed as (Bizzarri, 2012; Brodsky and Kanamori, 2001):

$$\tau(S) = \begin{cases} \mu_{static}\sigma_{eff} + \frac{w}{u}P_{lub}, & \text{if } S_0 < 1 \\ \frac{w}{u}P_{lub}, & \text{if } S_0 \geq 1 \end{cases} \quad (3.6)$$

where $S_0 = (P_f - P_{lub})/\sigma_n$ is the Sommerfeld number, $P_{lub} = 6\eta r U^2 V / (2w)^3$ the lubricant pressure, η the viscosity of the fluid, $r=0.001$ (Brodsky and Kanamori, 2001) the dimensionless roughness, U the slip distance, and w the average thickness of the slurry film, V the measured slip-rate. The Sommerfeld number describes the transition between three lubrication regimes (boundary, mixed or fully lubricated regimes) which are associated to the evolution of the strength of the fault. Unfortunately, a key parameter of the EHD model is the evolution of w with time and slip which is poorly constrained because it can only be measured before and at the end of the experiment. For this reason, differently to previous studies (Bizzarri, 2012), we assumed w proportional to the measured shortening δ , following the relation: $w = w_0 + \delta$. We performed a 2D Finite Element diffusion analysis to estimate the average temperature of

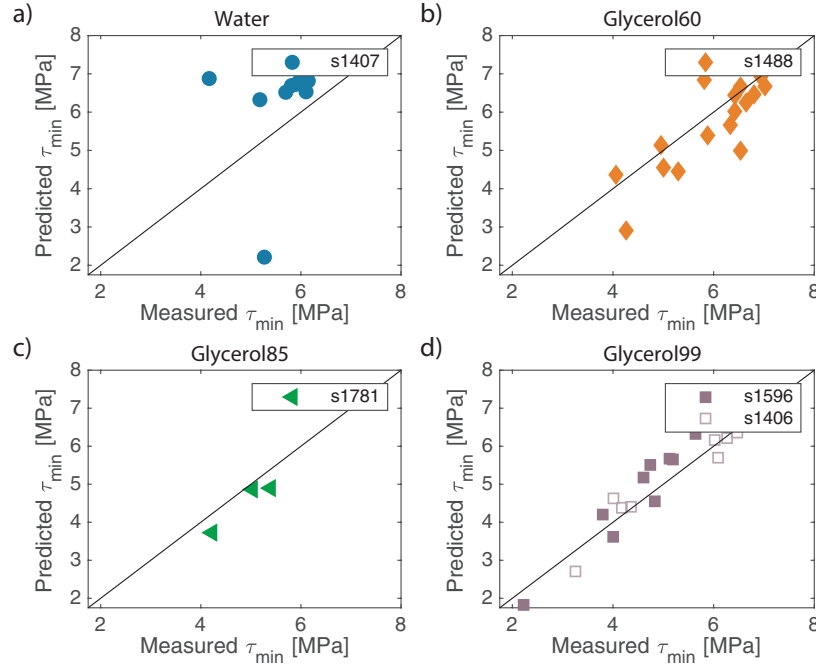


Figure 3.10: Comparison between minimum shear stress measured in the experiments and estimated in Finite Element Analysis 2D EHD models in the presence of a) 100% distilled water, b) 60%glyc/40%water, c) 85%glyc,15%water, d) 99% glycerol. The viscosity of the fluids was corrected for its temperature dependence (see main text). Note the good fit between measured and estimated minimum shear stress in the case of the experiments performed with the more viscous fluids. The good fit (panel b-d) and quantified in the diagram of Figure 3.11c, suggests that EHD mechanism could operate in these experiments.

the fluid trapped between the slip surfaces and the viscosity was corrected for temperature increase as described in Cornelio et al. (2019). In particular, we used the sample geometry (Figure 3.8a) and the same fluid properties (Table 3.3) of the model used for the TP but in the EHD model the fluid pressure is considered constant and equal to the imposed one measured by the fluid pressure transducers (Table 3.1). Using the average estimated temperature in the slip zone at $2/3 R$ ($R = 25$ mm is the external radius of the sample), we corrected the initial viscosities (at 20 °C) from the increase of temperature of the fluids due to frictional heating exploiting the empirical law proposed by Cheng (2008) for water/glycerol mixtures. The dynamic viscosity η of the mixture is:

$$\eta = \eta_w^\zeta \eta_{glyc}^{(1-\zeta)} \quad (3.7)$$

Where ζ is weighting factor, function of the concentration of glycerol C_m and of two empirical

factors a and b which are dependent of the temperature T

$$\zeta = 1 - C_m + \left(\frac{a(T) b(T) (1 - C_m)}{a(T) C_m + b(T) (1 - C_m)} \right) \quad (3.8)$$

Our model estimates of the minimum shear stress induced by EHD matched well the measured ones in the case of the experiments performed with mixtures of 40%water/60%glycerol, 15%water/85%glycerol for all the slip events occurring at cumulated slips larger than 0.25 m and 0.015 m (after the main first event), respectively (Figure 3.10b-c). In particular, the misfit between measured and modeled minimum shear stress decreases from ca. 52% for the experiments conducted with 100% distilled water to ca. 9% for the experiment conducted with 99% glycerol (Figure 3.11c). Moreover, EHD explains well all the stress drops recorded during the two experiment performed in the presence of a highly viscous fluid (99% glycerol) (Figure 3.10d). We conclude that FH is probably favored for low viscosity (< 1 mPa.s) fluids and room-humidity conditions, whereas EHD is the dominant weakening mechanisms in the case of fluids with higher viscosities than water.

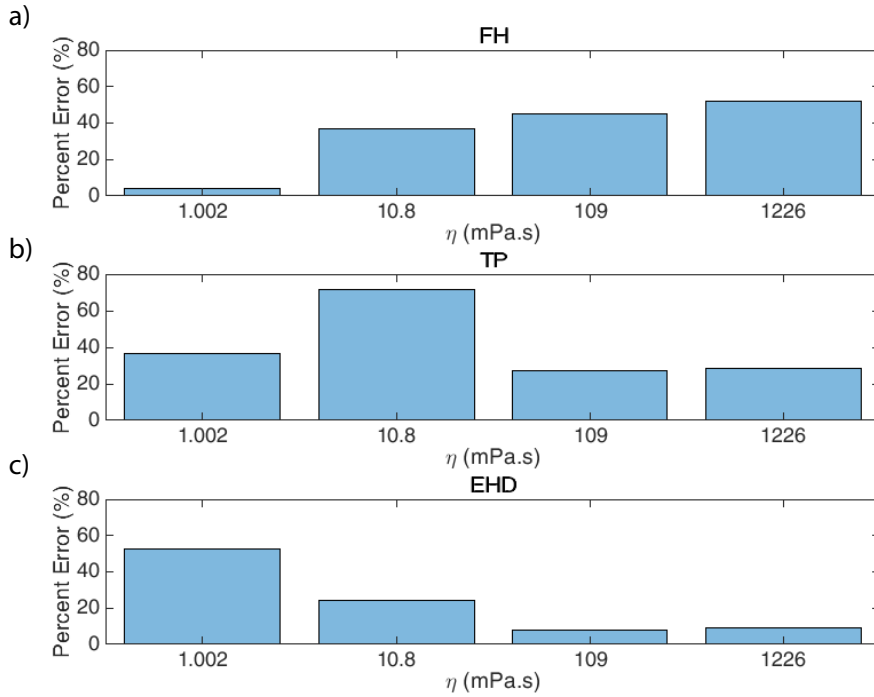


Figure 3.11: Misfit or percent error (3.3) between the measured minimum shear stress and the estimated one for a) Flash-Heating (FH), b) Thermal-Pressurization (TP) and c) Elastohydrodynamics (EHD) (see main text for discussion). According to this analysis, FH occurred only in the experiments performed with 100% distilled water, and EHD in the experiments performed with glycerol. Instead, modeling suggests that TP was never activated in the experiments.

3.5.2 Estimation of the breakdown work

The main outcome of the modeling and analysis presented in the previous section is that two mechanisms (FH and EHD) are activated during our experiments depending on the presence of fluids and their viscosities (Figure 3.11). Here we question if the type of weakening mechanism influences the amount of breakdown work dissipated during earthquake rupture propagation. Indeed, the activation of FH and EHD mechanisms have been invoked to estimate the breakdown work (W_b or energy dissipated in the breakdown zone during seismic rupture propagation) in earthquakes energy budgets (Brantut and Viesca, 2017; Cornelio et al., 2019; Rice, 2006). Therefore, we computed the breakdown work dissipated during both the short- and the long-lived slip events of stage III (Figure 3.4c). The W_b was calculated by integrating the evolution of shear stress with slip (Palmer and Rice, 1973):

$$W_b = \int_{U_{in}}^{U_{min}} [\tau(U) - \tau_{min}] dU \quad (3.9)$$

where U_{min} is the slip distance at which the measured shear stress is equal to τ_{min} and U_{in} is the slip distance at the beginning of the short or long-lived-slip events. For each slip event and independent of the presence and the viscosity of the fluid, W_b increased with slip following a power law relationship (Figure 3.12). A similar trend between W_b and slip distance has been attributed to thermal-pressurization by Viesca and Garagash (2015), suggesting that TP could be an effective weakening mechanism under conditions of low fluid viscosity and high normal stress. However, EHD is more efficient for high viscous fluids and at low normal stresses. This trend is very similar to the one measured in experiments performed on Westerly granite either under room-humidity conditions in triaxial configuration (Ohnaka, 2003; Passelègue et al., 2016b), or in the presence or absence of pressurized fluids in high velocity rotary shear configuration (Cornelio et al., 2019; Nielsen et al., 2016), as well as estimated for natural earthquakes (Abercrombie and Rice, 2005; Malagnini et al., 2014; Rice, 2006), human-induced earthquakes (Jost et al., 1998) and for dynamic source modelling of natural earthquakes (Spagnuolo, 2006; Tinti et al., 2005b; Venkataraman and Kanamori, 2004) (Figure 3.13). In particular, our new data-set fits well with the theoretical estimates of the W_b associated with fault slip due to flash heating processes (Brantut and Viesca, 2017), and consistent with the W_b estimated for the earthquakes at the KTB deep drilling project (Jost et al., 1998), independently of the activated mechanism in our experiments. Caution should be taken when comparing energies at different scales. On one hand, W_b is a quite robust seismological estimate as bias effects are reduced (Guatteri and Spudich, 2000) but suffers of strong uncertainties related to the signal treatment, to the assumptions made and blurred effects due to rupture related processes including off-fault damage. On the other hand theoretical models used to estimate the breakdown energy for natural and induced seismicity are often oversimplified as many

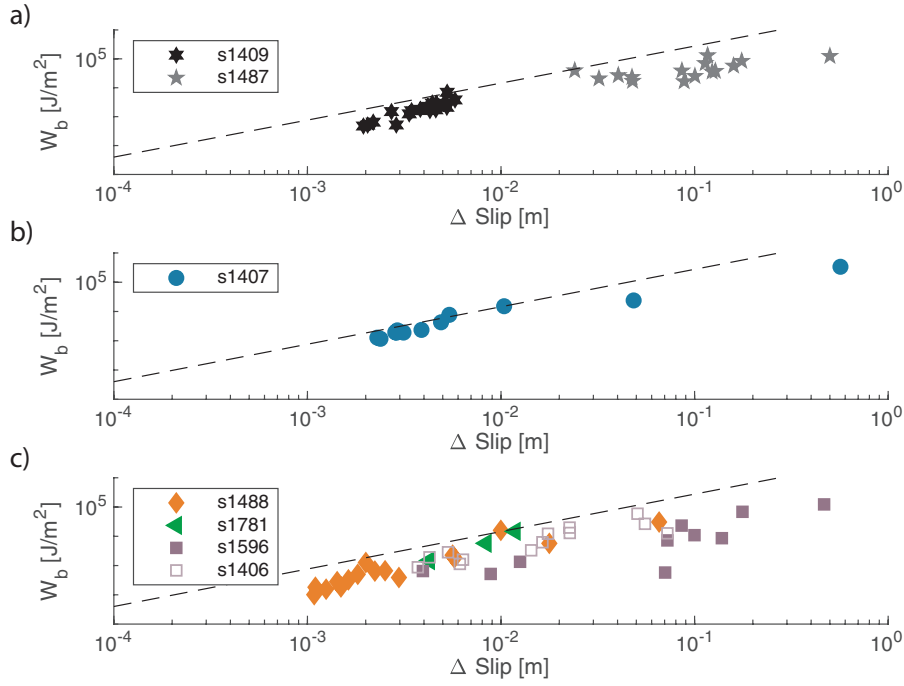


Figure 3.12: Breakdown work versus the $\Delta U = U_{min} - U_{in}$ for short-lived and long-lived events under a) room humidity conditions (black and grey stars), b) in the presence of water (blue dots), c) in presence of 60%glycerol/40%water mixtures (orange diamonds), 85%glycerol/15%water mixtures (green triangles), and 99% glycerol (purple squares).

variables like the work dissipated in the surrounding volume through grain crushing, off-fault damage (Cocco et al., 2006; Shipton et al., 2006) is often neglected, considering only the energy necessary to slip on the fault plane. Despite these limitations, the agreement of data across scales as shown in Figure 3.13 suggests that on average our experiments are pertinent and describe at least some of the frictional instabilities that may occur in nature. In particular, our results suggest that, at least for the experimental conditions discussed here, although two different weakening mechanisms (FH and EHD) trigger and control the evolution of dynamic fault strength in laboratory earthquakes, the energy required to weaken the fault for a given earthquake magnitude is independent of the lubrication processes.

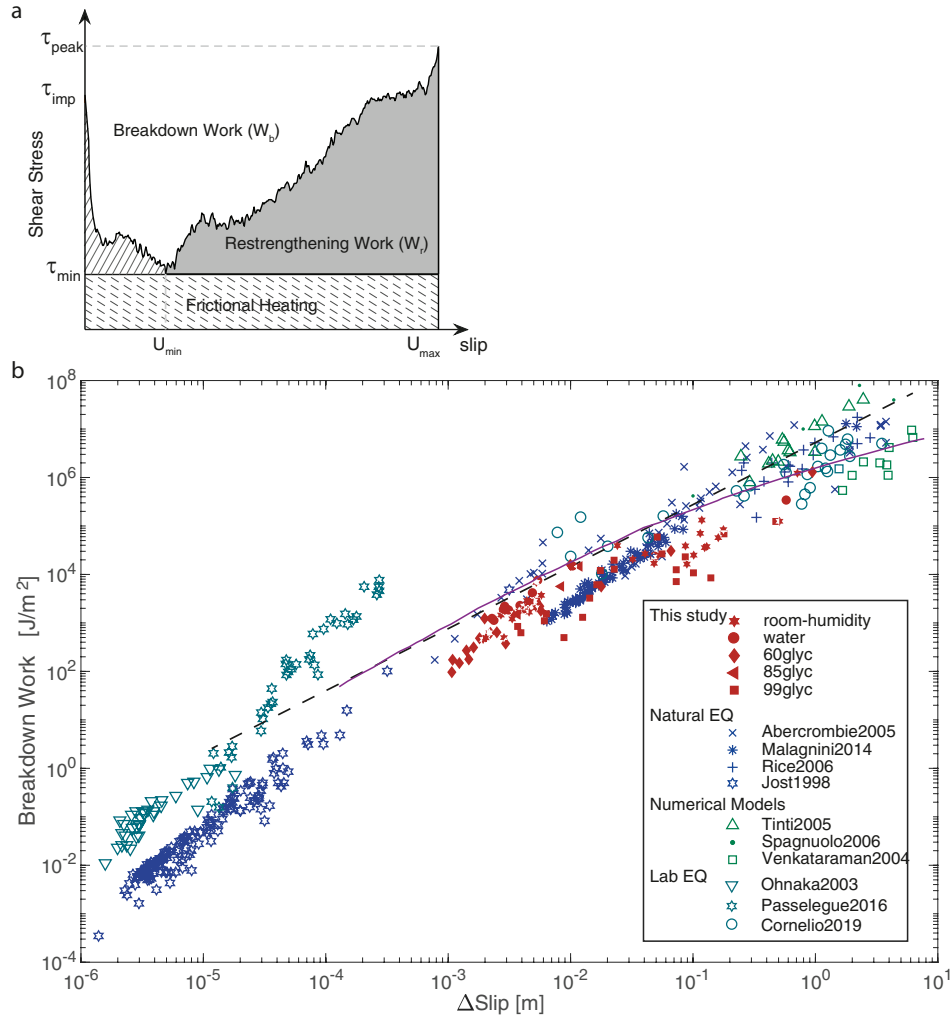


Figure 3.13: Energy budget and breakdown work in experimental and natural earthquakes. a) Schematic representation of the shear stress vs slip distance and energy partitioning during the first short-lived slip events of the experiment s1488 performed in presence of a mixture 60%glycerol/40%water. The area indicated by inclined segments below the curve connecting $(\tau_{imp}, 0)$ and (τ_{min}, U_{min}) corresponds to the breakdown work W_b . The light grey area between (τ_{min}, U_{min}) and (τ_{peak}, U_{max}) is the restrengthening work W_r (not discussed in this study). The dashed lines area $(\tau_{min}, 0) \times (\tau_{min}, U_{max})$ is the minimum frictional heat dissipated during sliding (Kanamori and Rivera, 2013). c) Experimental and seismological estimates of breakdown work. The red symbols correspond to the W_b for the short- and long-lived slip events during stage III (see Figure 3.4) presented in this study. Blue symbols correspond to seismological estimates of W_b for natural (Abercrombie and Rice, 2005; Malagnini et al., 2014; Rice, 2006) and induced earthquakes (Jost et al., 1998). Green symbols correspond to seismological estimates of W_b from numerical (inversion) models of earthquakes (Spagnuolo, 2006; Tinti et al., 2005b; Venkataraman and Kanamori, 2004); teal-blue symbol are for laboratory estimates of W_b (Ohnaka, 2003; Passelègue et al., 2016a; Cornelio et al., 2019). Dashed black line indicates the best fit proposed by Nielsen et al. (2016) with $E=5.25 \cdot 10^6 U^{1.28}$, where U is the slip distance in meter, and the purple line indicates the solution of the FH model proposed by Brantut and Viesca (2017)

3.6 Conclusions

The experiments presented here recognize that, at least at the investigated loading and ambient conditions (room temperature), the viscosity of the fluid does not influence the onset of fault reactivation in fluid-permeated faults (Figure 3.5). On the other hand, once the fault is frictionally unstable and slip-rates accelerate, the fault weakening mechanism that is activated is a function of the fluid viscosity. In particular, under the investigated loading conditions and for the particular roughness of the studied experimental faults, flash heating is active at room humidity conditions and in the presence of low (1 mPa·s) viscous fluids (100% distilled water). Thermal pressurization, as modeled here, is not clearly activated during our experiments. Indeed, EHD is dominant in the presence of high fluid viscosity where EHD prevails over FH. The activation of a particular weakening mechanism does not result in differences in the magnitude of the breakdown work (Figure 3.12). This might imply that changes in the viscosity of fluids that can be present in fault zones due to previous injection in reservoirs during hydraulic fracturing should not influence the static reactivation of a fault and the breakdown work (if the fluid pressure remains constant), but they might influence the evolution of the associated earthquake sequences in terms of stress drops. A similar analysis in the case of natural earthquake sequences suggest that the activation of pre-existing fault due to a quasi-static tectonic load is not influenced by the presence of a viscous fluid that only intervenes to control the way the same amount of energy is released.

4 Mechanical behaviour of fluid-lubricated faults

Authors: Chiara Cornelio¹, Elena Spagnuolo², Giulio Di Toro^{2,3}, Stefan Nielsen⁴, Marie Violay¹.

¹ Laboratory of Experimental Rock Mechanics (LEMR), ENAC, EPFL, Switzerland;

² Istituto Nazionale di Geofisica e Vulcanologia, INGV, Rome, Italy;

³ Dipartimento di Geoscienze, Università degli studi di Padova, Padua, Italy;

⁴ Department of Earth Sciences, University of Durham, Stockton Road, Durham DH1 3LE, UK.

Reference: Cornelio, C., Spagnuolo, E., Di Toro, G., Nielsen S., Violay, M. Mechanical behaviour of fluid-lubricated faults. *Nat Commun* 10, 1274 (2019). <https://doi.org/10.1038/s41467-019-09293-9>

Contributions: Original idea was from C. Cornelio and M. Violay. C. Cornelio, E. Spagnuolo and M. Violay performed the experiments. C. Cornelio performed the surface roughness measurements and developed the thermal model with input of M. Violay. C. Cornelio and M. Violay co-wrote the manuscript with the input of E. Spagnuolo, S. Nielsen and G. Di Toro. All the authors participated in the interpretation of the data and in the discussion of the paper.

Highlights:

- For the first time, we experimentally demonstrated that elasto-hydrodynamic lubrication may be an efficient fault weakening mechanism, independently from rock lithology.
- Slip rate necessary for elasto-hydrodynamic lubrication is much smaller than the slip rate necessary for the triggering of other weakening mechanisms, suggesting that elasto-hydrodynamic lubrication is a very efficient weakening mechanism.
- For small slip events, the presence of viscous fluid significantly increases the energy dissipated during rupture processes and might delay or inhibit the nucleation and

propagation of the rupture. Conversely, as seismic slip increases, rocks are more prone to slip in the presence of viscous fluid.

4.1 Abstract

Fluids are pervasive in fault zones cutting the Earth's crust; however, the effect of fluid viscosity on fault mechanics is mainly conjectured by theoretical models. We present 36 friction experiments performed on both dry and fluid-permeated silicate and carbonate bearing-rocks, at normal effective stresses up to 20 MPa, with a slip-rate ranging between 10 $\mu\text{m/s}$ and 1 m/s. Four different fluid viscosities were tested: distilled water ($\eta \sim 1 \text{ mPa s}$) and three mixtures of water with glycerol concentrations of 40%wt., 15%wt. and 0.1%wt. ($\eta=10.8, 109.2$ and 1226.6 mPa s , respectively). We show that both static and dynamic friction coefficients decrease with viscosity, and that dynamic friction depends on the dimensionless Sommerfeld number (S) as predicted by the elastohydrodynamic lubrication theory (EHD). Extrapolation of our results to crustal conditions suggests that EHD is an effective weakening mechanism during natural and induced earthquakes. However, at seismic slip-rate, the slip weakening distance (D_c) increases markedly for a range of fluid viscosities expected in the Earth, potentially favouring slow slip rather than rupture propagation for small to moderate earthquakes. Therefore, in the presence of high viscosity fluids, transition from slow nucleation to seismic propagation could not occur until rupture reaches metric to kilometric lengths.

4.2 Introduction

Fluids with variable composition (gas, water, brine, hydrocarbon seepage, wet gouge, and frictional melt), rheology, and physical state are pervasive within active tectonic faults. The viscosity of such fluids may vary over seven orders of magnitude, from 10^{-4} Pa s for liquid water to 10^3 Pa s for silicic melts at high temperature (Spray, 1993; Di Toro et al., 2011; Hirose and Shimamoto, 2005). Elastohydrodynamic lubrication (EHD), or the weakening induced by overpressure generated by the shearing of a thin viscous fluid between two subparallel and rough surfaces (Brodsky and Kanamori, 2001), has been recognised for a long time in industrial processes (Dowson and Longfield, 1963; Bair and Winer, 1982). EHD has also been invoked to explain the dramatic reduction of friction during earthquake slip in the presence of fluids (King Hubbert and Rubey, 1959; Lachenbruch and Sass, 1980). However, up to date, the possible triggering of EHD in natural faults relies on theoretical models only, and was not tested at deformation conditions typical of seismic faulting. Furthermore, the experimental studies investigating fluid-rock interaction almost exclusively considered water as the fluid at both sub-seismic (Scuderi et al., 2017) and seismic slip-rates (Violay et al., 2013, 2014b, 2015).

For sake of simplicity, tectonic faults can be described at seismogenic depths as rough surfaces separating two solids, which are in contact at a number of asperities (Dieterich and Kilgore, 1994) which represent only a fraction of the total fault area, and can be filled by fluids and gouges. During fault sliding and depending on how the normal stress is partitioned between

the asperities and the fluid, three different regimes can be distinguished (Brodsky and Kanamori, 2001; Persson, 2000e): the boundary lubrication regime (BL), where the normal stress is supported by solid-solid contacts; the fully lubricated regime (EHD), where the normal stress is supported by interstitial fluid; and the mixed lubrication regime (ML), where the normal stress is supported both by the solid-solid contacts and the fluid. The transition between these three regimes is controlled by the Sommerfeld number (Brodsky and Kanamori, 2001) $S = \frac{6\eta VL}{(H_0)^2 \sigma_{eff}}$ where V is the slip-rate, η is the lubricant dynamic viscosity at the estimated mean temperature (Persson, 2000e) of the slipping zone (defined as the zone where deformation is highly localized), L is the characteristic length over which the fluid pressure changes (related to the wavelength of the asperities), H_0 is the initial average gap between the asperities (related to the height of the asperities), and σ_{eff} is the effective normal stress ($\sigma_{eff} = \sigma_n - P_f$, where σ_n is the normal stress and P_f is the fluid pressure).

Recently, Bayart et al. (2016) provided evidence of the influence of fluid viscosity by performing laboratory stick-slip experiments as an analogue of seismic events (Brace and Byerlee, 1966). The setup consisted of poly-methylmethacrylate (PMMA) slabs lubricated by a film of viscous fluid (silicone and hydrocarbon oils). The presence of the fluid resulted in a smaller static friction with respect to that under room-humidity conditions. However, the fracture energy (i.e., the energy dissipated by crack propagation) increased in the presence of the fluid and was independent of the lubricant viscosity but dependent of the lubricant composition. Here, based on experimental and geological evidence, we discuss the effect of the viscosity of a fluid sandwiched between two rock slip surfaces at slip-rates characteristic of either earthquake nucleation (slip-rate from $\mu\text{m/s}$ to mm/s) (Dieterich, 1992) and propagation (mm/s to m/s) (Sibson, 1989; Heaton, 1990) and, in general, at slip-rates at which the ML and the EHD regimes might be activated.

4.3 Method

We performed 36 experiments with the rotary machine SHIVA (Di Toro et al., 2010) (INGV, Rome) on full cylinders (diameter $D=50$ mm) of Westerly Granite and Carrara Marble either in the presence of a liquid lubricant or under room-humidity conditions. Target slip-rates (V) ranged from $10 \mu\text{m/s}$ up to 3 m/s , acceleration and deceleration ramps were imposed to 6.5 m/s^2 and normal stresses were up to $\sigma_n = 22.6 \text{ MPa}$. Mechanical data (axial load, torque, axial displacement, and angular rotation) were acquired at a frequency between 250 Hz and 25 kHz , depending on the target slip-rate. Slip, slip-rate and shear stress were determined using the method outlined in Niemeijer et al. (2011) and Tsutsumi and Shimamoto (1997). All the experiments (Table 4.1) with fluids were performed under drained condition (i.e., pore pressure remained constant during the experiments), following the procedure described by

Violay et al. (2013).

The pressurizing system consisted of a pore fluid vessel and a membrane pump with a 30 cm³ fluid capacity, a pressure multiplier which imposes up to 15 MPa of fluid pressure, a pressure regulator and valves and pipes.

Table 4.1: Summary of the experimental conditions and results. WG = Westerly Granite, CM = Carrara Marble, V =slip-rate, σ_{eff} =effective normal stress, η_0 =initial kinematic viscosity of the fluid, μ_{static} =static friction coefficient, μ_{peak} = peak friction coefficient, μ_{dyn} = dynamic friction coefficient, W_b = breakdown work for m² fault, S = Sommerfeld number at μ_{dyn}

test	Cond.	V [mm/s]	σ_{eff} [MPa]	μ_{static} [-]	μ_{peak} [-]	μ_{dyn} [-]	D_c [mm]	W_b [MJ/m ²]	S
s1293	WG RH	0.01	10	0.661	0.765	0.767	20.00	0.039	-
s1399	WG RH	0.1	10	0.712	0.988	1.097	60.00	0.007	-
s1297	WG RH	10	10	0.530	0.644	0.501	901.06	0.609	-
s1301	WG RH	100	10	0.714	0.714	0.150	1801.90	6.293	2.80E4
s1321	WG RH	1000	10	0.660	0.660	0.210	1719.10	5.008	2.94E3
s1318	WG H2O	0.01	10	0.705	0.843	0.693	42.94	0.058	4.96E-6
s1319	WG H2O	0.1	10	0.636	0.667	0.646	7.80	7.366	4.88E-5
s1302	WG H2O	1	10	0.507	0.755	0.580	772.79	0.621	4.34E-4
s1320	WG H2O	10	10	0.438	0.963	0.350	1047.20	1.688	2.46E-3
s1394	WG H2O	10	10	0.418	0.716	0.335	1211.10	1.554	3.04E-3
s1386	WG H2O	100	10	0.390	0.546	0.211	1257.00	1.333	0.0284
s1303	WG H2O	1000	10	0.257	0.473	0.176	159.68	3.712	0.1393
s1393	WG H2O	1000	4	0.335	0.412	0.352	3461.00	5.026	0.0913
s1312	WG 60%gl	0.01	10	0.578	0.612	0.739	10.00	0.024	4.89E-5
s1313	WG 60%gl	0.1	10	0.507	0.600	0.700	57.00	0.163	4.67E-4
s1315	WG 60%gl	10	10	0.696	0.982	0.409	577.16	1.260	0.0080
s1317	WG 60%gl	100	10	0.588	0.616	0.329	1120.00	3.938	0.0215
s1316	WG 60%gl	1000	10	0.443	0.509	0.139	850.00	1.200	0.3048
s1306	WG 85%gl	0.01	10	0.488	0.681	0.723	18.00	0.011	0.0004
s1309	WG 85%gl	0.1	10	0.498	0.602	0.576	12.00	0.154	0.0045
s1304	WG 85%gl	1	10	0.686	0.951	0.357	550.00	1.836	0.0330
s1308	WG 85%gl	10	10	0.481	0.726	0.303	1890.00	2.801	0.0823
s1311	WG 85%gl	100	10	0.307	0.774	0.194	1250.00	9.247	0.0467
s1305	WG 85%gl	1000	10	0.315	0.355	0.197	826.00	0.462	0.9399
s1387	WG 99%gl	10	10	0.227	0.245	0.133	219.20	0.667	2.8149
s1388	WG 99%gl	100	10	0.346	1.240	0.159	261.10	0.417	5.1682
s1389	WG 99%gl	1000	10	0.248	0.722	0.392	1559.80	1.510	0.7770
s1390	WG 99%gl	1000	5	0.191	0.986	0.262	226.10	0.547	1.26E2
s1604	WG 99%gl	1000	5	0.293	0.347	0.148	637.25	1.363	46.7098
s1605	WG 99%gl	100	5	0.416	0.629	0.178	1676.12	4.467	0.1256
s1606	CM 99%gl	1000	10	0.353	0.546	0.116	502.50	3.346	1.6704
s1607	CM 99%gl	100	10	0.209	0.336	0.194	754.10	6.571	2.4175

s1608	CM 99%gl	1	10	0.425	0.739	0.203	731.10	8.870	0.1732
s1609	CM 99%gl	0.01	10	0.513	0.574	0.403	7.70	5.628	0.0145
s1610	CM 99%gl	0.01	20	0.371	0.502	0.441	13.93	0.184	0.0071
s1611	CM 99%gl	3000	5	0.331	0.410	0.138	516.63	0.159	16.3101
s1612	CM H2O	0.1	10	0.592	0.874	0.674	39.39	0.009	0.0002
s1613	CM H2O	1	10	0.429	0.545	0.498	137.19	0.039	0.0014

Westerly granite and Carrara marble were selected because (1) of their low porosity ($\leq 2\%$ measured using the triple-weighing method (Violay et al., 2010)), which limited fluid diffusion through the rock matrix out of the sliding surface during the experiments, (2) of their very small grain size and homogeneity and (3) because typical rocks of the seismogenic continental crust (Hans Wedepohl, 1995).

The sliding surfaces of all the samples were roughened by using 120 SiC abrasive paper. The 3D arithmetic surface roughness was determined on the sliding surface of 20 or 25 mm in diameter cores of the starting samples and post-mortem samples of Westerly granite and Carrara Marble using an optical profilometer ContourGT-I 3D Optical Microscope, Bruker Nano surfaces Division. The scan of the surfaces was performed imposing an overlap of 20% between two adjacent areas. RMS (root-mean-square) and the stitched images of the samples surface of Westerly Granite after the experiments performed under room humidity condition and in presence of the four different fluids at slip-rate of 1 m/s are shown in the Figure 4.7. The initial H_0 was \approx RMS=7-13 μm , for Carrara Marble and Westerly Granite respectively. We considered the perimeter of our sample (0.157 m) as the maximum characteristic wavelength L (i.e., the largest possible wavelength), due to the periodicity of rotation of the rock cylinders.

4.3.1 Bulk temperature model and viscosity correction

Various viscosities of the lubricant were obtained by mixing different volume proportions of distilled water to 99.9% glycerol. Glycerol (1, 2, 3-propanetriol) is a Newtonian, water-soluble, colourless fluid, which is stable under most conditions due to its high flash and fire points (177 °C and 207 °C, respectively), which prevent phase changes and fire hazards when exposed to high temperatures due to frictional heating. The viscosities at room temperature were 1.002 mPa s (pure distilled water), 10.8 mPa s (60 %wt. glycerol), 109.2 mPa s (85 %wt. glycerol) and 1226.6 mPa s (99.9% pure glycerol). The temperature increase with increasing slip due to frictional heating during the experiments is expected to lower the lubricant viscosity. The increase in the bulk temperature on the shearing surfaces was estimated using a 2D FEA time dependent model for heat diffusion.

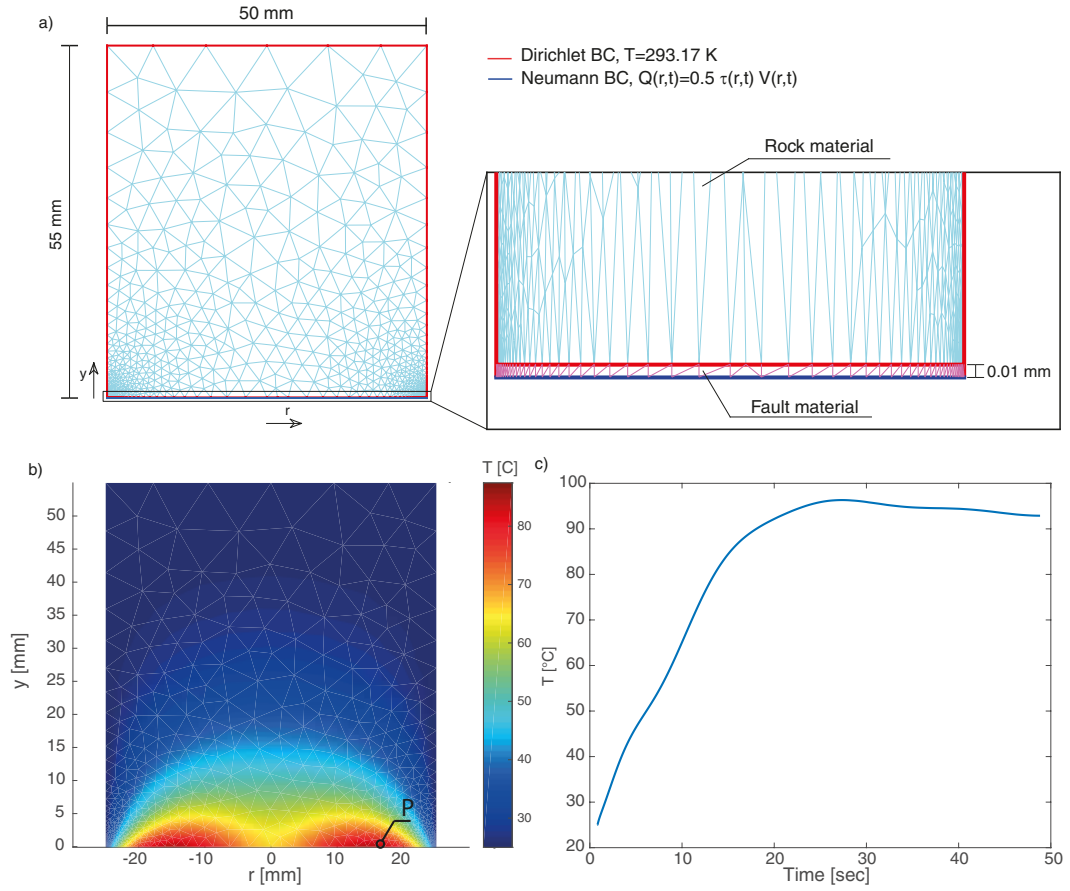


Figure 4.1: FEA 2D time dependent heat diffusion model. a) Mesh and Boundary Conditions of the model with zoom on the 0.01 mm-thick slip zone. b) Temperature distribution for the experiment s1315 at $t = 48$ s. c) Temperature evolution on the point P (x,y)=(0, 16.7 mm) for experiment s1315

The model reproduced the size of the experimental sample, (i.e. 50×55 mm diameter vs. height of the sample) with 1464 triangular mesh elements. Two different materials were used to simulate the slip zone and the bulk material. The slip zone was represented as a $13 \mu\text{m}$ -thick highly porous media. In agreement with the roughness measurements, we considered $\phi = 1 - A_r / A = 0.95$ where A_r was the real contact area and A was the nominal area. The bulk material was regarded as a very low porous media (3% porosity, measured with the helium pycnometer). We assumed that all the mechanical energy was converted into heat (because wear products were almost negligible in the fluid lubricated regime) and we neglected heat losses by radiation and fluid convection (the liquid was inside a vessel). As a consequence, half the instantaneous heat flow-rate $Q(r, t) = 0,5\tau(t) V(r, t)$, where r was the radial distance from the centre of the sample, τ was the shear stress, was applied as a Neumann boundary condition (Morse and Feshbach, 1953) to the edge of the model, which simulates the slip surface (i.e. slip zone Figure 4.1a). On the other three external boundaries, a constant temperature $T = 293.15$

K was imposed as the initial temperature of the two materials (energy dissipated by the steel of the pressure vessel). At the inner boundary between the slip zone and the wall-rock, the continuity of the solution was granted. The thermal properties of the slip zone were defined as a linear combination of the thermal properties of the fluid and of the rock (Table 4.2).

The thermal diffusivity of the slip zone was

$$\alpha_{eff} = \frac{\kappa_{eff}}{(\rho \cdot C)_{eff}} \quad (4.1)$$

with

$$\kappa_{eff} = (1 - \phi) \cdot \kappa_r + \phi \cdot \kappa_f \quad (4.2)$$

$$(\rho \cdot C)_{eff} = ((1 - \phi) \cdot \rho_r \cdot C_r) + (\phi \cdot \rho_f \cdot C_f) \quad (4.3)$$

where r and f were related to the rock and fluid properties, respectively. The diffusion of the heat was defined as:

$$(\rho C)_{eff,i} \cdot \frac{\partial T}{\partial t} = \nabla \cdot (\kappa_{eff,i} T) \quad (4.4)$$

where i identified the two materials (i.e., the slip zone and the bulk material).

Then, the estimated temperature at $r=2/3 R$, where $R=25$ mm was the external radius of the sample (Figure 4.1c), was used to correct the fluid viscosity following the empirical formula proposed by (Cheng, 2008) and to compute S . The dynamic viscosity η of the mixture was:

$$\eta = \eta_w^{\zeta_w} \cdot \eta_{glyc}^{(1-\zeta_w)} \quad (4.5)$$

Where ζ_w (4.6) was the weighting factor, a function of the concentration of glycerol C_m and of two empirical factors a and b which depended on the temperature T

$$\zeta_w = 1 - C_m + \frac{a(T) \cdot b(T) \cdot (1 - C_m)}{a(T) \cdot C_m + b(T) \cdot (1 - C_m)} \quad (4.6)$$

The initial fluid viscosity decreased with increasing temperatures associated to frictional

Table 4.2: Thermal properties of the fluid, Westerly granite and Carrara Marble. κ =thermal conductivity, ρ = density, C = specific heat, WG =Westerly granite. CM =Carrara marble a) Thermal properties of water from Goranson (1942), b) Thermal properties of water/glycerol mixtures from Bates (1936) c) Thermal properties of Westerly granite from Eppelbaum et al. (2014)

	H_2O^a	60%Glyc ^b	85%Glyc ^b	99%Glyc ^b	WG ^c	CM ^c
κ [W/(m K)]	0.6	0.3807	0.3096	0.2845	3.07	2.08
ρ [kg/m ³]	1000	1151	1219	1255.4	2650	2650
C [J/(kg K)]	4180	3121.6	2678.1	2430	900	525

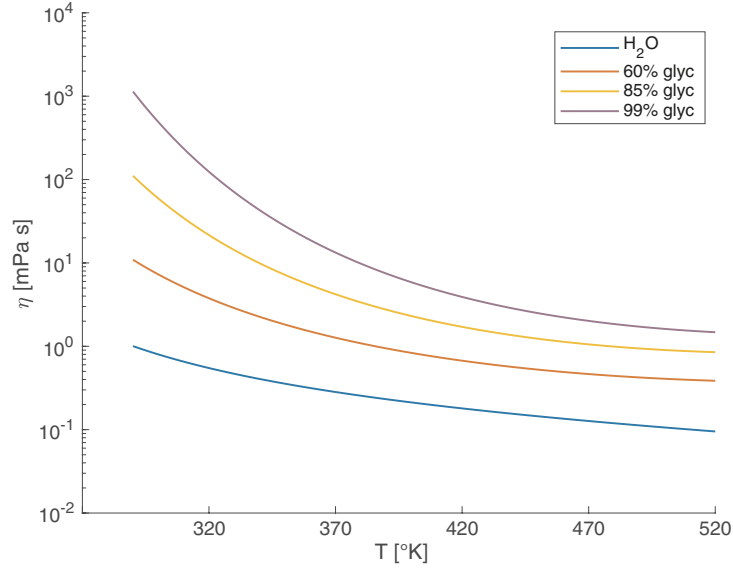


Figure 4.2: Evolution of fluids viscosity (water and glycerol/water mixtures) with temperature according to the empirical law of Cheng (2008).

sliding (Figure 4.2).

4.3.2 LuGre dynamic friction model

The LuGre dynamic friction model was proposed by Canudas de Wit et al. (1995) to describe friction forces as a function of slip-rate in the three lubrication regimes (boundary, mixed and elasto-hydrodynamic lubrication) in presence of viscous fluids. In this model, the behaviour of the asperities and/or the fluid during shearing was assimilated to the behaviour of some bristles whose deflection can be described as:

$$\frac{dz}{dt} = V - \frac{|V|}{g(V)} z \quad (4.7)$$

where z was the deflection of the bristles, V was the slip-rate and at steady state $z_{ss} = g(V)\text{sgn}(z)$. The friction generated from the bending of the bristles was

$$F_0 = Kz + \alpha_1 \frac{dz}{dt} + \alpha_2 V \quad (4.8)$$

where K is the stiffness, α_1 a damping coefficient and α_2 a viscous coefficient.

According to the model, in mixed and hydrodynamic regimes, the friction force for constant slip-rate at steady state was given by:

$$F_{ss} = g(V)\text{sgn}(V) + f(V) \quad (4.9)$$

where $g(V)$ seized Coulomb friction and the Stribeck effect and it was written as $g(V) = F_c + (F_s - F_c) e^{(\frac{V}{V_s})^j}$, where F_s corresponded to the stiction force (i.e., the force necessary to start the motion), and F_c is the Coulomb friction force, i.e., the force necessary to continue sliding in absence of lubricants, V was the slip-rate between the moving solid bodies. The characteristic slip-rate of the Stribeck function V_s determined how quickly $g(V)$ approached F_c and depended on fluid viscosity and loading conditions. As suggested by Li Chun Bo and Pavelescu (1982), the j parameter ranged between 0.5 and 1. Instead, $f(V)$ was the viscous friction (Reynolds, 1886) and typically was given in the form $f(V) = \alpha_2 V$ (Canudas de Wit et al., 1995). In this work, we found $\nu s \propto \sigma_{eff} H^2 / (\eta L)$ and $\alpha_2 \propto \eta L / (\sigma_{eff} H_0^2)$.

4.3.3 Pseudotachylyte-bearing faults (Gole Larghe fault zone in Adamello (Italy) and Bear Creek fault zone in Mount Abbot Quadrangle (USA))

Pseudotachylyte is the result of solidification of friction-induced melts produced during seismic slip. Here we consider two well exposed pseudotachylyte-bearing faults, estimate the coseismic S and compare these natural cases with the experimental results.

Case A: Gole Larghe fault zone (Adamello, Southern Italian Alps)

The normal stress acting on the sub-vertical faults at 10 km depth was estimated range between 112 and 182 MPa (Di Toro and Pennacchioni, 2005; Di Toro et al., 2006) and the dynamic shear stress between 14.9 and 48.1 MPa (Toro et al., 2009). These values yielded a dynamic friction coefficient between 0.4 and 0.08, well below the typical coefficient for tonalites (0.7). The microstructures found in the pseudotachylyte were consistent with temperature during seismic sliding ranging from 1050 to 1450 °C. The chemical composition of the pseudotachylyte matrix was reported in Di Toro and Pennacchioni (2004). Using the viscosity model for magmatic liquid proposed by Giordano et al. (2008), we estimated the pseudotachylyte viscosity during sliding ranging between 4.79 and 389 Pa s. Griffith et al. (2010) measured the 2D roughness of the pseudotachylyte wall rock boundary in two fault profiles. They identified $L = 0.1 - 3$ m, a Hurst exponent ζ ranging between 0.4 and 0.47 and a roughness amplitude factor $B \approx 0.1$. Based on Griffith et al. (2010) measurements, we computed $H = BL^\zeta = 0.034 - 0.168$ m. The above data yielded a value of $S = (1.01 \pm 0.55)10^3$ (Table 4.3)

Case B: Bear Creek fault (Mount Abbot Quadrangle, central Sierra Nevada)

Ague and Brimhall (1988) estimated the initial normal stress acting on the fault ranging between 200 and 400 MPa. Considering a stress drop on the fault between $\Delta\sigma = 90 - 250$ MPa (Griffith et al., 2009) and a initial shear stress of $0.65 - 0.8\sigma_n$, we can estimate a $\tau_{dyn} = (0.6 - 0.85)\sigma_n - \Delta\sigma$. The microstructures found in the pseudotachylyte matrix were consistent with temperatures during seismic slip ranging from 1000 to 1200 °C. The chemical composition of the pseudotachylyte matrix was reported in Griffith et al. (2008). Using the viscosity model for magmatic liquid proposed by Giordano et al. (2008), we estimated the pseudotachylytes

viscosity during sliding between 4.07 and 63.1 Pa s. From the study of Griffith et al. (2010) the wavelength of the pseudotachylite-wall rock boundary ranged between $L = 0.0001 - 0.01$ m, the Hurst exponent $\zeta = 0.4 - 1$, so the asperity size ranged between 0.0003 and 0.001 m. The above data yielded a value of $S = (3.78 \pm 3.34)10^3$ (Table 4.3).

Table 4.3: Parameters used for computing S and μ_{dyn} for natural exhumed faults with pseudo-tachylite.

	σ_n [MPa]	τ_{ss} [MPa]	T [°C]	η [Pa s]	L [m]	H [mm]	V [m/s]	S [$\cdot 10^3$]
Gole Larghe	112-182	14.9-48.1	1050-1450	4.79-389	0.1-3	34-168	1	1.01 ± 0.55
Bear Creek	200-400	10.0-70.0	1000-1200	4.07-63.10	(0.01-1)E2	0.3-1	1	3.78 ± 3.34

4.4 Results

4.4.1 Apparent friction coefficient

The apparent friction coefficient (μ) is the ratio of the shear stress to the effective normal stress. For both rock types, at the beginning of the experiments, the shear stress acting on the fault increased until the static friction coefficient μ_{static} was overcome and slip initiated (Figure 4.3). Immediately after slip initiation, a further increase in μ was observed (indicating slip-strengthening behaviour) until a peak friction μ_{peak} was achieved at $V \approx 1$ mm/s when the target V was higher than 1 mm/s. Subsequently, μ decreased with slip to a minimum and approximately steady-state dynamic friction coefficient (μ_{dyn}) during a transient slip weakening phase over a slip distance (D_c) (Mizoguchi et al., 2007) (Figure 4.3a).

In Figure 4.3b-e, we showed the evolution of the apparent friction coefficient μ versus displacement for four different experiments performed with SHIVA under 10 MPa effective normal stress (σ_{eff}), in presence of different mixtures of distilled water and glycerol in order to have an initial viscosity η_0 increasing of a factor ca. 10, with a fluid pressure $P_f = 2.7$ MPa. The apparent friction coefficient was fitted following the exponential decay function proposed by Mizoguchi et al. (2007) $\mu = \mu_{dyn} + (\mu_{peak} - \mu_{dyn})e^{(\ln(0.05)U/D_c)}$ and allowed us to calculate the weakening distance D_c . In our experiments, the achievement of this so called "steady-state dynamic friction coefficient" condition required slips of several millimetres to tens of centimetres depending on the applied effective normal stress (Di Toro et al., 2010), though steady-state conditions might not ever be achieved in nature (Mizoguchi et al., 2007). Under the same acceleration conditions, the magnitude of the friction drop ($\mu_{peak} - \mu_{dyn}$) increased with V . We studied the dependency of μ_{static} and μ_{peak} with η and S , respectively, for all the experiments (Figure 4.4). Independently of the rock type, μ_{static} slightly decreased from ≈ 0.55 at $\eta_0 = 10.8$ mPa s to ≈ 0.33 at $\eta_0 = 1226$ mPa s (Figure 4.4a). Instead, the μ_{peak} was 0.651 ± 0.222 (highly scattered) over the entire range of S (Figure 4.4b), had no significant correlation with

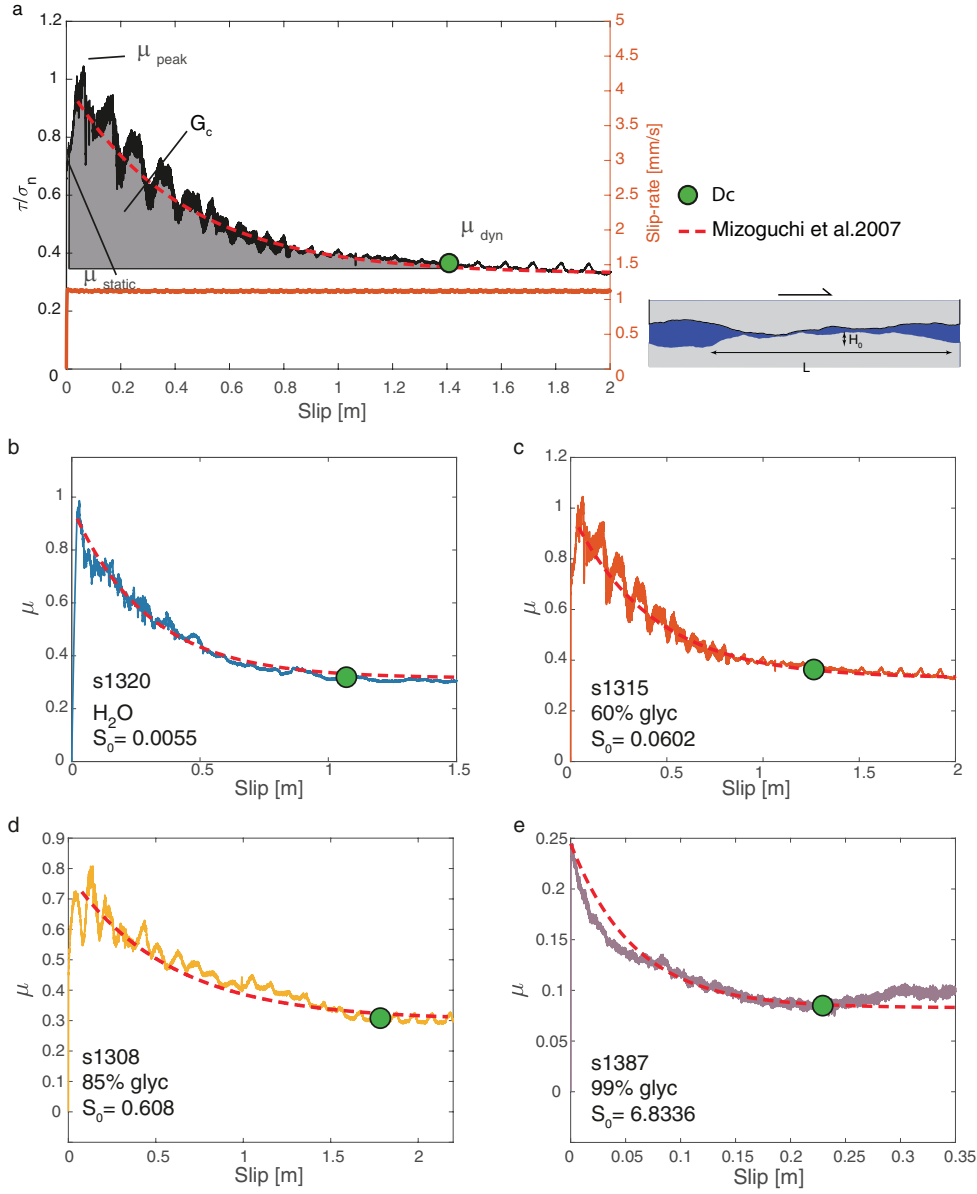


Figure 4.3: Apparent friction coefficient versus slip, friction coefficients versus viscosity, η , and Sommerfeld number $S = 6 V \eta L / (\sigma_{eff} H_0^2)$. Experiments were performed at an acceleration of 6.5 m s^{-2} and effective normal stress σ_{eff} up to 20 MPa. a) Apparent friction coefficient versus slip for experiment S1315 performed at $\sigma_{eff} = 10 \text{ MPa}$ in the presence of mixture 60% glycerol/40% water. μ_{static} , μ_{peak} , μ_{dyn} , W_b and D_C are represented. Apparent friction coefficient vs slip for experiments s1320, s1315, s1308, s1387 performed in presence of b) water, c) mixture 60%glycerol/40%water, d) mixture 85%glycerol/15%water and e) pure glycerol in order to have a η_0 increasing of a factor ~ 10 (i.e. Sommerfeld number S_0 at the target slip rate V increasing of a factor ~ 10).

either V (Figure 4.5a) or η , and its average value was similar to the μ_{peak} obtained under room-humidity conditions (Passelègue et al., 2016b).

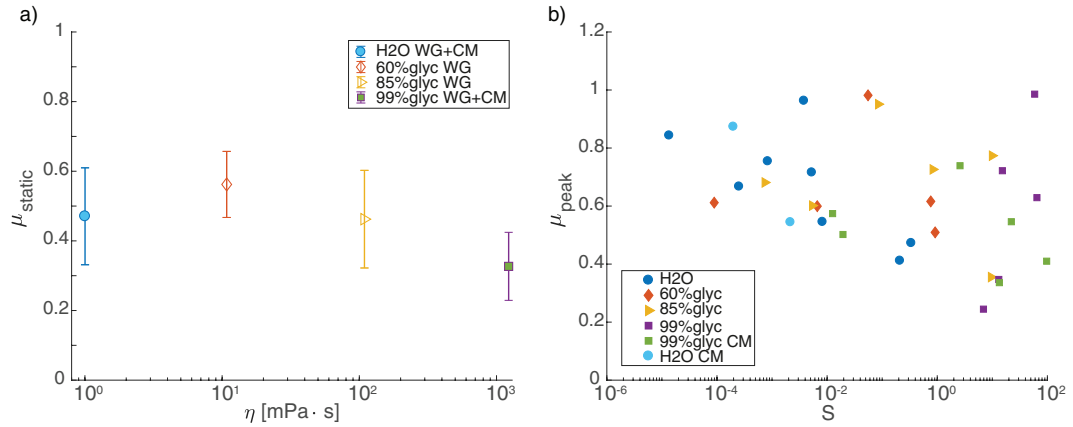


Figure 4.4: a) Static friction coefficient versus viscosity η . In the semi-logarithmic diagram, the static friction coefficient slightly decreases linearly with increasing η (all values are reported in Table 4.1). b) Peak friction coefficients versus Sommerfeld number. Experiments were performed under the following environmental and hydraulic conditions: 100% water (H2O, blue in colour dots), 60% glycerol/40% water (orange diamonds), 85% glycerol/15% water (yellow triangles) and pure glycerol (99% glycerol, purple squares)

4.4.2 Dynamic friction evolution with the Sommerfeld number

The μ_{dyn} varied with S (Figure 4.6): for $S < 10^{-3}$, μ_{dyn} was $\approx 0.70 \pm 0.05$ and nearly independent of S (velocity neutral, or BL regime); at $10^{-3} < S < 1$, μ_{dyn} decayed with S from ≈ 0.7 ($S=10^{-3}$) to ≈ 0.2 ($S=1$) (ML regime); at $S > 1$, μ_{dyn} slightly increased with increasing slip-rate (EHD regime). This "Stribeck-type" behaviour was similar for both water and water/glycerol mixtures but shifted to greater S values for the latter (Figure 4.6a).

Importantly, the behaviour was similar for the two rock types suggesting that the obtained Stribeck curve relates to the composition of the fluid mixtures rather than to the peculiar dynamic weakening mechanism of granite (flash and bulk melting Di Toro et al. (2010)) or Carrara Marble (temperature and grain-size dependent Green et al. (2015)). Note that μ_{dyn} slightly decreased with increasing V as proposed by Di Toro et al. (2010), but was highly scattered (Figure 4.5b).

Following the Stribeck model proposed by Canudas de Wit et al. (1995) and based on the solution on motion at so-called steady state conditions for metallic frictional interfaces, our friction data can be described by:

$$\mu_{dyn} = \mu_c + (\mu_{static} - \mu_c) e^{(-\xi \sqrt{S})} + \zeta S \quad (4.10)$$

where μ_{static} ($= 0.7$) was the Coulomb friction coefficient corresponding to μ_{dyn} under dry conditions (i.e., without fluid lubrication), μ_c ($= 0.1$) was the friction coefficient at the full film lubrication condition ($\sim \mu_{dyn}$ during EHD), and ξ and ζ were empirically determined linear

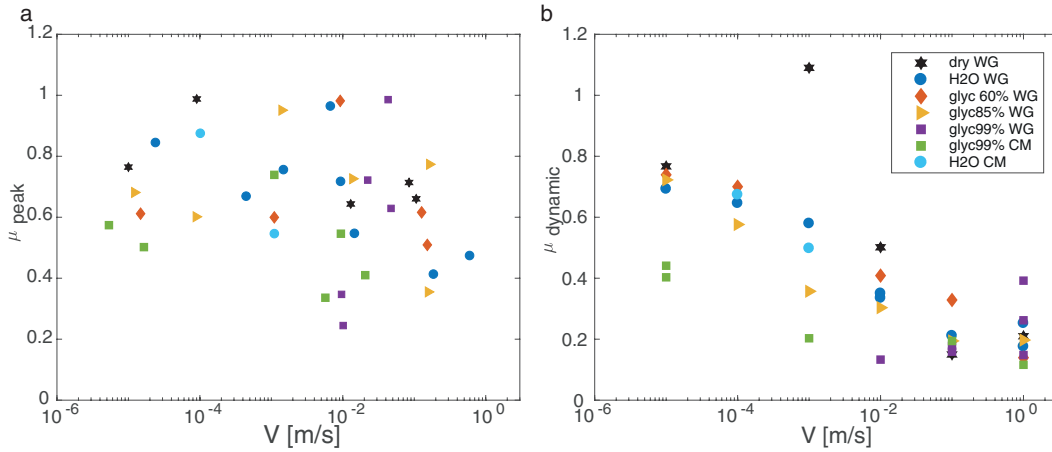


Figure 4.5: The a) μ_{peak} and b) μ_{dyn} vs slip-rate (V) for experiments performed in the presence of fluids and under room humidity conditions (dry, black stars). a) Independently of the initial viscosity of the fluid μ_{peak} did not show a particular dependence with slip-rate with an average value of 0.75 ± 0.14 . b) μ_{dyn} decreased with increasing V , but had a large scatter compared to its dependence with S (compare Figure 4.5 with Figure 4.6).

coefficients. The second and the third right-hand terms of 4.10 depicted, respectively, the Stribeck effect (the decrease in the friction coefficient due to an increase in V) and the viscous friction (the increase in the friction coefficient due to the presence of viscous fluids). We used a linear regression procedure to estimate the coefficients ξ and ζ for the original experimental dataset presented here, plus published experimental and field data (from Eq. 4.10, coefficient of determination $R^2=0.90$, $\xi=8.03$, and $\zeta=0.004$) (Figure 4.6b). In fact, this relation holds for other silicate-bearing rocks (gabbro, peridotite, etc (Violay et al., 2014b; Del Gaudio et al., 2009; Di Toro et al., 2006; Nielsen et al., 2008), complete list of experiment in Annex C), tested at seismic slip conditions, and where frictional melting occurred, highlighting the universality of EHD mechanism when fluids were present in the fault slipping zone (Figure 4.6b).

4.4.3 Microstructural investigation of slipping zones

Microstructural investigation of the slipping zones (Figure 4.8) recovered after the experiments performed on Westerly granite at $V=1$ m/s under room-humidity and water-flooded conditions (corresponding to $S < 1$), showed evidence of frictional melting (Passelègue et al., 2016b). Instead, there was no evidence of frictional melting in the slipping zones recovered from the experiments conducted on 85% and 99% of glycerol where the fully lubricated regime ($S > 1$) was achieved (Figure 4.7). Moreover, for $S > 1$ the roughness of the slip surfaces at the end of the experiments was comparable to the initial roughness (Figure 4.8). In the case of Carrara marble, the slipping zone after the experiments conducted at $V > 0.1$ m/s under either room humidity (Violay et al., 2013) or water-flooded conditions when $S < 1$, was made

of sub-micrometre in size (recrystallized) grains. Instead, there were no slipping zones made of sub-micrometre in size grains after the experiments conducted with 99% glycerol and at high slip-rate where the fully lubricated regime ($S > 1$) was achieved (Figure 4.9). As was the case for the experiments performed on Westerly Granite, the sheared samples had a surface roughness very similar to the initial non-sheared one (Figure 4.9, Figure 4.9c, Figure 4.9d), and roughness of two order of magnitude higher for $S < 1$ (Figure 4.9b). In the experiments performed at high slip-rate the presence of high viscous lubricants prevented the formation of melt and debris on the surfaces of Westerly Granite and Carrara Marble samples. In conclusion, microstructural observation and surface roughness measurements suggested that for $S > 1$ most of the shearing was accommodated within the glycerol-rich fluid, confirming the activation and effectiveness of EHD lubrication.

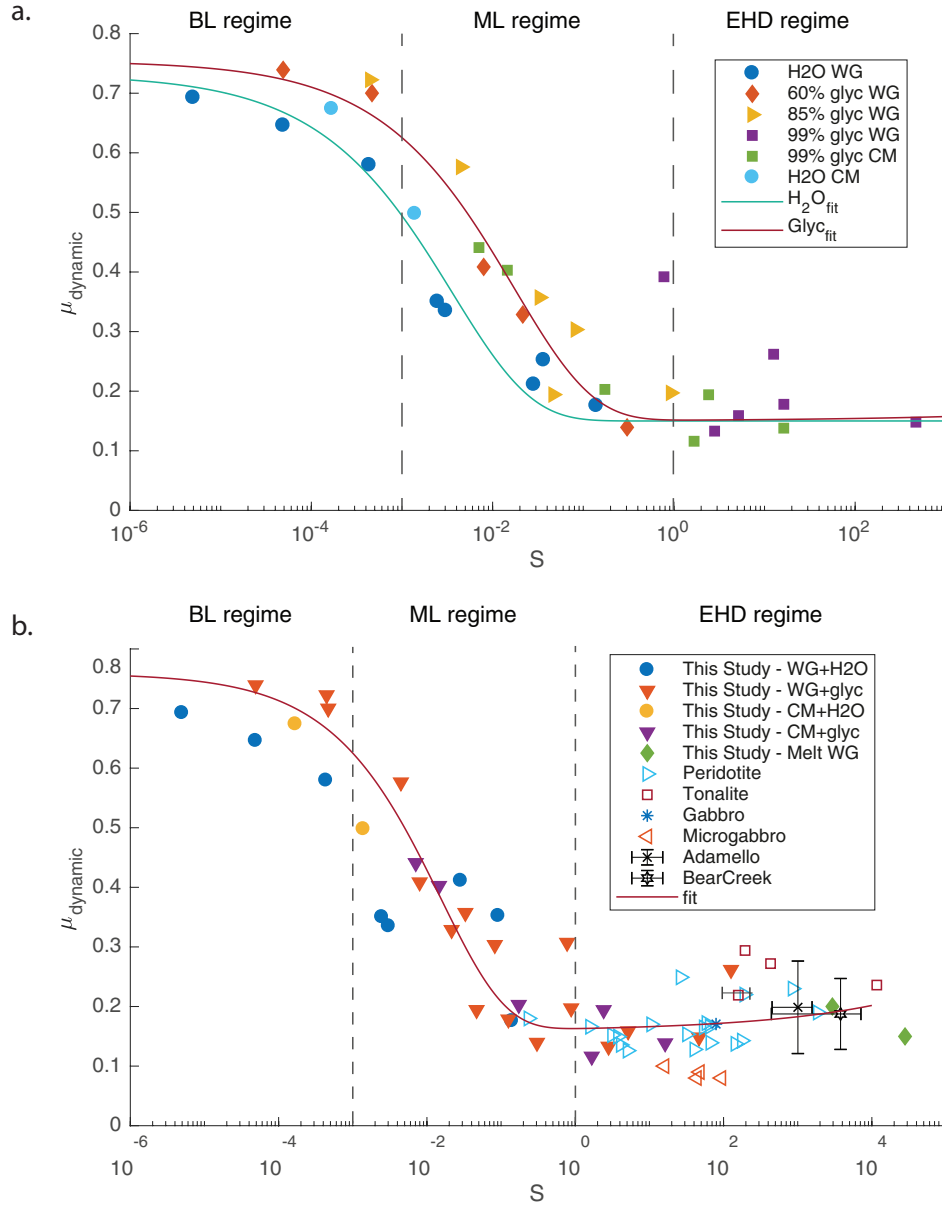


Figure 4.6: Dynamic friction coefficient versus Sommerfeld number S . For $S < 10^{-3}$, the dynamic friction coefficient decreased slightly with S . For $10^{-3} < S < 1$, the dynamic friction coefficient decreased dramatically with S . For $S > 1$, the dynamic friction increased slightly with S . a) Dynamic friction coefficient for experimental results of this study. The best fit curves were obtained using 4.10 and have coefficients of determination $R^2 = 0.95$ and $R^2 = 0.88$ for distilled water and glycerol mixtures, respectively. b) Comparison between experimental results of this study, experimental studies with frictional melting performed on peridotite (Del Gaudio et al., 2009), tonalite (Di Toro et al., 2006), gabbro (Nielsen et al., 2008) and microgabbro (Violay et al., 2014b) and two natural cases with field estimation of S from pseudotachylite-bearing faults (Gole Larghe fault zone in Adamello (Italy) and Bear Creek fault zone in Mount Abbot Quadrangle (USA)).

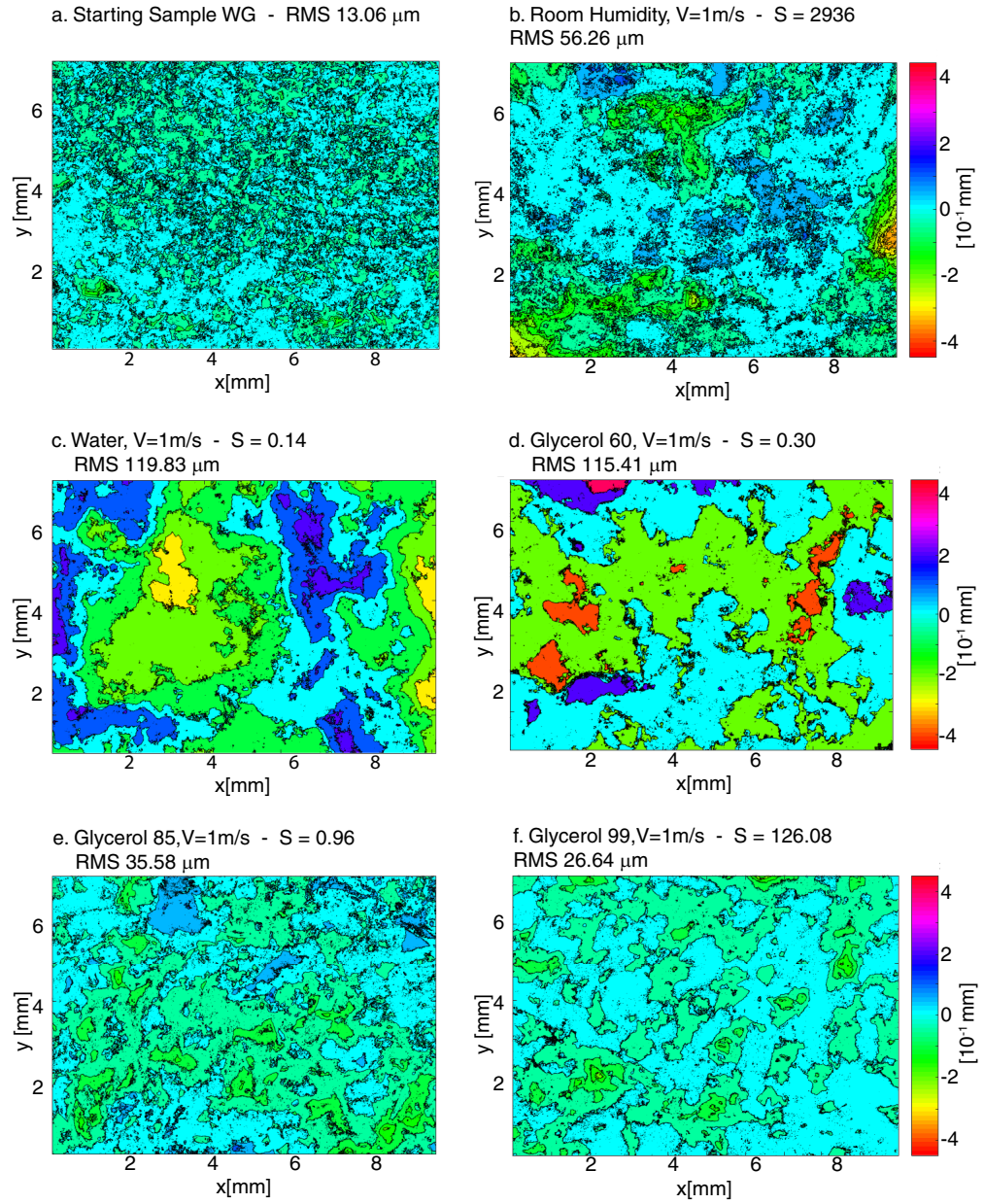


Figure 4.7: Roughness of the sliding surfaces and RMS values in Westerly Granite. a) Starting sample and sheared samples under b) room-humidity conditions (exp s1321), c) water (exp s1303), d) 60%glyc/40%water (exp s1316), e) 85%glyc/15%water (exp s1305), and f. 99%glyc (exp s1389). All the experiments were performed at $V = 1\text{m/s}$



Figure 4.8: Microphotos of the sliding surfaces and RMS values in Westerly Granite. a) Starting sample and sheared samples under b) room-humidity conditions (exp s1321), c) water (exp s1303), d) 60%glyc/40%water (exp s1316), e) 85%glyc/15%water (exp s1305), and f. 99%glyc (exp s1389). All the experiments were performed at $V = 1\text{m/s}$.

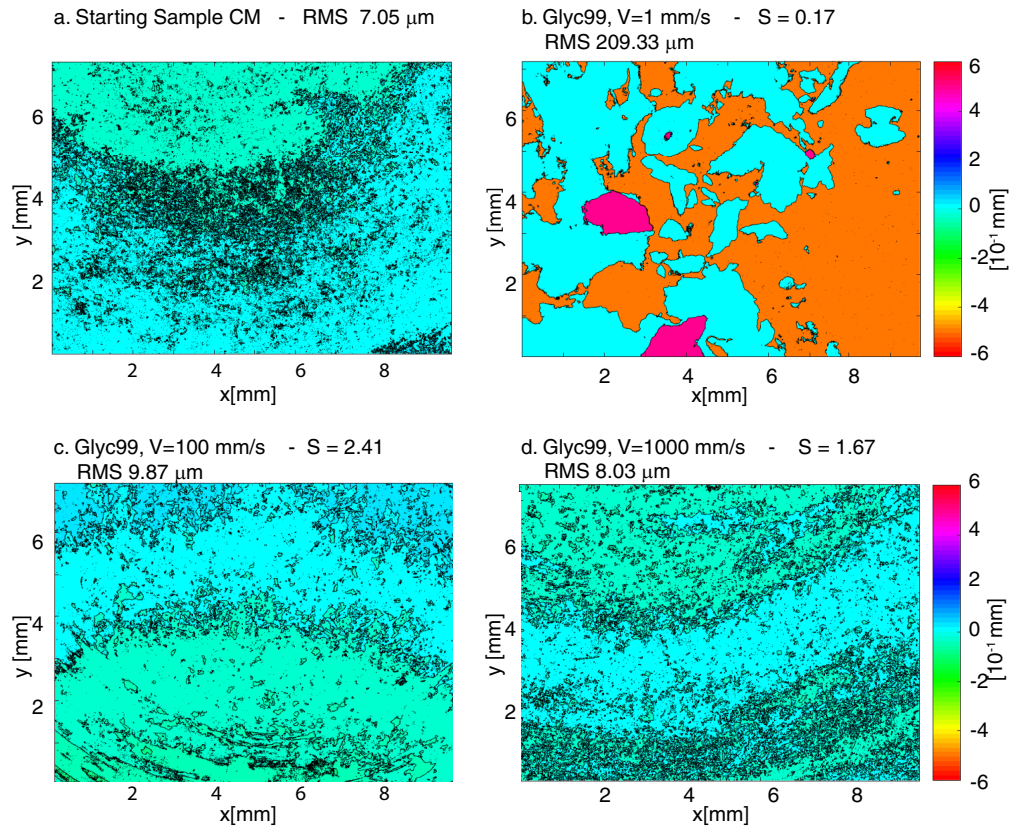


Figure 4.9: Roughness of the sliding surfaces and RMS values in Carrara Marble. a) Starting sample, and samples immersed in 99%glyc sheared at b) $V = 1$ mm/s (exp s1608), c) $V = 100$ mm/s (exp s1607), d) $V = 1000$ mm/s (exp s1606)

4.5 Discussion

4.5.1 Rupture propagation criteria

We now briefly discuss to what degree the lubrication processes measured here may promote rupture propagation and earthquake slip in a faulting scenario. Increasing S reduced the dynamic friction coefficient μ_{dyn} (Figure 4.6); however, this will come at the cost of increasing the breakdown work (G_c), at least in the BL and ML regimes ($S < 1$) (Figure 4.10). Indeed, G_c increased exponentially with S in BL and ML regime, i.e. $S < 1$ up to 9 MJ m^{-2} . Instead, at the boundary between the ML and the EHD regimes, G_c dropped sharply back to values of $\sim 1 \text{ MJ m}^{-2}$, evidencing the transition between ML and EHD regimes. Therefore, lubrication affected two competing mechanisms and did not necessarily promote dynamic earthquake rupture propagation. To illustrate this, we derived a simplified rupture propagation criterion. The energy change dW [J/m] for an advancement dL of a crack of length L (if homogeneous conditions were assumed and radiated energy was neglected, which was a realistic assumption for the early phase of nucleation with slow rupture velocity) was written as:

$$dW = -dLG_c + \frac{1}{2}\Delta\tau L dU \quad (4.11)$$

where $dU = C\Delta\tau/\mu' dL$ was the slip increment, μ' shear stiffness, $\Delta\tau$ the stress drop, and G_c the breakdown work. Therefore, the energy delivery rate, in a simplified form, was:

$$\frac{dW}{dL} = -G_c + \frac{1}{2}C \frac{\Delta\tau^2}{\mu'} L \quad (4.12)$$

with C a geometrical dimensionless constant.

For the crack to propagate the requirement was that $dW/dL \geq 0$, therefore

$$\frac{1}{2}C \frac{(\Delta\tau^2)}{\mu'} L \geq G_c \quad (4.13)$$

Substituting L with U by using $L = \mu'/(C\Delta\tau)U$ we obtained $1/2\Delta\tau U \geq CG_c$ where the stress drop was $\Delta\tau = \tau_0 - \tau_{dyn}$. Therefore we obtained:

$$\frac{1}{2}(\tau_0 - \tau_{dyn})U \geq G_c \quad (4.14)$$

where τ_0 was the initial shear stress on the fault (whose upper bound was $\tau_{static} = \mu_{static}\sigma_{eff}$), $\tau_{dyn} = \mu_{dyn}\sigma_{eff}$, and where the S dependence of $\tau_{dyn}(S)$ and $G_c(S)$ was made explicit. As seen in the left-hand term, the effectiveness of lubrication increased with the amount of fault slip U . A large value of G_c may prevent the dynamic propagation of smaller earthquakes, but as U increased the lubrication effect will become dominant. Because breakdown work will

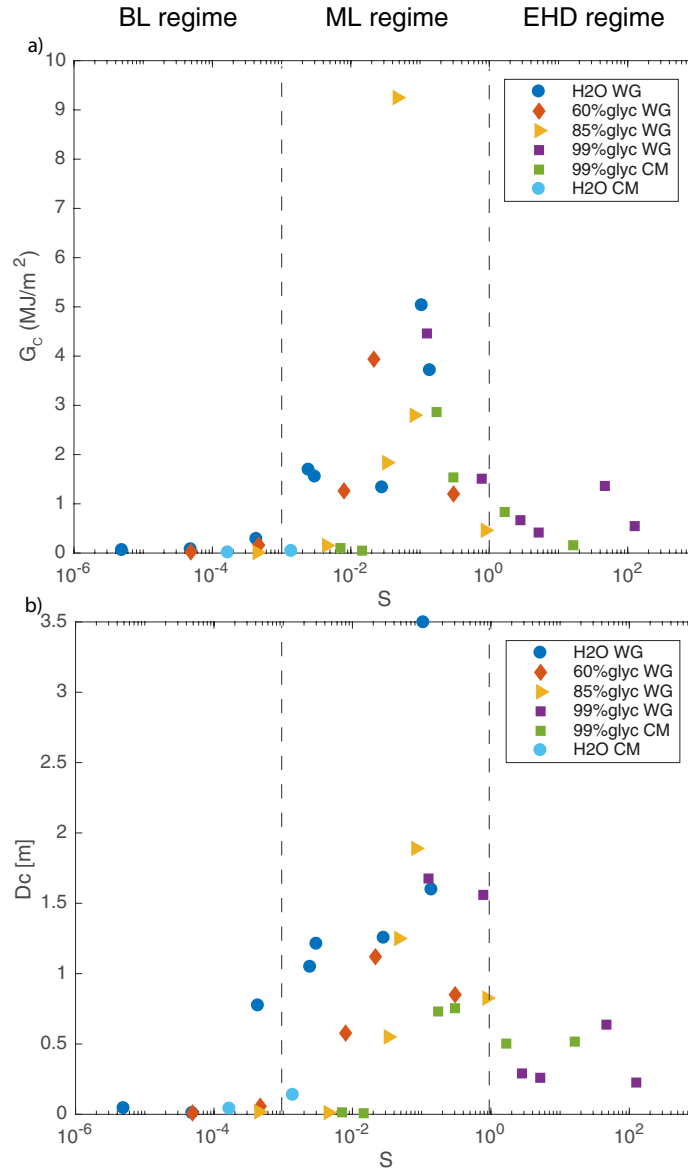


Figure 4.10: Breakdown work and D_c versus Sommerfeld number. The three lubrication regimes (BL, ML and EHD) are delimited by vertical black dashed lines. Experiments were performed at acceleration of 6.5 m s^{-2} , effective normal stress σ_{eff} up to 20 MPa in the presence of water, mixtures of glycerol and water and pure glycerol (see symbols in the figure where WG is Westerly Granite and CM is Carrara Marble a) Breakdown work vs Sommerfeld number. b) Slip weakening distance D_c vs Sommerfeld number

remain constant after the critical slip distance $U = D_c$ (Figure 4.3a), but the left-hand side of 4.14 will continue to increase with slip, the indicative value $U \approx D_c$ will mark the watershed between rupture-hindering and rupture-promotion by lubrication under intermediate S values. Note that when $S > 1$, both G_c and μ_{dyn} were small, favouring earthquake propagation.

4.5.2 Extrapolation to crustal earthquakes

Here below, we now discuss the scaling of our experimental observations to crustal earthquakes by estimating the values of the parameters ($\eta, V, \sigma_{eff}, L/H_0$) which control S in nature. Water is widespread in the Earth's crust (Lachenbruch and Sass, 1980; Sibson, 1973; Rice, 2006; Hickman et al., 1995). Considering the dependence of viscosity of water with temperature and pressure Huber et al. (2009), we first estimated the decrease of viscosity from the surface to 10 km depth in the Earth's crust. We considered a surface temperature of 293.15 K, a temperature gradient of 30 K/km and a linear increase of pressure σ_{eff} with depth.

Slip-rate during earthquakes was on average ~ 1 m/s (Heaton, 1990). The L parameter in S under EHD conditions, corresponded to the longest (and dominant) wavelength in the mismatch between two rough sliding surfaces. In natural faults, L corresponded to the asperity wavelength, the longest of which was proportional to slip (Brodsky and Kanamori, 2001) (and the magnitude) during a given earthquake. For earthquakes of magnitude ranging between 1 and 8, the average seismic slip and thus $L=1$ mm - 4 m (Sibson, 1989). Natural faults' surface roughness was almost self-similar (Brodsky et al., 2016) with a ratio $L/H_0 \sim 1000$: H_0 was ranging between 0.001 mm to 4 mm for a M1 earthquake and M8 earthquake respectively.

The lithostatic stress $\sigma_1 = \rho_r g z$ (with $\rho_r = 2700$ kg/m³ rock density, z depth and g gravity) minus the hydrostatic water pressure (with $\rho_w = 1000$ kg/m³) at the earthquake hypocentral depth yielded as an indicative value of $\sigma_{eff} = (\rho_r - \rho_w) g z / K$, with $K = (1 + \sin(\varphi)) / (1 - \sin(\varphi))$, friction angle $\varphi = \tan^{-1}(\mu)$, $\mu = 0.75$, acting on the fault; this resulted in σ_{eff} ranging from ~ 50 MPa (at $z=3$ km) to ~ 170 MPa (at $z=10$ km).

The above parameters ($V = 1$ m/s, $L=1$ mm-4 m, $H_0 \sim 0.001$ -4 mm, $\sigma_{eff} \leq 170$ MPa, $\eta(P, T)$ of the water) resulted in S ranging from $5 \cdot 10^{-3}$ to 10^{-6} at $z = 10$ km for Mw=1 to Mw=8 and from 70 to 0.07 at $z \sim 0$ km for Mw=1 to Mw=8 (Figure 4.11).

According to the modeled dependence of S with depth, in the presence of water, EHD lubrication may occur for small in magnitude earthquakes and in shallow fault sections, consistently with the data reported in Figure 4.6. However, fluids percolating natural faults can have various origin. Viscous fluids may be produced by frictional melting during seismic slip (Di Toro et al., 2011); a minimum value of 10 Pa s has been estimated (Nielsen et al., 2008) for frictional melt viscosity. Moreover, especially in the shallower section (< 5 km) of the seismogenic continental faults, fine grain gouge material mixed with water may also act as lubricant whose viscosity depends on the gouge grain size and the solid volume fraction. Viscosities of ~ 10 Pa s have been estimated for such fluid-saturated gouges (Major and Pierson, 1992; Brodsky et al., 2009; Rowe et al., 2012). Moreover, fluids commonly used in hydraulic fracturing operations in engineering reservoirs had viscosities ranging between 1 mPa s and 1 Pa s. As a result, the viscosity of fluids in the upper crust was estimated to range from 0.1 mPa s to more than 10 Pa s.

The presence of more viscous fluids (industrial fluids, friction melts) should extend the activa-

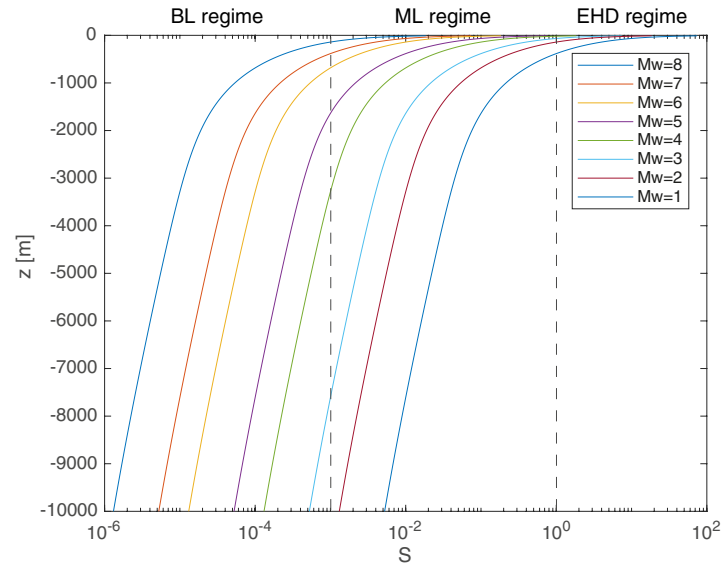


Figure 4.11: Sommerfeld number Vs depth for earthquakes magnitude ranging between 1 and 8.

tion of EHD lubrication to deeper levels in the crust. (Figure 4.12).

This natural S range was comparable to the S values obtained in our experiments, implying that BL, ML and EHD regimes can occur in the Earth's crust, depending on fluid viscosity, slip-rate and earthquake nucleation depth (Figure 4.12). Indeed, while the Sommerfeld number remained undetermined in most natural faults, few of well-exposed seismogenic fault zones (Gole Larghe and Bear Creek fault zones, Table 4.3) where the occurrence of co-seismic fluids was attested by the presence of pseudotachylytes (solidified friction melts produced during seismic slip) supported the trend indicated by our laboratory tests (Figure 4.6). This geological evidence suggested that EHD operated in our experiments but also in natural earthquakes.

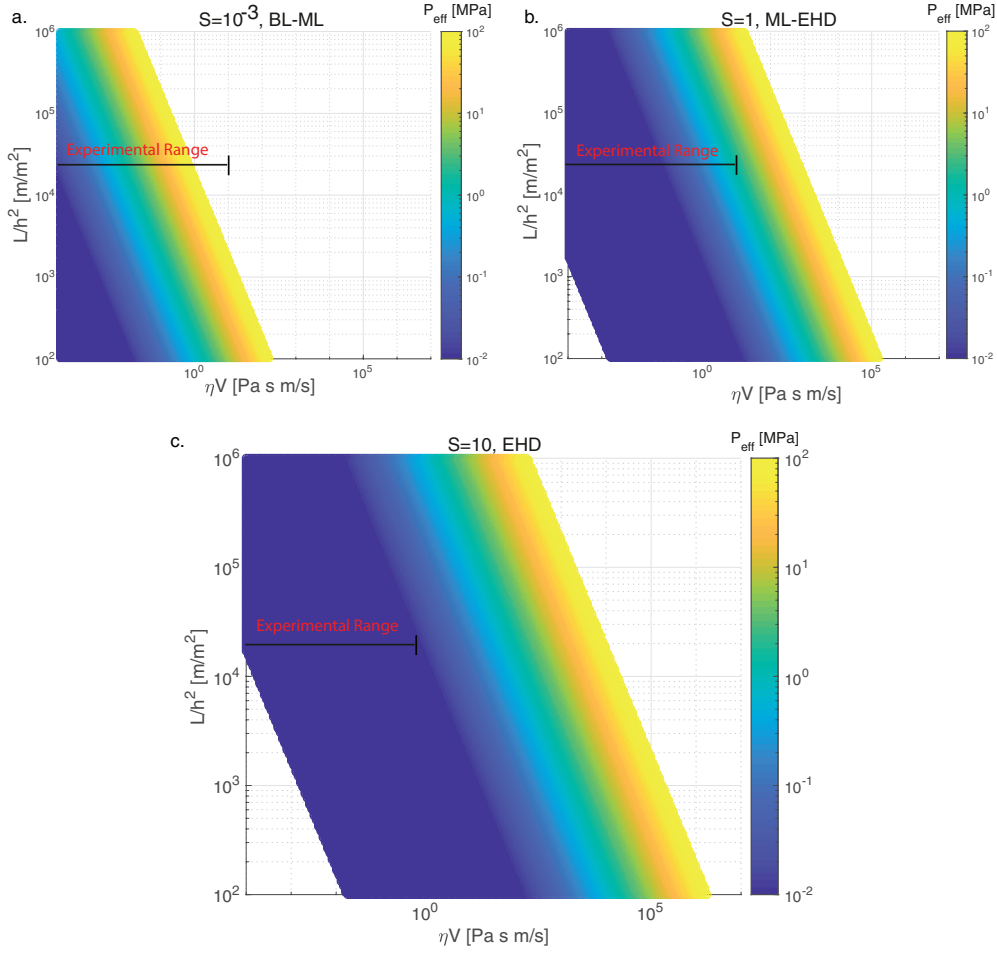


Figure 4.12: Range of values of η, V, L, H for which a) $S=0.001$, limit between boundary lubrication regime and mixed lubricated regime; b) $S=1$, limit between mixed lubrication regime and fully lubricated regime; c) $S=10$, fully lubricated regime.

4.6 Conclusions

We have experimentally demonstrated that fluid pressure and η are critical parameters that control slip dynamics in experimental faults and we suggest that similar effects should be expected in the case of both human-induced and natural earthquakes. In particular, highly viscous fluids (1) slightly reduce the static friction coefficient fostering fault reactivation and, (2) trigger EHD lubrication during seismic slip. However, for a large range of possible viscosity values of fault-permeating fluids, typical seismic slip-rates would result in intermediate values of the Sommerfeld number ($10^{-3} < S < 1$) and relatively large D_c values. As a consequence the fracture energy during seismic propagation of small events ($U < D_c$) is relatively large, inhibiting seismic rupture propagation in favour of slow strain energy relaxation by stable creep (S and D_c would both decrease at low slip-rate). In contrast, the presence of increasingly

viscous fluids decreases the fracture energy dissipated for large events, making the fault weaker and facilitating seismic rupture propagation. Therefore in the presence of highly viscous fluids, rupture is expected to grow quasi-statically on the fault until the slip of the order of tens of cm is attained (until D_c), which indicatively sets the transition from quasi-static nucleation to seismic rupture at lengths of a few hundred meters to a few kilometres. While the effect of fluid pressure in earthquake rupture has been previously explored mostly in terms of thermal pressurization and effective stress, we argue that the role of fluid viscosity is also important in understanding the dynamics of a lubricated fault system, with implications for rupture energy budget and seismic hazard potential of both natural and human-induced earthquakes.

5 Parametric analysis of the elastohydrodynamic lubrication efficiency on induced seismicity

Authors: Chiara Cornelio¹, Marie Violay¹.

¹ Laboratory of Experimental Rock Mechanics (LEMR), ENAC, EPFL, Switzerland;

Reference: Chiara Cornelio, Marie Violay, Parametric analysis of the elastohydrodynamic lubrication efficiency on induced seismicity, *Geophysical Journal International*, , ggaa180, <https://doi.org/10.1093/gji/ggaa180>

Contributions: Original idea was from C. Cornelio and M. Violay. C. Cornelio performed the literature review and the analysis of the induced seismicity cases. C. Cornelio and M. Violay co-wrote the manuscript.

Highlights:

- The viscosity of injected fluid influenced the weakening mechanism activated during earthquake propagation and the dynamic strength of the fault defined by the dimensionless Sommerfeld number S .
- Remarkably, the eight induced seismicity cases follow the decay of the dynamic friction coefficient as a function of the dimensionless Sommerfeld number as predicted by theory and demonstrated experimentally in Chapter 2 and 3, suggesting that elastohydrodynamic is an efficient fault weakening mechanism during earthquake propagation.

5.1 Abstract

During reservoir stimulations, the injection of fluids with variable viscosities can trigger seismicity. Several fault lubrication mechanisms have been invoked to explain the dynamic stress drop occurring during those seismic events. Here, we perform a parametric analysis of the elastohydrodynamic fault lubrication mechanism to assess its efficiency during fluid-induced earthquakes. The efficiency of the mechanism is measured with the dimensionless Sommerfeld number S . Accordingly, we analyzed eight well-documented cases of induced seismicity associated with the injection of fluids whose viscosities range from 1 mPas (water) to 100 mPas (proppant). We collected information related to the in situ stress field, fault orientation and geometry, moment of magnitude and static stress drop of the events. These parameters allow us to analyze the variation in the Sommerfeld number. Our results show that the estimated dynamic friction on the fault during the event is compatible with the fault weakening predicted by the elastohydrodynamic lubrication theory, particularly for highly viscous fluids.

5.2 Introduction

In the last 30 years, the increase in human-induced earthquakes associated with wastewater disposal, gas storage or geothermal exploitation (Ellsworth, 2013; Zoback and Kohli, 2019) has become an important scientific and social issue (Grigoli et al., 2017; Suckale, 2009). The seismicity induced by fluid injection was first shown by Evans (1966) and Healy et al. (1968) for the earthquakes occurring after the beginning of injection of waste fluids near to Denver, Colorado. Later, Raleigh et al. (1976) conducted the first water injection field experiment at high pressure in the Rangely Oil Field, Colorado. It has also been demonstrated that the volume and rate of fluid injection (McGarr et al., 2014; Weingarten et al., 2015) control the fluid pressure increase (Hsieh and Bredehoeft, 1981) and determine the number and magnitude of the events.

However, fluid overpressure is not the only parameter governing fault reactivation and the associated seismicity (Noël et al., 2019). Recent studies have demonstrated that the thermal properties of fluids (i.e., compressibility, latent heat, and thermal diffusivity) and physical properties (i.e., density and viscosity) can influence the rock-fluid interactions (Acosta et al., 2018) and, in general, the fault strength. In particular, Cornelio et al. (2019, 2020) have recently shown that high fluid viscosity might also play a role in decreasing the dynamic fault strength and, consequently, promoting the propagation of earthquakes. They experimentally showed that the onset of reactivation is independent of the on-fault fluid viscosity (i.e., the static friction coefficient is not a function of the viscosity) and the possible activation of the elastohydrodynamic lubrication (EHD) mechanism on the fault during seismic slip.

Chapter 5. Parametric analysis of the elastohydrodynamic lubrication efficiency on induced seismicity

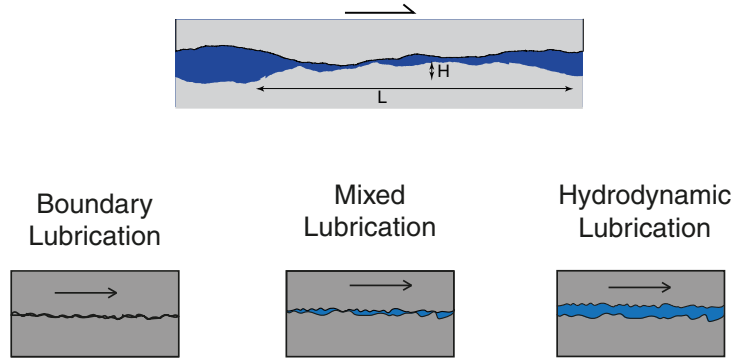


Figure 5.1: Schematic representation of the asperity contacts in the three different regimes. In the boundary lubrication regime, the load is supported by the asperity, and the fluid has no influence on the slip propagation. In the mixed lubrication regime, the load is partially supported by the asperity and partially supported by the film fluid present between the two sliding surfaces. In hydrodynamic lubrication, all the stress is supported by the fluid film, which completely controls the behavior of the slipping surface.

Within the EHD theory, the state of the sliding surfaces can be distinguished in three different lubrication regimes as a function of the dimensionless Sommerfeld number S , defined as $S = 6\eta VL / (P_{eff} H^2)$, where η is the fluid viscosity at the mean estimated surface temperature under steady state, V is the slip rate, P_{eff} is the effective normal stress, L is the characteristic slip length, and H is the initial average asperity height (Figure 5.1). In particular, for almost planar surfaces with asperities that are intermediately in contact during co-seismic sliding, the average asperity height H is of the same order of the average fluid film thickness Brodsky and Kanamori (2001).

Faults under i) a boundary lubrication regime (BL) occur when $S < 10^{-3}$ and the normal stress is supported by the solid–solid contacts and when the dynamic friction coefficient is close to static friction coefficient; faults under ii) a fully lubricated regime (EHD) occur when $S > 1$ and the normal stress is supported by the interstitial fluid; and faults under iii) a mixed lubrication regime (ML) occur when $10^{-3} < S < 1$ and the normal stress is partially supported both by the solid–solid contacts and partially supported by the (criteria of lubrications regimes are derived from experimental studies, see Cornelio et al. 2019). In both cases ii) and iii), the dynamic friction coefficient is strongly reduced compared to the static friction coefficient. Cornelio et al. (2019) also showed that the EHD mechanism is independent of the rock lithology.

Here, we analyze the possible ranges of the five parameters (η, V, L, P_{eff}, H^2) that define the Sommerfeld numbers S for natural earthquakes, and we compare them with the estimated values of the same five parameters for eight cases of induced seismicity associated with the injection of different viscous fluids (water, brine, wastewater and proppant). We aimed to understand whether the EHD can be an efficient lubrication mechanism involved in induced earthquakes propagation.

5.3 S parameters for induced seismicity

We will now discuss the possible range in values of the five parameters (η, V, L, P_{eff}, H^2), which define the S number for natural earthquakes. In particular, we will determine the minimum and maximum values of I) the fault geometrical parameters (L/H^2), II) the fluid viscosity (η), III) the effective normal stress (P_{eff}) and IV) the coseismic slip rate (V) during earthquake propagation.

- I. L/H^2 : H (m) is the average fault asperity height, and L (m) is the characteristic dimension of pressure change, i.e. the length over which the pressure of the film changes significantly compared to the average pressure on the fault interface. L is proportional to the wavelength of the surface roughness (Brodsky and Kanamori, 2001). The most favorable scenario for the activation of elastohydrodynamic lubrication (maximum value for S) results from the largest possible L , i.e., maximum wavelength of the surface roughness that correspond to the finite slip of the event (Brodsky and Kanamori, 2001). Moreover, the roughness of naturally exposed faults follows a power law function of wavelength $H = BL^\zeta$, with B being a constant prefactor ranging between 10^{-3} and 0.1 for naturally exposed faults (Brodsky et al., 2011). Surfaces described by the power law scaling with $\zeta = 1$ are defined as self-similar, while those with $\zeta \neq 1$ are known as being self-affine. ζ of the natural fault is between 0.6 and 1 (Brodsky et al., 2016) and references herein). Therefore, the H/L ratio for natural faults ranges between 0.001 and 0.01 . Considering that earthquake slip can vary from a few millimeters ($L \sim 0.001$ m) to several meters ($L \sim 10$ m), L/H^2 ranges from $\sim 10^3$ m/m² to $\sim 10^9$ m/m².
- II η : Fluids with variable compositions and viscosities (gas, water, brine, hydrocarbon seepage, wet gouge and frictional melt) are widespread within active tectonic faults. For instance, water viscosity ranges from ~ 1 mPas at subsurface conditions (~ 1 km depth) to ~ 0.1 mPas at a depth of 10 km (considering $\eta(T, P_f)$, a thermal gradient of 30 °Ckm⁻¹ and a linear increase in P_f with depth (Eppelbaum et al., 2014)). Alternatively, faults can be filled by the viscous melt produced by frictional heating during earthquake coseismic slip, with a minimum viscosity of 1 kPas (Giordano et al., 2008). Faults can contain gouge material, which can behave as a fluid with a viscosity that depends on the gouge grain size and the solid volume fraction (Otsuki et al., 2003) but generally is approximately ~ 10 Pas. Fluids commonly used in hydraulic fracturing operations in engineering reservoirs have viscosities ranging between 1 mPas and 1 Pas (Economides and Boney, 2000). Moreover, the fluid viscosity varies with in situ temperature and pressure.
- III P_{eff} : the normal effective stress applied to the fault. The field stress applied on the fault plane can be described as a function of the effective principle stresses σ'_1 and σ'_3 , with

$\sigma'_1 > \sigma'_3$. If we can consider a linear increase in pressure with depth, the effective normal stress can be written as $P_{eff} = (\sigma'_1 + \sigma'_3)/2 + (\sigma'_1 - \sigma'_3)/2 \cos(2\theta)$ with θ is the angle of the fault plane with the horizontal stress. Assuming Coulomb friction law, it can be shown that for an optimally oriented fault plane $\theta = \pi/4 + \phi/2$ (Allmendinger et al., 2011). The principal stresses $\sigma'_1 = \max\{\sigma'_i, \sigma'_j\}$, $\sigma'_3 = \min\{\sigma'_i, \sigma'_j\}$, where $\sigma'_i = \rho_r gz - \rho_f gz$ and $\sigma'_j = K\sigma'_i$ ρ_r is the rock density and is 2700 kg m^{-3} , ρ_f is the water density and is $1/3 \rho_r$, $g = 9.81 \text{ m s}^{-2}$, z is the depth in m. The ratio between the principal stresses K , is ~ 0.6 for the normal fault (lower K boundary value) and it is ~ 2.3 (Zoback, 2007b) for the reverse fault (upper K boundary value), $\phi = \tan^{(-1)}\mu$, and μ is the friction coefficient according to the Byerlee frictional law and is 0.75 (Byerlee, 1978). Therefore, the effective pressure acting on a fault between 0 and 10 km depth ranges between 0 and 100 MPa.

- IV V : co-seismic slip-rates. Usually, the average coseismic slip rate is on the order of 1 m/s (Heaton, 1990; Sibson, 1986), but more generally, Rowe and Griffith (2015) showed that slip rates V between 10^{-4} m/s and 10 m/s are peculiar to earthquakes. Note, we only consider the weakening mechanism activated during coseismic phase of an earthquake.

5.4 Case studies of induced seismicity

We determined the same parameters (L/H^2 , η , P_{eff} , and V) for eight well-documented human-induced earthquakes, which were caused by fluid injection during reservoir stimulation in various rock formations. These human-induced earthquakes were selected because they were associated with the reactivation of a pre-existing fault that occurred very close to the fluid injection borehole and because the movement between the two fault surfaces was almost planar.

- 1 L/H^2 . The fault geometrical parameter L/H^2 has been estimated based on the seismic moment of magnitude (M_0) and the static stress drops ($\Delta\tau$) recorded during the events. Moreover, we assumed L equals the finite slip during the events δ as it is the largest possible value of L . For all events, we considered a circular rupture, so the fault surface ruptured area (A) can be calculated as $A = \pi r^2$ and $\Delta\tau = 7/16 M_0 / r^3$ (Abercrombie and Rice, 2005) with r as the characteristic fault geometry. The slip $\delta (= L)$ is proportional to the moment of magnitude and rupture area.

$$\delta = \frac{M_0}{GA} \quad (5.1)$$

where G is the shear modulus ($\sim 30 \text{ GPa}$ typical for the upper crustal rocks, (McGarr et al., 2014)). Therefore,

$$L = \frac{M_0}{G\pi(7/16 M_0 / \Delta\tau)^{2/3}} \quad (5.2)$$

where L is proportional to $M_0^{1/3}$. Finally, using the relation between the slip δ and the geometry of the fault proposed by Brodsky et al. (2016, 2011), it is possible to estimate the asperity height H and the wavelength L for each case study

$$H = B L^\zeta \quad (5.3)$$

with $\zeta = 0.6-1$.

- 2 η . The human-induced seismicity is usually associated with the injection of water ($\eta \sim 1$ mPas), brine ($\eta \sim 3-5$ mPas), wastewater ($\eta \sim 3-50$ mPas) and a mixture of water and proppant ($\eta \sim 100-200$ mPas) in many lithologies. The viscosity of the fluids was chosen considering the description of the injected fluid and the uncertainty in the η value was included in the error for the estimation of S . With the exception of the Basel and Bowland Shale site (see the sections on each dedicated case), the injection procedure for all studied cases involved long-term low-pressure injections to minimize the associated seismicity. Therefore, we can consider that the viscous fluid had time to diffuse and flow throughout the whole rupture area of the fault surface. Moreover, the proppant is usually mixed with fluid and injected at high pressure and flow rate. This mixture is highly non Newtonian (Novotny, 1977), and can be considered as a fluid until the pressure injection is high (Holditch et al., 1988). After the injection, the fluid component of the initial mixture is dissipated into the rock matrix, while the proppant solid particles remain in the fracture to keep them open. Because, most of the seismic events analyzed here, happened during injection or just after, we consider the fluid-proppant mixture as a fluid and not a solid. For each studied case, due to a lack of information about the precise fluid composition and fluid properties, we neglected the decrease in viscosity with increasing temperature at depth and with shear heating.
- 3 P_{eff} . To compute the effective normal stress for each studied case, we used the field stress measured near the fault that triggered the earthquake and the fault orientation. The field stresses are usually given in terms of overburden stress (S_v), maximum ($S_{H,max}$) and minimum ($S_{h,min}$) horizontal stresses and fault orientation. For all case studies, we reported the principal stresses (total σ_1 and σ_3 and effective σ'_1 and σ'_3) (Allmendinger et al., 2011a) as well as the fault Byerlee rupture criterion ($\mu = 0.6$ and $\mu = 0.85$) (Byerlee, 1978) in Mohr's circles for a three-dimensional stress state (Figure 5.2). We distinguished between the total stress state (gray circles in (Figure 5.2)) and the effective stress state (blue circles in (Figure 5.2)) using the fluid pressure P_f measured at the wellbore before the beginning of the injection procedures. Shear stress τ and effective normal stress acting on the fault plane σ'_n (green points on (Figure 5.2)) are derived from the projection of the fault plane (strike and dip angle) in the principal effective stress space, while the total normal stress σ_n is obtained with the projection of the fault plane in the principal

total stress space. The reported failure rupture criteria in (Figure 5.2) are derived from Byerlee's rule, and they are only valid for the faults and not for the rock mass.

- 4 Slip-rate V . Due to lack of information and technical difficulties in assessing the slip rate during earthquake propagation, we either fixed $V = 1$ m/s or let V be unknown in our problem, and we studied its variation in the three lubrication regimes defined by the Sommerfeld number S . This was done only for the earthquake propagation phase, and it is not valid for the initiation of the rupture.

5.5 Case studies

ML=3.4 Basel, Switzerland

The Deep Heat Mining Project (DHM), close the city of Basel in Switzerland, was initiated in 2006 to develop an enhanced geothermal system (EGS) in the granite basement. The largest event ML=3.4 occurred on 8 December 2006 at a depth of 3-4 km (Deichmann and Giardini, 2009) after six days of water injection ($\eta = 1$ mPa·s). The orientation of the principal stress was deduced from the acoustic borehole imager log in the crystalline basement section. $S_{h,min}$ (the minimum horizontal stress) was oriented along an azimuth of $54^\circ \pm 14^\circ$, and the azimuth of $S_{H,max}$ was $144^\circ \pm 14^\circ$ (Valley and Evans, 2019). The optimal angle between $S_{H,max}$ and the fault strike was between 22° and 30° , respectively (Häring et al., 2008). The estimations of $S_{H,max}$ and $S_{h,min}$ were 160 MPa and 74 MPa, respectively (Häring et al., 2008). The fluid pressure P_f was estimated to be approximately 9.8 MPa (Goertz-Allmann et al., 2011). We estimated an effective normal stress of 88.45 ± 5.37 MPa acting on the fault (Figure 5.2a). The radius of the rupture area was approximately 101 m, and the seismic moment of the main event was $1.60 \cdot 10^{14}$ N·m (McGarr et al., 2014). Following 5.2 and 5.3 the coseismic slip of the event is estimated to be 0.156 m, and the asperity height is $H=0.16-0.45$ mm. The geometry parameters are $L/H^2 = (3.58 \pm 1.41) \cdot 10^6$ m/m².

Mw 4.3 Paradox Basin, Colorado, USA.

Since 1991, the Paradox Valley Unit project was involved in the injection of brine in southwest Colorado. On 27 May 2000, an earthquake of Mw 4.3 was recorded in the Paradox Valley in Colorado. The Paradox Valley project consisted of an ~ 100 m depth shallow well, which, from January 2002, was mostly used for the injection of Paradox Valley Brine (PVB) with freshwater (70% PVB-30% freshwater) or 100% PVB (Ake et al., 2005). The two mixtures had viscosities ranging between 0.001 Pa·s and 0.003 Pa·s. The Paradox Basin close to the Paradox Valley is a collapsed diapiric salt anticline. Well logs from nearby wells, seismic reflection profiles and in situ studies (Bremkamp and Harr, 1988) indicated the presence of the Wray Mesa fault, which

trends subparallel to the strike of the Paradox Valley. The injection well was sited to optimize fluid migration into and along these faults. The inversion of the focal mechanisms of Paradox valley-induced earthquakes showed an orientation of the maximum horizontal stress $S_{H,max}$ of N45°W-N54°W (Block et al., 2015) with a stress gradient at a depth of $23.95 \cdot 10^{-3}$ MPa/m for $S_{H,max}$ and at $16.2 \cdot 10^{-3}$ MPa/m for $S_{h,min}$ (Ake et al., 2005). The earthquake depth was between 3.5 km and 6.5 km. The hydrostatic pressure gradient was $9.95 \cdot 10^{-3}$ MPa/m in this area, while the vertical pressure gradient was $16.8 \cdot 10^{-3}$ MPa/m (King et al., 2014). Considering that the activated fault was striking at N78°E and dipping at 84°, the normal stress acting on the fault plane ranged between 60 and 99 MPa, while the effective normal stress was 32.5 ± 3.5 MPa (Figure 5.2b). The moment magnitude of the earthquake was $3.16 \cdot 10^{15}$ Nm (McGarr et al., 2014), and the rupture radius was ~ 0.4 - 0.6 km (Yeck et al., 2015). Using the relation between seismic moment, rupture radius and slip, it was possible to estimate the coseismic slip of the fault (0.09-0.20 m), the fault geometry parameter of $H = 0.1$ - 0.2 mm and that L/H^2 is $(4.02 \pm 0.59) \cdot 10^6$ m/m².

Mw 3.9 Youngstown, Ohio, USA.

Since 2010, five deep injection wells have been used for the injection of brine that is used for hydraulic fracturing in the area of Youngstown. On 31 December 2011, an earthquake of magnitude Mw 3.9 was detected in that area following the injection through a well into the Precambrian granite at a total depth of 2802 m (Kim, 2013). The viscosity of the injected water was between $\eta = 0.001$ - 0.003 Pas. The earthquake hypocenter depth was between 3.55 km and 3.68 km (ODNR, 2012). The results of the focal mechanism modeling and the inversion indicate that the focal mechanism of the event is predominantly strike-slip faulting with a strike of 265°, dip of 72° and seismic moment of $M_0 = 8.30 \pm 8.0 \cdot 10^{14}$ Nm (Kim, 2013). The estimation of normal stress on the plane fault is 30.2 MPa (Kim, 2013). Considering the fluid pressure of 30.5 MPa, the effective normal stress is 46.9 MPa (Figure 5.2c).

The rupture area was $4 \cdot 10^5$ m² (Morris et al., 2017). Considering a circular rupture, we can estimate a radius of the rupture area to be approximately 357 m, a coseismic slip of 0.09 ± 0.03 m and an asperity size of $H \sim 0.19$ mm. The geometry of the fault can be described as $L/H^2 = (8.32 \pm 0.23) \cdot 10^5$ m/m².

Mw 5.7 Prague, Oklahoma, USA.

The oil and gas reservoirs in the northern region of Oklahoma have been exploited since the early 20th century. The area was often subjected to induced earthquakes caused by wastewater injection ($\eta = 30$ - 50 mPas). Three earthquakes with Mw values of 5.0, 5.7, and 5.0 occurred near Prague, Oklahoma, on 5, 6, and 8 November 2011 in the Wilzetta fault system at hypocentral

depths of 3.1 km, 5.2 km and 5 km, respectively (Keranen et al., 2013). Walsh and Zoback (2016) performed stress inversions using a focal mechanism analysis of 15 earthquakes near Prague to determine stress orientations and magnitudes in the area. The overburden gradient was $S_v=25$ MPa/km, the fluid pressure gradient was $P_p=9$ MPa/km, and the static friction coefficient was $\mu=0.7$. The fault regime was found to be strike-slip, and the orientation of the maximum principal stress was found to be N83°E. The minimum and maximum horizontal stress gradients were estimated as $S_{h,min}=15$ MPa/km and $S_{H,max}=30$ MPa/km, respectively. Considering the principal stresses magnitude and orientation, the normal stress acting on the fault can range between 70.4 and 88 MPa, while the effective normal stress was 38.7 ± 2.15 MPa (Figure 5.2d).

The seismic moment of the main event was between $3.37 \cdot 10^{17}$ Nm (Sun and Hartzell, 2014) and $3.92 \cdot 10^{17}$ Nm (McGarr et al., 2014) with a stress drop $\Delta\tau=6.75$ -27.64 MPa (Cramer, 2017). Therefore, considering a circular rupture, the coseismic slip was 0.77-0.16 m, and the asperity height was $H \sim 1.88$ mm. These values were comparable with those proposed by Sun and Hartzell (2014). For the Prague main event, L/H^2 was $(4.87 \pm 2.12) \cdot 10^5$ m/m².

Mw 4.8 Timpson, Texas, USA.

The 17 May 2012 Mw 4.8 earthquake near Timpson, east Texas, occurred after wastewater was injected ($\eta=30$ -50 mPas) into two nearby disposal wells into the Rodessa Formation. Epicenters of smaller events following the Mw 4.8 event and located using a portable seismic array were aligned parallel to a fault that was previously mapped using seismic reflection surveys (Frohlich et al., 2014). The focal depths of these events ranged between 2.5 and 4.6 km (Frohlich et al., 2014). The fault dipped at approximately $63^\circ \pm 2^\circ$ to the southwest. An average gradient of the vertical stress S_v of 24 MPa/km was calculated by (Thiercelin and Plumb, 1994). The minimum horizontal stress $S_{h,min}$ and the fluid pressure had gradients of 14 MPa/km and 10.08 MPa/km, respectively (Fan et al., 2016). It was reasonable to suppose that $S_{H,max} = S_v$ (Fan et al., 2016); i.e., a transitional stress state exists between a strike-slip and normal faulting stress regime. Using the procedure proposed in Fan et al. (2016), we determined the effective normal stress acting on the fault at the hypocentral depth of 19-39.5 MPa (Figure 5.2e).

The seismic moment of the event was $2.21 \cdot 10^{16}$ Nm (McGarr et al., 2014) and the stress drop was $\Delta\tau = 12.32$ -33.80 MPa (Cramer, 2017). Considering a circular rupture, the radius of the rupture area was 698 ± 22.1 m, the coseismic slip was 0.40 ± 0.07 m and the asperity height was $H \sim 1.93$ mm. The geometry of the fault can be described as $L/H^2 = (1.83 \pm 0.90) \cdot 10^6$ m/m².

Mw 5.8 Pawnee, Oklahoma, USA.

Since 2009, saltwater disposal ($\eta = 30\text{-}50$ mPa s) in the north-central area of Oklahoma has caused an increase in the background seismicity in the area. In particular, the 3 September 2016, Mw 5.8 Pawnee mainshock resulted from a left-lateral slip across an unmapped fault (Pawnee fault or Sooner Lake fault), striking west-northwestward. The mainshock was located at a depth of 5.6 km with an uncertainty of 0.7 km (Pollitz et al., 2017). The stress orientation obtained from both the wellbore data and focal mechanism inversion showed a direction $N83^\circ \pm 3^\circ E$ with a plunge of 14.9° (Alt and Zoback, 2017). The fault had a strike of 283° and dip of 77° . The effective normal stress gradient can be assumed to be equal to 17 MPa/km (Huang et al., 2017). The depth of the causative fault involved in the mainshock remains poorly constrained (Grandin et al., 2017), but the aftershock seismicity was concentrated at ~ 6 km depth, and the majority of earthquakes in north-central Oklahoma are at 5–6 km depth (McNamara et al., 2015).

The stress drop $\Delta\tau$ during the main event was between 10.15 and 34.27 MPa (Cramer, 2017). The seismic moment of the main event was $4.67 \cdot 10^{17}$ N m. Considering a circular rupture, the radius of the rupture area involved in the main event was 2.1–2.4 km. The slip associated with the event was 1.09 ± 0.21 m, and the asperity size was $H \sim 10.25$ mm. We can describe the geometry of the fault as $L/H^2 = (7.48 \pm 3.72) \cdot 10^5$ m/m².

Mw = 4.1 Fox Creek, Alberta, CA.

The Duvernay Formation, close to the Fox Creek area, hosts hydrocarbon resources, which have become economically feasible since June 2010. The Mw 4.1 earthquake on 13 June 2015 was recorded in the Fox Creek area in the Duvernay Formation. The area was characterized by the presence of more than 290 wells between depths of 2.6 and 4.0 km. During the site hydrofracking procedure, the stimulation phase (e.g., injection of fluid) was merged with the postprocess (e.g., shut-in) phases. The main event occurred during the shut-in phase; the average mean pressures, pumping rates, total pumped fluid volume, and proppant weight in the well for individual stages were 62.6 MPa, $9.4 \text{ m}^3/\text{min}$, 1200 m^3 , and 240 t, respectively (Schultz et al., 2017). The fluid viscosity was estimated as $\eta = 0.1\text{-}0.2$ Pa s. The uncertainty on the viscosity of the injected fluid is included in the error bar of the Sommerfeld number.

Focal mechanisms suggested strike-slip motion on a subvertical fault (strike of 354° and dip of 83°) (Schultz et al., 2017; Wang et al., 2016), and the inversion of the moment tensor suggested a 3–4 km hypocentral depth (Wang et al., 2016).

The azimuth of the field stress was $\sim N45^\circ E$ (Schultz et al., 2017). The maximum horizontal stress $S_{H,max}$ plunge was $35^\circ\text{--}42^\circ$, and its gradient was estimated to be 33 ± 2 kPa/m (Shen et al., 2018). The minimum stress to depth ratio was constrained between ~ 17 and ~ 21 kPa/m, and the fluid pressure to depth ratio ranged from ~ 10 to ~ 21 kPa/m (Shen et al., 2018). The

fault plane was identified by strikes and dips of 354°N and 83°, respectively.

Considering the orientation of the principal stresses and of the plane, the normal stress and the effective normal stress acting on the fault can range between 74.2 and 97.6 MPa and 20-22 MPa, respectively (Figure 5.2g).

The seismic moment of the event was $3.9 \cdot 10^{15}$ - $8.343 \cdot 10^{15}$ N m (Atkinson et al., 2016), and the stress drop $\Delta\tau = 5.45 \text{ MPa} \pm 1.28 \text{ MPa}$ (Clerc et al., 2016). Using 5.1 and 5.2, we computed a rupture radius between 654.6 and 694.31 m, a slip between 0.07-0.12 m and an asperity size of $H \sim 0.19 \text{ mm}$. Using the relation between the slip and the geometry of the fault (5.2 and 5.3), we computed $L/H^2 = (7.74 \pm 1.36) \cdot 10^6 \text{ m/m}^2$.

Mw 2.3 Bowland Shale, Lancashire, UK.

In spring 2011, Caudrilla Resources conducted a vertical multistage hydraulic fracture operation into the Carboniferous Bowland Shales in Lancashire. The 27 May 2011 earthquake of magnitude 2.3 was recorded in the Bowland Shale Formation after injection of a mixture of fluid and proppant ($\eta = 0.1$ - 0.2 Pas). The uncertainty on the viscosity of the injected fluid is included in the error bar of the Sommerfeld number. The focal mechanism was strike-slip failure. Consistent with the regional Carboniferous faulting observed in the seismic reflection data (Eisner et al., 2013), we considered the fault nodal plane dipping at 70° with a strike of 40°. The maximum horizontal stress direction, deduced from both the drilling-induced tensile fractures and the fast shear wave arrival, had an orientation of 30° to this probable fault plane, which was identified from the focal mechanism and the 3-D seismic data. The orientation of the maximum horizontal stress was a plunge of 175°-205° and trend of 20°-25°. The $S_{H,max}$ magnitude in the Bowland shale was approximately 28.33-29.46 MPa/km, and the average minimum stress $S_{h,min}$ was approximately 17-18.3 MPa/km, while the vertical stress gradient was approximately 23.57 MPa/km (de Pater and Baisch, 2011). The normal stress acting on the fault plane ranged between 65.42 and 72.41 MPa (Figure 5.2h). Considering that a fluid pressure at the hypocentral depth of 3.5 km was approximately $P_p = 55 \text{ MPa}$ (de Pater and Baisch, 2011), we can estimate the effective normal stress acting on the fault as 13.7-25.5 MPa (Figure 5.2h).

The seismic moment of the event was $3.20 \cdot 10^{12} \text{ N m}$ (McGarr et al., 2014). Considering a circular rupture, the radius of the rupture area can be estimated to be 53.9-53.8 m (Green et al., 2012) with a stress drop of 6.7-9.1 MPa. The coseismic slip associated with the event was estimated to be approximately 0.01 m and $H \sim 0.008 \text{ mm}$. Considering the relation between coseismic slip and fault geometry (5.2 and 5.3), we can estimate $L/H^2 = (3.35 \pm 1.22) \cdot 10^8 \text{ m/m}^2$. Summary of the analyzed case studies are reported in Table 5.1.

5.5. Case studies

Table 5.1: Summary of the case study reporting the magnitude, viscosity of the injected fluid, average values of depth, effective stress P_{eff} , moment of magnitude M_0 , stress drop $\Delta\tau$, slip of the event $\delta=L$, asperity size of the fault H and the Sommerfeld number for $V=1$ m/s.

Place	Mag	η [mPa s]	depth [km]	σ_n [MPa]	P_{eff} [MPa]	M_0 [10^{14} Nm]	$\Delta\tau$ [MPa]	L [m]	H [mm]	S ($V=1$ m/s)
Basel	3.4	1	4.7	97.95	88.45	1.60	6.81	0.16	0.31	$2.46 \cdot 10^{-4}$
Paradox Valley	4.3	10-30	4.2	79.75	32.49	31.60	10.00	0.14	0.18	$1.72 \cdot 10^{-3}$
Youngstown	3.9	10-30	3.7	77.40	46.86	12.30	11.83	0.08	0.19	$2.27 \cdot 10^{-3}$
Prague	5.6	30-50	4.5	79.17	38.67	3645.00	17.20	0.57	1.88	$2.23 \cdot 10^{-3}$
Timpson	4.7	30-50	3.5	64.85	29.21	221.00	23.06	0.48	1.93	$1.49 \cdot 10^{-2}$
Pawnee	5.7	30-50	5.5	93.50	93.50	4670.00	22.21	0.98	10.25	$1.39 \cdot 10^{-3}$
Fox Creek	3.9	100-200	3.5	85.90	21.79	61.22	27.25	0.13	0.19	$3.17 \cdot 10^{-1}$
Bowland Shale	2.3	100-200	3.6	73.73	18.73	0.03	15.88	0.01	0.01	$1.89 \cdot 10^1$

Chapter 5. Parametric analysis of the elastohydrodynamic lubrication efficiency on induced seismicity

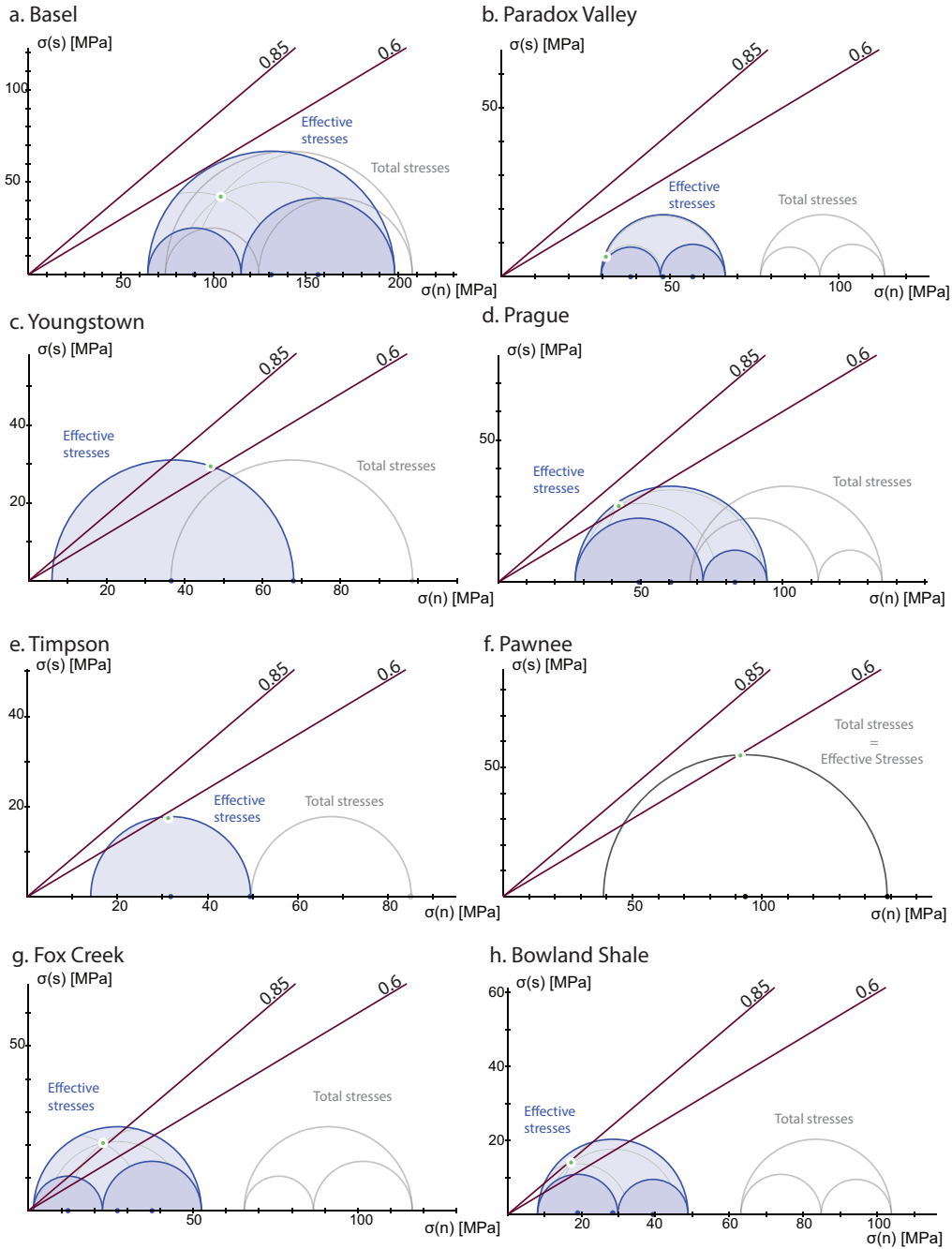


Figure 5.2: Mohr-Coulomb circles representing the average in situ stress, fault orientation and Byerlee failure criteria for the a) Basel earthquake, b) Paradox Valley earthquake, c) Youngstown earthquake, d) Prague earthquake, e) Timpson earthquake, f) Pawnee earthquake, g) Fox Creek earthquake, and h) Bowland Shale. The red lines are the failure envelope for the fault following the Byerlee law. The gray circles are the average Mohr-Coulomb circles without fluid pressure (total stresses), and the blue circles are the average Mohr-Coulomb circles with estimated hydrostatic fluid pressure (effective stresses). The green points are the resolved effective stresses for the average specified activated fault.

5.6 Comparison with theoretical and experimental frameworks

Fluid overpressure generated by the injection of water, brine, wastewater or proppants acts against normal stress, reduces the effective normal stress, and facilitates fault reactivation (King Hubbert and Rubey, 1959). The failure conditions to initiate ruptures are often evaluated by using the isotropic Mohr-Coulomb theory, where the critical shear stress (τ_{crit}) is given by $\tau_{crit} = \mu(\sigma_n - P_f)$, where σ_n is the total normal stress and P_f is the fluid pressure. Large overpressure can potentially activate unfavorable oriented faults (Figure 5.2b).

However, the Mohr-Coulomb theory only describes the onset of fault reactivation, and it ignores the significant weakening and lubrication that faults experience toward seismic slip (Reches and Lockner, 2010), which is mandatory to understand fluid-induced earthquake propagation. Until now, lubrication during coseismic sliding (i.e., sliding velocity $V \sim 1$ m/s) has been interpreted as a consequence of a number of processes, such as flash heating (Rice, 2006) and melting (Rempel and Rice, 2006), decomposition reactions (Han et al., 2007), super-plastic flow (Green et al., 2015; De Paola et al., 2015) and thermal pressurization (Acosta et al., 2018; Rice, 2006; Violay et al., 2015); many of these processes are actually thermally triggered (Di Toro et al. (2011) and references therein). Recently, Cornelio et al. (2019) proposed that a single mechanism, the EHD, can explain fault weakening when fluids with high viscosity are involved. The EHD efficiency is governed by a dimensionless parameter called the Sommerfeld number (S). Determining the parameters that define the Sommerfeld number for fluid-induced earthquakes is not always possible due to the lack of seismological monitoring of the events. Here, we analyzed eight well-documented case studies of induced seismicity for which it was possible to determine the parameters required in the calculation of the S number. The S number of these events is now compared with those expected by theory and experimental investigations. The coseismic slip rate V is fixed at 1 m/s (Heaton, 1990; Sibson, 1986) (Figure 5.3). Considering the static stress drop $\Delta\tau$ as the upper bound for the dynamic stress drop during the event, we computed the maximum dynamic friction as

$$\mu_{dyn} = \frac{(\mu_s \sigma_n - \Delta\tau)}{\sigma_n} \quad (5.4)$$

where $\mu_s = 0.65-0.8$ is the static friction coefficient defined by Byerlee's law. Figure 5.3 reports the 8 case studies as well as the theoretical prediction and experimental data of Cornelio et al. (2019). The vertical dashed lines define the limit of the three lubrication regimes. Remarkably, the eight case studies follow the same trend as the experimental and theoretical predictions. For most of the analyzed events, the event occurs under the mixed lubrication regime, in which the load is partially supported by the fluid layers and partially supported by the solid asperities present on the fault. These events are also characterized by an intermediate viscosity of injected fluids (wastewater and brine). The events in which proppant was injected appear to be more on the right part of Figure 5.3, close to the transition between the mixed and the

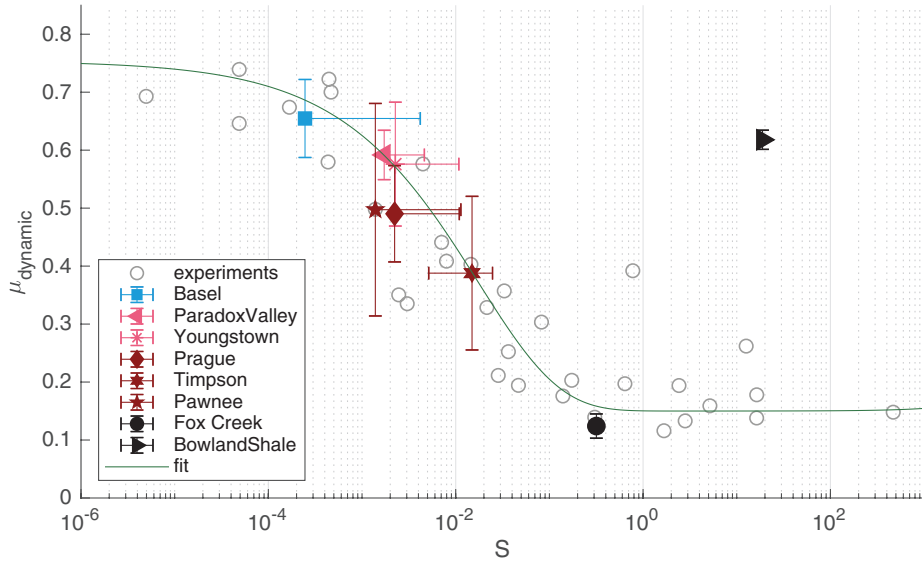


Figure 5.3: Estimated dynamic friction coefficient vs the Sommerfeld number for induced seismicity cases. The gray empty circles are the experimental data of Cornelio et al. (2019), while the full markers are the estimated values of dynamic friction and Sommerfeld number for the cases studied (see legend in the figure). The three lubrication regimes (BL, ML, and EHD) are delimited by the vertical black dashed lines. The dynamic friction coefficient μ_{dyn} in the three lubrication regimes decays from 0.75 in the boundary lubrication regime to 0.1 at the boundary between the mixed and fully lubricated regimes.

elastohydrodynamic lubrication regime or in the fully lubrication regime where the stress is only supported by the fluid film on the slip surface.

To investigate the possible effect of a slip-rate V lower or higher than 1 m/s, we use a 3-axis plot (Figure 5.4); in the background, we reported the possible variation in the coseismic slip-rate V with the color bar (from 10^{-4} to 10 m/s), the geometrical factor L/H^2 on the y-axis and the fluid parameters η/P_{eff} on the x-axis in the characteristic range of values of the boundary lubrication regime ($S = 0.001$, Figure 5.4a), in the mixed lubrication regime ($S = 0.01$, Figure 5.4b) and in the elastohydrodynamic lubrication regime ($S = 1$, Figure 5.4c).

Figure 5.4 shows the following:

- 1 The Basel main event, produced by the injection of water (blue marker), cannot be explained by the EHD theory. In fact, the Sommerfeld number for this event, considering the typical coseismic slip rate ($V < 10$ m/s), ranges within the boundary lubrication regime, and the EHD theory cannot explain the estimated drop in the shear stress of 12.5 MPa (Goertz-Allmann et al., 2011).
- 2 The injection of proppant (black markers), i.e., the Fox Creek and Bowland Shale Formation locations, can allow the fault to slip into the fully elastohydrodynamic lubrication

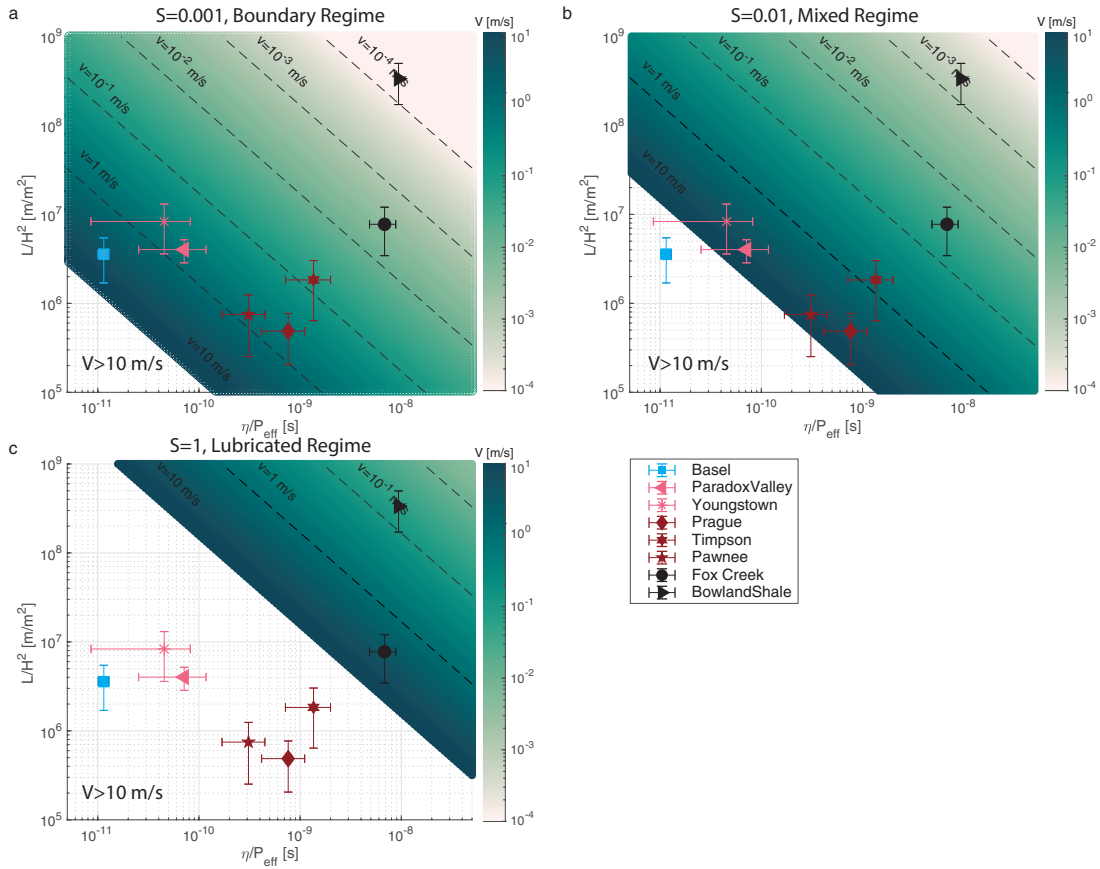


Figure 5.4: The multiaxis plot of the Sommerfeld number for the human-induced seismicity range of values and real events for a. $S=0.001$ (end of the boundary lubrication regime), b. $S=0.01$ (in the mixed lubrication regime), and c. $S=1$ (beginning of the mixed lubrication regime). The blank areas of the graphs show the combination of μ/P_{eff} and L/H^2 , which required $V > 10$ m/s to obtain the imposed S values ($S=0.001$, $S=0.01$ and $S=1$).

regime, associated with a smaller friction coefficient (i.e., a lower fault strength).

- Most of the human-induced events studied in this paper involve the injection of wastewater (red markers) and brine (pink markers), which is characterized by an intermediate viscosity. In the studied cases, the lower viscosity of the wastewater and of the brine compared to the proppant do not allow the fault to reach the elastohydrodynamic lubrication regime. In these cases, sliding during the human-induced event could occur in the mixed lubrication regime (Figure 5.2b).

5.7 Conclusions

We performed a parametric analysis of the parameters that describe the Sommerfeld number, which is a key parameter assessing the effectiveness of EHD during seismic sliding. We

Chapter 5. Parametric analysis of the elastohydrodynamic lubrication efficiency on induced seismicity

analyzed eight well-documented cases of induced seismicity events by considering elastohydrodynamic theory. We observed the following:

- Under the assumption of a constant coseismic slip-rate $V = 1$ m/s, the eight induced seismicity cases follow the decay of the dynamic friction coefficient as a function of the dimensionless Sommerfeld number, which was predicted by theory and demonstrated experimentally by Cornelio et al. (2019);
- Removing the assumption of a constant coseismic slip rate, earthquakes triggered by the injection of proppant can achieve full EHD lubrication, whereas most of the other cases where fluids with intermediate viscosities were injected fall into the mixed lubrication regime. Only earthquakes triggered by water injection fall into the boundary lubrication regime and cannot be explained in the framework of the EHD theory.

In conclusion, in some conditions of effective normal stress P_{eff} and fault geometry L/H^2 the high viscosity of the injected fluid during hydraulic reservoir stimulations, can enhanced fault weakening, through elastohydrodynamic lubrication processes and facilitate the rupture propagation of human-induced earthquakes.

6 Conclusions and Perspectives

6.1 Summary

During geo-energy activities, injection or extraction of fluids from the underground reservoirs can perturb the state of stress around existing faults, resulting in fault reactivation and induced seismicity. The injected fluids are characterized by a viscosity, which can be orders of magnitude higher than that of water.

In this Ph.D. thesis, we investigated the role of fluid viscosity in fault mechanics at the laboratory scale for the first time. In our experiments, granite saw-cut samples were chosen as a proxy of crustal faults and four water and glycerol mixtures were used to simulate the range of viscosity of the injected fluid used during the activities related to human induced seismicity. We analyzed the mechanical behaviour of a lubricated fault at the various stages of the earthquake cycle, from the nucleation to the reactivation and propagation of co-seismic slip. The mechanical behaviour of a fault under the three lubrication regimes was analyzed, by combining mechanical data, roughness analyses and numerical modelling. The lubrication theory, extended to rock mechanics by Brodsky and Kanamori (2001), was demonstrated here to be valid at the laboratory scale. The lubrication regimes are defined by the Sommerfeld number S which is proportional to the slip-rate of the fault and fluid viscosity on the fault plane. The major findings for each stage of the earthquake cycle in relation to the involved fluid viscosity and, more generally, the Sommerfeld number will now be presented.

6.1.1 Nucleation phase in presence of viscous fluids

We have performed ten frictional tests using a triaxial deformation apparatus in a direct shear configuration on pre-cut Laperyte granite samples to analyze the fault stability in the presence of pressurized mixtures of water and glycerol (Chapter 2). During each experiment, we performed velocity steps at 30 MPa and 50 MPa constant effective normal stress, changing

fluid viscosity. Velocity steps were modelled with a rate and state friction law. In the presence of viscous fluid, we use the Persson law to define the state variable of the rate and state friction law. Under these conditions, we observed that fluid viscosity has an important influence on the fault stability. In particular, as the $(a - b)$ parameters decreases with increasing viscosity, and become negative, nucleation of earthquakes is promoted.

6.1.2 Reactivation phase in presence of viscous fluids

Fault reactivation was triggered under 10 MPa constant effective normal-stress conditions by increasing the shear stress acting on the fault in a step-wise manner ($\Delta\tau = 0.5$ MPa every 1000 seconds) in a rotary shear configuration. The slip-rate and the slip were allowed to adjust spontaneously (Chapter 3).

Our results showed that, independent of the viscosity, fault reactivation followed a Coulomb-failure criterion ($\mu_s > 0.6$). At the onset of reactivation, irregular slip episodes occurred. This unstable slip phase was accompanied by multiple and rapid spontaneous shear stress drops. We divided this unstable phase into a sequence of short-lived events ending with a long-lived slip-event. Modelling of these events showed that fluid viscosity affected the fault weakening mechanism: flash-heating was the dominant weakening mechanism in room-humidity and water-saturated conditions, whereas the presence of more viscous fluids favoured the activation of elasto-hydrodynamic lubrication.

6.1.3 Propagation phase in presence of viscous fluid

To study the propagation phase of an earthquake in the presence of viscous fluids, we performed 38 experiments on pre-cut samples of Westerly granite and Carrara Marble in a rotary shear configuration (Chapter 4). We imposed a slip-rate (V) ranging from $10 \mu\text{m/s}$ to 1 m/s , effective normal stress up to 20 MPa, and fluid pressure varying from 0 (i.e., room-humidity conditions) to 2 MPa. With this series of experiments we were able to reproduce the entire Stribeck curve for lubricated rocks and we distinguished the three lubrication regimes as a function of the Sommerfeld number S . If $S < 10^{-3}$, the dynamic friction coefficient μ_{dyn} was about 0.7, independent of fluid viscosity, slip-rate and rock lithology (boundary lubrication regime). At intermediate S ($10^{-3} < S < 1$), the dynamic friction coefficient was strongly influenced by both viscosity and slip-rate, with μ_{dyn} dropping from ~ 0.7 to ~ 0.2 (mixed lubrication regime). At high S ($S > 1$), μ_{dyn} slightly increased with increasing slip-rate (hydrodynamic lubrication regime). Moreover, we compared the surface roughness measurements of the rock surface before and after the experiments, to determine accurately the asperity height H . We observed that for $S > 1$ most of the shearing was accommodated within the fluid layer, confirming the activation and effectiveness of EHD lubrication. Instead, for $S < 1$, we observed

the formation of gouge or patches of melt on the sample surface, which are a sign of the asperities supporting the stress.

6.1.4 Energy budget for earthquakes in presence of viscous fluids

Performing experiments in a rotary shear configuration, we were also able to quantify the slip distance necessary to reach steady state as a function of the Sommerfeld number S (Chapter 4). In particular, we observed that this distance increased with S under boundary and mixed lubrication regimes ($S < 1$), but drastically decreased under elasto-hydrodynamic regime ($S > 1$). Integration of the measured shear stress with slip up to the critical distance allowed us to quantify the breakdown work. The breakdown work is an important parameter of the energy budget which limits the slip propagation. We observed an important drop in the breakdown work in elasto-hydrodynamic regime ($S > 1$). We concluded that for small-magnitude earthquakes, highly viscous fluids might increase the breakdown work dissipated on the fault surface, hindering earthquake propagation. Instead, for large-magnitude earthquakes, the dominant effect of increased viscosity will be to reduce breakdown work, therefore promoting earthquake propagation.

6.1.5 Up-scaling to induced seismic events

Finally, we performed a parametric analysis based on the elasto-hydrodynamic theory, constraining the lower and upper boundary of the five parameters which define the Sommerfeld number S . We showed that elasto-hydrodynamics can be an efficient weakening mechanism active during natural (Chapter 4) and human-induced earthquakes (Chapter 5).

In particular, in Chapter 5 we reported the average values of the parameters which defined the Sommerfeld number for 8 well-studied induced seismic events worldwide. The analyzed earthquakes occurred by the reactivation of a pre-existing fault near the fluid injection borehole. Moreover, previous studies have shown that the movement between the two fault surfaces was almost planar, as required from elasto-hydrodynamic theory. We showed that the viscosity of injected fluid played a key role in the reduction of the fault strength during co-seismic slip. Indeed the computed dynamic strength of the fault followed the same decay with the dimensionless Sommerfeld number expressed by the experimental results in Chapter 4.

6.2 Ongoing work

Although this work has answered many of the questions initially posed, other scenarios of interaction between a viscous fluid and fault surface have not been investigated yet. In particular, in this thesis, we investigated the fault behaviour when the fluid was at initial pressure

equilibrium on the fault plane and diffusion processes were not investigated. To understand the slip behaviour of a fault when fluid pressure is not in equilibrium, we performed dedicated experiments of direct injection of viscous fluids on the fault plane.

6.2.1 Methods

We performed experiments on bare surfaces of axially pre-cut Lapeyrate granite cylinders using a triaxial deformation apparatus, oil-confining medium called FIRST, located at EPFL, Switzerland (see Cornelio and Violay (2020a) for full description of the apparatus). The experimental assembly consisted of two semi-cylinders of 37 mm diameter cut along a vertical axis plane. Each half cylinder presented a 5-mm diameter borehole drilled from the cylinder base to the fault surface with a 45° angle. Two ~10 mm-high silicon spacers were used to offset the two half cylinders creating an initial contact area of ~1950 mm². During the experiments the axial deformation of the two rubbers allowed up to 5 mm displacement (Figure 6.1). In this experimental configuration, the normal stress on the fault was equal to the confining pressure, $\sigma_n = P_c$, and shear stress τ was proportional to the pressure of the vertical piston σ_a :

$$\tau = \sigma_a A_0 / A_{sliding} \quad (6.1)$$

where A_0 was the two semi-cylinder base area, and $A_{sliding}$ was the sliding surface contact area $A_{sliding} = A_i - 2r\delta(t)$, where A_i was the initial contact area, $2r$ was the sample diameter and $\delta(t)$ was the slip of the fault.

The two semi-cylinder samples were placed in a viton jacket equipped with 6 differential pressure sensors directly positioned along the experimental fault (Figure 6.1a). Each differential pressure sensor consisted of a steel cylindrical cap with the internal part of the cap characterized by an empty dome shape. The external flat base of the cap was equipped with axial strain gauges. The strain gauges measured the elastic distortion of the steel due to differing pressures between the external confining pressure and the internal fluid pressure. The slip of the fault was recorded by two LVDTs internal to the pressure vessel with a resolution of 1 μ m. The average evolution of the cumulative slip recorded by the two internal LVDTs which were corrected for elastic deformation of the sample.

We ran experiments under initial drained fault conditions with a confining pressure P_c of 24 MPa, and an initial fluid pressure $P_f=4$ MPa. The used fluids were 100% distilled water (water in the following figures) and 99%glycerol (the remaining 1% being impurities, glyc99 in the following figures). Viscosity values were measured using a calibrated Ubbelohde capillary viscometer (Cannon Instrument Company) at a temperature of 20 °C.

The shear stress at the onset of fault slip under constant pore pressure conditions τ_p , was determined by conducting of an axial loading test. The axial stress was decreased down to

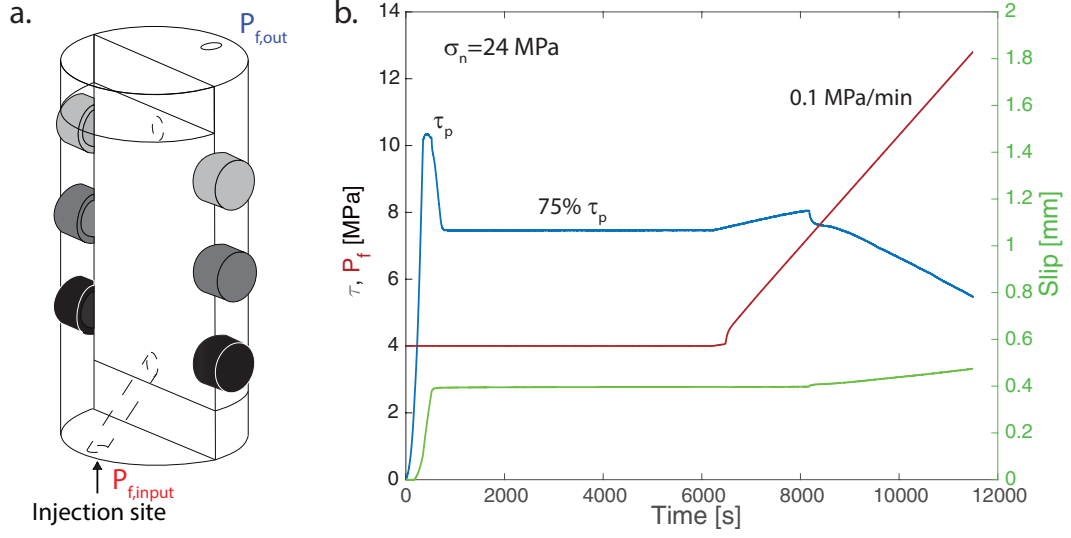


Figure 6.1: Sketch of the experimental configuration and experimental procedure. a) The pressure sensors are equally spaced along the fault plane. The same color for the sensors on the sketch corresponds to the same distance of the sensors from the injection point. The input fluid pressure $P_{f,input}$ is imposed and measured outside the pressure vessel before entering the sample. Another pressure transducer recorded the output fluid pressure $P_{f,out}$ after exiting the sample and outside the pressure vessel. b) Experimental procedure for experiment ds054 performed with water fluid and injection rate equal to 0.1 MPa/min.

$75\% \tau_p$, and the actuator position was maintained constant by a servo-controlled loop on the external displacement transducers during the pore fluid re-equilibration.

A flow rate of 0.01 ml/min was then imposed on the axial piston and fluid was injected through the bottom borehole at a constant pressure rate. The injection rate was $Q=0.1$ MPa/min for experiments performed with water and glycerol. Moreover, to keep $\eta/\rho Q$ constant, experiment with water injection at $Q=97$ MPa/min was performed. During injection the mechanical data were recorded at ~ 100 Hz.

6.2.2 Preliminary results

Fluid injection at a constant pressure rate led to a decrease in the effective normal stress on the fault plane. Figure 6.2 shows the evolution of the shear stress and effective normal stress computed considering the pressure of the fluids at the injection points ($P_{f,input}$). Once a critical state was reached (stars symbols in Figure 6.2), the fault started to slip and the shear stress on the fault decreased as the fluid pressure continued to increase. The critical values in the state of stress corresponded to $\mu_s=0.460\pm0.019$ for experiments performed at 0.1 MPa/min fluid pressure injection rate and 0.699 for experiment performed at 97.0 MPa/min (Figure 6.2).

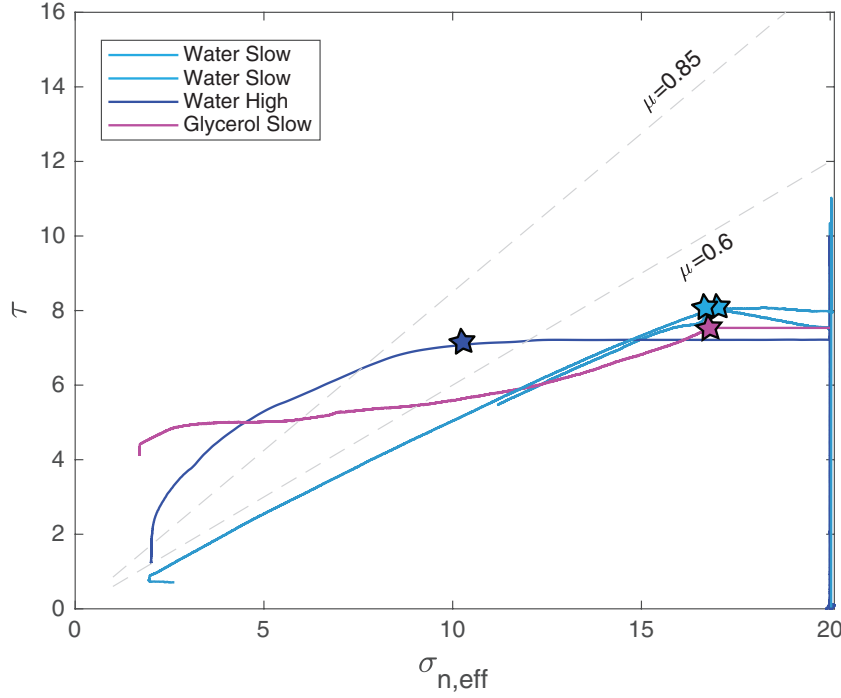


Figure 6.2: Fault reactivation due to fluid injection. Effective normal stress decreased during the experiments due to increases in fluid pressure on the fault plane. Dashed lines correspond to frictional strength using friction coefficients of 0.6 and 0.85. Symbols correspond to the state of stress at the onset of the fault slip and the decrease of the shear strength of the fault.

The evolution of the fluid pressure along the fault during the injection phase is shown in Figure 6.3. The fluid pressure was almost homogeneous along the fault for injected water at 0.1 MPa/min (Figure 6.3a), while a differential pressure of 20 MPa between the top and the bottom of the sample was recorded for water injection at 97 MPa/min (Figure 6.3c). The experiment performed with the injection of glycerol showed a distributed increase of fluid pressure along the fault with a differential fluid pressure between the top and the bottom of the sample equal to 7 MPa (Figure 6.3d).

The cumulative slip at the end of the injection phase was ~ 0.19 mm for the experiment with 0.1 MPa/min injected water, 0.28 mm for experiment with 97 MPa/min injected water and 0.30 mm for the experiment with 0.1 MPa/min injected glycerol.

Our preliminary results showed that the presence of pressurized glycerol on the fault plane has a weakening effect on the shear strength which cannot be explain only considering the fluid pressure increase along the fault.

In order to better understand our results we are planning to:

- perform experiments at different initial normal stress (σ_n);

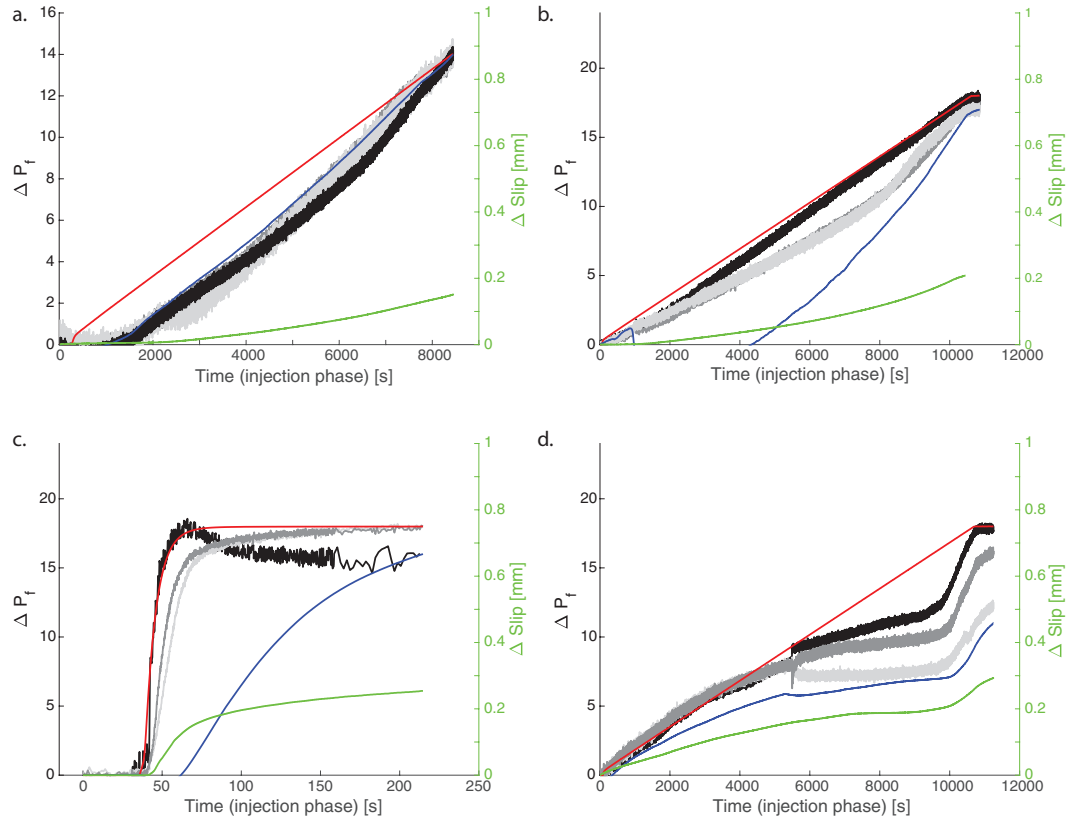


Figure 6.3: Differential fluid pressure evolution along the fault plane during fluid injection. a) and b) Water injection at 0.1 MPa/min, c) water injection at 97 MPa/min and d) glycerol injection at 0.1 MPa/min. The black lines represent the average fluid pressure recorded by the pressure sensors closer to the injection point. The grey lines represent the average pressure recorded by the pressure sensors located at the halfway point along the fault, and the light grey lines represent the average pressure recorded at the top of the sample fault (see Figure 6.1).

- compute the fault transmissivity adapting the method proposed by Rutter and Mecklenburgh (2018); Rutter and Hackston (2017) to our experimental configuration;
- compute the fluid layer thickness H by inverting the transmissivity evolution;
- estimating the evolution of the Sommerfeld number S during our experiments due to changes in the effective normal pressure and fluid film thickness;
- model the fluid flow and pressure front during our experiments.

The results of this work will shed light on the effect of fluid viscosity on the evolution of pressure fronts and fault transmissivity.

6.3 Future work

In this PhD thesis, earthquake propagation was mostly analyzed in terms of friction and evolution of fault strength in the three lubrication regimes. However, energy partition and fracture mechanics are also key parameters to understand earthquake mechanics. Dedicated experiments to understand rupture propagation in the presence of viscous fluids under the three lubrication regimes will be conducted. Experiments will be performed in pre-cut samples of Westerly granite in the triaxial apparatus FIRST at EPFL. The samples will be equipped with dynamic strain gauges in order to record the effect of fluid viscosity on the near-fault stress field and velocity rupture.

A HighSTEPS: A High Strain TEMperature Pressure and Speed Apparatus to study Earthquake mechanics

Authors: Marie Violay¹, Carolina Giorgetti¹, Chiara Cornelio¹, Giuseppe Di Stefano², Laurent Gastaldo¹, Felix Aeschiman³, Stefan Wiemer⁴, Jean-Pierre Burg⁴.

¹ Laboratory of Experimental Rock Mechanics (LEMR), ENAC, EPFL, Switzerland;

² Istituto Nazionale di Geofisica e Vulcanologia, INGV, Rome, Italy;

³ Mequadrat, Luzern, Switzerland;

⁴ Department of Earth Science, EHZ, Zurich, Switzerland.

Status: Under review in *International journal of rock mechanics and mining sciences*.

Contributions: M. Violay designed the experimental apparatus, C. Giorgetti and C. Cornelio actively participate to the development of the apparatus. C. Giorgetti and C. Cornelio has prepared and characterized samples used in this study. C. Giorgetti and C. Cornelio have run the experiments. All authors have contributed to the testing strategy and methodology. M. Violay has written the manuscript. All the co-authors have edited and guided discussion of the manuscript. M. Violay has acted as a supervisor and main responsible author of the publication.

Highlights:

- The apparatus combines the advantages of biaxial friction apparatuses, i.e., simple geometry, high normal forces, confining pressure and pore fluid pressure, and with the advantages ones of the rotary shear apparatuses, i.e. high slip velocity implemented thanks to the presence of electromagnetic motors;
- Under these unique boundary conditions, the new apparatus allows the investigation- contributes to the understanding of the entire seismic cycle (inter-seismic, nucleation

Appendix A. HighSTEPS: A High Strain TEMperature Pressure and Speed Apparatus to study Earthquake mechanics

and propagation) and would be of interest to a broad spectrum of geoscientists.

A.1 Abstract

We present a state-of-the-art biaxial apparatus able to study both earthquake rupture nucleation and propagation at conditions typical of the seismogenic zone. The HighSTEPS, High Strain TEMperature Pressure Speed, apparatus simulates fault deformation in a wide range of slip velocities, i.e., from 10 $\mu\text{m/s}$ to 0.25 m/s. Within this velocity range, it is possible to study, the rate-and-state friction, the fault dynamic weakening, and healing under unique boundary conditions, i.e., normal stress up to 100 MPa, confining pressure up to 100 MPa, pore fluid pressure up to 100 MPa and temperature up to 120 °C. The apparatus consists of a hydraulic system integrated with four linear motors. The hydraulic system allows for the application of normal stress, confining pressure and pore fluid pressure.

The main peculiarity of this apparatus is the system of four linear motors that are mounted in series in order to apply shearing velocities up to 0.25 m/s, accelerations up to 10 m/s^2 and shear stresses up to 200 MPa. Moreover, both experiments in sliding velocity control or shear stress control on the experimental faults are possible. Preliminary experiments on carbonate and silicate bearing rocks are coherent with the previous literature. The investigation of fault friction under a wide range of velocities, normal stresses, confining pressures and pore fluid pressures will provide insights into the mechanics of earthquakes and reduce the gap between natural and laboratory observations.

A.2 Introduction

Physics of earthquake source can be investigated by monitoring active faults from borehole observatory in reservoirs (Maxwell et al., 2010) or by interpretation of seismic waves at the earth's surface (Shearer, 2019). Indeed, most information on earthquake mechanics is retrieved from seismology (e.g., Lee and Ladd (2002)). However, the low resolution of these indirect techniques (cm to km scale) yields limited information on the physical and chemical deformation mechanisms active during earthquake rupture nucleation and propagation (Kanamori and Anderson, 1975).

Experimental studies of frictional instabilities on fault gouge material or pre-existing surfaces (e.g., (Brace and Byerlee, 1966)) may overcome those limitations (Scholz, 1998; Marone, 1998; Persson, 2000d). For instance, friction controls earthquake nucleation and propagation, the static and dynamic stress drops, the frictional heat generated during slip, and consequently the energy budget of earthquakes (Scholz, 2019b; Di Toro et al., 2011). All these processes can be investigated and monitored through laboratory experiments. In the last decades, rock friction properties have long been investigated using triaxial apparatuses in saw-cut configuration (Jaeger, 1959; Byerlee, 1967; Handin, 1969), in which the fault is loaded at low velocities, typically orders of $\mu\text{m/s}$, and accumulates small displacements, typically few mm. In a seminal

Appendix A. HighSTEPS: A High Strain TEMperature Pressure and Speed Apparatus to study Earthquake mechanics

paper, (Brace and Byerlee, 1966) suggested that the stick-slip phenomenon observed in these rock friction experiments is analogous to natural earthquakes. Furthermore, to address the problem of earthquakes nucleation, biaxial apparatuses were developed and have long been used to study frictional properties of experimental faults under sub-seismic slip velocities in double-direct shear configuration (Dieterich, 1972; Mair et al., 2002; Collettini et al., 2014). The biaxial apparatus developed at USGS (USA) is amongst the first biaxial apparatuses used to investigate rock frictional properties (Dieterich, 1972). Other pioneering biaxial apparatuses are the one in the Rock and Sediment Mechanics Laboratory at the Pennsylvania State University (USA) (Mair et al., 2002) and BRAVA (Brittle Rock deformAtion Versatile Apparatus) installed at INGV in Rome (Italy) (Collettini et al., 2014). Although the biaxial apparatuses developed in the past 50 years are characterized by different boundary conditions in terms of forces, pressures, temperatures and size of the samples, all of them takes advantages from the double-direct shear configuration that allows a good control of the normal and shear forces acting of the fault, accurate measurements of fault slip and dilation/compaction, and constant contact area.

Friction studies conducted with triaxial and biaxial deformation apparatuses are characterized by sub-seismic slip velocities and limited amount of slip, $< 1 \text{ mm s}^{-1}$ and few cm respectively (Jaeger, 1959; Byerlee, 1967; Brace and Byerlee, 1966; Handin, 1969; Byerlee, 1978; Paterson and Wong, 2005a; Lockner and Beeler, 2002; Mair et al., 2002; Savage and Marone, 2007; Samuelson et al., 2009; Carpenter et al., 2016). These experiments showed that the apparent friction coefficient μ (i.e., $\mu = \tau / \sigma_{n,eff}$, where τ is the shear stress and $\sigma_{n,eff}$ the effective normal stress acting on the fault) is between 0.60 and 0.85 for most rocks (Byerlee's rule; except for phyllosilicates-rich rocks (Byerlee, 1978)), for normal stresses up to 2 GPa, and temperatures up to 780 K. The apparent friction can thus be expressed as a function of slip velocity and a state variable, and modelled with the empirical rate- and state-dependent friction law (Dieterich, 1979; Ruina, 1983). Additionally, at velocities typical of earthquake nucleation phase, the apparent friction varies only a few percents for small changes in slip velocity, determining if a fault is or not prone to nucleate earthquakes.

Although Byerlee's rule and the rate-and-state law have many applications in earthquake mechanics (inter-seismic and nucleation phase of earthquakes), these experiments were performed at slip velocities and displacements orders of magnitude smaller than those of earthquakes. Therefore, these experiments are unable to characterize the propagation phase of earthquakes. In the last 15 years, the multiplication of the rotary shear apparatus, designed to achieve slip velocities higher than 1 m/s and infinite displacement, overcome those limitations and produced unexpected results (Di Toro et al., 2010). A pioneering rotary shear apparatus capable of achieving seismic slip velocities up to 1.3 m/s were built and installed in Japan (Shimamoto, 1994). Among others (see Di Toro et al. (2010) and references therein), a state-of-art rotary shear apparatus (SHIVA, Slow to High Velocity Shear Apparatus) capable of deforming samples at slip rates up to 9 m/s has been installed at INGV in Rome (Italy)

(Di Toro et al., 2010). Studies performed with these rotary shear apparatuses have shown a significant decrease in fault strength with increasing slip and slip velocity. They also reveal various dynamic fault-weakening mechanisms (frictional melting, thermal pressurization, silica gel, elastohydrodynamic lubrication) that are likely active during earthquakes, including mechanisms that were unknown before conducting these experiments.

Though this new frontier is promising, key aspects of earthquake mechanics laboratory investigation, like being able to conduct high slip velocity experiments on rocks under elevated pore fluid pressure and temperatures characteristic of natural and induced earthquakes, remain beyond current experimental capabilities. Furthermore, studying links between pore-fluid pressure, permeability, and frictional properties remains a challenge. To date, very few high velocity friction experiments have been performed in presence of pore fluid pressure (Tanikawa et al., 2012a,b, 2014; Violay et al., 2014b, 2015, 2019; Cornelio et al., 2019, 2020). In this paper, we present a new state-of-art apparatus combining the advantages of biaxial apparatuses, i.e., simple geometry, high normal forces, confining pressure and pore fluid pressure, and the advantages of the rotary shear apparatuses, i.e. high slip velocity implemented thanks to the presence of electromagnetic motors. Building on the design of recent low-velocity biaxial machines implemented with pressure vessels (Samuelson et al., 2009; Collettini et al., 2014) and implementing the system with powerful electrical motors (Di Toro et al., 2010), the new HighSTEPS (High Strain TEMperature Pressure Speed) apparatus is able to reproduce the deformation conditions typical of the seismogenic crust, i.e., confining pressure up to 100 MPa, slip velocity from 1 $\mu\text{m/s}$ to 0.25 m/s, temperature up to 120 °C, pore pressure up to 100 MPa. Under these unique boundary conditions, the new apparatus allows the investigation of the entire seismic cycle (inter-seismic, nucleation and propagation).

A.3 Design of the apparatus

The machine is 1.90 m long, 0.7 m wide and 2.5 m high, and it weighs around 3000 kg. The apparatus consists of a hydraulic system integrated with four linear motors (Figure A.1, Figure A.2a). The normal stress is applied by a horizontal hydraulic piston. The confining pressure is applied through a confining medium (i.e., silicon oil) by a hydraulic intensifier connected to a vessel implemented within the biaxial frame. The pore fluid pressure is applied by two pore fluid intensifiers connected to the sample, which also allow for permeability measurements. In addition, the vessel is equipped with two heating plates and feedthroughs for acoustic sensors and strain gauges. The main peculiarity of this apparatus is the system of four linear motors mounted in parallel in order to drive the vertical piston and apply to the samples shearing velocities up to 0.25 m/s, accelerations up to 10 m/s² and shear stresses up to 100 MPa.

Appendix A. HighSTEPS: A High Strain Temperature Pressure and Speed Apparatus to study Earthquake mechanics

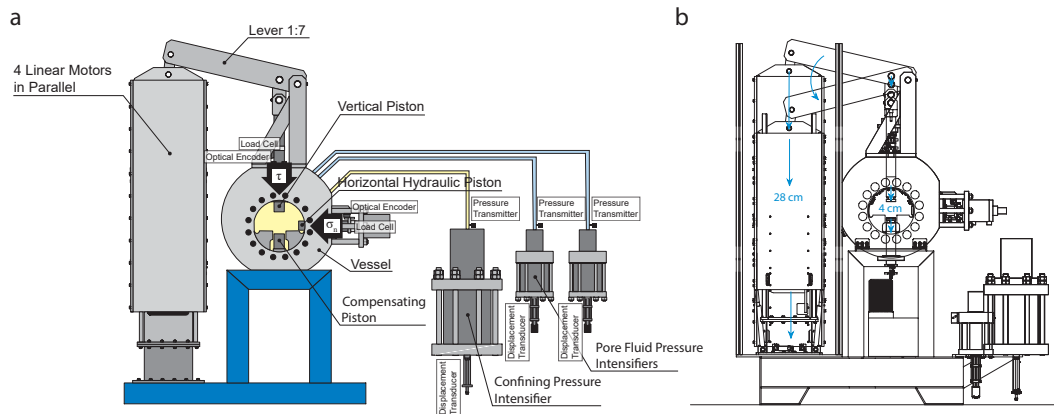


Figure A.1: a) Schematics of the HighSTEPS apparatus. 4 linear motors are mounted in parallel to apply vertical force to the sample through a 1:7 lever. The vertical piston is equipped with an optical linear encoder and a load cell. The horizontal hydraulic piston applies horizontal load and it is equipped with a linear optical encoder and a load cell. Two pore pressure intensifiers apply pore fluid pressure and they are equipped with displacement transducers and pressure transmitters. The confining pressure intensifier applies confining isotropic pressure and it is equipped with a displacement transducer and two pore pressure transmitters. The intensifiers are connected to the pressure vessel. b) Sketch of the working principle of the lever 1:7 that imposes the shear displacement and shear stress to the experimental fault.

The hydraulic power supply and oil circuit

The hydraulic power supply, weight of 300 kg, has a size of 1400 x 850 x 900 mm³ and it is located in a room next to the laboratory, about 5 m away from the machine. It was built by Polytec, S.a.s, located in Padua, Italy. It supplies pressure to the oil circuit connected to the hydraulic intensifiers and piston of the machine and includes a main oil pump driven by a 7.5 kW electrical motor, and a recycling oil pump, an oil tank, oil and air filters, a pressure accumulator to stabilize the pressure, pressure and level sensors, and finally an electro-valve allowing pressure regulation in the oil circuit. The main pump is characterized by a maximum pressure of 160 bars and a maximum flow rate of 23 l/min. The oil tank of a capacity of 75 l contains mineral oil is equipped with the recycling oil pump connected to a cooling system composed of a chiller and a heat exchanger. The recycling oil pump is characterized by a maximum pressure of 8 bars and a maximum flow rate of 24.5 l/min respectively.

The three intensifiers and the hydraulic piston

The three hydraulic pressure intensifiers and the hydraulic piston were designed and built by Polytec, S.a.s., located in Padua, Italy (Figure A.3a). They work with a supplied pressure of 70-160 bar generated by the hydraulic power unit.

The horizontal hydraulic piston, with a stroke of 30 mm, is fixed on the pressure vessel and it

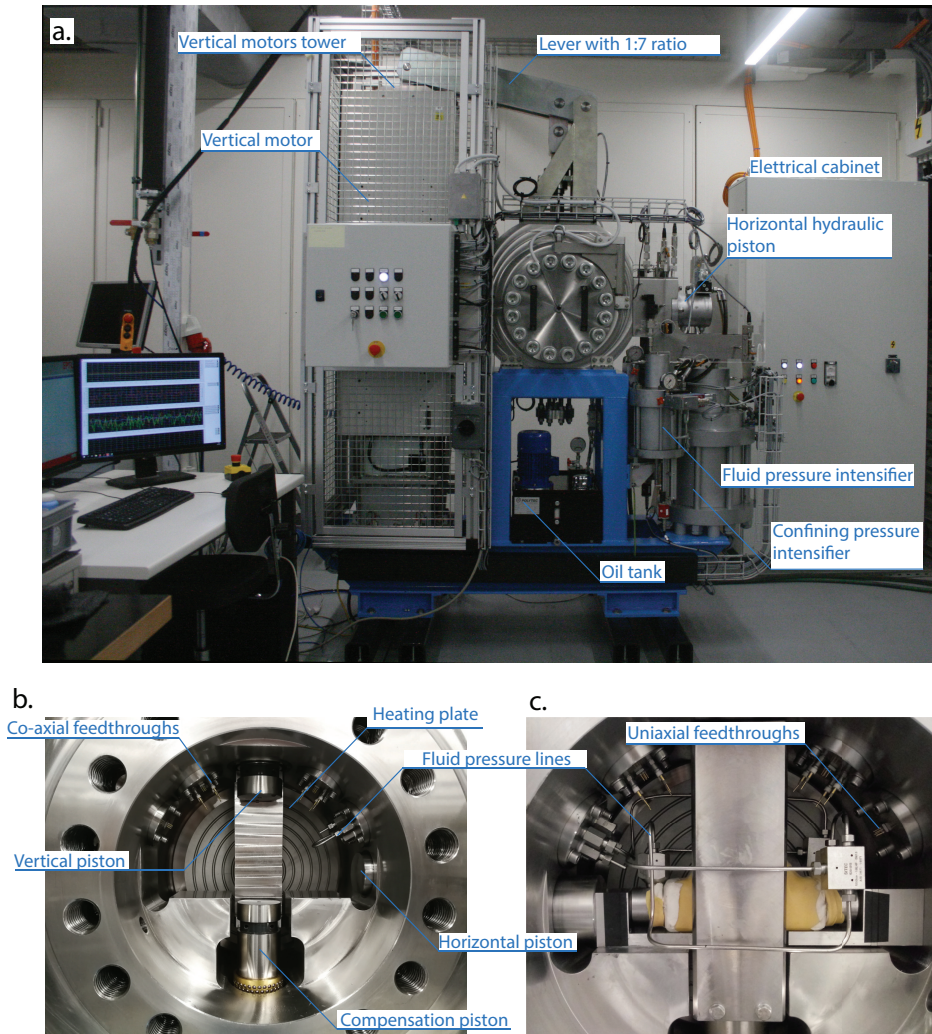


Figure A.2: a) Picture of the HighSTEPS machine. b) Details of the pressure vessel with high pressure ports for pore fluid and confining oil, and uniaxial and coaxial feedthroughs for electronics. c) Jacketed sample with pore pressure lines connected to the pore pressure ports.

can exert a force up to 160 kN. The piston is controlled by a servovalve (MOOG D638-390-0001 Type R02TO1M0HEE2MAOK1B1) mounted on the piston (Figure 3a). The piston is equipped with a linear optical encoder Renishaw (RL 26BSS005C30 A) mounted on a single-track scale (RSLA ABS) which allows displacement measurement with a resolution of 5 nm. The horizontal force is measured thanks to a load cell (FUTEK LCM 550) located in the middle of the piston with a resolution ± 0.03 kN over the range 0-220 kN.

Two hydraulic intensifiers are used for fluid pressure generation up to 100 MPa, fluid flow up to $60 \text{ cm}^3/\text{min}$ through the sample, and dilatancy and permeability measurements. The intensifiers volume is 130 mm^3 each. Permeability can be measured by steady state, transient and harmonic flows methods. The two intensifiers are controlled by servo-valves (MOOG

Appendix A. HighSTEPS: A High Strain TEMperature Pressure and Speed Apparatus to study Earthquake mechanics

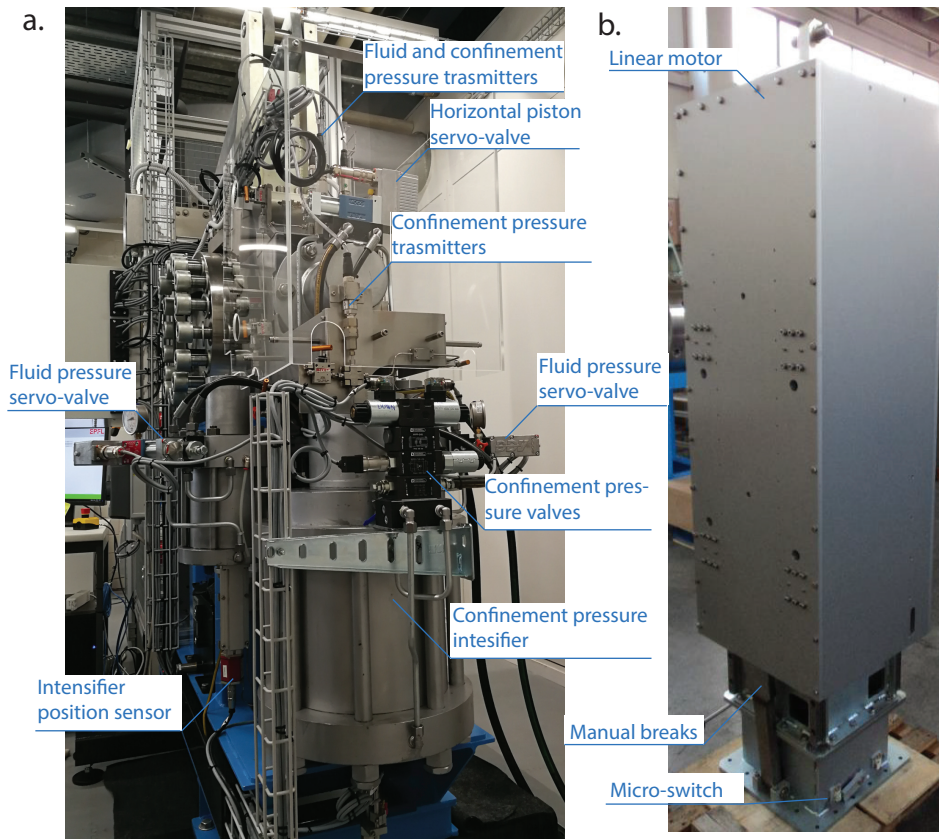


Figure A.3: a) detailed of the intensifiers, B) details of the motor tower.

D633-592B Type R01KO1D0NSS2) mounted on the top of the intensifiers. Fluid pressure is measured by a pressure transmitter (Gefran TSPA series) with a resolution of 100 kPa. The intensifiers displacement is measured by two magneto-restrictive transducers (TEMPOSONIC RP-V-0100M-D70-1-S1B1100) with a resolution of $0.5 \mu\text{m}$.

The third intensifier is used to apply oil confining pressure up to 100 MPa and has a larger volume than the pore fluid intensifiers, i.e., 1425.5 cm^3 . Confining pressure intensifier is controlled by a bi-directional valve (D DS3-S3/11N-D24K1) and a single-stage proportional valve (MZE4/58-24, MVPP-D/50, MERS-GD/50) fixed on the intensifier. Confining pressure is measured by two pressure transmitters (Gefran TSPA series) with a resolution of 100 kPa, one located close to the intensifier, and the other one located close to the pressure vessel (Figure A.3). Intensifier displacement is measured by Gefran ICC150EM linear potentiometer with a stroke of 150 mm.

Pressure vessel

The pressure vessel was built by RMP S.r.l., located in Rome, Italy. It is made in stainless steel, weighs about 500 kg, and has an external diameter of 700 mm and an internal diameter

of 300 mm (Figure A.2b). It is designed to support 100 MPa confining pressure. The vessel holds up the vertical and horizontal pistons. To close the vessel, two doors of 130 kg each are equipped with 20 M36-size bolts. To ensure perfect sealing of the chamber, high-pressure and temperature dynamic seals are mounted on each door and on the pistons. To ensure easy opening and closing, the doors are supported by swing arms. Three pore pressure lines (two connected to one pore pressure intensifier and one connected to the other pore pressure intensifier, see Figure A.2b-c and Figure A.4a) and one oil confining pressure line are connected to the pressure vessel. The pressure vessel is equipped with eight high pressure co-axial feedthroughs from Kemlon for acoustic sensors connection, 24 uniaxial feedthroughs for strain gauge connection, and 3 type K thermocouple feedthroughs (Figure Figure A.2b-c). Another access port located at the bottom of the vessel is used to fill and empty the vessel with the confining oil. The confining medium is a silicon oil from Green Star High Tech lubricants.. The oil tank is equipped with a pump which is used to fill the pressure vessel above (Figure A.2a).

Heating system

The heating system, composed of two heating plates of 26 mm diameters with a high resistance, are fixed on the inner part of the vessel doors (Figure A.2b-c). The maximum temperature of 120 °C is limited by the confining oil flash point and the maximum temperature supported by the seals located on the vessel doors. Temperature is measured within the 2 heating plates and in the confining medium by 3 K-type thermocouples. Temperature is controlled by a closed loop regulation.

The four linear motors and vertical pistons

The motion of the vertical piston of the machine (applying the shearing velocity and shear force to the experimental fault) represents the most innovative aspect of the apparatus. It consists in four linear motors from Kollmorgen, Type IC44-200 A3 AC TS C1, which are mechanically mounted and electrically connected in parallel (Figure A.3b). These motors are controlled by four motor controllers (one master and 3 slaves), Brushless Drive KOLLMORGEN type AKD 48A-AKD-10038. Each motor is equipped with 1 optical linear encoder Renishaw (RL 26BAT050B30A) with a resolution of 50 nm mounted on a single track-scale RSLA ABS, for a total of 4 encoders (1 master and 3 slaves) used to control the displacement, velocity and acceleration of the vertical piston. The Kollmorgen motors are frameless permanent magnet, three phase brushless servo motors composed of a coil assembly (also called the slider) and a magnet track (also called the magnet way). The mechanical support for the four motors is composed of a fixed frame where the coil assembly are screwed resulting in a total weight

Appendix A. HighSTEPS: A High Strain TEMperature Pressure and Speed Apparatus to study Earthquake mechanics

of 185 kg, and a moving part where 4 aluminum plates of 35 kg each are equipped with the permanent magnet tracks. A safety block composed of two manual breaks and micro-switches is fixed at the bottom of the frame and allows motor parking between the experiments. A second safety block, composed of two rigid springs, is fixed at the top of the frame and allows safe deceleration of the motors. The motors are water cooled during long term experiments to avoid over heating of the magnetic coils. To turn on the motors, the machine is equipped with its own 125 A electrical panel. The connection between the motors and this panel is made of 4 electrical power cables and Ethernet cables for the four optical encoders (one for each motor). The four motors allow a nominal force up to 28 kN (6.9 kN each motor) and a peak force up to 37 kN (8.4 kN each motor), velocities from $\sim 7 \mu\text{m/s}$ to 2.9 m/s and acceleration up to 70 m/s^2 . The motors are able to imposed a velocity function with a given acceleration, deceleration and target velocity.

The vertical piston driven by the linear motors is fixed on the pressure vessel and connected to the motors frame with a lever of 1:7 ratio (Figure A.1 and Figure A.2a), allowing a maximum force applied on the sample of 193 kN with a maximum stroke of 5 cm. However, due to the lever, velocity and acceleration on the sample side are reduced to maximum 0.25 m/s and 10 m/s^2 respectively. The vertical piston is equipped with an optical linear encoder Renishaw (RL 26BSS005C30 A) mounted on a single track-scale RSLA ABS which allows displacement measurement with a resolution of 5 nm. The vertical force is measured and controlled thanks to a load cell (FUTEK LCM 550) mounted in series with the piston with a resolution $\pm 0.03 \text{ kN}$ over the range 0-220 KN. The vertical piston located in the upper part of the vessel is equipped with a compensation piston (co-axial and passive) in the lower part of the vessel, to avoid confining oil overpressure during fast vertical movements. The compensation piston is mechanically connected to the vertical piston thanks to 2 metallic clamps inside the pressure vessel (Figure A.2b-c). During shearing experiments, the vertical piston moves downward entering in the vessel and contemporaneously the compensation piston moves downward exiting the vessel, resulting in oil volume and oil pressure kept constant inside the vessel during the entire experiment. Moreover, the mechanical connection between the vertical piston and the compensation piston during the entire experiments ensures that the confining pressure does not contribute in the vertical load measured by the load cell. The sample assembly is located in between the vertical and the compensation pistons (Figure A.2b).

Sample holders

Experiments can be carried out on both bare surface's samples and powdered samples, for which two different sample holders are used. The sample holders are designed for double-direct shear configuration and are composed of three forcing blocks of stainless steel: a central block of dimension $110 \times 50 \times 34 \text{ mm}^3$ and 2 side blocks of dimension $69 \times 34 \times 34 \text{ mm}^3$ (Figure

A.4). A constant contact area of $34 \times 20 \text{ mm}^2$ for bare surfaces and $34 \times 34 \text{ mm}^2$ for rock powder is kept constant during experiments. For experiments with powdered samples the forcing blocks are grooved allowing shearing within the sample and not at the boundary between the sample and the forcing blocks. For bare surfaces the forcing blocks present housing of the exact size of the samples to keep well-aligned during shearing. The forcing blocks are equipped with high pressure fluid ports and channels allowing high pore fluid pressure experiment (Figure A.4a), and permeability and dilatancy measurement during shearing. The two side blocks are also equipped with holes for piezo electrical transducer of 9 mm diameters. For experiments performed with confining pressure, the samples are isolated from the confining medium by using a double layer of latex jackets. This jacketing ensures limited biasing in terms of friction and can handle a large amount of deformation (maximum of 3 cm slip) before the jacket failure.

Control and acquisition systems

The control and acquisition system was built by MEquadrat, based in Root, near Lucerne, Switzerland. It consists of a real-time IO Controller CompactRIO (National Instruments), which allows data acquisition at rates up to 50 kHz and real-time control of the normal stress, confining pressure, pore fluid pressure, temperature and slip velocity or shear stress. Additionally, up to 4 quarter-bridge strain gauges can be measured.

The horizontal piston can be controlled both in position mode and in force mode thanks to closed loop servo control. The two pore fluid pressure intensifiers can be controlled in position, flow and pressure mode thanks to the closed loop servo control. Additionally, it is possible to impose sinusoidal oscillations of pressure. The confining oil pressure intensifier can only be controlled in pressure feedback servo control mode.

The vertical piston is controlled by a dedicated motion controller, which is controlled by the real-time IO Controller, allowing very short regulation times. The piston can be controlled in position, velocity and force mode thanks to closed loop servo control.

Appendix A. HighSTEPS: A High Strain TEMperature Pressure and Speed Apparatus to study Earthquake mechanics

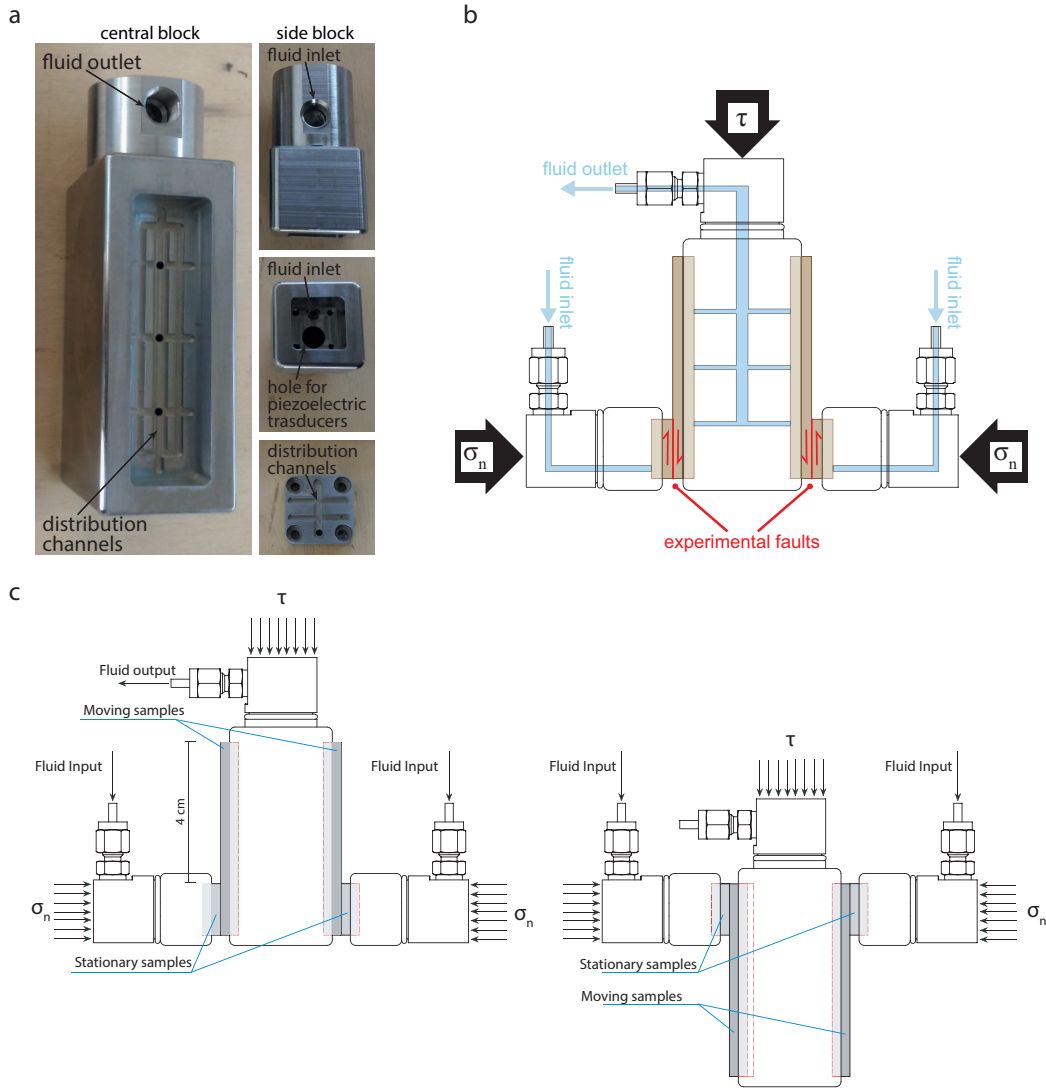


Figure A.4: Experimental double direct shear configuration: a) pictures of the central block showing the fluid inlet and the distribution channels, pictures of the side block showing fluid inlet, hole for piezoelectric transducer and distribution channels. b) Schematics of the experimental double-direct-shear configuration. The sample holders are equipped with internal pore fluid channels for application of pore fluid pressure, injection of fluids and measurement of permeability/dilatancy of the fault rocks. c) Sketch of the working principle of the double-direct shear configuration.

A.4 First Tests on the machine

Machine Stiffness

To determine the apparatus distortion during deformation of samples, we deformed steel blocks of known stiffness (Young modulus $E = 210$ GPa) with both the vertical and horizontal pistons. We measured the resulting displacement of the apparatus by removing the contribution of the elastic deformation of the steel blocks (Figure A.5). We performed the tests under room pressure and temperature conditions, imposing force steps of 1 kN at forces below 5 kN, steps of 5 kN at forces below 80 and 100 kN, for the horizontal and vertical piston respectively, and steps of 10 kN at higher forces. After reaching 160 kN, we performed down-steps in force on the horizontal axis. Figure 5 shows the displacement versus load for both up-steps and down-steps measurements. Machine stiffness is defined as the slope of the linear regression between the points. Horizontal machine stiffness is 1786 kN/mm at load > 60 kN, vertical machine stiffness is 1379 kN/mm at load > 15 kN. Low stiffness at low normal stresses could be due to bad closure of the interfaces between the steel block and the piston/vessel.

Preliminary results on calcite and quartz

Effect of normal stress

We used both gouge and bare surfaces of calcite (Carrara marble) to test the normal stress dependence of the frictional strength and compare the measurements performed with the new machine with previous experiments. Experiments were run under double-direct shear configuration for gouge and single direct shear for bare surfaces.

To produce calcite gouge, Carrara marble was crushed and sieved to $< 200 \mu\text{m}$ grain size. Gouge layers of 5 mm thickness were sandwiched between the grooved steel blocks. To produce calcite bare surfaces samples, Carrara marble slabs of 12 mm thickness were cut into pieces with dimension of $20 \times 34 \times 12 \text{ mm}^3$ and $70 \times 34 \times 12 \text{ mm}^3$, to ensure a $34 \times 20 \text{ mm}^2$ constant contact area during shearing. The two surfaces in contact during the experiment were polished with a P60 grit SiC abrasive paper. Experiments were performed without confining pressure, under room temperature and nominally dry conditions.

Steady state friction coefficient was determined at slip velocity from $33 \mu\text{m/s}$ to 33 mm/s and normal stresses from 5 MPa to 50 MPa, for gouge, and at slip velocity of $10 \mu\text{m/s}$ and normal stresses from 5 MPa and 12.5 MPa for bare surfaces.

The shear stress versus displacement curves for gouge samples at slip velocity of 6.6 mm/s are shown A.6a. In all experiments, the shear stress first increased linearly with the displacement (i.e., elastic phase). Following elastic deformation, the shear stress showed a nonlinear decreasing as a function of displacement (i.e., slip hardening phase) prior to peak stress. Then,

Appendix A. HighSTEPS: A High Strain TEMperature Pressure and Speed Apparatus to study Earthquake mechanics

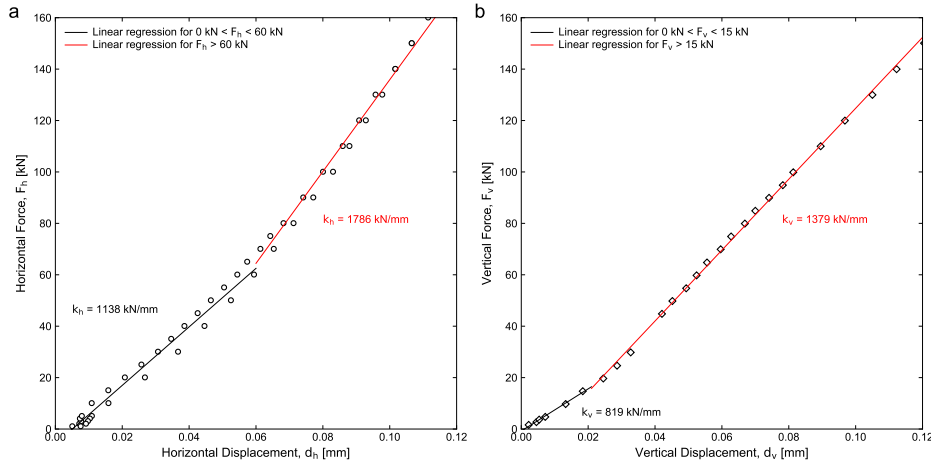


Figure A.5: a) Horizontal and b) vertical machine stiffness measure with steel blocks. The horizontal stiffness is 1786 kN/mm for vertical force (F_h) higher than 60 kN. The vertical stiffness is 1379 kN/mm for horizontal force (F_v) higher than 15 kN.

the sample sheared at a constant shear stress (i.e., steady state phase) following the attainment of peak stress, expect for the sample deformed at 50 MPa, that showed a slip softening phase after 5 mm displacement. Figure A.6b shows the linear pressure dependence of calcite frictional strength (Byerlee, 1978). The steady state friction coefficient is obtained from the linear regression of the steady state shear stress versus applied normal stress and it is 0.53 for bare surfaces and 0.50 for gouge. The intercept of the linear regression shows the negligible cohesion of imbrication of the bare surfaces (0.44 MPa) and the gouge (0.88 MPa). The steady state apparent friction during experiments at low velocity (3.3 and 33 $\mu\text{m/s}$) and 10 MPa normal stress is $\mu \approx 0.6$ in agreement with previous studies (Verberne et al., 2014b; Carpenter et al., 2015, 2016). Increasing the velocity to 6.6 cm/s, the apparent friction of calcite slightly decreases to values $\mu \approx 0.50$ -0.55, as expected based on the rate-and-state friction law for velocity weakening rocks (Marone, 1998; Marone and Saffer, 2015; Moore and Lockner, 2011) and on previous observations (Violay et al., 2014b; Pozzi et al., 2019).

Effect of velocity

Faults respond to perturbations depending on their stability state by remaining locked (stage 1), undergoing slow and stable sliding (stage 2), experiencing local on-fault short-lived unstable events (earthquake precursory sequence) (stage 3), or accelerating toward catastrophic seismic slip (main event) (Kaneko et al., 2010) (stage 4). The transition from stage 1 to 2, 3 or 4 controls the slip behavior during fault reactivation, i.e., the earthquake potential of a fault. Rate- and- state friction (RSF) laws provide a comprehensive analysis of the slip behavior. In this framework, the frictional response of a fault varies with the previous loading history

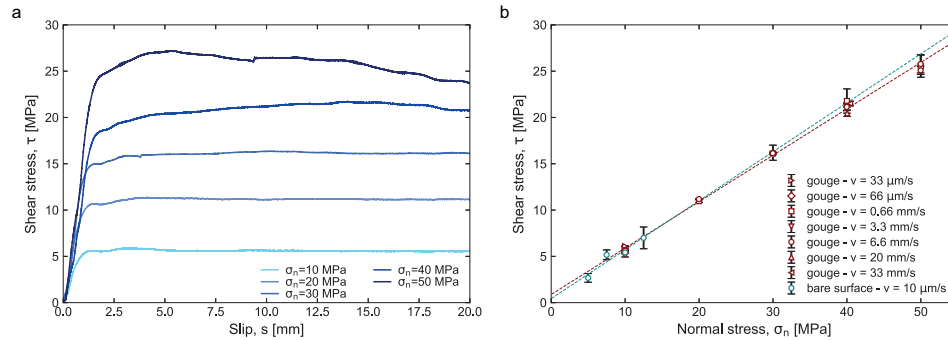


Figure A.6: Calcite (Carrara marble) gouge and bare surfaces frictional experiments: a) shear stress versus slip during frictional sliding at $v = 6.6 \text{ cm/s}$ and normal stresses from 10 MPa to 50 MPa. Experiments were performed under double-direct shear configuration on gouge material. d) Steady state shear strength versus normal stress for both gouge material and bare surfaces. Data plot along a single line with a slope of 0.6, in agreement with Byerlee's rule (Byerlee, 1978).

and depends on both the instantaneous slip velocity, normal stress, and a state variable that describes the progressive evolution of the sliding interfaces (Dieterich, 1972; Ruina, 1983; Dieterich, 1992). Depending on the frictional evolution in response to an instantaneous change in slip velocity or normal stress, the rate-and-state law evaluates the capability of a fault to nucleate earthquakes or to creep aseismically. Stage 4 controls earthquake propagation. During this stage, the slip velocity and power density (shear stress by velocity) increase drastically, inducing strong fault frictional weakening. Frictional weakening is controlled by a number of processes, such as flash heating and melting (Rice, 2006), decomposition reactions (Han et al., 2007), and superplastic flow and thermal pressurization (Violay et al., 2015). Many of these processes are actually thermally triggered (Di Toro et al. (2011) and references therein). Currently, (1) how the transition from slow slip velocity (RSF, slip velocity $\sim \mu\text{m/s}$) to high velocity weakening behavior (slip velocity $> \text{cm/s}$) occurs, and (2) the conditions that drive faults through the aforementioned stages 1 to 4 are not clear. The HighSTEPS apparatus cover slip velocity from $\mu\text{m/s}$ to m/s (i.e., stages 1 to 4), enabling the measurement of the rate-and- state friction parameters and friction evolution during fault weakening and lubrication. Therefore, a complete collection of the mechanical data that are required to assess a constitutive equation for rock-friction will be possible. In Figure A.7, examples of a slide-hold-slide sequence (Figure A.8a), single velocity step (Figure A.7b), high velocity friction experiment (Figure A.8c) and shear stress control experiment (Figure A.8d) are shown.

Slide-hold-slide sequences are performed to measure friction healing after a period of hold and thus to simulate fault re-strengthening during the inter-seismic phase. During this sequence, calcite gouge layers were sheared at a constant velocity of $10 \mu\text{m/s}$ followed by a hold period

Appendix A. HighSTEPS: A High Strain Temperature Pressure and Speed Apparatus to study Earthquake mechanics

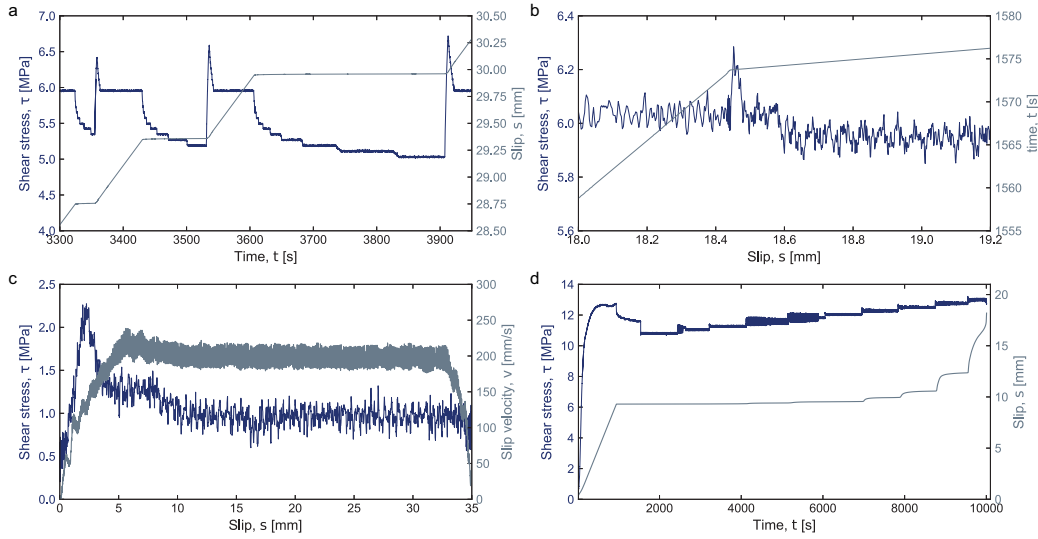


Figure A.7: Example of velocity control and shear stress control experiments performed: a) slide-hold-slide test performed on calcite gouge at 10 MPa normal stress under room temperature and wet conditions; b) velocity step test on quartz gouge at 10 MPa normal stress under room temperature and room humidity conditions; c) high slip velocity friction test on calcite bare surface at 10 MPa normal stress under room temperature and room humidity conditions; d) shear stress control test on calcite gouge at 20 MPa normal stress under room temperature and room humidity conditions.

(t_h) during which the vertical ram stopped and gouge layers were under quasi-stationary contact. The slide-hold-slide sequence was conducted under wet conditions (CaCO₃-equilibrated water). The hold periods showed in Figure A.7a are 30, 100 and 300 s. After each hold period, the gouge was re-sheared at 10 $\mu\text{m/s}$, as is shown in Figure A.7a. We observe an increase of friction upon re-shear, followed by a decay to the previous steady state value. This difference in friction between the peak and the steady state ($\Delta\mu$) is defined as the frictional healing and is typical of granular gouge material (Marone, 1998; Richardson and Marone, 1999).

The frictional healing rate $\beta = \Delta\mu / \Delta \log_{10}(t_h)$ measured for calcite gouge under wet conditions is $\beta = 0.029$ in agreement with previous works (Giorgetti et al., 2015; Carpenter et al., 2016).

The velocity step was performed on quartz gouge with grain size $< 125 \mu\text{m/s}$ (Figure A.7b) and showed an abrupt change in friction (direct effect, a parameter in rate-and-state law) and a pronounced evolution effect (b parameter in rate-and-state law). The resulting negative $a - b$ value is in agreement with previous studies on quartz gouge (Marone, 1998; Marone and Saffer, 2015; Moore and Lockner, 2011).

High velocity friction experiment was performed on calcite bare surfaces at slip rate of 0.2 m/s, acceleration and deceleration of 5 m/s² and normal stress of 10 MPa (Figure A.7c). Once the velocity function was applied, the sample initially deformed elastically (i.e., the shear stress increased linearly with time), until the static friction was overcome and slip on the sample

initiated. Consistently with previous experimental observations, the shear stress decayed towards a steady state friction value of 1 MPa corresponding a steady state friction coefficient of 0.2 (Violay et al., 2014b).

The vast majority of previously described experiments, either under slow or high slip velocity, has been conducted by imposing velocity functions. However, it is more realistic boundary condition to describe fault loading in terms of acting stress, whether it is virtually constant, slowly increasing due to tectonic loading, or increasing/decreasing in sudden steps (stress transfer) due to ruptures in the vicinity of the fault. Thus, controlling the shear stress and allowing the slip velocity to adjust spontaneously, rather than the contrary, is closer to natural conditions where the “far field” stress, together with the frictional properties of the fault materials, controls the mechanical response of the fault zone. To this end, HighSTEPS apparatus is able to impose up and down shear stress steps. Figure A.7d shows an experiment conducted in shear stress control mode. Initially, the calcite gouge sample was deformed under double-direct shear configuration at constant velocity of 10 $\mu\text{m/s}$ and normal stress of 20 MPa, room pressure and temperature condition, until the steady state shear stress was achieved and the fault accumulated 10 mm of displacement. Then we switched the controlled mode into shear stress control mode, and the shear stress was gradually increased by small (0.5 MPa) stepwise increments. The response to the loading is measured in terms of slip velocities. After each shear increment, we waited until either a quasi-static balance or a steady-state sliding is achieved before applying of the next stress increment. The process is repeated until the onset of the main instability, that is, the catastrophic acceleration of slip to 100 $\mu\text{m/s}$. We observe slip pulses which develop right after the instantaneous shear stress increase. During the last stress step, the fault gouge spontaneously evolved from primary, to secondary, and tertiary creep (Scholz, 1968).

Test with the pressure vessel, temperature and pore fluid pumps

First tests conducted within the pressure vessel, applying confining pressure, pore pressure and temperature have been performed without shearing the sample, i.e., vertical motion. Figure A.8 shows that the vessel and the confining and pore fluid intensifiers can support pressure up to 80 MPa testifying the accurate control of these parameters. Figure A.8d shows also that temperature control is accurate ($\pm 3\text{-}4^\circ\text{C}$).

Appendix A. HighSTEPS: A High Strain TEMperature Pressure and Speed Apparatus to study Earthquake mechanics

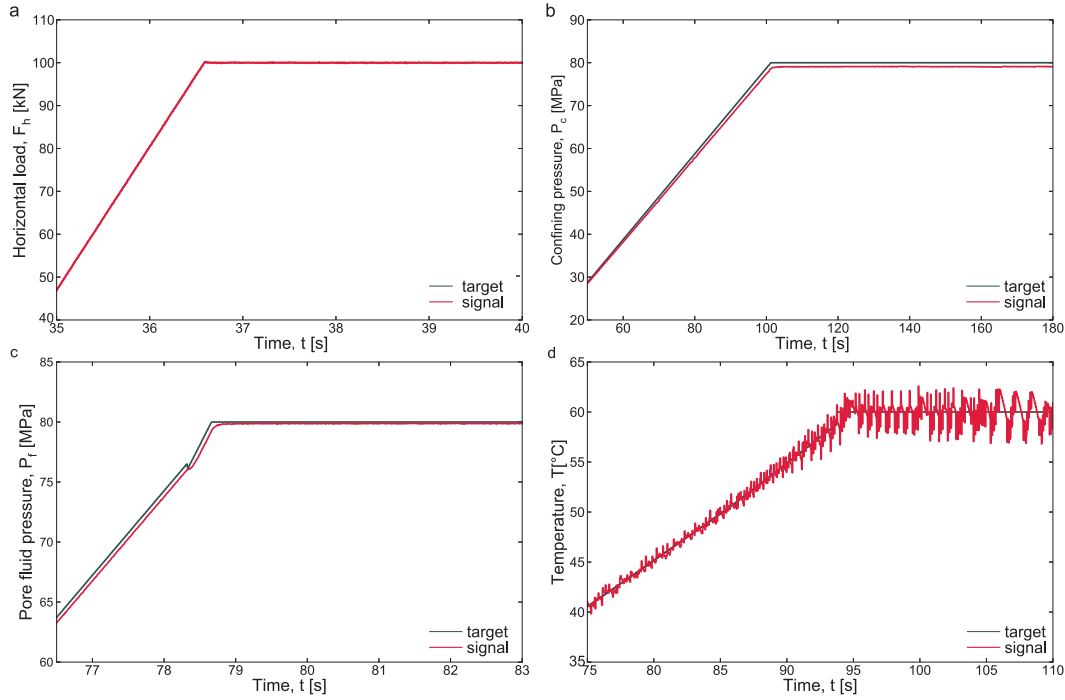


Figure A.8: a) Horizontal load versus time showing the load control in ramp (kN/s) and constant value (100 kN). b) Confining pressure versus time showing the control in pressure up to 80 MPa. c) Pore fluid pressure versus time showing the control in pore fluid pressure. d) Temperature versus time showing the control in temperature up to 60 °C.

A.5 Future machine development

We are currently finalizing the design of the jacketing system that will allow us to run experiments under both low and high slip velocities, high confining pressure, high pore pressure and high temperature. Using this jacketing system (Figure A.2c), we will be able to measure fault dilatancy and permeability. This new jacketing system will also allow to use up to 8 acoustic sensors glued directly on the rock samples and up to 4 quarter-bridge strain gauges. With this new equipment, we aim at better understanding the evolution of frictional properties of fault rocks over the entire seismic cycle, going from long inter-seismic period, earthquake nucleation to propagation.

B Effect of water and rock composition on re-strengthening of cohesive faults during the deceleration phase of seismic slip pulses

Authors: Marie Violay¹, Francois Passelègue¹, Elena Spagnuolo², Giulio Di Toro^{2,3}, Chiara Cornelio¹.

¹ Laboratory of Experimental Rock Mechanics (LEMR), ENAC, EPFL, Switzerland;

² Istituto Nazionale di Geofisica e Vulcanologia, INGV, Rome, Italy;

³ Dipartimento di Geoscienze, Università degli studi di Padova, Padua, Italy;

Reference: Violay, M., et al. "Effect of water and rock composition on re-strengthening of cohesive faults during the deceleration phase of seismic slip pulses." *Earth and Planetary Science Letters* 522 (2019): 55-64.

Contributions: M. Violay and E. Spagnuolo performed the experiments. E. Spagnuolo and G. Di Toro have contributed to the testing strategy and methodology. M. Violay has prepared and characterized samples used in this study. C. Cornelio performed the numerical models of the paper with the input of M. Violay and F. Passelègue. M. Violay has written the manuscript. All the co-authors have edited and guided discussion of the manuscript.

Highlights:

- Effect of rock composition and water content on fault re-strengthening during earthquakes.
- Re-strengthening rate is faster in carbonate-than silicate-bearing rocks at low power density.
- In silicate rocks, re-strengthening rate increases with power density and in presence of

Appendix B. Effect of water and rock composition on re-strengthening of cohesive faults during the deceleration phase of seismic slip pulses

water.

- In carbonate rocks, re-strengthening rate decreases with power density and in presence of water.
- Silicate rocks promote intense high frequency radiation during deceleration of the seismic slip.

B.1 Abstract

The elastic strain energy release rate and seismic waves emitted during earthquakes are controlled by the on-fault temporal evolution of the shear stress during rupture propagation. High velocity friction experiments highlighted that shear stress on the fault surface evolves rapidly during seismic slip pulses. This temporal evolution of shear stress is controlled by both fault weakening at seismic slip initiation and re-strengthening rate towards the end of slip. While numerous studies focused on fault weakening, less attention was given to co-seismic re-strengthening processes. Here we performed 53 friction experiments (normal stress ≤ 30 MPa, slip-rate $\leq 6.5 \text{ m s}^{-1}$) imposing constant slip acceleration and deceleration (7.8 m s^{-2}), on cohesive Carrara marble (99% calcite) and micro-gabbro (silicate-built rock) under dry, vacuum and water pressurized conditions. Microstructural observations showed that micro-gabbro accommodated seismic slip by bulk melting of the sliding surfaces, whereas Carrara marble by coupled decarbonation and grain-size dependent crystal plastic processes. Under room humidity conditions and low imposed power density (i.e., product of normal stress per slip rate), re-strengthening rate during the deceleration stage was up to ~ 17 times faster in marble than in microgabbro. In the latter, the re-strengthening rate increased slightly with the power density. The presence of water enhanced further this trend. On the contrary, in marbles the re-strengthening rate decreased drastically with power density and in the presence of water. Our experimental observations highlighted the first order importance of the mineralogy and rheology of the slip zone materials and, to a second order, of the presence of water in controlling co-seismic re-strengthening of faults during seismic slip deceleration.

B.2 Introduction

Earthquakes are the result of sudden slip along faults, which releases the elastic strain and gravitational energy stored in the wall rocks (Reid, 1910; Kanamori and Rivera, 2006).

Damage associated with earthquakes is due to the radiation of elastic waves during seismic rupture propagation (Stein and Wysession, 2009; Madariaga and Olsen, 2002; Marty et al., 2019) and to dynamic stress concentration at the rupture front (e.g., Andrews (2005)). The intensity and the frequency of seismic waves (ground motions) are controlled by the rupture length and by the abrupt variations in rupture and slip velocities along fault during earthquakes (Brune, 1970; Madariaga, 1976). Seismic rupture ($\sim \text{km/s}$) and slip velocities ($\sim \text{m/s}$) depend in particular on the temporal evolution of the shear stress along the fault during sliding (i.e., fault strength weakening and re-strengthening) (Ida, 1972; Ruina, 1983).

Friction experiments, performed with rotary shear machines designed to impose on rock specimens slip and slip rates typical of natural earthquakes, proved that experimental faults weakened due to several rock-type and environmental-dependent thermally activated weak-

Appendix B. Effect of water and rock composition on re-strengthening of cohesive faults during the deceleration phase of seismic slip pulses

ening mechanisms, including melt lubrication, grain-size dependent processes, thermal and thermomechanical pressurization of pore fluids, etc. (Tsutsumi and Shimamoto, 1997; Di Toro et al., 2004; Han et al., 2010; Rice, 2006; Ferri et al., 2010; Di Toro et al., 2011; Green et al., 2015; De Paola et al., 2015; Spagnuolo et al., 2015; Violay et al., 2015).

Field studies of exhumed natural seismogenic faults support the evidence of rapid weakening and fault lubrication during earthquakes (Sibson et al., 1975; Di Toro et al., 2006). The rheology of the fault is related to the physical state (e.g., liquid vs. solid) of the slipping zone (Rice, 2006), the slip rate and slip acceleration (Di Toro et al., 2004; Niemeijer et al., 2011; Chang et al., 2012), the rock composition (Di Toro et al., 2011; Goldsby and Tullis, 2011; Green et al., 2015), the presence of water (Violay et al., 2013, 2014a,b), the ambient and local temperature (Lockner et al., 1987; Verberne et al., 2015), and in presence of non-cohesive rocks, on the gouge grain size (De Paola et al., 2015). Indeed, in cohesive rocks, slip is highly localized from the very initiation of sliding and the rise of the temperature in the slipping zone increases with slip rate, effective normal stress and square root of the duration of sliding (Rice, 2006; Aubry et al., 2018). In cohesive rocks, the abrupt increase in temperature favors flash heating and weakening mechanisms (Goldsby and Tullis, 2011) which may eventually evolve, for some silicate-built cohesive rocks, in bulk melting (Hirose and Shimamoto, 2005; Niemeijer et al., 2011; Violay et al., 2013; Aubry et al., 2018). On the contrary, in the presence of gouges, some slip is required before strain localization is achieved (Beeler and Tullis, 1996; Marone et al., 1990; Smith et al., 2015; Platt et al., 2014, 2015; Rice et al., 2014; Rempe et al., 2017). As a consequence, heat production is more distributed in the slipping zone and other processes including thermal (if fluids are already present in the pores of the slipping zone) and thermomechanical (if fluids like CO₂ and H₂O are released by the breakdown of the minerals of the slipping zone) pressurization might be favored before bulk melting of the slipping zone occurs (Rice, 2006; Segall and Rice, 2006; Brantut et al., 2008; Ferri et al., 2010; Acosta et al., 2018).

While the physical parameters controlling fault weakening have been extensively studied, little attention has been dedicated on the processes associated to frictional re-strengthening observed during slip deceleration in seismic velocity pulses (Del Gaudio et al., 2009; Chang et al., 2012; Liao et al., 2014; Proctor et al., 2014; Sone and Shimamoto, 2009). However, fault strength evolution, i.e. both strength weakening and re-strengthening, coupled with electro-dynamic rupture propagation contributes actively to the slip rate evolution during seismic faulting and to the release of seismic waves (Sone and Shimamoto, 2009). In addition, co-seismic re-strengthening processes controls the energy budget of earthquakes, as well as the transition from crack-like to pulse-like rupture, which implies a strong fault re-strengthening after the passage of the rupture front (Beeler and Tullis, 1996). Few mechanisms of fault re-strengthening have been proposed so far: (1) temporal variation of stress conditions on the rupture interface during the passage of the rupture front (e.g., punctual pore fluid pressurization) (Lykotrafitis et al., 2006), (2) spatial variation of the initial stress field (barrier model) (Peyrat et al., 2001; Latour et al., 2011), (3) high dependence of friction to sliding velocity, i.e.,

“self-healing” behavior during sliding velocity deceleration (Beeler and Tullis, 1996; Sone and Shimamoto, 2009; Proctor et al., 2014; Perrin et al., 1995; McLaskey et al., 2015; Zheng and Rice, 1998). Here, we present friction experiments that, by reproducing seismic slip conditions, aim at understanding the effect of rock composition and water content on fault re-strengthening during slip deceleration. In particular, we focused on cohesive rocks (calcitic marble and microgabbro) where strain is localized from slip initiation to the final re-strengthening stage and the temperature evolution in the slipping zone is simpler than in case for non-cohesive rocks (gouges). Moreover, the analysis of the data reported here exploit the achievement of the so-called “steady-state” shear stress conditions in the experiments. This achievement requires slips of several centimeters to tens of centimeters depending on the applied effective normal stress (Di Toro et al., 2011). Consequently, the results presented here should be valid for moderate to large in magnitude earthquakes, though steady-state conditions might not ever be achieved in nature (Liao et al., 2014). The experimental evidences suggest that rock composition and environmental conditions play a pivotal role in fault re-strengthening during seismic faulting, with dramatic consequences in the radiation pattern of the emitted seismic waves.

B.3 Methods

We performed 53 high speed friction experiments on hollow cylinders (30/50 mm internal/external diameter) of carbonate-built rock (Carrara marble, 99% calcite) and silicate-bearing rock (micro-gabbro) (for sample preparation, see Nielsen et al. (2012)). Carbonate-built rocks and gabbros often host earthquakes sequences in nature, as attested by geological evidence (Sibson, 1975). The experiments were performed with SHIVA, a rotary shear machine installed at the HP-HT INGV laboratories in Rome (Table B.1). SHIVA was equipped with two brushless engines (max power 300 kW) and an air actuator (2000 kg amplified to 5000 kg thanks to a lever) in a rotary shear configuration to slide the two contacting hollow rock cylinders under the desired conditions (Di Toro et al., 2010). Experiments were performed either in the presence of pressurized liquid water, room humidity or under vacuum (10^{-4} mbar). In the experiments with liquid water, SHIVA was equipped with a pressurizing system which consisted of (1) a fluid pressure vessel (i.e., the samples were fully immersed in water), (2) a membrane pump with a 30 cm³ fluid capacity, (3) a pressure multiplier that imposes up to 15 MPa of fluid pressure (P_f), (4) a pressure regulator and, (5) valves and pipes (Violay et al., 2013). Normal stress (σ_n) and pore pressure (P_f) (drained conditions) were kept constant during experiments to target values ranging between 10 and 40 MPa and 0 (nominally dry) and 15 MPa, respectively. To mimic the sliding velocity at a given point of the fault during propagation and arrest of seismic slip, we imposed a trapezoidal slip velocity function by imposing constant acceleration and deceleration (7.8 m s^{-2}) and target slip velocities ranging

Appendix B. Effect of water and rock composition on re-strengthening of cohesive faults during the deceleration phase of seismic slip pulses

from 1 m s^{-1} to 6.5 m s^{-1} . Total slip ranged from 0.83 m to 18.37 m.

Mechanical data (axial load, torque, axial displacement, and angular rotation) were acquired at a frequency up to 25 kHz (for description of the installed instrumentation, their calibration and acquisition rates, see Niemeijer et al. (2011)). Normal stress, shear stress (τ) and slip-rate (V) were computed from experimental measurements following Tsutsumi and Shimamoto (1997) and Di Toro et al. (2010).

Table B.1: Summary of experimental conditions and results. PF: Pore fluid, RH: Room Humidity, VAC: Vacuum. μ_p peak friction coefficient, μ_{dyn} steady state or dynamic friction coefficient, $\dot{\mu}_r$ friction re-strengthening rate

Exp	Lithology	Cond.	V [m/s]	σ_n [MPa]	P_f [MPa]	μ_p	μ_{dyn}	Final slip [m]	$\dot{\mu}_r$ [s ⁻¹]
s227	Carrara Marble	PF	1	15	5	0.8	0.1	4.27	2
s252	Carrara Marble	PF	1	15	5	0.79	0.08	3.35	1.67
s264	Carrara Marble	PF	1	15	5	0.6	0.09	15.82	0.98
s415	Carrara Marble	PF	1	15	5	0.56	0.11	4.66	1.15
s220	Carrara Marble	PF	2	15	5	0.85	0.1	11.22	0.48
s418	Carrara Marble	PF	2	15	5	0.65	0.07	10.41	0.4
s413	Carrara Marble	PF	3	15	5	0.64	0.06	14.36	0.38
s298	Carrara Marble	PF	4	15	5	0.55	0.05	12.45	0.21
s296	Carrara Marble	PF	6.5	15	5	0.5	0.06	14.3	0.03
s234	Carrara Marble	PF	1	20	10	0.8	0.12	4.45	0.98
s341	Carrara Marble	PF	1	20	5	0.82	0.12	5.95	1.43
s240	Carrara Marble	PF	1	25	15	0.87	0.09	2.96	1.1
s407	Carrara Marble	PF	1	25	5	0.41	0.06	2.62	1.21
s414	Carrara Marble	PF	1	25	15	0.55	0.08	3.62	0.16
s615	Carrara Marble	PF	3	25	5	0.68	0.03	15.17	0.19
s409	Carrara Marble	RH	1	35	5	0.48	0.04	3.79	0.6
s163	Carrara Marble	RH	1	10	0	0.77	0.1	6.57	3.68
s224	Carrara Marble	RH	1	10	0	0.76	0.11	9.03	2.35
s254	Carrara Marble	RH	1	10	0	0.7	0.16	2.89	2.9
s257	Carrara Marble	RH	1	10	0	0.81	0.16	2.9	2.22
s331	Carrara Marble	RH	1	10	0	0.72	0.06	8.4	2.23
s305	Carrara Marble	RH	1	20	0	0.82	0.14	1.5	2.13
s306	Carrara Marble	RH	1	20	0	0.48	0.2	0.83	1.9
s307	Carrara Marble	RH	3	20	0	0.64	0.05	8.17	0.36
s308	Carrara Marble	RH	6.5	20	0	0.68	0.02	18.37	0.23
s464	Carrara Marble	RH	1	20	0	0.38	0.19	2.33	0.79
s338	Carrara Marble	VAC	1	10	0	0.52	0.08	11.71	2.25
s340	Carrara Marble	VAC	1	10	0	0.83	0.15	7.3	3
s468	Carrara Marble	VAC	1	10	0	0.75	0.1	2.37	2
s614	Carrara Marble	VAC	3	20	0	0.64	0.03	15.09	0.58
s570	Micro-Gabbro	PF	3	10	5	0.33	0.17	7.23	0.32

s617	Micro-Gabbro	PF	1	15	5	0.6	0.2	7.92	0.34
s568	Micro-Gabbro	PF	3	15	5	0.52	0.11	17.04	0.25
s569	Micro-Gabbro	PF	3	15	5	0.48	0.15	8.05	0.34
s566	Micro-Gabbro	PF	1	25	5	0.6	0.14	9.35	0.25
s567	Micro-Gabbro	PF	3	25	5	0.55	0.08	11.37	0.26
s572	Micro-Gabbro	PF	3	35	5	0.61	0.08	10.29	0.43
s573	Micro-Gabbro	PF	3	40	5	0.7	0.07	7.74	0.44
s565	Micro-Gabbro	RH	1	5	0	0.66	0.31	7.88	0.06
s559	Micro-Gabbro	RH	3	5	0	0.69	0.25	9.89	0.16
s562	Micro-Gabbro	RH	6	5	0	0.65	0.16	12.47	0.18
s564	Micro-Gabbro	RH	1	10	0	0.64	0.16	9.5	0.05
s609	Micro-Gabbro	RH	2	10	0	0.7	0.15	6.31	0.12
s554	Micro-Gabbro	RH	3	10	0	0.7	0.15	13.51	0.11
s610	Micro-Gabbro	RH	4.5	10	0	0.59	0.14	9.46	0.19
s558	Micro-Gabbro	RH	6	10	0	0.65	0.15	7.16	0.21
s563	Micro-Gabbro	RH	1	20	0	0.59	0.1	9.18	0.05
s555	Micro-Gabbro	RH	3	20	0	0.68	0.09	8.66	0.13
s560	Micro-Gabbro	RH	6	20	0	0.71	0.08	10.56	0.15
s557	Micro-Gabbro	RH	3	40	0	0.61	0.06	10.93	0.18
s584	Micro-Gabbro	VAC	3	5	0	0.6	0.2	1.79	0.13
s586	Micro-Gabbro	VAC	1	10	0	0.53	0.17	7.18	0.02
s585	Micro-Gabbro	VAC	3	20	0	0.57	0.08	11.95	0.18

B.4 Results

In all the experiments, once the slip velocity function was applied, the apparatus and the sample initially deformed elastically until the static friction coefficient μ_p ($\mu = \tau / \sigma'_n$ with $\sigma'_n = \sigma_n - P_f$) was overcome and slip initiated (Figure B.1). Then, the friction coefficient decreased exponentially with slip over a weakening distance D_w down to a so-called steady-state friction coefficient μ_{dyn} . Towards the end of the experiment, during slip velocity deceleration, the friction coefficient recovered with time and slip to a final value μ_r at the offset of slip (Figure B.1a–b). The effects of rock composition and environmental conditions on fault weakening and μ_p , μ_{dyn} and D_w were discussed in Violay et al. (2013, 2014a,b). As well as for initial fault weakening (Di Toro et al., 2011), the recovery of the friction coefficient during the deceleration stage of the velocity pulse is a function of the sliding velocity (Figure B.1c–d) (Goldsby and Tullis, 2011; Passelègue et al., 2014; Proctor et al., 2014). The value of μ_r ranged from 0.08 to 0.63 for Carrara marble and 0.11 to 0.37 for micro-gabbro, respectively, and independently of (1) the environmental conditions, (2) the final slip and (3) of the initial power ($\sigma'_n V$) imposed on the fault (Figure B.2, Figure B.3).

Appendix B. Effect of water and rock composition on re-strengthening of cohesive faults during the deceleration phase of seismic slip pulses

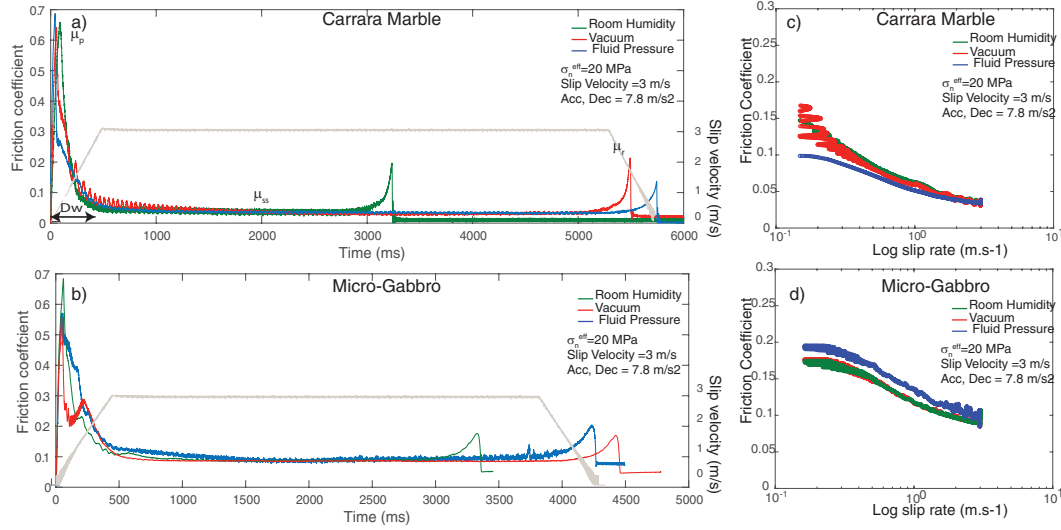


Figure B.1: Evolution of the friction coefficient with time and slip rate for Carrara marble and micro-gabbro slid at seismic slip rates. a) and b) Evolution of the friction coefficient with time in Carrara marble and micro-gabbro. c) and d) Evolution of the friction coefficient measured during deceleration versus log of the sliding velocity. The experiments were conducted at target velocity $V_t = 3 \text{ ms}^{-1}$, acceleration and deceleration $= 7.8 \text{ ms}^{-2}$, and $\sigma_{eff,n} = 20 \text{ MPa}$ (effective normal stress $= \sigma_n - P_f$). Blue curves (S615 and S567): fluid pressure experiments $\sigma_n = 25 \text{ MPa}$, $P_f = 5 \text{ MPa}$; green curves (S307 and S555): room humidity experiments; red curves (S614 and S585): vacuum experiments were run at $P_{vacuum} = 10^{-4} \text{ mbar}$. Two examples of sliding velocity function are drawn in grey. (For interpretation of the colors in the figure(s), the reader is referred to the web version of this article.)

To investigate the physics of the re-strengthening processes, we computed, for each experiment, the friction re-strengthening rate $d\mu/dt = (\mu_r - \mu_{dyn})/(t_r - t_{dyn})$, where $(t_r - t_{dyn})$ is the deceleration duration from end of the steady-state to the end of slip (Figure B.1a-b). At constant acceleration and deceleration rate, in the experiments conducted at low initial power density ($\sigma'_n V < 20 \text{ MWm}^{-2}$) and under both room humidity and vacuum conditions, the re-strengthening rate was ~ 17 times faster in Carrara marble (from 2.00 to 3.68 s^{-1}) than in micro-gabbro (from 0.02 to 0.16 s^{-1}) (Figure B.4). In both rock types, re-strengthening rate was initial power density-dependent and work density independent (i.e., slip independent) (Figure B.4). In Carrara marble, independently of the environmental conditions, the friction re-strengthening rate decreased with increasing power density (Figure B.3, Figure B.4). This trend was amplified in pressurized water conditions, and at the largest power densities tested, re-strengthening rate became almost negligible (Figure B.4a). The opposite behavior was observed in micro-gabbro. The re-strengthening rate slightly increased with the power density, and this effect was amplified in presence of pressurized water (Figure B.4b). Moreover, in Carrara marble the re-strengthening rate was about two times (at low power density) slower in the presence of pressurized liquid water than under room and vacuum conditions (Figure B.4).

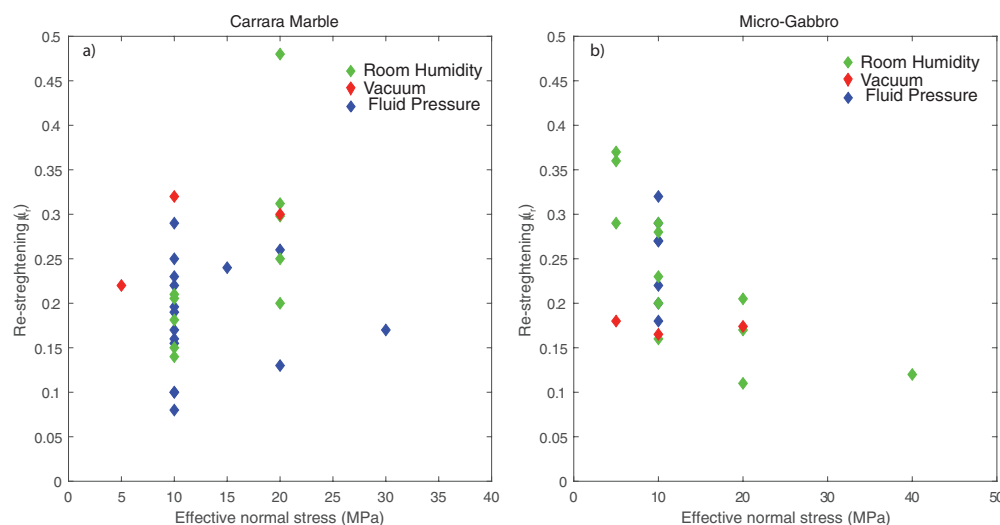


Figure B.2: Influence of $\sigma_{eff,n}$ on the re-strengthening for a) Carrara marble and b) micro-gabbro. Blue dots: fluid pressure experiments; green dots: room humidity experiments; red dots: vacuum experiments $P_{vacuum}=10^{-4}$ mbar.

Instead, in micro-gabbro, the frictional re-strengthening rate was about three times faster in the presence of pressurized liquid water than under room humidity and vacuum conditions (Figure B.4). Therefore, pressurized liquid water had an opposite effect on the frictional re-strengthening rate of Carrara marble with respect to the one of micro-gabbro.

Regarding the microstructures, mineralogy and geochemistry of the slipping zones and slip surfaces recovered after the experiments, we refer to previous studies performed (1) on several samples from the experiments presented here (Violay et al., 2013, 2014a,b) and (2) on slipping zone produced in experiments conducted on similar rocks (e.g., gabbro, basalts and Carrara marbles) under very similar deformation conditions (Han et al., 2010; Di Toro et al., 2011). In the case of micro-gabbro, the slipping zone consisted of a continuous ca. 200 μm thick layer of a quenched melt (see composition in Table B.3), independently of the presence or absence of liquid water (Figure B.5a) (Violay et al., 2015, 2014a,b; Nielsen et al., 2008, 2010; Niemeijer et al., 2011; Giacomel et al., 2018). In the case of the Carrara marble, the slipping zone after experiments conducted under vacuum and room humidity consisted of a 50 to 100 μm thick layer of nano- to micro-grained, poorly cohesive material made of calcite and, to a minor extent, lime (Violay et al., 2013; Spagnuolo et al., 2015) (Figure B.5b). Unfortunately, due to the poorly cohesive nature of the nano- to micro-grained deformed layer, most of the slipping zone was flushed away during sample recovery in the experiments performed in the presence of liquid water. However, the few micro-fault patches recovered from the slip surface showed the presence of nano- to micro-grained slipping zones (Violay et al., 2013, 2015) and evidence of calcite decarbonation attested by the presence of vacuoles within the grains. Violay et al. (2013) also showed evidence of CO_2 increase in the fluids recovered

Appendix B. Effect of water and rock composition on re-strengthening of cohesive faults during the deceleration phase of seismic slip pulses

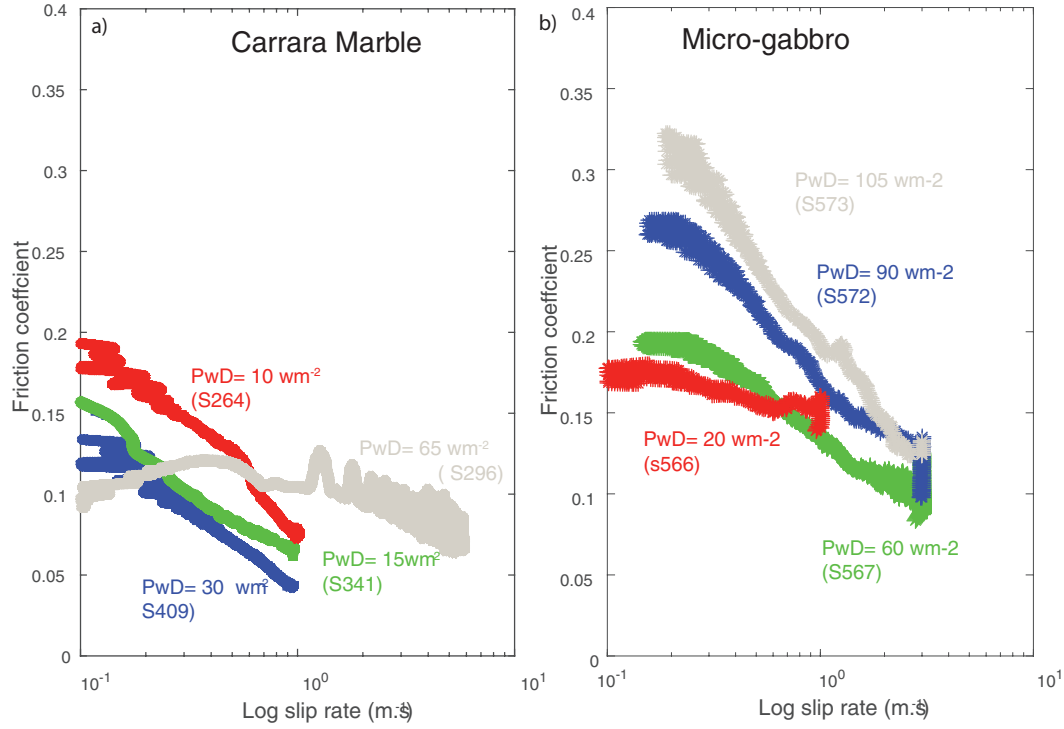


Figure B.3: Evolution of the friction coefficient during slip deceleration versus log of the sliding velocity for a) Carrara marble (S409, S341, S296, S264) and b) micro-grabbro (S566, S567, S572 and S573). Experiments were conducted at different power density ($\sigma_{eff,n} V_t$). Target velocity (V_t) ranging from 1 and 6.5 ms^{-1} , acceleration and deceleration $= 7.8 \text{ ms}^{-2}$, and $\sigma_{eff,n}$ from 10 to 30 MPa (effective normal stress $= \sigma_n - P_f$). The experiments were all performed under fluid pressure conditions ($P_f = 5 \text{ MPa}$).

after high-speed friction experiments performed on carbonate bearing rocks. We infer that also in the case of the experiments performed with Carrara marble, the slipping had the same microstructure independently of the presence or absence of liquid water.

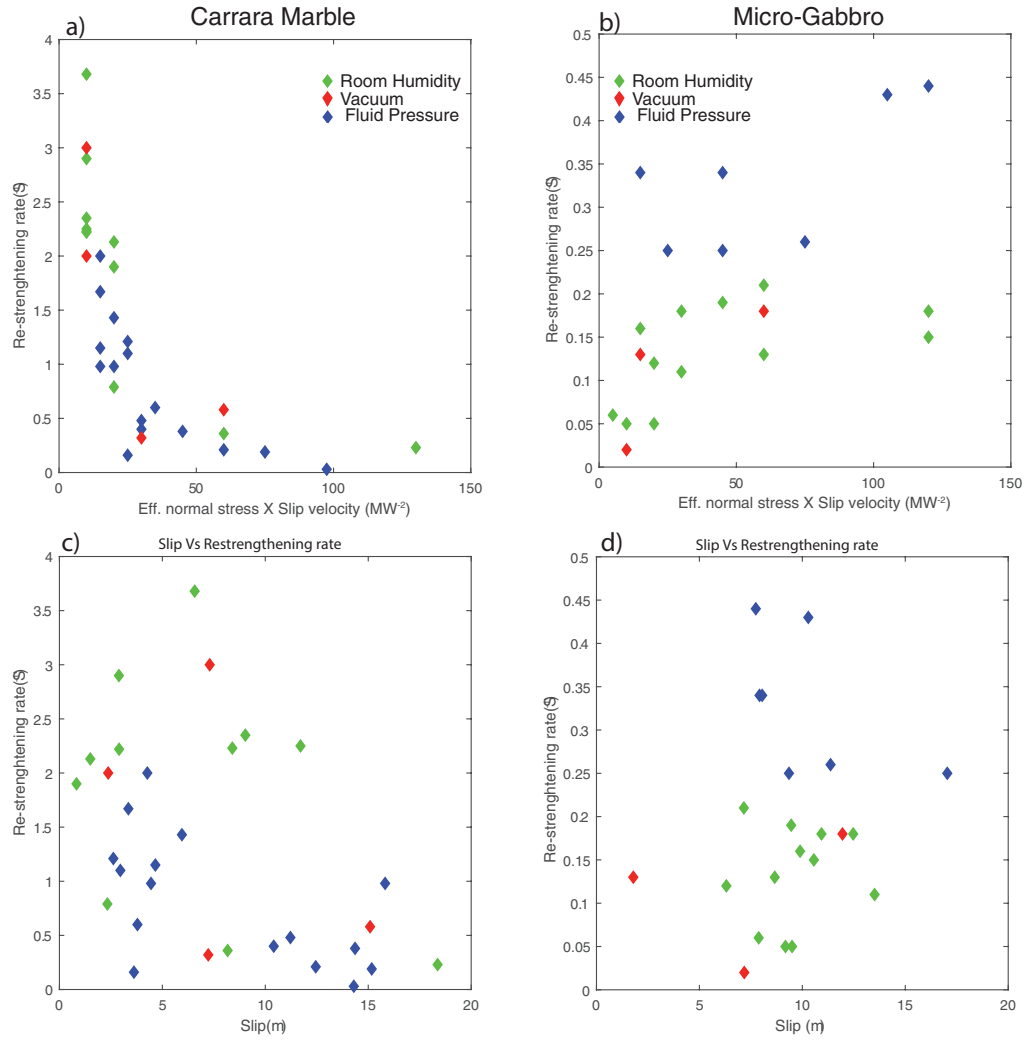


Figure B.4: Influence of power density (a, b) ($\sigma_{eff,n} V t$) and slip (c, d) on the friction re-strengthening rate. Blue dots: fluid pressure experiments; green dots: room humidity experiments; red dots: vacuum experiments $P_{vacuum}=10^{-4}$ mbar.

B.5 Discussion

B.5.1 Effect of water on friction re-strengthening rate

The different effect of the presence of pressurized liquid water on the frictional re-strengthening rate of micro-gabbro and Carrara marble suggested that different micro-physical processes operated during the deceleration phase of the slip pulse, as clearly supported by microstructural evidence (Figure B.5). It is well-known that fault surfaces of micro-gabbro melt with seismic slip under room humidity and vacuum conditions (Tsutsumi and Shimamoto, 1997; Hirose and Shimamoto, 2005; Nielsen et al., 2008; Niemeijer et al., 2011), but also in the presence of liquid water (Violay et al., 2014a,b). On the contrary, slipping zones of Carrara marble did not record microstructural evidence of frictional melting. Instead, the slipping zones were made of sub-micrometer to nanometer in size grains (Spagnuolo et al., 2015). These microstructures can be associated to grain-size dependent crystal plastic processes (Green et al., 2015; De Paola et al., 2015; Spagnuolo et al., 2015). Similarly to what occurred during the initial weakening stage, was the rheology of the materials building the slipping zone that controlled the final frictional re-strengthening. In our experiments, the rheology of the slipping zone depended on the physical state of the sheared materials (melt vs. nano-grains), on the slip and strain rate, on the normal stress, as well as on the environmental conditions and, for Carrara marble, on grain size.

In the case of micro-gabbro, the viscosity and thickness of the melt layer and its extrusion rate from the slipping zone controlled the viscous strength of the experimental fault (Nielsen et al., 2008). Violay et al. (2014a) showed that the initial fault weakening by frictional melts was delayed by the presence of liquid water that cools the asperity contacts. Here, we hypothesize that frictional re-strengthening might be enhanced by an increase of the viscous strength of the melt layer due to water-cooling. To test this hypothesis, we implemented a Finite Element Methods numerical model which included the rock specimens and the steel-made pressure vessel (Figure B.6a, b, c). The slipping zone was modeled as a 200 μm -thick layer (red in color in Figure B.6a), consistently with the typical thickness of the solidified melt layers recovered at the end of the experiments (Nielsen et al., 2008), made by melt plus water or melt plus air with a constant volume ratio (ϕ) ranging from 0.5 to 0.9 in agreement with microstructural observations (Brown and Fialko, 2012; Violay et al., 2014a,a) (Figure B.5). The melt temperature during slip deceleration was computed using the mechanical data of the samples sheared under vacuum conditions as a reference. In fact, under vacuum conditions, most of the frictional work was dissipated into heat (the contribution to wear and rock fragmentation was negligible, see Niemeijer et al. (2011)) and very limited heat was lost by radiation. Consequently, the heat flux Q was a function of shear stress and slip rate that evolved with time t (Figure B.1) and

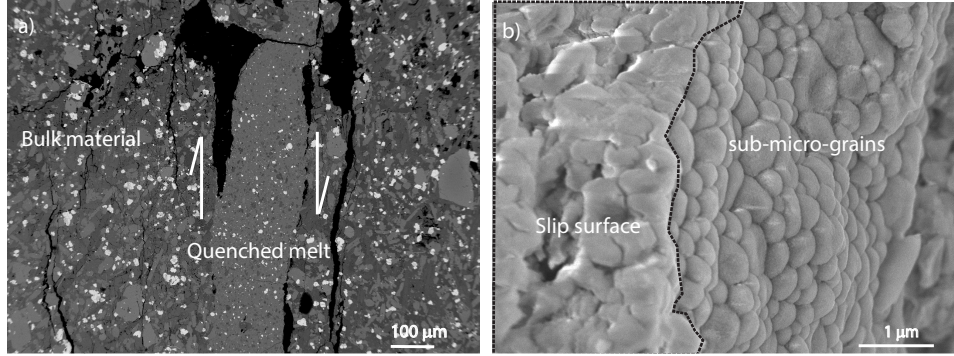


Figure B.5: Microstructural observations of experimental slip surfaces and slipping zones after shearing. (a) Slipping zone after an experiment performed on micro-gabbro (s585, $V=3 \text{ ms}^{-1}$, $\sigma_n=20 \text{ MPa}$, Vacuum conditions see also Violay (2014); Violay et al. (2014a)). The slipping zone is made by quenched melt (i.e., glass matrix, see composition in Table B.3) which wraps grains of plagioclase and pyroxene that survived from frictional melting (Scanning Electron Microscope, back scatter electron image). (b) Slip surface after an experiment performed on calcitic Carrara marble (s614, $V=3 \text{ ms}^{-1}$, $\sigma_n=20 \text{ MPa}$, Vacuum conditions, see Violay (2014); Violay et al. (2014a)). The slip surface is made by micro- to nano-grains of calcite and lime. Small decarbonation vacuoles decorate the recrystallized calcite grains (Scanning Electron Microscope, secondary electron image).

Table B.2: Thermal properties of the fluid (air and water) and micro-gabbro used in the FEM numerical model, as well as the thermal properties of Carrara marble used for the coupled diffusion model and plasticity flow law. K = thermal conductivity, ρ = density, C = specific heat. Φ the liquid fraction.

	Micro-gabbro	Carrara marble	Water	Air	Melt	Steel
$K [10^{-6} \text{ m}^2/\text{s}]$	0.8	1.48	0.15	1.5	0.344	4.2
$\rho [\text{kg}/\text{m}^3]$	2990	2700	1000	1.2	2591	2000
$C [\text{J}/(\text{kg K})]$	949	700	4200	1000	1484	460

varied along the sample radius r :

$$Q(r, t) = 0.5 \tau(t) V(r, t) \quad (\text{B.1})$$

For experiments performed under room humidity conditions and in the presence of water, we imposed that the melt layer was cooled by air or water (2D heat diffusion model), respectively. Then, as representative of the entire slipping zone, we used the estimated temperature achieved by the friction melt at $2/3$ of the sample radius. The properties of the slipping zone (indicated by the subscript *eff* for effective) were considered as a linear combination of the thermal properties of the fluid (air or water) and those of the melt (Table B.2). Therefore, the

Appendix B. Effect of water and rock composition on re-strengthening of cohesive faults during the deceleration phase of seismic slip pulses

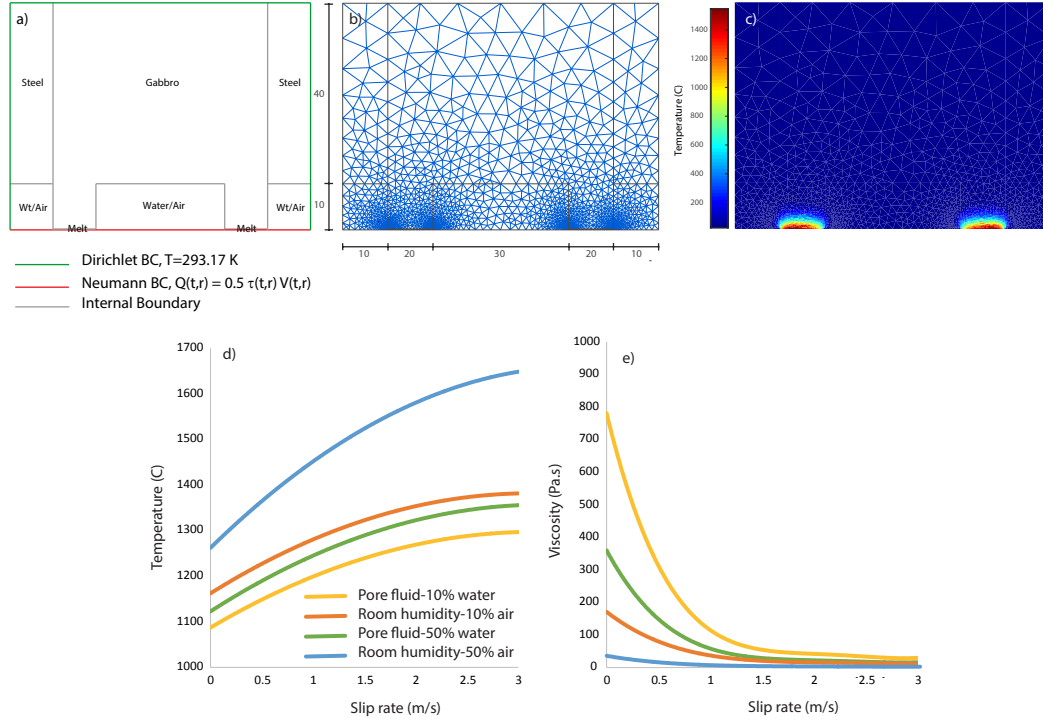


Figure B.6: FEM 2D time dependent heat diffusion model. a) and b) Model geometry with description of the boundary conditions and mesh geometry. c) The snapshot of the temperature distribution at the end of the experiment s585 conducted on gabbro. d) Temperature evolution of the slip zone during slip deceleration ($\tau_r - \tau_{ss}$). e) Melt viscosity evolution during slip deceleration.

“effective” thermal diffusivity in the slip zone was:

$$\alpha_{eff} = \frac{K_{eff}}{(\rho c)_{eff}} \quad (B.2)$$

where

$$K_{eff} = (1 - \phi) K_r + \phi K_f \quad (B.3)$$

and

$$(\rho c)_{eff} = (1 - \phi) (\rho c)_r + \phi (\rho c)_f \quad (B.4)$$

with K , the thermal conductivity ($\text{W m}^{-1} \text{K}^{-1}$), C the specific heat capacity ($\text{J kg}^{-1} \text{K}^{-1}$), ρ the density (kg m^{-3}) and ϕ the liquid fraction in the melt. Index R and f are related to the rock and fluid properties, respectively. Then, the heat diffusion is:

$$(\rho c)_{eff} \frac{\partial T}{\partial t} = \nabla(k_{eff,i} T) \quad (B.5)$$

where i represents the two different materials (water/air and rock) in the model of Figure B.6. Values of thermal conductivity, specific heat capacity and density are reported in Table B.2. The melt viscosity (η) was computed with the viscosity simulator for silicate melts of Giordano et al. (2008) (we did not take into account the crystal fraction in the melt). The model predicts the non-Arrhenius temperature dependence of viscosity for naturally-occurring silicate melts at atmospheric pressure:

$$\log(\eta) = A + \frac{B}{T(K) - C} \quad (\text{B.6})$$

where A is a constant independent of composition and B and C are adjustable parameters depending on melt composition. The glass chemical composition was published by Violay et al. (2014a,b) and reported in Table B.3. Numerical modeling results highlighted that the melt viscosity, because of cooling of the melt, increases with decreasing sliding velocity (Figure B.6), in agreement with the logarithmic increase of the “friction coefficient” during the deceleration stage (Figure B.1, Figure B.3). In addition, the increase of melt viscosity during slip deceleration was significantly faster in experiments performed in the presence of pressurized water than under room humidity conditions, suggesting that water-cooling was an efficient mechanism of re-strengthening. Moreover, the efficiency of water-cooling was proportional to the fluid-to-melt ratio in the slipping zone, and therefore of the temperature of the melt before deceleration. Indeed, higher was the melt temperature at the steady-state, which was slightly proportional to the imposed power density, faster was the increase of melt viscosity during slip deceleration. Instead, given the same conditions, the observation that the re-strengthening rate was independent of slip (Figure B.4d) was related to the large shortening rate of the rock specimens during frictional melting (mm per meters of slip, Violay et al. (2014a,b)). At steady-state conditions, the isotherms were almost fixed in space while the rock specimen passes through them and got melted and extruded (see discussion in Nielsen et al. (2008)). As a consequence, once steady-state had been achieved (always the case for the experiments presented here), during deceleration and melt cooling, the wall rocks were at similar temperatures independently of the cumulated slip and the re-strengthening is independent of slip.

In the case of Carrara marble, the slower re-strengthening rate in the presence of water than under room humidity conditions (Figure B.4a) cannot be explained by water cooling of the slipping zone or by thermal fluid depressurization (i.e., fluid pressure decrease after a short period of expansion caused by frictional heating). Indeed, neither melt was produced nor pressurization was observed during these experiments where fluid pressure was kept constant under drained conditions (Violay et al., 2015). Moreover, both melt lubrication and thermal pressurization would lead to a faster re-strengthening in presence of water than under room humidity conditions. However, this is at odds with the experimental evidence: re-strengthening rate is faster under vacuum conditions (Figure B.4). Note also that calcite decarbonation as potential re-strengthening mechanism can be ruled out in our experiments.

Appendix B. Effect of water and rock composition on re-strengthening of cohesive faults during the deceleration phase of seismic slip pulses

Table B.3: Chemical composition of the micro-gabbro (XRD) and of the glass for experiment s585 performed under vacuum conditions (Electron Microprobe Analysis). The analysis does not close to about 100% because only Fe²⁺ was determined.

Sample	Micro-gabbro	s585	
Phase	crystalline	glass	s.d.
#		7	
Al ₂ O ₃	14.27	15.68	0.74
Na ₂ O	4.49	4.26	0.91
CaO	9.22	10.21	1.43
SiO ₂	45.48	45.22	0.9
K ₂ O	2.71	2.71	0.57
MgO	7.15	6.88	0.57
P ₂ O ₅	1.88	1.14	0.14
FeO	10.28	8.31	0.34
TiO ₂	3.02	2.88	0.38
MnO	0.19	0.17	0.05
Total	98.69	97.46	

This mechanism would lead to faster re-strengthening at high power density (i.e., higher temperature), which it is just the opposite of our experimental evidence.

We suggest that the slower recovery of the frictional strength in the presence of liquid water during slip deceleration can be due to the strain rate sensitive, grain size dependent crystal plasticity of calcite in the presence of water (e.g., grain boundary sliding aided by diffusion creep) (Rutter, 1974; Schmid et al., 1980, 1987; Walker et al., 1990; Renner et al., 2002). Decarbonation reaction can probably help this mechanism because it triggers the formation of nanoparticles allowing the activation of grain size depend processes. Despite relevant differences between our experimental protocol and those reported in the above-mentioned studies (high pressure – high temperature triaxial tests performed at very low strain rates, 10^{-6} - 10^{-4} s⁻¹, compared to those achieved in our experiments, 10^2 - 10^4 s⁻¹), a comparison with those studies may help to understand better the mechanisms accommodating deformation in our experiments. At high temperature (> 400 °C), calcite strength is temperature and strain rate dependent (Rutter, 1972, 1974), and governed by crystal-plastic and grain size-dependent deformation mechanisms (intracrystalline plasticity and grain boundary sliding diffusion-assisted plasticity). Similar deformation mechanisms were inferred to be operating at sub-seismic and seismic slip rates in calcite (Verberne et al., 2015; De Paola et al., 2015; Spagnuolo et al., 2015). Rutter (1972) showed that calcite strength is inversely proportional to water content due to the reduction of the surface energy at calcite grain boundaries (Boozer et al., 1963) and its strain rate sensitive behavior decreased with increasing water content. Rutter (1974) had also shown that water effect is relatively small in Carrara marble. If crystal-plastic and grain-size dependent processes were triggered during high velocity friction experiments,

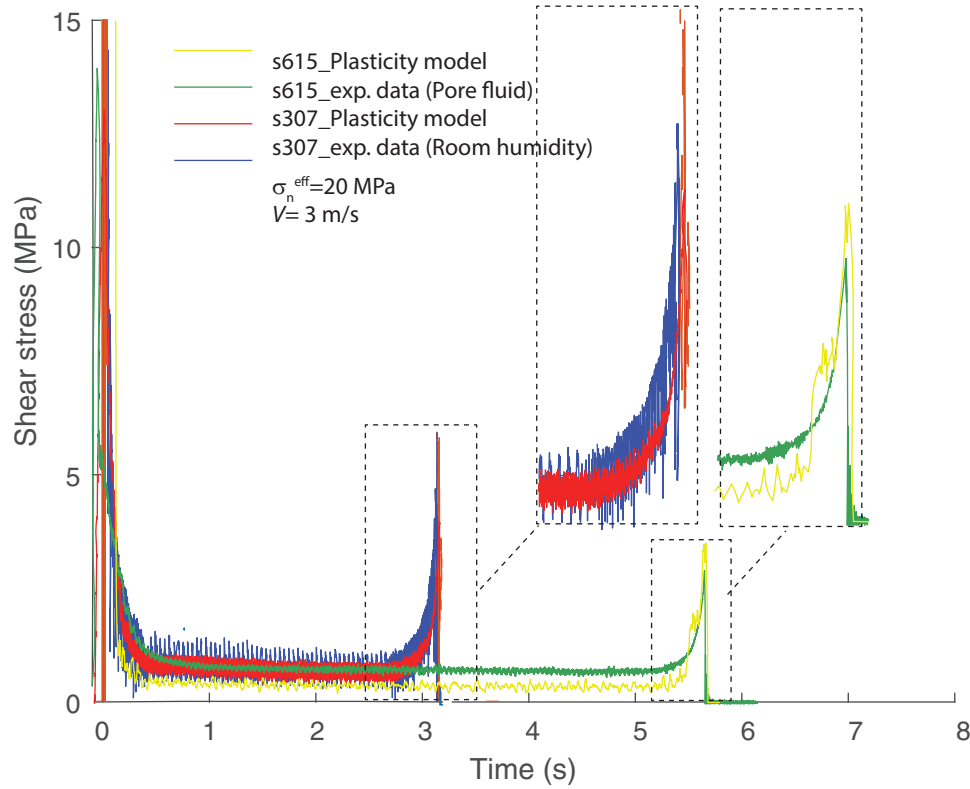


Figure B.7: Results of the 1D time dependent heat diffusion model fully coupled with diffusion creep flow law for both room humidity (blue and red curves) and pore fluid (green and yellow curves) conditions.

they would therefore result in a negative dependence of strain-rate on residual flow stress, and may explain the inhibition of the frictional re-strengthening in Carrara marbles especially at large power densities. In fact, for larger power densities, higher temperatures should be achieved in both the slipping zone and wall rocks. This should be the case especially once the so-called steady-steady conditions were achieved (note that, because of the power-law decay in Carrara marble, “steady-state” conditions remain an approximation, see Nielsen et al. (2016)). In fact, because of the absence or negligible shortening of the marble specimens, contrary to what happens in micro-gabbro, heat diffused in the wall rocks. Hotter wall rocks and the different deformation mechanism involved would result in slower cooling of the slipping zone, especially if compared to the frictional melting case (compare Figure B.4a with Figure B.4b). In the presence of water, the efficiency of grain size dependent and diffusion-controlled processes should be enhanced due to lower activation energy in presence of water, explaining the lower re-strengthening rate. However, the slipping zone was flushed away at the end of slip preventing sample recovery for micro-analytical investigations (Violay et al., 2013, 2014a,b). To test this hypothesis, we performed a one dimension-time dependent diffusion temperature model fully coupled with grain-size diffusion creep flow law (Figure B.7). Calcite

Appendix B. Effect of water and rock composition on re-strengthening of cohesive faults during the deceleration phase of seismic slip pulses

thermal properties are reported on Table B.2. The slipping zone was modeled by a 100 μm – layer composed of 100 nm grain size calcite, in agreement with microstructural observations (Violay et al., 2013, 2015) (Figure B.5). The heat flux and diffusion were computed following B.1 and B.5. The predicted flow stress for diffusion creep plasticity can be modeled by the constitutive flow law (B.8 and B.9).

$$\frac{\partial V}{\partial t} = \frac{1}{2} \tau(t) V(t) + \frac{k}{C_p \rho} \frac{\partial^2 T}{\partial x^2} \quad (\text{B.7})$$

$$\tau(t) = \frac{\dot{\gamma}}{A D^{-b} e^{-\frac{H}{RT(t)}}} \quad (\text{B.8})$$

$$\dot{\gamma} = \frac{1}{l} \frac{\partial V}{\partial t} \quad (\text{B.9})$$

where $\dot{\gamma}$ is the shear strain rate, A the pre-exponential factor, H the apparent activation energy for creep, R the gas constant, T the temperature, τ the shear stress at time step (t), n the stress exponent, D the grain size with b the grain size exponent, l is the layer thickness, and $V(t)$ is the slip velocity function.

Following (De Paola et al., 2015), under room-humidity conditions, $b = 2$, $n = 1$, $H = 217 \text{ kJ mol}^{-1}$, $A = 9.55 \cdot 10^5 \text{ s}^{-1} \text{ Bar}^{-n}$, $R = 8.314 \text{ J K mol}^{-1}$. In presence of water, we supposed a reduction of the activation energy (H) of about 20%, with $H = 176 \text{ kJ mol}^{-1}$ (see discussion in Rutter (1972)). Flow stress estimates based on B.7, B.8 and B.9 (Figure B.7) showed that grain boundary sliding aided by diffusion mechanism can explained both the strength weakening at the beginning of the experiments, the steady state friction and the final re-strengthening. Moreover, a decrease of the activation energy of only 20% under pore fluid conditions (Rutter, 1972) may justify the faster re-strengthening observed under dry rather than under pore fluid conditions (Figure B.1c).

B.5.2 Implications for natural earthquakes

Our experiments demonstrated that the slip deceleration can result in rapid fault re-strengthening, up to 10 to 90% of the initial peak stress, depending on the rheology of the material building the slip zone which depends on lithology and environmental conditions (Figure B.1). Because the friction coefficient is strongly velocity-dependent (Sone and Shimamoto, 2009), the magnitude of the re-strengthening depends mainly on the imposed deceleration rate (Del Gaudio et al., 2009). The extrapolation of these results to natural earthquakes can be gained by (1) comparing the friction re-strengthening rate between experiments performed with different rock types and under environmental conditions, and (2) using the dependency of the re-strengthening rate with the power density.

Here below, we estimate the slip-velocity, acceleration and power density of natural earth-

quakes and compare them to the imposed parameters during our experiments. Slip-velocity functions during earthquake rupture propagation are obtained by inverting ground motion waveforms. Slip acceleration and deceleration during earthquakes are $\sim 1\text{--}10\text{ m s}^{-2}$ (and larger, Tinti et al. (2005a)) and slip rates, on average, $\sim 1\text{ m s}^{-1}$ (Heaton, 1990). Therefore, acceleration, deceleration as well as slip-velocity imposed in our experiments are somehow comparable to those of natural earthquakes. The main differences between tests and earthquakes are in the shape of the velocity function (trapezoidal in our case) and on the normal stress imposed. Indeed, crustal earthquakes nucleate between 5 and 15 km depth, possibly at effective normal stresses of $\sim 100\text{--}200\text{ MPa}$ (Zoback and Harjes, 1997), and at power densities perhaps up to ten times higher than those imposed in the experiments discussed here. Extrapolation of our results to realistic stresses conditions suggest that in cohesive carbonate-bearing rocks, frictional re-strengthening during slip-velocity deceleration is probably almost negligible whereas in cohesive silicate bearing-rocks, re-strengthening processes are highly deceleration-dependent, especially in the presence of water.

Indeed, our results demonstrate that, due to the large expected power densities during natural earthquakes, small variations in the slip velocity could induce strong variations in friction promoting further changes in the slip velocity history due to co-seismic re-strengthening, especially in the case of calcite-built rocks. Moreover, the frequency content of the radiated energy is affected by the abruptness of velocity changes (emission of higher frequency waves is expected under abrupt decelerations) and thus, by the re-strengthening rate. Based on our results, cohesive silicate-bearing faults that undergo to frictional melting, also in the presence of liquid water (see natural case discussed by Brantut and Mitchell, 2018) will have the largest re-strengthening rates at the highest power densities (5–15 km depth) and should promote more intense high frequency radiation during slip deceleration. However, according to Figure B.4, the re-strengthening rates in micro-gabbro are much smaller than those achieved in calcitic-built cohesive rocks. In the latter rocks, if grain-size dependent processes are activated, intense high frequency radiation should occur especially at low power densities (perhaps corresponding to shallow depths, $<2\text{ km}$) and dry conditions, when re-strengthening rates are the highest (Figure B.4).

B.6 Conclusions

We performed a series of experiments simulating seismic slip under different environmental conditions (vacuum, room humidity and pressurized water) on two common cohesive crustal rocks (calcitic Carrara marble and micro-gabbro). In general, independently of the environmental conditions, the fault re-strengthening rate at the end of slip is up to one order of magnitude larger in Carrara marble than in micro-gabbro, especially at low power densities (Figure B.4). This large difference in re-strengthening rates is due to the different on-fault

Appendix B. Effect of water and rock composition on re-strengthening of cohesive faults during the deceleration phase of seismic slip pulses

deformation processes operating during seismic slip: crystal plastic and grain-size dependent for Carrara marble, melt lubrication for micro-gabbro. The two deformation mechanisms have different constitutive equations and dependence with temperature. With increasing power density, which may correspond to increasing crustal depths, the fault re-strengthening rate becomes almost negligible for Carrara marble whereas it slightly increases for micro-gabbro.

We also found some intriguing second order differences in the magnitude of the re-strengthening rate for the two rock types. These differences are due to the environmental conditions which impact on the efficiency of the particular co-seismic deformation mechanism of the rock. Under vacuum and room-humidity conditions, fault re-strengthening rate at the end of simulated seismic slip in Carrara marble is significantly faster than in the presence of pressurized water, especially at low power densities (Figure B.4). Instead, in micro-gabbro, fault re-strengthening rate is faster in the presence of pressurized water than under room humidity and vacuum conditions (Figure B.4). We interpreted these well-reproducible second order variations in the re-strengthening rate as the consequence of the change in rate-dependent plasticity in the presence of water for Carrara marble and water-cooling of the frictional interface for micro-gabbro. Our results suggest that both rock composition and presence of water affect the elastic strain energy release rate and the seismic waves radiation pattern during rupture propagation.

C Table of rotary shear experiments performed by other authors

Table C.1: Published experimental data reported in 4.6.b. σ_n =normal stress, V slip-rate, μ_{peak} = peak friction coefficient, μ_{dyn} = dynamic friction coefficient, T = estimated temperature at μ_{dyn} , η = melt estimated viscosity, S = Sommerfeld number, Ref.= paper references.

Rock	Run	σ_n [MPa]	V [m s ⁻¹]	μ_{peak}	μ_{dyn}	T [°C]	η [Pa s]	S	Ref.
Peridotite	HVR616	15.00	1.14	0.67	0.17	1443	1.82	10.50	(Di Toro et al., 2006)
Peridotite	HVR617	20.00	1.14	0.73	0.18	2031	0.05	0.24	(Di Toro et al., 2006)
Peridotite	HVR615	10.00	1.14	0.62	0.22	1214	21.88	190.63	(Di Toro et al., 2006)
Peridotite	HVR618	5.00	1.14	0.8	0.23	1156	48.98	853.53	(Di Toro et al., 2006)
Peridotite	HVR620	13.00	1.14	0.50	0.13	1321	6.02	40.39	(Del Gaudio et al., 2009)
Peridotite	HVR623	15.59	1.14	0.40	0.15	1326	5.75	32.16	(Del Gaudio et al., 2009)
Peridotite	HVR633	16.13	1.14	0.60	0.17	1276	10.00	54.02	(Del Gaudio et al., 2009)
Peridotite	HVR634	7.78	1.14	0.63	0.17	1334	5.25	58.78	(Del Gaudio et al., 2009)
Peridotite	HVR635	5.37	1.14	0.52	0.19	1103	114.82	1863.00	(Del Gaudio et al., 2009)
Peridotite	HVR640	10.42	1.14	0.573	0.14	1295	7.94	66.42	(Del Gaudio et al., 2009)
Peridotite	HVR676	12.99	1.14	0.45	0.14	1200	26.30	176.43	(Del Gaudio et al., 2009)
Peridotite	HVR677	13.00	0.76	0.43	0.14	1186	32.36	144.60	(Del Gaudio et al., 2009)
Peridotite	HVR621	10.40	1.14	0.51	0.17	1299	7.76	65.04	(Del Gaudio et al., 2009)
Peridotite	HVR641	13.00	1.14	0.69	0.15	1594	0.56	3.77	(Del Gaudio et al., 2009)
Peridotite	HVR643	13.01	0.23	0.68	0.25	1222	19.50	26.35	(Del Gaudio et al., 2009)
Peridotite	HVR644	12.98	0.92	0.69	0.14	1553	0.75	4.11	(Del Gaudio et al., 2009)
Peridotite	HVR645	13.01	0.76	0.65	0.17	1660	0.35	1.58	(Del Gaudio et al., 2009)
Peridotite	HVR651	13.00	1.14	0.69	0.15	1621	0.47	3.14	(Del Gaudio et al., 2009)
Peridotite	HVR652*	13.02	1.14	0.61	0.13	1551	0.76	5.08	(Del Gaudio et al., 2009)
Tonalite	HVR373	15.00	1.14	0.65	0.27	1377	74.13	430.62	(Di Toro et al., 2006)
Tonalite	HVR375	10.00	1.14	0.80	0.29	1499	22.39	195.07	(Di Toro et al., 2006)
Tonalite	HVR377	20.00	1.14	0.50	0.22	1447	36.31	158.18	(Di Toro et al., 2006)
Tonalite	HVR379	15.00	1.20	0.40	0.24	1126	1905.46	11651.22	(Di Toro et al., 2006)
Gabbro	s555	20.00	3.00	0.68	0.09	1249	3.38	47.88	(Violay et al., 2014b)

Appendix C. Table of rotary shear experiments performed by other authors

Gabbro	s563	20.00	1.00	0.59	0.1	1250	3.39	15.96	(Violay et al., 2014b)
Gabbro	s567	25.00	3.00	0.55	0.08	1149	6.61	93.36	(Violay et al., 2014b)
Gabbro	s585	20.00	3.00	0.57	0.08	1221	3.09	43.67	(Violay et al., 2014b)
Gabbro	HVR687	15.50	1.14	0.65	0.17	1338	14.13	79.22	(Nielsen et al., 2008)



Bibliography

- Abercrombie, R. E. and Rice, J. R. (2005). Can observations of earthquake scaling constrain slip weakening? *Geophysical Journal International*, 162(2):406–424.
- Acosta, M., Passelègue, F. X., Schubnel, A., and Violay, M. (2018). Dynamic weakening during earthquakes controlled by fluid thermodynamics. *Nature Communications*, 9(1):3074.
- Ague, J. J. and Brimhall, G. H. (1988). Magmatic arc asymmetry and distribution of anomalous plutonic belts in the batholiths of California: Effects of assimilation, crustal thickness, and depth of crystallization. *Bulletin of the Geological Society of America*, 100(6):912–927.
- Ake, J., Mahrer, K., O’Connell, D., and Block, L. (2005). Deep-injection and closely monitored induced seismicity at Paradox Valley, Colorado. *Bulletin of the Seismological Society of America*, 95(2):664–683.
- Allmendinger, R. W., Cardozo, N., and Fisher, D. M. (2011). *Tensors*, page 81–97. Cambridge University Press.
- Alt, R. C. and Zoback, M. D. (2017). In Situ Stress and Active Faulting in Oklahoma. *Bulletin of the Seismological Society of America*, 107(1):216–228.
- Amontons, G. (1699). De la resistance cause’e dans les machines (1). *JOURNAL-JAPANESE SOCIETY OF TRIBOLOGISTS*, 44:229–235.
- Andrews, D. J. (1976). Rupture velocity of plane strain shear cracks. *Journal of Geophysical Research (1896-1977)*, 81(32):5679–5687.
- Andrews, D. J. (2005). Rupture dynamics with energy loss outside the slip zone. *Journal of Geophysical Research: Solid Earth*, 110(B1).
- Aretusini, S., Spagnuolo, E., Dalconi, M. C., Di Toro, G., and Rutter, E. H. (2019). Water availability and deformation processes in smectite-rich gouges during seismic slip. *Journal of Geophysical Research: Solid Earth*, 124(11):10855–10876.

Bibliography

- Asanuma, H., Nozaki, H., Niitsuma, H., and Wyborn, D. (2005). Interpretation of microseismic events with larger magnitude collected at cooper basin, australia. *Geothermal Resources Council Transactions*, 29(0193-):87–92.
- Atkinson, G. M., Eaton, D. W., Ghofrani, H., Walker, D., Cheadle, B., Schultz, R., Shcherbakov, R., Tiampo, K., Gu, J., Harrington, R. M., Liu, Y., van der Baan, M., and Kao, H. (2016). Hydraulic Fracturing and Seismicity in the Western Canada Sedimentary Basin. *Seismological Research Letters*, 87(3):631–647.
- Aubry, J., Passelègue, F. X., Deldicque, D., Girault, F., Marty, S., Lahfid, A., Bhat, H. S., Escartin, J., and Schubnel, A. (2018). Frictional heating processes and energy budget during laboratory earthquakes. *Geophysical Research Letters*, 45(22):12,274–12,282.
- Badt, N. Z., Tullis, T. E., Hirth, G., and Goldsby, D. L. (2020). Thermal pressurization weakening in laboratory experiments. *Journal of Geophysical Research: Solid Earth*, 125(5):e2019JB018872. e2019JB018872 2019JB018872.
- Bair, S. and Winer, W. O. (1982). Some Observations in High Pressure Rheology of Lubricants. *Journal of Lubrication Technology*, 104(3):357–364.
- Baisch, S., Voros, R., Weidler, R., and Wyborn, D. (2009). Investigation of Fault Mechanisms during Geothermal Reservoir Stimulation Experiments in the Cooper Basin, Australia. *Bulletin of the Seismological Society of America*, 99(1):148–158.
- Baisch, S., Vörös, R., Rothert, E., Stang, H., Jung, R., and Schellschmidt, R. (2010). A numerical model for fluid injection induced seismicity at soultz-sous-forêts. *International Journal of Rock Mechanics and Mining Sciences*, 47(3):405 – 413.
- Baisch, S., Weidler, R., Voros, R., Wyborn, D., and de Graaf, L. (2006). Induced Seismicity during the Stimulation of a Geothermal hfr Reservoir in the Cooper Basin, Australia. *Bulletin of the Seismological Society of America*, 96(6):2242–2256.
- Bando, S., Takemura, E., Nishio, M., Hihara, E., and Akai, M. (2004). Viscosity of aqueous nacl solutions with dissolved co2 at (30 to 60) °c and (10 to 20) mpa. *Journal of Chemical & Engineering Data*, 49(5):1328–1332.
- Barbour, A. J., Xue, L., Roeloffs, E., and Rubinstein, J. L. (2019). Leakage and increasing fluid pressure detected in oklahoma’s wastewater disposal reservoir. *Journal of Geophysical Research: Solid Earth*, 124(3):2896–2919.
- Bates, O. K. (1936). Binary Mixtures of Water and Glycerol - Thermal Conductivity of Liquids. *Industrial & Engineering Chemistry*, 28(4):494–498.

- Bayart, E., Svetlizky, I., and Fineberg, J. (2016). Slippery but Tough: The Rapid Fracture of Lubricated Frictional Interfaces. *Physical Review Letters*, 116(19):194301.
- Beeler, N. M. and Tullis, T. E. (1996). Self-healing slip pulses in dynamic rupture models due to velocity-dependent strength. *Bulletin of the Seismological Society of America*, 86(4):1130–1148.
- Beeler, N. M. and Tullis, T. E. (1997). The roles of time and displacement in velocity-dependent volumetric strain of fault zones. *Journal of Geophysical Research: Solid Earth*, 102(B10):22595–22609.
- Beeler, N. M., Tullis, T. E., and Goldsby, D. L. (2008). Constitutive relationships and physical basis of fault strength due to flash heating. *Journal of Geophysical Research: Solid Earth*, 113(1):1–12.
- Bennour, Z., Ishida, T., Chen, Y., Nagaya, Y., Chen, Q., Sekine, K., and Nagano, Y. (2015). Crack extension in hydraulic fracturing of shale cores using viscous oil, water, and liquid carbon dioxide. *Rock Mechanics and Rock Engineering*, 48(4):1463 – 1473.
- Beroza, G. C. and Jordan, T. H. (1990). Searching for slow and silent earthquakes using free oscillations. *Journal of Geophysical Research: Solid Earth*, 95(B3):2485–2510.
- Biegel, R. L., Wang, W., Scholz, C. H., Boitnott, G. N., and Yoshioka, N. (1992). Micromechanics of rock friction 1. effects of surface roughness on initial friction and slip hardening in westerly granite. *Journal of Geophysical Research: Solid Earth*, 97(B6):8951–8964.
- Biran, O., Hatzor, Y., and Ziv, A. (2009). Micro-scale roughness effects on the friction coefficient of granite surfaces under varying levels of normal stress. *Meso-Scale Shear Physics in Earthquake and Landslide Mechanics*, Ed. Y. Hatzor, J. Sulem, I. Vardoulakis, pages 145–156.
- Bissell, R., Vasco, D., Atbi, M., Hamdani, M., Okwelegbe, M., and Goldwater, M. (2011). A full field simulation of the in salah gas production and co2 storage project using a coupled geo-mechanical and thermal fluid flow simulator. *Energy Procedia*, 4:3290 – 3297. 10th International Conference on Greenhouse Gas Control Technologies.
- Bizzarri, A. (2012). The mechanics of lubricated faults: Insights from 3-D numerical models. *Journal of Geophysical Research: Solid Earth*, 117(5):1–23.
- Blanpied, M. L., Lockner, D. A., and Byerlee, J. D. (1995). Frictional slip of granite at hydrothermal conditions. *Journal of Geophysical Research: Solid Earth*, 100(B7):13045–13064.
- Blanpied, M. L., Marone, C. J., Lockner, D. A., Byerlee, J. D., and King, D. P. (1998). Quantitative measure of the variation in fault rheology due to fluid-rock interactions. *Journal of Geophysical Research: Solid Earth*, 103(B5):9691–9712.

Bibliography

- Block, L. V., Wood, C. K., Yeck, W. L., and King, V. M. (2015). Induced seismicity constraints on subsurface geological structure, Paradox Valley, Colorado. *Geophysical Journal International*, 200(2):1172–1195.
- Boozer, G., Hiller, K., and Serdengecti, S. (1963). Effects of pore fluids on the deformation behavior of rocks subjected to triaxial compression. *Proc. Fifth Sympos. Rock Mechanics. Univ. Minnesota*.
- Borgomano, J. V. M., Gallagher, A., Sun, C., and Fortin, J. (2020). An apparatus to measure elastic dispersion and attenuation using hydrostatic- and axial-stress oscillations under undrained conditions. *Review of Scientific Instruments*, 91(3):034502.
- Boulton, C., Yao, L., Faulkner, D. R., Townend, J., Toy, V. G., Sutherland, R., Ma, S., and Shimamoto, T. (2017). High-velocity frictional properties of alpine fault rocks: Mechanical data, microstructural analysis, and implications for rupture propagation. *Journal of Structural Geology*, 97:71 – 92.
- Bowden, F. P. and Tabor, D. (1950). *The Friction and Lubrication of Solids*. Oxford University Press.
- Bowden, F. P., Tabor, D., and Taylor, G. I. (1939). The area of contact between stationary and moving surfaces. *Proceedings of the Royal Society of London. Series A. Mathematical and Physical Sciences*, 169(938):391–413.
- Brace, W. (1972). Laboratory studies of stick-slip and their application to earthquakes. *Tectonophysics*, 14(3):189 – 200.
- Brace, W. F. and Byerlee, J. D. (1966). Stick-Slip as a Mechanism for Earthquakes. *Science*, 153(3739):990–992.
- Brantut, N. and Platt, J. D. (2017). Dynamic Weakening and the Depth Dependence of Earthquake Faulting. pages 171–194.
- Brantut, N., Schubnel, A., Rouzaud, J.-N., Brunet, F., and Shimamoto, T. (2008). High-velocity frictional properties of a clay-bearing fault gouge and implications for earthquake mechanics. *Journal of Geophysical Research*, 113(B10):B10401.
- Brantut, N. and Viesca, R. C. (2015). Earthquake nucleation in intact or healed rocks. *Journal of Geophysical Research: Solid Earth*, 120(1):191–209.
- Brantut, N. and Viesca, R. C. (2017). The fracture energy of ruptures driven by flash heating. *Geophysical Research Letters*, 44(13):6718–6725.

- Bremkamp, W. and Harr, C. L. (1988). Area of least resistance to fluid movement and pressure rise, Paradox Valley Unit, Salt Brine Injection Project, Bedrock, Colorado: Bureau of Reclamation. *Bureau of Reclamation*.
- Brodsky, E. E., Gilchrist, J. J., Sagy, A., and Collettini, C. (2011). Faults smooth gradually as a function of slip. *Earth and Planetary Science Letters*, 302(1-2):185–193.
- Brodsky, E. E. and Kanamori, H. (2001). Elastohydrodynamic lubrication of faults. *Journal of Geophysical Research: Solid Earth*, 106(B8):16357–16374.
- Brodsky, E. E., Kirkpatrick, J. D., and Candela, T. (2016). Constraints from fault roughness on the scale-dependent strength of rocks. *Geology*, 44(1):19–22.
- Brodsky, E. E., Rowe, C. D., Meneghini, F., and Moore, J. C. (2009). A geological fingerprint of low-viscosity fault fluids mobilized during an earthquake. *Journal of Geophysical Research: Solid Earth*, 114(B1):1–14.
- Brown, K. M. and Fialko, Y. (2012). ‘melt welt’ mechanism of extreme weakening of gabbro at seismic slip rates. *Nature*, 488(7413):638–641.
- Brown, S. R. (1998). Frictional heating on faults: Stable sliding versus stick slip. *Journal of Geophysical Research: Solid Earth*, 103(B4):7413–7420.
- Brune, J. N. (1970). Tectonic stress and the spectra of seismic shear waves from earthquakes. *Journal of Geophysical Research (1896-1977)*, 75(26):4997–5009.
- Byerlee, J. (1978). Friction of rocks. *Pure and Applied Geophysics PAGEOPH*, 116(4-5):615–626.
- Byerlee, J. D. (1967). Frictional characteristics of granite under high confining pressure. *Journal of Geophysical Research*, 72(14):3639–3648.
- Byerlee, J. D. and Brace, W. F. (1968). Stick slip, stable sliding, and earthquakes—effect of rock type, pressure, strain rate, and stiffness. *Journal of Geophysical Research (1896-1977)*, 73(18):6031–6037.
- Caine, J. S., Evans, J. P., and Forster, C. B. (1996). Fault zone architecture and permeability structure. *Geology*, 24(11):1025–1028.
- Calais, E., Camelbeeck, T., Stein, S., Liu, M., and Craig, T. J. (2016). A new paradigm for large earthquakes in stable continental plate interiors. *Geophysical Research Letters*, 43(20):10,621–10,637.
- Calò, M., Dorbath, C., and Frogneux, M. (2014). Injection tests at the egs reservoir of soultz-sous-forêts. seismic response of the gpk4 stimulations. *Geothermics*, 52:50 – 58. Analysis of Induced Seismicity in Geothermal Operations.

Bibliography

- Cammenga, H. K., Schulze, F. W., and Theuerl, W. (1977). Vapor Pressure and Evaporation Coefficient of Glycerol. *Journal of Chemical and Engineering Data*, 22(2):131–134.
- Campillo, M. and Ionescu, I. R. (1997). Initiation of antiplane shear instability under slip dependent friction. *Journal of Geophysical Research: Solid Earth*, 102(B9):20363–20371.
- Canudas de Wit, C., Olsson, H., Astrom, K., and Lischinsky, P. (1995). A new model for control of systems with friction. *IEEE Transactions on Automatic Control*, 40(3):419–425.
- Carlson, J. M. and Batista, A. A. (1996). Constitutive relation for the friction between lubricated surfaces. *Physical Review E*, 53(4):4153–4165.
- Carpenter, B., Mollo, S., Viti, C., and Collettini, C. (2015). Influence of calcite decarbonation on the frictional behavior of carbonate-bearing gouge: Implications for the instability of volcanic flanks and fault slip. *Tectonophysics*, 658:128 – 136.
- Carpenter, B. M., Ikari, M. J., and Marone, C. (2016). Laboratory observations of time-dependent frictional strengthening and stress relaxation in natural and synthetic fault gouges. *Journal of Geophysical Research: Solid Earth*, 121(2):1183–1201.
- Chambon, G. and Rudnicki, J. W. (2001). Effects of normal stress variations on frictional stability of a fluid-infiltrated fault. *Journal of Geophysical Research: Solid Earth*, 106(B6):11353–11372.
- Chang, J. C., Lockner, D. A., and Reches, Z. (2012). Rapid acceleration leads to rapid weakening in earthquake-like laboratory experiments. *Science*, 338(6103):101–105.
- Chang, K. W. and Segall, P. (2016). Injection-induced seismicity on basement faults including poroelastic stressing. *Journal of Geophysical Research: Solid Earth*, 121(4):2708–2726.
- Charl  ty, J., Cuenot, N., Dorbath, L., Dorbath, C., Haessler, H., and Frogneux, M. (2007). Large earthquakes during hydraulic stimulations at the geothermal site of soultz-sous-for  ts. *International Journal of Rock Mechanics and Mining Sciences*, 44(8):1091 – 1105.
- Chen, X., Madden, A. S., Bickmore, B. R., and Reches, Z. (2013). Dynamic weakening by nanoscale smoothing during high-velocity fault slip. *Geology*, 41(7):739–742.
- Chen, X., Madden, A. S. E., and Reches, Z. (2017). *Powder Rolling as a Mechanism of Dynamic Fault Weakening*, chapter 7, pages 133–150. American Geophysical Union (AGU).
- Chen, Z. (2012). Finite element modelling of viscosity-dominated hydraulic fractures. *Journal of Petroleum Science and Engineering*, 88-89:136 – 144. Unconventional hydrocarbons exploration and production Challenges.

- Cheng, N.-s. (2008). Formula for Viscosity of Glycerol-Water Mixture. *Industrial and Engineering Chemistry Research*, 47:3285–3288.
- Cheryan, M. and Rajagopalan, N. (1998). Membrane processing of oily streams. wastewater treatment and waste reduction. *Journal of Membrane Science*, 151(1):13 – 28.
- Chester, F. M. and Logan, J. M. (1986). Implications for mechanical properties of brittle faults from observations of the punchbowl fault zone, california. *pure and applied geophysics*, 124(1):79 – 106.
- Clerc, F., Harrington, R. M., Liu, Y., and Gu, Y. J. (2016). Stress drop estimates and hypocenter relocations of induced seismicity near crooked lake, alberta. *Geophysical Research Letters*, 43(13):6942–6951.
- Cocco, M., Spudich, P., and Tinti, E. (2006). On the Mechanical Work Absorbed on Faults During Earthquake Ruptures. *Agu monograph: Earthquakes: Radiated Energy and the Physics of Faulting*, pages 237–254.
- Collettini, C., Di Stefano, G., Carpenter, B., Scarlato, P., Tesei, T., Mollo, S., Trippetta, F., Marone, C., Romeo, G., and Chiaraluce, L. (2014). A novel and versatile apparatus for brittle rock deformation. *International Journal of Rock Mechanics and Mining Sciences*, 66:114–123.
- Cornelio, C., Passelègue, F. X., Spagnuolo, E., Di Toro, G., and Violay, M. (2020). Effect of fluid viscosity on fault reactivation and coseismic weakening. *Journal of Geophysical Research: Solid Earth*, 125(1):e2019JB018883. e2019JB018883 2019JB018883.
- Cornelio, C., Spagnuolo, E., Di Toro, G., Nielsen, S., and Violay, M. (2019). Mechanical behaviour of fluid-lubricated faults. *Nature Communications*, 10(1):1274.
- Cornelio, C. and Violay, M. (2020a). Effect of fluid viscosity on earthquake nucleation. *Geophysical Research Letters*. (Link).
- Cornelio, C. and Violay, M. (2020b). Parametric analysis of the elastohydrodynamic lubrication efficiency on induced seismicity. *Geophysical Journal International*, 222(1):517–525.
- Cornet, F. (2016). Seismic and aseismic motions generated by fluid injections. *Geomechanics for Energy and the Environment*, 5(January 2016):42–54.
- Cornet, F., Bérard, T., and Bourouis, S. (2007). How close to failure is a granite rock mass at a 5 km depth? *International Journal of Rock Mechanics and Mining Sciences*, 44(1):47–66.
- Cornet, F. H., Helm, J., Poitrenaud, H., and Etchecopar, A. (1997). Seismic and aseismic slips induced by large-scale fluid injections. *Pure and Applied Geophysics*, 150(3-4):563–583.

Bibliography

- Coulomb, C. A. (1821). *Théorie des machines simples en ayant égard au frottement de leurs parties et à la roideur des cordages*. Bachelier.
- Cox, S. and Scholz, C. (1988). On the formation and growth of faults: an experimental study. *Journal of Structural Geology*, 10(4):413 – 430.
- Cramer, C. H. (2017). Brune Stress Parameter Estimates for the 2016 M w 5.8 Pawnee and Other Oklahoma Earthquakes. *Seismological Research Letters*, 88(4):1005–1016.
- De Barros, L., Daniel, G., Guglielmi, Y., Rivet, D., Caron, H., Payre, X., Bergery, G., Henry, P., Castilla, R., Dick, P., Barbieri, E., and Gourlay, M. (2016). Fault structure, stress, or pressure control of the seismicity in shale? insights from a controlled experiment of fluid-induced fault reactivation. *Journal of Geophysical Research: Solid Earth*, 121(6):4506–4522.
- De Paola, N., Hirose, T., Mitchell, T., Di Toro, G., Viti, C., and Shimamoto, T. (2011). Fault lubrication and earthquake propagation in thermally unstable rocks. *Geology*, 39(1):35–38.
- De Paola, N., Holdsworth, R. E., Viti, C., Collettini, C., and Bullock, R. (2015). Can grain size sensitive flow lubricate faults during the initial stages of earthquake propagation? *Earth and Planetary Science Letters*, 431:48–58.
- de Pater, C. J. and Baisch, S. (2011). Geomechanical Study of Bowland Shale Seismicity. *Seismik, Q-con, Geosphere, StrateGen, Baker-GMI*, (November):71.
- Deichmann, N. and Ernst, J. (2009). Earthquake focal mechanisms of the induced seismicity in 2006 and 2007 below Basel (Switzerland). *Swiss Journal of Geosciences*, 102(3):457.
- Deichmann, N. and Giardini, D. (2009). Earthquakes Induced by the Stimulation of an Enhanced Geothermal System below Basel (Switzerland). *Seismological Research Letters*, 80(5):784–798.
- Del Gaudio, P., Di Toro, G., Han, R., Hirose, T., Nielsen, S., Shimamoto, T., and Cavallo, A. (2009). Frictional melting of peridotite and seismic slip. *Journal of Geophysical Research*, 114(B6):B06306.
- Dempsey, D. and Suckale, J. (2017). Physics-based forecasting of induced seismicity at groningen gas field, the netherlands. *Geophysical Research Letters*, 44(15):7773–7782.
- Di Toro, G., Goldsby, D. L., and Tullis, T. E. (2004). Friction falls towards zero in quartz rock as slip velocity approaches seismic rates. *Nature*, 427(6973):436–439.
- Di Toro, G., Han, R., Hirose, T., De Paola, N., Nielsen, S., Mizoguchi, K., Ferri, F., Cocco, M., and Shimamoto, T. (2011). Fault lubrication during earthquakes. *Nature*, 471(7339):494–498.

- Di Toro, G., Hirose, T., Nielsen, S., Pennacchioni, G., and Shimamoto, T. (2006). Natural and Experimental Evidence of Melt Lubrication of Faults During Earthquakes. *Science*, 311(5761):647–649.
- Di Toro, G., Niemeijer, A., Tripoli, A., Nielsen, S., Di Felice, F., Scarlato, P., Spada, G., Alessandrini, R., Romeo, G., Di Stefano, G., Smith, S., Spagnuolo, E., and Mariano, S. (2010). From field geology to earthquake simulation: a new state-of-the-art tool to investigate rock friction during the seismic cycle (SHIVA). *RENDICONTI LINCEI*, 21(S1):95–114.
- Di Toro, G. and Pennacchioni, G. (2004). Superheated friction-induced melts in zoned pseudotachylytes within the Adamello tonalites (Italian Southern Alps). *Journal of Structural Geology*, 26(10):1783–1801.
- Di Toro, G. and Pennacchioni, G. (2005). Fault plane processes and mesoscopic structure of a strong-type seismogenic fault in tonalites (Adamello batholith, Southern Alps). *Tectonophysics*, 402(1-4):55–80.
- Dieterich, J. H. (1972). Time-dependent friction in rocks. *Journal of Geophysical Research*, 77(20):3690–3697.
- Dieterich, J. H. (1978). Time-dependent friction and the mechanics of stick-slip. *Pure and Applied Geophysics PAGEOPH*, 116(4-5):790–806.
- Dieterich, J. H. (1979). Modeling of rock friction: 1. Experimental results and constitutive equations. *Journal of Geophysical Research*, 84(B5):2161.
- Dieterich, J. H. (1992). Earthquake nucleation on faults with rate-and state-dependent strength. *Tectonophysics*, 211(1-4):115–134.
- Dieterich, J. H. and Kilgore, B. D. (1994). Direct observation of frictional contacts: New insights for state-dependent properties. *Pure and Applied Geophysics PAGEOPH*, 143(1-3):283–302.
- Dost, B., Edwards, B., and Bommer, J. J. (2018). The Relationship between M and ML: A Review and Application to Induced Seismicity in the Groningen Gas Field, The Netherlands. *Seismological Research Letters*, 89(3):1062–1074.
- Dowson, D. and Longfield, M. D. (1963). An Elastohydrodynamic Lubrication Experiment. *Nature*, 197(4867):586–586.
- Eberhart-Phillips, D. and Oppenheimer, D. H. (1984). Induced seismicity in the geysers geothermal area, california. *Journal of Geophysical Research: Solid Earth*, 89(B2):1191–1207.
- Economides, M. J. and Boney, C. (2000). Reservoir Stimulation. In *Reservoir Stimulation*, chapter 1, page pp. 856. John Wiley & Sons, 3rd editio edition.

Bibliography

- Edenhofer, O., Jakob, M., Creutzig, F., Flachsland, C., Fuss, S., Kowarsch, M., Lessmann, K., Mattauch, L., Siegmeier, J., and Steckel, J. C. (2015). Closing the emission price gap. *Global Environmental Change*, 31:132 – 143.
- Eisner, L., Gei, D., Hallo, M., Opršal, I., and Ali, M. Y. (2013). The peak frequency of direct waves for microseismic events. *GEOPHYSICS*, 78(6):A45–A49.
- Ellsworth, W. L. (2013). Injection-induced earthquakes. *Science*, 341(6142).
- Eppelbaum, L., Kutasov, I., and Pilchin, A. (2014). Thermal Properties of Rocks and Density of Fluids. In *Applied Geothermics*, Lecture Notes in Earth System Sciences, chapter 2, page 757. Springer Berlin Heidelberg, Berlin, Heidelberg.
- Esmaeilirad, N., Terry, C., Kennedy, H., Adam, P., and Carlson, K. (2016a). Recycling fracturing flowback water for use in hydraulic fracturing: Influence of organic matter on stability of carboxyl-methyl-cellulose-based fracturing fluids. *SPE Journal*, 21:1358–1369.
- Esmaeilirad, N., White, S., Terry, C., Prior, A., and Carlson, K. (2016b). Influence of inorganic ions in recycled produced water on gel-based hydraulic fracturing fluid viscosity. *Journal of Petroleum Science and Engineering*, 139:104 – 111.
- Evans, D. M. (1966). The denver area earthquakes and the rocky mountain arsenal disposal well. *The Mountain Geologist*.
- Evans, J. P., Forster, C. B., and Goddard, J. V. (1997). Permeability of fault-related rocks, and implications for hydraulic structure of fault zones. *Journal of Structural Geology*, 19(11):1393 – 1404.
- Fallahzadeh, S. H., James Cornwell, A., Rasouli, V., and Hossain, M. (2015). The impacts of fracturing fluid viscosity and injection rate on the near wellbore hydraulic fracture propagation in cased perforated wellbores. In *ARMA 49th U.S. Rock Mechanics/Geomechanics Symposium*, Berlin, Germany. American Rock Mechanics Association.
- Fan, Z., Eichhubl, P., and Gale, J. F. W. (2016). Geomechanical analysis of fluid injection and seismic fault slip for the M w 4.8 Timpson, Texas, earthquake sequence. *Journal of Geophysical Research: Solid Earth*, 121(4):2798–2812.
- Faulkner, D., Jackson, C., Lunn, R., Schlische, R., Shipton, Z., Wibberley, C., and Withjack, M. (2010). A review of recent developments concerning the structure, mechanics and fluid flow properties of fault zones. *Journal of Structural Geology*, 32(11):1557 – 1575. Fault Zones.
- Faulkner, D. R., Mitchell, T. M., Behnsen, J., Hirose, T., and Shimamoto, T. (2011). Stuck in the mud? earthquake nucleation and propagation through accretionary forearcs. *Geophysical Research Letters*, 38(18).

- Faulkner, D. R., Sanchez-Roa, C., Boulton, C., and den Hartog, S. A. M. (2018). Pore fluid pressure development in compacting fault gouge in theory, experiments, and nature. *Journal of Geophysical Research: Solid Earth*, 123(1):226–241.
- Ferri, F., Di Toro, G., Hirose, T., and Shimamoto, T. (2010). Evidence of thermal pressurization in high-velocity friction experiments on smectite-rich gouges. *Terra Nova*, 22(5):347–353.
- Foulger, G. R., Wilson, M. P., Gluyas, J. G., Julian, B. R., and Davies, R. J. (2018). Global review of human-induced earthquakes. *Earth-Science Reviews*, 178:438 – 514.
- Frohlich, C., Ellsworth, W., Brown, W. A., Brunt, M., Luetgert, J., MacDonald, T., and Walter, S. (2014). The 17 May 2012 M 4.8 earthquake near Timpson, East Texas: An event possibly triggered by fluid injection. *Journal of Geophysical Research: Solid Earth*, 119(1):581–593.
- Fu, H. (2017). Treatment of oilfield fracturing wastewater. *Petroleum Science and Technology*, 35(17):1743–1749.
- Garagash, D. I. and Germanovich, L. N. (2012). Nucleation and arrest of dynamic slip on a pressurized fault. *Journal of Geophysical Research: Solid Earth*, 117(B10).
- Giacomel, P., Spagnuolo, E., Nazzari, M., Marzoli, A., Passelègue, F. X., Youbi, N., and Di Toro, G. (2018). Frictional instabilities and carbonation of basalts triggered by injection of pressurized H₂O and CO₂ rich fluids. *Geophysical Research Letters*, 45(12):6032–6041.
- Giordano, D., Russell, J. K., and Dingwell, D. B. (2008). Viscosity of magmatic liquids: A model. *Earth and Planetary Science Letters*, 271(1-4):123–134.
- Giorgetti, C., Carpenter, B. M., and Collettini, C. (2015). Frictional behavior of talc-calcite mixtures. *Journal of Geophysical Research: Solid Earth*, 120(9):6614–6633.
- Goertz-Allmann, B. P., Goertz, A., and Wiemer, S. (2011). Stress drop variations of induced earthquakes at the Basel geothermal site. *Geophysical Research Letters*, 38(9):n/a–n/a.
- Goldsby, D. L. and Tullis, T. E. (2002). Low frictional strength of quartz rocks at subseismic slip rates. *Geophysical Research Letters*, 29(17):25–1–25–4.
- Goldsby, D. L. and Tullis, T. E. (2011). Flash heating leads to low frictional strength of crustal rocks at earthquake slip rates. *Science*, 334(6053):216–218.
- Gomberg, J., Blanpied, M. L., and Beeler, N. M. (1997). Transient triggering of near and distant earthquakes. *Bulletin of the Seismological Society of America*, 87(2):294–309.
- Goranson, R. W. (1942). Heat Capacity; Heat of Fusion. In Chairman, F. B., Schairer, J. F., and Spicer, H. C., editors, *Handbook of Physical Constants*. Geological Society of America.

Bibliography

- Grandin, R., Vallée, M., and Lacassin, R. (2017). Rupture Process of the M w 5.8 Pawnee, Oklahoma, Earthquake from Sentinel-1 InSAR and Seismological Data. *Seismological Research Letters*, 88(4):994–1004.
- Green, C. A., Styles, P., and Babbie, B. J. (2012). Preese hall shale gas fracturing: Review and recommendations for induced seismic mitigation. Technical report.
- Green, H. W., Shi, F., Bozhilov, K., Xia, G., and Reches, Z. (2015). Phase transformation and nanometric flow cause extreme weakening during fault slip. *Nature Geoscience*, 8(6):448–489.
- Griffith, W. A., Di Toro, G., Pennacchioni, G., and Pollard, D. D. (2008). Thin pseudotachylytes in faults of the Mt. Abbot quadrangle, Sierra Nevada: Physical constraints for small seismic slip events. *Journal of Structural Geology*, 30(9):1086–1094.
- Griffith, W. A., Nielsen, S., Di Toro, G., and Smith, S. A. (2010). Rough faults, distributed weakening, and off-fault deformation. *Journal of Geophysical Research: Solid Earth*, 115(8):1–22.
- Griffith, W. A., Toro, G. D., Pennacchioni, G., Pollard, D. D., and Nielsen, S. (2009). Static stress drop associated with brittle slip events on exhumed faults. *Journal of Geophysical Research: Solid Earth*, 114(2):1–13.
- Grigoli, F., Cesca, S., Priolo, E., Rinaldi, A. P., Clinton, J. F., Stabile, T. A., Dost, B., Fernandez, M. G., Wiemer, S., and Dahm, T. (2017). Current challenges in monitoring, discrimination, and management of induced seismicity related to underground industrial activities: A european perspective. *Reviews of Geophysics*, 55(2):310–340.
- Gu, J.-C., Rice, J. R., Ruina, A. L., and Tse, S. T. (1984). Slip motion and stability of a single degree of freedom elastic system with rate and state dependent friction. *Journal of the Mechanics and Physics of Solids*, 32(3):167–196.
- Guatteri, M. and Spudich, P. (2000). What can strong-motion data tell us about slip-weakening fault-friction laws? *Bulletin of the Seismological Society of America*, 90(1):98–116.
- Guglielmi, Y., Cappa, F., Avouac, J.-P., Henry, P., and Elsworth, D. (2015). Seismicity triggered by fluid injection-induced aseismic slip. *Science*, 348(6240):1224–1226.
- Guilhem, A., Hutchings, L., Dreger, D. S., and Johnson, L. R. (2014). Moment tensor inversions of m 3 earthquakes in the geysers geothermal fields, california. *Journal of Geophysical Research: Solid Earth*, 119(3):2121–2137.
- Han, R., Hirose, T., and Shimamoto, T. (2010). Strong velocity weakening and powder lubrication of simulated carbonate faults at seismic slip rates. *Journal of Geophysical Research: Solid Earth*, 115(B3).

- Han, R., Shimamoto, T., Hirose, T., Ree, J.-H., and Ando, J.-i. (2007). Ultralow Friction of Carbonate Faults Caused by Thermal Decomposition. *Science*, 316(5826):878–881.
- Handin, J. (1969). On the coulomb-mohr failure criterion. *Journal of Geophysical Research (1896-1977)*, 74(22):5343–5348.
- Hans Wedepohl, K. (1995). The composition of the continental crust. *Geochimica et Cosmochimica Acta*, 59(7):1217–1232.
- Harbord, C. W., Nielsen, S. B., De Paola, N., and Holdsworth, R. E. (2017). Earthquake nucleation on rough faults. *Geology*, 45(10):931–934.
- Harris, R. A. (1998). Introduction to Special Section: Stress Triggers, Stress Shadows, and Implications for Seismic Hazard. *Journal of Geophysical Research: Solid Earth*, 103(B10):24347–24358.
- He, C., Ma, S., and Huang, J. (1998). Transition between stable sliding and stick-slip due to variation in slip rate under variable normal stress condition. *Geophysical Research Letters*, 25(17):3235–3238.
- Healy, J., Rubey, W., Griggs, D., and Raleigh, C. (1968). The denver earthquakes. *Science*, 161(3848):1301–1310.
- Heaton, T. H. (1990). Evidence for and implications of self-healing pulses of slip in earthquake rupture. *Physics of the Earth and Planetary Interiors*, 64(1):1 – 20.
- Heslot, F., Baumberger, T., Perrin, B., Caroli, B., and Caroli, C. (1994). Creep, stick-slip, and dry-friction dynamics: Experiments and a heuristic model. *Physical Review E*, 49(6):4973–4988.
- Hickman, S., Sibson, R., and Bruhn, R. (1995). Introduction to special section: Mechanical involvement of fluids in faulting. *Journal of Geophysical Research: Solid Earth*, 100(B7):12831–12840.
- Hirose, T., Mizoguchi, K., and Shimamoto, T. (2012). Wear processes in rocks at slow to high slip rates. *Journal of Structural Geology*, 38:102 – 116. Physico-Chemical Processes in Seismic Faults.
- Hirose, T. and Shimamoto, T. (2005). Growth of molten zone as a mechanism of slip weakening of simulated faults in gabbro during frictional melting. *Journal of Geophysical Research*, 110(B5):B05202.
- Hofmann, R. (2016). Groningen pressure maintenance (gpm) study, progress report february 2016.

Bibliography

- Holditch, S., Ely, J., Semmelbeck, M., Carter, R., Hinkel, J., and Jeffrey, R.G., J. (1988). Enhanced recovery of coalbed methane through hydraulic fracturing. *Society of Petroleum Engineers*, pages 1–43.
- Hornbach, M. J., Jones, M., Scales, M., DeShon, H. R., Magnani, M. B., Frohlich, C., Stump, B., Hayward, C., and Layton, M. (2016). Ellenburger wastewater injection and seismicity in north texas. *Physics of the Earth and Planetary Interiors*, 261:54 – 68. Microseismicity from all scales.
- Hsieh, P. A. and Bredehoeft, J. D. (1981). A reservoir analysis of the Denver earthquakes: A case of induced seismicity. *Journal of Geophysical Research: Solid Earth*, 86(B2):903–920.
- Huang, Y., Ampuero, J.-P., and Kanamori, H. (2014). Slip-weakening models of the 2011 tohoku-oki earthquake and constraints on stress drop and fracture energy. *Pure and Applied Geophysics*, 171(10):2555–2568.
- Huang, Y., Ellsworth, W. L., and Beroza, G. C. (2017). Stress drops of induced and tectonic earthquakes in the central United States are indistinguishable. *Science Advances*, 3(8):e1700772.
- Huber, M. L., Perkins, R. A., Laesecke, A., Friend, D. G., Sengers, J. V., Assael, M. J., Metaxa, I. N., Vogel, E., Mareš, R., and Miyagawa, K. (2009). New international formulation for the viscosity of h₂O. *Journal of Physical and Chemical Reference Data*, 38(2):101–125.
- Häring, M. O., Schanz, U., Ladner, F., and Dyer, B. C. (2008). Characterisation of the basel 1 enhanced geothermal system. *Geothermics*, 37(5):469 – 495.
- Ida, Y. (1972). Cohesive force across the tip of a longitudinal-shear crack and Griffith's specific surface energy. *Journal of Geophysical Research*, 77(20):3796–3805.
- Ikari, M. J., Marone, C., Saffer, D. M., and Kopf, A. J. (2013). Slip weakening as a mechanism for slow earthquakes. *Nature Geoscience*, 6(6):468–472.
- Ikari, M. J., Saffer, D. M., and Marone, C. (2009). Frictional and hydrologic properties of clay-rich fault gouge. *Journal of Geophysical Research*, 114(March):1–18.
- Irwin, G. (1968). Linear fracture mechanics, fracture transition, and fracture control. *Engineering Fracture Mechanics*, 1(2):241 – 257.
- Ishibashi, T., Elsworth, D., Fang, Y., Riviere, J., Madara, B., Asanuma, H., Watanabe, N., and Marone, C. (2018). Friction-stability-permeability evolution of a fracture in granite. *Water Resources Research*, 54(12):9901–9918.
- Ishida, T., Chen, Q., Mizuta, Y., and Roegiers, J.-C. (2004). Influence of Fluid Viscosity on the Hydraulic Fracturing Mechanism . *Journal of Energy Resources Technology*, 126(3):190–200.

- Iwasa, K. and Yoshioka, N. (1998). An experimental trial to detect precursory slips by transmission waves across a fault. *Geophysical Research Letters*, 25(20):3907–3910.
- Jaeger, J. C. (1959). The frictional properties of joints in rock. *Geofisica pura e applicata*, 43:148–158.
- Jaeger, J. C., Cook, N. G. W., and Zimmerman, R. W. (2007). *Deformation and Failure of Rock*, pages 80–105. Blackwell Malden, Mass. ; Oxford, 4th ed. edition.
- Jost, M. L., Büßelberg, T., Jost, Ö., and Harjes, H. P. (1998). Source parameters of injection-induced microearthquakes at 9 km depth at the KTB deep drilling site, Germany. *Bulletin of the Seismological Society of America*, 88(3):815–832.
- Kanamori, H. (1981). The nature of seismicity patterns before large earthquakes.
- Kanamori, H. and Anderson, D. (1975). Theoretical basis of some empirical relations in seismology. *Bulletin of the Seismological Society of America*, 65(5):1073–1095.
- Kanamori, H. and Hauksson, E. (1992). A slow earthquake in the Santa Maria basin, California. *Bulletin of the Seismological Society of America*, 82(5):2087–2096.
- Kanamori, H. and Rivera, L. (2006). Energy partitioning during an earthquake. In *Earthquakes: Radiated Energy and the Physics of Faulting*, pages 3–13.
- Kanamori, H. and Rivera, L. (2013). *Energy Partitioning During an Earthquake*, pages 3–13. American Geophysical Union (AGU).
- Kaneko, Y., Avouac, J.-P., and Lapusta, N. (2010). Towards inferring earthquake patterns from geodetic observations of interseismic coupling. *Nature Geoscience*, 3(5):363–369.
- Keranen, K. M., Savage, H. M., Abers, G. A., and Cochran, E. S. (2013). Potentially induced earthquakes in Oklahoma, USA: Links between wastewater injection and the 2011 Mw 5.7 earthquake sequence. *Geology*, 41(6):699–702.
- Keranen, K. M., Weingarten, M., Abers, G. A., Bekins, B. A., and Ge, S. (2014). Sharp increase in central oklahoma seismicity since 2008 induced by massive wastewater injection. *Science*, 345(6195):448–451.
- Kilb, D., Gombert, J., and Bodin, P. (2000). Triggering of earthquake aftershocks by dynamic stresses. *Nature*, 408(6812):570–574.
- Kilgore, B. D., Blanpied, M. L., and Dieterich, J. H. (1993). Velocity dependent friction of granite over a wide range of conditions. *Geophysical Research Letters*, 20(10):903–906.
- Kim, W.-Y. (2013). Induced seismicity associated with fluid injection into a deep well in Youngstown, Ohio. *Journal of Geophysical Research: Solid Earth*, 118(7):3506–3518.

Bibliography

- King, V. M., Block, L. V., Yeck, W. L., Wood, C. K., and Derouin, S. A. (2014). Geological structure of the Paradox Valley Region, Colorado, and relationship to seismicity induced by deep well injection. *Journal of Geophysical Research: Solid Earth*, 119(6):4955–4978.
- King Hubbert, M. and Rubey, W. W. (1959). Role of Fluid Pressure in Mechanics of Overthrust Faulting. *Geological Society of America Bulletin*, 70(2):115.
- Lachenbruch, A. H. and Sass, J. H. (1980). Heat Flow and Energetics of the San Andreas Fault Zone. *Journal of Geophysical Research*, 85(10):6185–6222.
- Latour, S., Campillo, M., Voisin, C., Ionescu, I. R., Schmedes, J., and Lavallée, D. (2011). Effective friction law for small-scale fault heterogeneity in 3d dynamic rupture. *Journal of Geophysical Research: Solid Earth*, 116(B10).
- Lee, J. and Ladd, A. J. C. (2002). A computer simulation study of multiphase squeezing flows. *Physics of Fluids*, 14(5):1631–1641.
- Leeman, J. R., Marone, C., and Saffer, D. M. (2018). Frictional mechanics of slow earthquakes. *Journal of Geophysical Research: Solid Earth*, 123(9):7931–7949.
- Lei, X., Ma, S., Chen, W., Pang, C., Zeng, J., and Jiang, B. (2013). A detailed view of the injection-induced seismicity in a natural gas reservoir in zigong, southwestern sichuan basin, china. *Journal of Geophysical Research: Solid Earth*, 118(8):4296–4311.
- Lei, X., Yu, G., Ma, S., Wen, X., and Wang, Q. (2008). Earthquakes induced by water injection at 3 km depth within the rongchang gas field, chongqing, china. *Journal of Geophysical Research: Solid Earth*, 113(B10).
- Li Chun Bo and Pavelescu, D. (1982). The friction-speed relation and its influence on the critical velocity of stick-slip motion. *Wear*, 82(3):277–289.
- Liao, Z., Chang, J. C., and Reches, Z. (2014). Fault strength evolution during high velocity friction experiments with slip-pulse and constant-velocity loading. *Earth and Planetary Science Letters*, 406:93–101.
- Linde, A. T., Gladwin, M. T., Johnston, M. J. S., Gwyther, R. L., and Bilham, R. G. (1996). A slow earthquake sequence on the San Andreas fault. *A slow earthquake sequence on the San Andreas fault*, 383:65–68.
- Linker, M. F. and Dieterich, J. H. (1992). Effects of variable normal stress on rock friction: Observations and constitutive equations. *Journal of Geophysical Research*, 97(B4):4923.
- Lockner, D. and Byerlee, J. (1986). *Laboratory measurements of velocity-dependent frictional strength*. Citeseer.

- Lockner, D. A. and Beeler, N. M. (2002). Rock failure and earthquakes. *International Geophysics Series*, 81(A):505–538.
- Lockner, D. A., Kilgore, B. D., Beeler, N. M., and Moore, D. E. (2017). *The Transition From Frictional Sliding to Shear Melting in Laboratory Stick-Slip Experiments*, chapter 6, pages 103–131. American Geophysical Union (AGU).
- Lockner, D. A., Summers, R., and Byerlee, J. D. (1987). *Effects of Temperature and Sliding Rate on Frictional Strength of Granite*, pages 445–469. Birkhäuser Basel, Basel.
- Lu, M. and Wei, X. (2011). Treatment of oilfield wastewater containing polymer by the batch activated sludge reactor combined with a zerovalent iron/edta/air system. *Bioresource Technology*, 102(3):2555 – 2562.
- Lykotrafitis, G., Rosakis, A. J., and Ravichandran, G. (2006). Self-healing pulse-like shear ruptures in the laboratory. *Science*, 313(5794):1765–1768.
- Madariaga, R. (1976). Dynamics of an expanding circular fault. *Bulletin of the Seismological Society of America*, 66(3):639–666.
- Madariaga, R. and Olsen, K. B. (2002). Earthquake dynamics. In *International Geophysics Series*, volume 81, pages 175–194. ACADEMIC PRESS LTD.
- Mair, K., Frye, K. M., and Marone, C. (2002). Influence of grain characteristics on the friction of granular shear zones. *Journal of Geophysical Research: Solid Earth*, 107(B10):ECV 4–1–ECV 4–9.
- Majer, E. L., Baria, R., Stark, M., Oates, S., Bommer, J., Smith, B., and Asanuma, H. (2007). Induced seismicity associated with Enhanced Geothermal Systems. *Geothermics*, 36(3):185–222.
- Major, J. J. and Pierson, T. C. (1992). Debris Flow Rheology: Experimental Analysis of Fine-Grained Slurries. *Water Resources Research*, 28(3):841–857.
- Malagnini, L., Mayeda, K., Nielsen, S., Yoo, S.-H., Munafo', I., Rawles, C., and Boschi, E. (2014). Scaling Transition in Earthquake Sources: A Possible Link Between Seismic and Laboratory Measurements. *Pure and Applied Geophysics*, 171(10):2685–2707.
- Marone, C. (1998). Laboratory-Derived Friction Laws and Their Application To Seismic Faulting. *Annual Review of Earth and Planetary Sciences*, 26(1):643–696.
- Marone, C., Raleigh, C. B., and Scholz, C. H. (1990). Frictional behavior and constitutive modeling of simulated fault gouge. *Journal of Geophysical Research: Solid Earth*, 95(B5):7007–7025.

Bibliography

- Marone, C. and Saffer, D. (2015). *The Mechanics of Frictional Healing and Slip Instability During the Seismic Cycle*, volume 4, pages 111–138. Elsevier Inc., United States.
- Marty, S., Passelègue, F. X., Aubry, J., Bhat, H. S., Schubnel, A., and Madariaga, R. (2019). Origin of high-frequency radiation during laboratory earthquakes. *Geophysical Research Letters*, 46(7):3755–3763.
- Maruyama, M. (1963). Basic elements in misunderstandings ii. *Dialectica*, 17(2-3):99–109.
- Maxwell, S. C., Rutledge, J., Jones, R., and Fehler, M. (2010). Petroleum reservoir characterization using downhole microseismic monitoring. *GEOPHYSICS*, 75(5):75A129–75A137.
- McGarr, A., Benkins, B., Burkardt, N., Dewey, J., Earle, P., Ellsworth, W., Ge, S., Hickman, S., Holland, A., Major, E., Rubinstein, J., and Sheehan, A. (2014). Coping with earthquakes induced by fluid injection. *Journal of Geophysical Research: Solid Earth*, pages 1–12.
- McLaskey, G. C., Kilgore, B. D., and Beeler, N. M. (2015). Slip-pulse rupture behavior on a 2 m granite fault. *Geophysical Research Letters*, 42(17):7039–7045.
- McNamara, D. E., Benz, H. M., Herrmann, R. B., Bergman, E. A., Earle, P., Holland, A., Baldwin, R., and Gassner, A. (2015). Earthquake hypocenters and focal mechanisms in central Oklahoma reveal a complex system of reactivated subsurface strike-slip faulting. *Geophysical Research Letters*, 42(8):2742–2749.
- Miller, S. A., Collettini, C., Chiaraluce, L., Cocco, M., Barchi, M., and Kaus, B. J. P. (2004). Aftershocks driven by a high-pressure CO₂ source at depth. *Nature*, 427(6976):724–727.
- Mitchell, E. K., Fialko, Y., and Brown, K. M. (2016). Velocity-weakening behavior of westerly granite at temperature up to 600°C. *Journal of Geophysical Research: Solid Earth*, 121(9):6932–6946.
- Mitchell, T. and Faulkner, D. (2009). The nature and origin of off-fault damage surrounding strike-slip fault zones with a wide range of displacements: A field study from the atacama fault system, northern chile. *Journal of Structural Geology*, 31(8):802 – 816.
- Mizoguchi, K., Hirose, T., Shimamoto, T., and Fukuyama, E. (2007). Reconstruction of seismic faulting by high-velocity friction experiments : An example of the 1995 Kobe earthquake. *Geophysical Research Letters*, 34(L01308).
- Mizoguchi, K., Hirose, T., Shimamoto, T., and Fukuyama, E. (2009). High-velocity frictional behavior and microstructure evolution of fault gouge obtained from nojima fault, southwest japan. *Tectonophysics*, 471(3):285 – 296.

- Moore, D. E. and Lockner, D. A. (2004). Crystallographic controls on the frictional behavior of dry and water-saturated sheet structure minerals. *Journal of Geophysical Research: Solid Earth*, 109(B3).
- Moore, D. E. and Lockner, D. A. (2011). Frictional strengths of talc-serpentine and talc-quartz mixtures. *Journal of Geophysical Research: Solid Earth*, 116(B1).
- Moore, D. E. and Lockner, D. A. (2013). Chemical controls on fault behavior: Weakening of serpentinite sheared against quartz-bearing rocks and its significance for fault creep in the san andreas system. *Journal of Geophysical Research: Solid Earth*, 118(5):2558–2570.
- Morris, A., Ferrill, D., Walter, G., Price, A., Smart, K., Skoumal, R., Brudzinski, M., and Currie, B. (2017). Lessons learned from the youngstown, ohio induced earthquake sequence from january 2011 to january 2012. *Journal of Rock Mechanics and Geotechnical Engineering*, 9(5):783 – 796.
- Morris, J., Hao, Y., Foxall, W., and McNab, W. (2011a). In salah co2 storage jip: hydromechanical simulations of surface uplift due to co2 injection at in salah. *Energy Procedia*, 4:3269 – 3275. 10th International Conference on Greenhouse Gas Control Technologies.
- Morris, J. P., Detwiler, R. L., Friedmann, S. J., Vorobiev, O. Y., and Hao, Y. (2011b). The large-scale geomechanical and hydrogeological effects of multiple co2 injection sites on formation stability. *International Journal of Greenhouse Gas Control*, 5(1):69 – 74.
- Morse, P. M. and Feshbach, H. (1953). *Methods of Theoretical Physics: Part 1*. McGraw-Hill, New York.
- Mukuhira, Y., Asanuma, H., Niitsuma, H., Häring, M., and Deichmann, N. (2010). Estimation of source parameter of microseismic events with large magnitude collected at basel, switzerland in 2006. *Geothermal Resources Council Transactions*, 34:407–412.
- Nakamura, Y., Muto, J., Nagahama, H., Shimizu, I., Miura, T., and Arakawa, I. (2012). Amorphization of quartz by friction: Implication to silica-gel lubrication of fault surfaces. *Geophysical Research Letters*, 39(21).
- Nasseri, M. H. B., Schubnel, A., Benson, P. M., and Young, R. P. (2009). Common Evolution of Mechanical and Transport Properties in Thermally Cracked Westerly Granite at Elevated Hydrostatic Pressure. *Pure and Applied Geophysics*, 166:927–948.
- Nielsen, S., Di Toro, G., and Griffith, W. A. (2010). Friction and roughness of a melting rock surface. *Geophysical Journal International*, 182:no–no.
- Nielsen, S., Di Toro, G., Hirose, T., and Shimamoto, T. (2008). Frictional melt and seismic slip. *Journal of Geophysical Research*, 113(B1):B01308.

Bibliography

- Nielsen, S., Spagnuolo, E., Smith, S. A. F., Violay, M., Di Toro, G., and Bistacchi, A. (2016). Scaling in natural and laboratory earthquakes. *Geophysical Research Letters*, 43(4):1504–1510.
- Nielsen, S., Spagnuolo, E., and Violay, M. (2012). Composite Sample Mount Assembly (SAMOA): The Ultimate Sample Preparation for Rotary Shear Experiments. Technical report, INGV.
- Niemeijer, A., Di Toro, G., Nielsen, S., and Di Felice, F. (2011). Frictional melting of gabbro under extreme experimental conditions of normal stress, acceleration, and sliding velocity. *Journal of Geophysical Research*, 116(B7):B07404.
- Niemeijer, A. R. and Collettini, C. (2014). Frictional Properties of a Low-Angle Normal Fault Under In Situ Conditions : Thermally-Activated Velocity Weakening. *Pure and Applied Geophysics*, 171:2641–2664.
- Nobakht, M., Moghadam, S., and Gu, Y. (2007). Effects of viscous and capillary forces on co2 enhanced oil recovery under reservoir conditions. *Energy & Fuels*, 21(6):3469–3476.
- Noël, C., Passelègue, F. X., Giorgetti, C., and Violay, M. (2019). Fault reactivation during fluid pressure oscillations: Transition from stable to unstable slip. *Journal of Geophysical Research: Solid Earth*, 124(11):10940–10953.
- Novotny, E. (1977). Proppant transport. *Society of Petroleum Engineers*.
- ODNR (2012). Preliminary Report on the North Star 1 Class II Injection Well and the Seismic Events in the Youngstown, Ohio, Area. *Ohio Department of Natural Resources*, (March):1–24.
- O'Hara, K., Mizoguchi, K., Shimamoto, T., and Hower, J. C. (2006). Experimental frictional heating of coal gouge at seismic slip rates: Evidence for devolatilization and thermal pressurization of gouge fluids. *Tectonophysics*, 424(1):109 – 118.
- Ohnaka, M. (2003). A constitutive scaling law and a unified comprehension for frictional slip failure, shear fracture of intact rock, and earthquake rupture. *Journal of Geophysical Research: Solid Earth*, 108(B2).
- Ohnaka, M. (2013). *Fundamentals of rock failure physics*, page 6–27. Cambridge University Press.
- Ohnaka, M. and Shen, L.-f. (1999). Scaling of the shear rupture process from nucleation to dynamic propagation: Implications of geometric irregularity of the rupturing surfaces. *Journal of Geophysical Research: Solid Earth*, 104(B1):817–844.
- Okubo, P. G. and Dieterich, J. H. (1984). Effects of physical fault properties on frictional instabilities produced on simulated faults. *Journal of Geophysical Research: Solid Earth*, 89(B7):5817–5827.

- Otsuki, K., Monzawa, N., and Nagase, T. (2003). Fluidization and melting of fault gouge during seismic slip: Identification in the Nojima fault zone and implications for focal earthquake mechanisms. *Journal of Geophysical Research: Solid Earth*, 108(B4).
- Palmer, A. C. and Rice, J. R. (1973). The Growth of Slip Surfaces in the Progressive Failure of Over-Consolidated Clay. *Proceedings of the Royal Society A: Mathematical, Physical and Engineering Sciences*, 332(1591):527–548.
- Passelègue, F. X., Brantut, N., and Mitchell, T. M. (2018). Fault Reactivation by Fluid Injection: Controls From Stress State and Injection Rate. *Geophysical Research Letters*, page 2018GL080470.
- Passelègue, F. X., Goldsby, D. L., and Fabbri, O. (2014). The influence of ambient fault temperature on flash-heating phenomena. *Geophysical Research Letters*, 41(3):828–835.
- Passelègue, F. X., Schubnel, A., Nielsen, S., Bhat, H. S., Deldicque, D., and Madariaga, R. (2016a). Dynamic rupture processes inferred from laboratory microearthquakes. *Journal of Geophysical Research: Solid Earth*, 121:4343–4365.
- Passelègue, F. X., Spagnuolo, E., Violay, M., Nielsen, S., Di Toro, G., and Schubnel, A. (2016b). Frictional evolution, acoustic emissions activity, and off-fault damage in simulated faults sheared at seismic slip rates. *Journal of Geophysical Research: Solid Earth*, 121(10):7490–7513.
- Paterson, M. S. and Wong, T.-f. (2005a). *Experimental Rock Deformation: The Brittle Field, 2nd Edition*. Springer Science & Business Media.
- Paterson, M. S. and Wong, T.-f. (2005b). *Micromechanics of Brittle Fracture*, pages 115–145. Springer Berlin Heidelberg, Berlin, Heidelberg.
- Perrin, G., Rice, J. R., and Zheng, G. (1995). Self-healing slip pulse on a frictional surface. *Journal of the Mechanics and Physics of Solids*, 43(9):1461 – 1495.
- Persson, B. N. J. (2000a). *Area of Real Contact: Elastic and Plastic Deformations*, pages 45–91. Springer Berlin Heidelberg, Berlin, Heidelberg.
- Persson, B. N. J. (2000b). *Boundary Lubrication*, pages 313–334. Springer Berlin Heidelberg, Berlin, Heidelberg.
- Persson, B. N. J. (2000c). *Lubricated Friction Dynamics*, pages 395–413. Springer Berlin Heidelberg, Berlin, Heidelberg.
- Persson, B. N. J. (2000d). *Sliding Friction*. NanoScience and Technology. Springer Berlin Heidelberg, Berlin, Heidelberg.

Bibliography

- Persson, B. N. J. (2000e). *Sliding on Lubricated Surfaces*, pages 101–170. Springer Berlin Heidelberg, Berlin, Heidelberg.
- Petrov, N. (1883). Friction in machines and the effect of the lubricant. *Inzh. Zh., St-Peterb.*
- Peyrat, S., Olsen, K., and Madariaga, R. (2001). Dynamic modeling of the 1992 landers earthquake. *Journal of Geophysical Research: Solid Earth*, 106(B11):26467–26482.
- Platt, J. D., Brantut, N., and Rice, J. R. (2015). Strain localization driven by thermal decomposition during seismic shear. *Journal of Geophysical Research: Solid Earth*, 120(6):4405–4433.
- Platt, J. D., Rudnicki, J. W., and Rice, J. R. (2014). Stability and localization of rapid shear in fluid-saturated fault gouge: 2. localized zone width and strength evolution. *Journal of Geophysical Research: Solid Earth*, 119(5):4334–4359.
- Pollitz, F. F., Wicks, C., Ellsworth, W., Murray, M., and Schoenball, M. (2017). *Geodetic Slip Model of the 3 September 2016 M w 5.8 Pawnee, Oklahoma, Earthquake: Evidence for Fault-Zone Collapse*, volume 88.
- Pozzi, G., Paola, N. D., Holdsworth, R. E., Bowen, L., Nielsen, S. B., and Dempsey, E. D. (2019). Coseismic ultramylonites: An investigation of nanoscale viscous flow and fault weakening during seismic slip. *Earth and Planetary Science Letters*, 516:164 – 175.
- Proctor, B. P., Mitchell, T. M., Hirth, G., Goldsby, D., Zorzi, F., Platt, J. D., and Di Toro, G. (2014). Dynamic weakening of serpentinite gouges and bare surfaces at seismic slip rates. *Journal of Geophysical Research: Solid Earth*, 119(11):8107–8131.
- Rabinowicz, E. (1958). The intrinsic variables affecting the stick-slip process. *Proceedings of the Physical Society*, 71(4):668–675.
- Raleigh, A. C. B., Healy, J. H., and Bredehoeft, J. D. (1976). An Experiment in Earthquake Control at Rangely, Colorado. *Science*, 191(4233):1230–1237.
- Rathbun, A. P., Marone, C., Alley, R. B., and Anandakrishnan, S. (2008). Laboratory study of the frictional rheology of sheared till. *Journal of Geophysical Research: Earth Surface*, 113(2):1–14.
- Reches, Z. and Lockner, D. A. (2010). Fault weakening and earthquake instability by powder lubrication. *Nature*, 467(7314):452–455.
- Reid, H. F. (1910). The mechanics of the earthquake. *The California Earthquake of April 18, 1906, Report of the State Earthquake Investigation Commission*.
- Rempe, M., Mitchell, T., Renner, J., Nippres, S., Ben-Zion, Y., and Rockwell, T. (2013). Damage and seismic velocity structure of pulverized rocks near the san andreas fault. *Journal of Geophysical Research: Solid Earth*, 118(6):2813–2831.

- Rempe, M., Smith, S., Mitchell, T., Hirose, T., and Toro, G. D. (2017). The effect of water on strain localization in calcite fault gouge sheared at seismic slip rates. *Journal of Structural Geology*, 97:104 – 117.
- Rempel, A. W. and Rice, J. R. (2006). Thermal pressurization and onset of melting in fault zones. *Journal of Geophysical Research*, 111(B9):B09314.
- Rempel, A. W. and Weaver, S. L. (2008). A model for flash weakening by asperity melting during high-speed earthquake slip. *Journal of Geophysical Research*, 113(B11):B11308.
- Renner, J., Evans, B., and Siddiqi, G. (2002). Dislocation creep of calcite. *Journal of Geophysical Research: Solid Earth*, 107(B12):ECV 6–1–ECV 6–16.
- Reynolds, O. (1886). IV. On the theory of lubrication and its application to Mr. Beauchamp tower's experiments, including an experimental determination of the viscosity of olive oil. *Philosophical Transactions of the Royal Society of London*, 177(0):157–234.
- Rice, J. R. (1968). A Path Independent Integral and the Approximate Analysis of Strain Concentration by Notches and Cracks. *Journal of Applied Mechanics*, 35(2):379–386.
- Rice, J. R. (2006). Heating and weakening of faults during earthquake slip. *Journal of Geophysical Research: Solid Earth*, 111(B5):n/a–n/a.
- Rice, J. R., Rudnicki, J. W., and Platt, J. D. (2014). Stability and localization of rapid shear in fluid-saturated fault gouge: 1. linearized stability analysis. *Journal of Geophysical Research: Solid Earth*, 119(5):4311–4333.
- Rice, J. R. and Ruina, a. L. (1983). Stability of Steady Frictional Slipping. *Journal of Applied Mechanics*, 50(2):343.
- Rice, J. R., Sammis, C. G., and Parsons, R. (2005). Off-fault secondary failure induced by a dynamic slip pulse. *Bulletin of the Seismological Society of America*, 95(1):109–134.
- Richardson, E. and Marone, C. (1999). Effects of normal stress vibrations on frictional healing. *Journal of Geophysical Research: Solid Earth*, 104(B12):28859–28878.
- Ross, A., Foulger, G. R., and Julian, B. R. (1999). Source processes of industrially-induced earthquakes at the geysers geothermal area, california. *GEOPHYSICS*, 64(6):1877–1889.
- Rowe, C. D. and Griffith, W. A. (2015). Do faults preserve a record of seismic slip: A second opinion. *Journal of Structural Geology*, 78:1–26.
- Rowe, C. D., Kirkpatrick, J. D., and Brodsky, E. E. (2012). Fault rock injections record paleo-earthquakes. *Earth and Planetary Science Letters*, 335–336:154–166.

Bibliography

- Rowe, C. D., Lamothe, K., Rempe, M., Andrews, M., Mitchell, T. M., Di Toro, G., and White, Joseph Clancy and Aretusini, S. (2019). Earthquake lubrication and healing explained by amorphous nanosilica. *Nature Communications*, 10(1):79 – 106.
- Ruina, A. (1983). Slip instability and state variable friction laws. *Journal of Geophysical Research: Solid Earth*, 88(B12):10359–10370.
- Rutqvist, J., Vasco, D. W., and Myer, L. (2010). Coupled reservoir-geomechanical analysis of CO₂ injection and ground deformations at In Salah, Algeria. *International Journal of Greenhouse Gas Control*, 4(2):225 – 230. The Ninth International Conference on Greenhouse Gas Control Technologies.
- Rutter, E. and Hackston, A. (2017). On the effective stress law for rock-on-rock frictional sliding, and fault slip triggered by means of fluid injection. *Philosophical Transactions of the Royal Society A: Mathematical, Physical and Engineering Sciences*, 375(2103):20160001.
- Rutter, E. H. (1972). The influence of interstitial water on the rheological behaviour of calcite rocks. *Tectonophysics*, 14(1):13 – 33.
- Rutter, E. H. (1974). The influence of temperature, strain rate and interstitial water in the experimental deformation of calcite rocks. *Tectonophysics*, 22(3):311 – 334.
- Rutter, E. H. and Mecklenburgh, J. (2018). Influence of Normal and Shear Stress on the Hydraulic Transmissivity of Thin Cracks in a Tight Quartz Sandstone, a Granite, and a Shale. *Journal of Geophysical Research: Solid Earth*, 123:1262–1285.
- Samuelson, J., Elsworth, D., and Marone, C. (2009). Shear-induced dilatancy of fluid-saturated faults: Experiment and theory. *Journal of Geophysical Research: Solid Earth*, 114(12):1–15.
- Savage, H. M. and Marone, C. (2007). Effects of shear velocity oscillations on stick-slip behavior in laboratory experiments. *Journal of Geophysical Research: Solid Earth*, 112(B2).
- Schmid, S., Panozzo, R., and Bauer, S. (1987). Simple shear experiments on calcite rocks: rheology and microfabric. *Journal of Structural Geology*, 9(5):747 – 778.
- Schmid, S., Paterson, M., and Boland, J. (1980). High temperature flow and dynamic recrystallization in Carrara marble. *Tectonophysics*, 65(3):245 – 280.
- Scholz, C. and Engelder, J. (1976). The role of asperity indentation and ploughing in rock friction — I: Asperity creep and stick-slip. *International Journal of Rock Mechanics and Mining Sciences & Geomechanics Abstracts*, 13(5):149 – 154.
- Scholz, C. H. (1968). Mechanism of creep in brittle rock. *Journal of Geophysical Research (1896-1977)*, 73(10):3295–3302.

- Scholz, C. H. (1998). Earthquakes and friction laws. *Nature*, 391(6662):37–42.
- Scholz, C. H. (2002). *The Mechanics of Earthquakes and Faulting - Second Edition*, volume 74. Cambridge University Press.
- Scholz, C. H. (2019a). *Brittle fracture of rock*, page 1–42. Cambridge University Press, 3 edition.
- Scholz, C. H. (2019b). *The mechanics of earthquakes and faulting*. Cambridge university press.
- Schultz, R., Wang, R., Gu, Y. J., Haug, K., and Atkinson, G. (2017). A seismological overview of the induced earthquakes in the Duvernay play near Fox Creek, Alberta. *Journal of Geophysical Research: Solid Earth*, 122(1):492–505.
- Scuderi, M. M., Collettini, C., and Marone, C. (2017). Frictional stability and earthquake triggering during fluid pressure stimulation of an experimental fault. *Earth and Planetary Science Letters*, 477:84–96.
- Scuderi, M. M., Marone, C., Tinti, E., Di Stefano, G., and Collettini, C. (2016). Precursory changes in seismic velocity for the spectrum of earthquake failure modes. *Nature Geoscience*, 9(9):695–700.
- Segall, P. and Lu, S. (2015). Injection-induced seismicity: Poroelastic and earthquake nucleation effects. *Journal of Geophysical Research: Solid Earth*, 120(7):5082–5103.
- Segall, P. and Rice, J. R. (1995). Dilatancy, compaction, and slip instability of a fluid-infiltrated fault. *Journal of Geophysical Research: Solid Earth*, 100(B11):22155–22171.
- Segall, P. and Rice, J. R. (2006). Does shear heating of pore fluid contribute to earthquake nucleation? *Journal of Geophysical Research: Solid Earth*, 111(B9).
- Shapiro, S. and Dinske, C. (2009). Fluid-induced seismicity: Pressure diffusion and hydraulic fracturing. *Geophysical Prospecting*, 57(2):301–310.
- Shearer, P. M. (2019). *Introduction to seismology*. Cambridge university press.
- Shen, L., Schmitt, D. R., and Haug, K. (2018). Measurements of the States of In Situ Stress for the Duvernay Formation near Fox Creek , West-Central Alberta. Technical report, Alberta Energy Regulator Alberta Geological Survey.
- Shimamoto, T. (1994). A new rotary-shear high-speed frictional testing machine : its basic design and scope of research. *Jour. Tectonic Res. Group of Japan*, 39:65–78.
- Shimizu, H., Murata, S., and Ishida, T. (2011). The distinct element analysis for hydraulic fracturing in hard rock considering fluid viscosity and particle size distribution. *International Journal of Rock Mechanics and Mining Sciences*, 48(5):712 – 727.

Bibliography

- Shipton, Z. K., Evans, J. P., Abercrombie, R. E., and Brodsky, E. E. (2006). The Missing Sinks : Slip Localization in Faults , Damage Zones , and the Seismic Energy Budget. *Geophysical Monograph Series*, 170:217–222.
- Sibson, R., Moore, J. M. M., and Rankin, A. (1975). Seismic pumping—a hydrothermal fluid transport mechanism. *Journal of the Geological Society*, 131(6):653–659.
- Sibson, R. H. (1973). Interactions between Temperature and Pore-Fluid Pressure during Earthquake Faulting and a Mechanism for Partial or Total Stress Relief. *Nature Physical Science*, 243(126):66–68.
- Sibson, R. H. (1975). Generation of Pseudotachylyte by Ancient Seismic Faulting. *Geophysical Journal of the Royal Astronomical Society*, 43(3):775–794.
- Sibson, R. H. (1986). Brecciation processes in fault zones: Inferences from earthquake rupturing. *Pure and Applied Geophysics PAGEOPH*, 124(1-2):159–175.
- Sibson, R. H. (1989). Earthquake faulting as a structural process. *Journal of Structural Geology*, 11(1-2):1–14.
- Sibson, R. H. (1992). Fault-valve behavior and the hydrostatic-lithostatic fluid pressure interface. *Earth Science Reviews*, 32(1-2):141–144.
- Sibson, R. H., Robert, F., and Poulsen, K. H. (1988). High-angle reverse faults, fluid-pressure cycling, and mesothermal gold-quartz deposits. *Geology*, 16(6):551–555.
- Smith, S., Nielsen, S., and Di Toro, G. (2015). Strain localization and the onset of dynamic weakening in calcite fault gouge. *Earth and Planetary Science Letters*, 413:25 – 36.
- Solberg, P. and Byerlee, J. D. (1984). A note on the rate sensitivity of frictional sliding of westerly granite. *Journal of Geophysical Research: Solid Earth*, 89(B6):4203–4205.
- Sommerfeld, A. (1964). *Mechanics of deformable bodies*. Academic Press.
- Sone, H. and Shimamoto, T. (2009). Frictional resistance of faults during accelerating and decelerating earthquake slip. *Nature Geoscience*, 2(10):705–708.
- Spagnuolo, E. (2006). *Evoluzione della trazione dinamica sulla faglia durante I forti terremoti*,. PhD thesis, Univ. degli Studi di Roma “La Sapienza”.
- Spagnuolo, E., Nielsen, S., Violay, M., and Di Toro, G. (2016). An empirically based steady state friction law and implications for fault stability. *Geophysical Research Letters*, 43(7):3263–3271.

- Spagnuolo, E., Plümper, O., Violay, M., Cavallo, A., and Di Toro, G. (2015). Fast-moving dislocations trigger flash weakening in carbonate-bearing faults during earthquakes. *Scientific Reports*, 5(1):16112.
- Spray, J. G. (1993). Viscosity determinations of some frictionally generated silicate melts: Implications for fault zone rheology at high strain rates. *Journal of Geophysical Research: Solid Earth*, 98(B5):8053–8068.
- Spray, J. G. (2005). Evidence for melt lubrication during large earthquakes. *Geophysical Research Letters*, 32(7).
- Stein, S. and Wysession, M. (2009). *An introduction to seismology, earthquakes, and earth structure*. John Wiley & Sons.
- Stesky, R., Brace, W., Riley, D., and Robin, P.-Y. (1974). Friction in faulted rock at high temperature and pressure. *Tectonophysics*, 23(1):177 – 203.
- Stribeck, R. (1902). Die wesentlichen eigenschaften der gleit- und rollenlager (characteristics of plain and roller bearings). *Zeitschrift des Vereines Seutscher Ingenieure*, 46(38):1342–1348.
- Suckale, J. (2009). Induced Seismicity in Hydrocarbon Fields. In *Advances in Geophysics*, volume 51, pages 55–106. Elsevier Inc.
- Sun, X. and Hartzell, S. (2014). Finite-fault slip model of the 2011 Mw 5.6 Prague, Oklahoma earthquake from regional waveforms. *Geophysical Research Letters*, 41(12):4207–4213.
- Szafranski, D. and Duan, B. (2018). *Integrating Poroelastic Effects of Wastewater Injection and Rupture Dynamics to Understand Induced Seismicity*, pages 2557–2576.
- Tanikawa, W., Mukoyoshi, H., and Tadai, O. (2012a). Experimental investigation of the influence of slip velocity and temperature on permeability during and after high-velocity fault slip. *Journal of Structural Geology*, 38:90 – 101. Physico-Chemical Processes in Seismic Faults.
- Tanikawa, W., Mukoyoshi, H., Tadai, O., Hirose, T., Tsutsumi, A., and Lin, W. (2012b). Velocity dependence of shear-induced permeability associated with frictional behavior in fault zones of the nankai subduction zone. *Journal of Geophysical Research: Solid Earth*, 117(B5).
- Tanikawa, W., Tadai, O., and Mukoyoshi, H. (2014). Permeability changes in simulated granite faults during and after frictional sliding. *Geofluids*, 14(4):481–494.
- Thiercelin, M. J. and Plumb, R. A. (1994). A Core-Based Prediction of Lithologic Stress Contrasts in East Texas Formations. *SPE Formation Evaluation*, 9(04):251–258.

Bibliography

- Tinti, E., Fukuyama, E., Piatanesi, A., and Cocco, M. (2005a). A kinematic source-time function compatible with earthquake dynamics. *Bulletin of the Seismological Society of America*, 95(4):1211–1223.
- Tinti, E., Spudich, P., and Cocco, M. (2005b). Earthquake fracture energy inferred from kinematic rupture models on extended faults. *Journal of Geophysical Research: Solid Earth*, 110(12):1–25.
- Toro, G. D., Pennacchioni, G., and Nielsen, S. (2009). Chapter 5 pseudotachylytes and earthquake source mechanics. In *Fault-Zone Properties and Earthquake Rupture Dynamics*, volume 94 of *International Geophysics*, pages 87 – 133. Academic Press.
- Tsutsumi, A. and Shimamoto, T. (1997). High-velocity frictional properties of gabbro. *Geophysical Research Letters*, 24(6):699–702.
- Tullis, T. and Goldsby, D. (2004). Laboratory experiments on fault shear resistance relevant to coseismic earthquake slip.
- Tullis, T. E. and Weeks, J. D. (1986). Constitutive behavior and stability of frictional sliding of granite. *Pure and Applied geophysics*, 124(3):383–414.
- Uenishi, K. and Rice, J. R. (2003). Universal nucleation length for slip-weakening rupture instability under nonuniform fault loading. *Journal of Geophysical Research: Solid Earth*, 108(B1).
- Ujiie, K., Tanaka, H., Saito, T., Tsutsumi, A., Mori, J. J., Kameda, J., Brodsky, E. E., Chester, F. M., Eguchi, N., and Toczko, S. (2013). Low coseismic shear stress on the tohoku-oki megathrust determined from laboratory experiments. *Science*, 342(6163):1211–1214.
- Ujiie, K., Tsutsumi, A., and Kameda, J. (2011). Reproduction of thermal pressurization and fluidization of clay-rich fault gouges by high-velocity friction experiments and implications for seismic slip in natural faults. *Geological Society, London, Special Publications*, 359(1):267–285.
- Valley, B. and Evans, K. F. (2019). Stress magnitudes in the basel enhanced geothermal system. *International Journal of Rock Mechanics and Mining Sciences*, 118:1 – 20.
- van Elk, J., Doornhof, D., Bommer, J. J., Bourne, S. J., Oates, S. J., Pinho, R., and Crowley, H. (2017). Hazard and risk assessments for induced seismicity in groningen. *Netherlands Journal of Geosciences*, 96(5):s259–s269.
- van Thienen-Visser, K. and Breunese, J. N. (2015). Induced seismicity of the groningen gas field: History and recent developments. *The Leading Edge*, 34(6):664–671.

- Venkataraman, A. and Kanamori, H. (2004). Observational constraints on the fracture energy of subduction zone earthquakes. *Journal of Geophysical Research*, 109.
- Verberne, B. A., Niemeijer, A. R., De Bresser, J. H. P., and Spiers, C. J. (2015). Mechanical behavior and microstructure of simulated calcite fault gouge sheared at 20–600°C: Implications for natural faults in limestones. *Journal of Geophysical Research: Solid Earth*, 120(12):8169–8196.
- Verberne, B. A., Plümpner, O., De Winter, D. A. M., and Spiers, C. J. (2014a). Superplastic nanofibrous slip zones control seismogenic fault friction. *Science*, 346(6215):1342–1344.
- Verberne, B. A., Spiers, C. J., Niemeijer, A. R., De Bresser, J. H. P., De Winter, D. A. M., and Plümpner, O. (2014b). Frictional properties and microstructure of calcite-rich fault gouges sheared at sub-seismic sliding velocities. *Pure and Applied Geophysics*, 171(10):2617–2640.
- Verdon, J. P., Stork, A. L., Bissell, R. C., Bond, C. E., and Werner, M. J. (2015). Simulation of seismic events induced by CO₂ injection at In Salah, Algeria. *Earth and Planetary Science Letters*, 426:118 – 129.
- Viesca, R. C. and Garagash, D. I. (2015). Ubiquitous weakening of faults due to thermal pressurization. *Nature Geoscience*, 8(11):875–879.
- Violay, M. (2014). GSA Data Repository 2014 007 M. Violay* et al. pages 1–13.
- Violay, M., Di Toro, G., Gibert, B., Nielsen, S., Spagnuolo, E., Del Gaudio, P., Azais, P., and Scarlato, P. G. (2014a). Effect of glass on the frictional behavior of basalts at seismic slip rates. *Geophysical Research Letters*, 41(2):348–355.
- Violay, M., Di Toro, G., Nielsen, S., Spagnuolo, E., and Burg, J. P. (2015). Thermo-mechanical pressurization of experimental faults in cohesive rocks during seismic slip. *Earth and Planetary Science Letters*, 429:1–10.
- Violay, M., Nielsen, S., Gibert, B., Spagnuolo, E., Cavallo, A., Azais, P., Vinciguerra, S., and Di Toro, G. (2014b). Effect of water on the frictional behavior of cohesive rocks during earthquakes. *Geology*, 42(1):27–30.
- Violay, M., Nielsen, S., Spagnuolo, E., Cinti, D., Di Toro, G., and Di Stefano, G. (2013). Pore fluid in experimental calcite-bearing faults: Abrupt weakening and geochemical signature of co-seismic processes. *Earth and Planetary Science Letters*, 361:74–84.
- Violay, M., Passelegue, F., Spagnuolo, E., Di Toro, G., and Cornelio, C. (2019). Effect of water and rock composition on re-strengthening of cohesive faults during the deceleration phase of seismic slip pulses. *Earth and Planetary Science Letters*, 522:55–64.

Bibliography

- Violay, M., Pezard, P. A., Ildefonse, B., Belghoul, A., and Laverne, C. (2010). Petrophysical properties of the root zone of sheeted dikes in the ocean crust: A case study from Hole ODP/IODP 1256D, Eastern Equatorial Pacific. *Tectonophysics*, 493(1-2):139–152.
- Walker, A., Rutter, E., and Brodie, K. (1990). Experimental study of grain-size sensitive flow of synthetic, hot-pressed calcite rocks. *Geological Society, London, Special Publications*, 54(1):259–284.
- Walsh, F. R. and Zoback, M. D. (2016). Probabilistic assessment of potential fault slip related to injection-induced earthquakes: Application to north-central Oklahoma, USA. *Geology*, 44(12):991–994.
- Wang, R., Gu, Y. J., Schultz, R., Kim, A., and Atkinson, G. (2016). Source analysis of a potential hydraulic-fracturing-induced earthquake near Fox Creek, Alberta. *Geophysical Research Letters*, 43(2):564–573.
- Wang, W. and Scholz, C. H. (1995). Micromechanics of rock friction: 3. quantitative modeling of base friction. *Journal of Geophysical Research: Solid Earth*, 100(B3):4243–4247.
- Weingarten, M., Ge, S., Godt, J. W., Bekins, B. A., and Rubinstein, J. L. (2015). High-rate injection is associated with the increase in U.S. mid-continent seismicity. *Science*, 348(6241):1336–1340.
- Wibberley, C. A. and Shimamoto, T. (2005). Earthquake slip weakening and asperities explained by thermal pressurization. *Nature*, 436(7051):689–692.
- Wildenschild, D., Armstrong, R. T., Herring, A. L., Young, I. M., and Carey, J. W. (2011). Exploring capillary trapping efficiency as a function of interfacial tension, viscosity, and flow rate. *Energy Procedia*, 4:4945–4952.
- Williams, B. (1970). Fluid loss from hydraulically induced fractures. *Journal of Petroleum Technology*, 22:882 – 888.
- Wilson, B., Dewers, T., Reches, Z., and Brune, J. (2005). Particle size and energetics of gouge from earthquake rupture zones. *Nature*, 434(7034):749–752.
- Wilson, M. P., Foulger, G. R., Gluyas, J. G., Davies, R. J., and Julian, B. R. (2017). HiQuake: The Human-Induced Earthquake Database. *Seismological Research Letters*, 88(6):1560–1565.
- Wong, T.-f. (1982). Shear fracture energy of Westerly granite from post-failure behavior. *Journal of Geophysical Research: Solid Earth*, 87(B2):990–1000.
- Wu, Q., Chapman, M., and Chen, X. (2018). Stress-Drop Variations of Induced Earthquakes in Oklahoma. *Bulletin of the Seismological Society of America*, 108(3A):1107–1123.

- Ye, Z. and Ghassemi, A. (2018). Injection-Induced Shear Slip and Permeability Enhancement in Granite Fractures. *Journal of Geophysical Research: Solid Earth*, 123(10):9009–9032.
- Yeck, W. L., Block, L. V., Wood, C. K., and King, V. M. (2015). Maximum magnitude estimations of induced earthquakes at Paradox Valley, Colorado, from cumulative injection volume and geometry of seismicity clusters. *Geophysical Journal International*, 200(1):322–336.
- Yuan, D., Shen, X., Sui, X., and Wang, B. (2015). Chemical compositions and viscosity-temperature characteristics of produced fluid from high concentrated polymer flooding. *Journal of Applied Science and Engineering Innovation Vol*, 2(4):106–111.
- Zhang, G., Liu, H., Zhang, J., Wu, H., and Wang, X. (2010). Three-dimensional finite element simulation and parametric study for horizontal well hydraulic fracture. *Journal of Petroleum Science and Engineering*, 72(3):310 – 317.
- Zhang, H., Eaton, D. W., Rodriguez, G., and Jia, S. Q. (2019). Source-Mechanism Analysis and Stress Inversion for Hydraulic-Fracturing-Induced Event Sequences near Fox Creek, Alberta. *Bulletin of the Seismological Society of America*, 109(2):636–651.
- Zheng, G. and Rice, J. R. (1998). Conditions under which velocity-weakening friction allows a self-healing versus a cracklike mode of rupture. *Bulletin of the Seismological Society of America*, 88(6):1466–1483.
- Zoback, M., Rummel, F., Jung, R., and Raleigh, C. (1977). Laboratory hydraulic fracturing experiments in intact and pre-fractured rock. *International Journal of Rock Mechanics and Mining Sciences & Geomechanics Abstracts*, 14(2):49 – 58.
- Zoback, M. D. (2007a). *Reservoir Geomechanics*. Cambridge University Press, Cambridge.
- Zoback, M. D. (2007b). *Rock failure in compression, tension and shear*, page 84–139. Cambridge University Press.
- Zoback, M. D. and Harjes, H.-P. (1997). Injection-induced earthquakes and crustal stress at 9 km depth at the KTB deep drilling site, Germany. *Journal of Geophysical Research: Solid Earth*, 102(B8):18477–18491.
- Zoback, M. D. and Kohli, A. H. (2019). *Unconventional reservoir geomechanics*. Cambridge University Press.

Chiara Cornelio

Personal Information

Name and Surname Chiara Cornelio
Birthday 16 May 1991
OrcID 0000-0003-2009-4123

Education

- 05/2016-now **Ph.D**, *Laboratory of Experimental Rock Mechanincs, EPFL*, Lausanne, CH.
Working thesis title: Mechanical behaviour of lubricated faults during earthquakes nucleation and propagation. Supervisor: Marie Violay
- 09/2013-12/2015 **Civil Engineering, Master Degree**, *Politecnico di Torino*, Torino, IT, 106/110.
Thesis title: Geothermal activation of Line 2 of Turin metro. Supervisors: Marco Barla, Alice Di Donna
- 09/2010-07/2013 **Civil and environmental Engineering, Bachelor Degree**, *Univeristà Politecnica delle Marche*, Ancona, IT, 106/110.
Thesis title: Comparison of Italian and European Geotechnical regulation. Supervisor: Giuseppe Scarpelli

Publications and Conferences

Publications in peer-reviewed scientific journals

- [1] C. Cornelio, F. X. Passelègue, E. Spagnuolo, G. Di Toro, and M. Violay. Effect of Fluid Viscosity on Fault Reactivation and Coseismic Weakening. *J. Geophys. Res. Solid Earth*, 125(1):1–18, jan 2020. ([Link](#)).
- [2] C. Cornelio, E. Spagnuolo, G. Di Toro, S. Nielsen, and M. Violay. Mechanical behaviour of fluid-lubricated faults. *Nat. Commun.*, 10(1):1274, mar 2019. ([Link](#)).
- [3] C. Cornelio and M. Violay. Effect of fluid viscosity on earthquake nucleation. *Geophysical Research Letters*, 2020. ([Link](#)).
- [4] C. Cornelio and M. Violay. Parametric analysis of the elastohydrodynamic lubrication efficiency on induced seismicity. *Geophysical Journal International*, 222(1):517–525, 04 2020. ([Link](#)).
- [5] M. Violay, F. Passelegue, E. Spagnuolo, G. Di Toro, and C. Cornelio. Effect of water and rock composition on re-strengthening of cohesive faults during the deceleration phase of seismic slip pulses. *Earth Planet. Sci. Lett.*, 522:55–64, sep 2019. ([Link](#)).

Peer-reviewed conference proceedings

- [6] C. Cornelio, A. Di Donna, and M. Barla. Energy diaphragm walls for Turin metro. In *Eur. Geotherm. Congr.*, number Sept, pages 19–24, Strasbourg, France, 2016. ([Link](#)).
- [7] C. Cornelio, E. Spagnuolo, G. Di Toro, and M. Violay. Fluid viscosity controls earthquakes nucleation. In *Int. Symp. Energy Geotechnics SEG-2018*, Lausanne, 2018. ([Link](#)).

Talks and Poster presentations

- Dec 2019 **AGU Fall Meeting 2019**, *Earthquake reactivation and seismic slip in presence of viscous fluids*, C. Cornelio, F.X. Passelegue, E. Spagnuolo, G. Di Toro, M. Violay.
- Jul 2019 **Geoproc 2019**, *Role of fluid viscosity in earthquakes nucleation*, C. Cornelio, F.X. Passelegue, E. Spagnuolo, G. Di Toro, M. Violay.
- Apr 2019 **EGU General Assembly 2019**, *Earthquake nucleation in presence of viscous fluids: Thermal Pressurization or Elastohydrodynamic Lubrication?*, C. Cornelio, F.X. Passelegue, E. Spagnuolo, G. Di Toro, M. Violay.
- Dec 2018 **16th Swiss Geoscience Meeting**, *The different effect of fluid viscosity in earthquake nucleation and propagation.*, Cornelio C., Passelegue F., Spagnuolo E., Nielsen S., Di Toro G., Violay M..
- Apr 2018 **EGU General Assembly 2018**, *Fluid viscosity controls earthquakes nucleation*, Cornelio C., Passelegue F., Spagnuolo E., Di Toro G., Violay M..
- Oct 2017 **EARTHQUAKES**, *Effect of fluid viscosity on fault frictional behavior*, C. Cornelio; E. Spagnuolo; G. Di Toro; M. Violay.
- Apr 2017 **EGU General Assembly 2017**, *Effect of fluid viscosity on fault frictional behavior*, C. Cornelio; E. Spagnuolo; G. Di Toro; M. Violay.
- Nov 2016 **14th Swiss Geoscience Meeting**, *Viscosity fluid influence on stick-slip motions*, C. Cornelio; M. Violay; E. Spagnuolo.

Invited Talk

- Oct 2018 **GeoMod 2018**, *Mechanical behaviour of fluid-lubricated faults*, C. Cornelio, E. Spagnuolo, F.X. Passelegue, S. Nielsen, G. Di Toro, M. Violay.

Teaching activities and supervision of students

Teaching assistant

- Bachelor courses: Rock Mechanics and Tunnelling Engineering (Autumn 2016, Autumn 2017, Autumn 2018, Autumn 2019)
- Master courses: Geophysics for Engineers (Spring 2017, Spring 2018, Spring 2019)

Co-supervisor Bachelor and Master projects

- Fikret Can Yilmaz, Influence of Roughness on Joint Mechanical Behavior (2018)
- Matthias Wojnarowicz, Numerical analysis of permeability and shearing test (2018)
- Richard Wyss, Injection of a fluid into a hot rock fractured by fault (2018)
- Ali Nejjar, Westerly granite, Frictional studied compilation (2017)
- Jonas Kasmi, Stimulation chimique dans les reservoirs geothermaux (2017)
- Julien Lepin, Acid stimulation in geothermal reservoirs (2016)

Grants and Fellowship

Jan 2020 **Outstanding Student Presentation Award**, AGU 2019, San Francisco.

For the oral presentation: Earthquake reactivation and seismic slip in presence of viscous fluids

Feb 2016-Apr 2016 **Research fellowship**, Politecnico di Torino, Torino.

Thermo-hydraulic numerical analysis for energy diaphragms.

Oct 2015 **Scholar Grant**, EDISU-Politecnico di Torino, Torino.

Books and journals digitization in collaboration with BCI Library

Sept 2014 **Scholar Grant**, Politecnico di Torino, Torino.

Achievement of first year MS annual CFU

Languages

Italian Mother-tongue

English Fluent, IELTS 6.0 (2016)

French Basic, B1 (2017)

Computer skills

Advanced Matlab, Feflow, Phase2, Rockfall, Dips, SAP2000, Latex

Intermediate Illustrator, SeismoSignal, Strata, AutoCAD, Comsol, Vision64

Basic Python, Ubuntu